The H_3^+ + H_2 isotopic system

Origin of deuterium astrochemistry

Inaugural-Dissertation
zur
Erlangung des Doktorgrades
der Mathematisch-Naturwissenschaftlichen Fakultät
der Universität zu Köln

vorgelegt von

Edouard Hugo
aus Alençon

Köln 2008

Berichterstatter: Prof. Dr. S. Schlemmer
                            Prof. Dr. P. Jensen

Tag der mündlichen Prüfung: 10 Februar 2009

"Neither North nor South will overcome their addiction to growth without a collective and comprehensive detoxification programme. The growth doctrine is like a disease and a drug. As Rahnema says[1], Homo economicus had two strategies for taking over virgin territories: one operated like HIV, the other like a drug pusher. Growth economics, like HIV, destroys societies immune systems against social ills. And growth needs a constant supply of new markets to survive so, like a drug dealer, it deliberately creates needs and dependencies that did not exist before. The fact that the dealers in the supply chain, mainly transnational corporations, benefit so much from our addiction will make it difficult to overcome. But our ever-increasing consumption is not sustainable; sooner or later we will have to give it up."

Serge Latouche,
Le Monde Diplomatique (english edition), November 2004

[1] Majid Rahnema & Victoria Bawtree, *Quand la misère chasse la pauvreté*

English abstract

Dense cold molecular clouds reckoned to be stellar nurseries are the scene of an extreme molecular deuteration. Despite the cosmic D/H ratio of $\sim 10^{-5}$, molecular species in prestellar cores are observed to contain nearly as much deuterium as hydrogen. This astonishing deuterium enrichment promoted by low temperatures is the work of H_3^+. It is the key species which unlocks the deuterium from its HD reservoir via reactions like $H_3^+ + HD \rightleftharpoons H_2D^+ + H_2$ and drags it further to other species in successive reactions. For this reason, the $H_3^+ + H_2$ isotopic system is outstandingly critical for the astrochemistry of cold environments. However, its understanding is yet incomplete and insufficient.

This thesis thus focuses on the $H_3^+ + H_2$ isotopic system from a theoretical, experimental and astronomical point of view giving a particular look into the role of nuclear spins.

As a first step, the stringent nuclear spin selection rules in associative, dissociative and reactive collisions are investigated. This purely theoretical study zooms into the details of the nuclear spin wavefunctions and shows that their permutation symmetry representation is necessary and sufficient, contrary to their angular momentum representation. Additionally, a new deterministic interpretation of nuclear spins in chemical reactions is proposed.

Based on these considerations, a complete set of state–to–state rate coefficients for all $H_3^+ + H_2$ isotopic variants is calculated using a microcanonical model leaned on phase space theory. An experimental study is conducted in parallel with a 22–pole ion trap apparatus in order to inspect the influences of temperature and H_2 *ortho–to–para* ratio. The good overall agreement between experimental and theoretical results supports the validity and utility of the calculated set of rate coefficients. Furthermore, the potentiality of the 22–pole ion trap apparatus is explored via the Laser Induced Reaction (LIR) technique applied to our system of interest. High resolution overtone, combination and fundamental vibrational spectroscopy of H_2D^+ and D_2H^+ is thereby achieved with cw–OPO and diode lasers.

Finally, astronomical implications are inferred on an observational basis through the case of the prestellar core L183 using simple chemical models which account for the *ortho*, *meta* and *para* characters of the H_3^+ and H_2 isotopologues and rely on the rate coefficients derived in this thesis. Above all, the results show that the non–thermal *ortho–to–para* ratio of H_2 is a serious limiting factor for the enhancement of deuterium fractionations. It is a first–class parameter for the astrochemistry of very cold interstellar medium.

Deutsche Kurzzusammenfassung

Dunkle und kalte molekulare Wolken sind die Geburtsstätten neuer Sterne und ein Ort extremer molekularer Deuterierung. Trotz des kosmischen D/H-Verhältnisses von $\sim 10^{-5}$ beobachtet man in prestellaren Kernen Moleküle, die fast soviel Deuterium wie Wasserstoff enthalten. Diese erstaunliche Anreicherung bei niedrigen Temperaturen ist auf das H_3^+-Ion zurückzuführen. Es ist ein Schlüsselmolekül, welches Deuterium durch Reaktionen der Form $H_3^+ + HD \rightleftharpoons H_2D^+ + H_2$ aus seinem HD Reservoir entnimmt und anderen Spezies in aufeinanderfolgenden Reaktionen weitergibt. Aus diesem Grund ist das $H_3^+ + H_2$ Reaktionssystem in all seinen isotopischen Varianten sehr wichtig für die Astrochemie kalter Regionen. Jedoch ist dessen Verständnis noch unvollständig und unausreichend.

Diese Arbeit widmet sich dem $H_3^+ + H_2$ isotopischen Reaktionssystem aus theoretischer, experimenteller und astronomischer Sicht, mit besonderem Schwerpunkt auf der Rolle der Kernspins.

Als ein erster Schritt werden die Kernspin-Auswahlregeln in assoziativen, dissoziativen und reaktiven Kollisionen untersucht. Diese rein theoretische Arbeit studiert die Details der Kernspinwellenfunktionen und zeigt, dass die Darstellung durch Permutationssymmetrien ausreichend und notwendig ist, die Drehimpulsdarstellung jedoch nicht. Zusätzlich wird eine neue deterministische Interpretation der Kernspins in chemischen Reaktionen vorgeschlagen.

Auf diesen Überlegungen basierend werden mit einem mikrokanonischen Modell die zustandsspezifischen Ratenkoeffizienten aller isotopischen Varianten der Reaktion $H_3^+ + H_2$ berechnet. Ein paralleles Experiment mit einer 22-Pol Ionenfalle untersucht den Einfluss der Temperatur und des ortho-para Verhältnisses von H_2. Die gute Übereinstimmung zwischen Experiment und den Rechnungen unterstützt die Gültigkeit und Nützlichkeit der berechneten Ratenkoeffizienten. Ausserdem wird das Potential der Ionenfalle zusammen mit der Methode der laserinduzierten Reaktionen (LIR) erkundet, um die hier auftauchenden Fragestellungen zu beantworten. Es werden hochauflösende Spektren von Oberton–, Kombinations– und fundamentalen Schwingungsbanden von H_2D^+ und D_2H^+ mit einem cw–OPO und Diodenlasern ausgeführt.

Schliesslich wurde ein astrochemisches Modell auf die Observationen des prestellaren Kerns L183 angewendet. In diesem Modell, in dem die zustandsspezifischen Ratenkoeffizienten dieser Arbeit berücksichtigt wurden, wurde zwischen den *ortho*, *meta* und *para* Zuständen der H_3^+ und H_2 Isotopomere unterschieden. Die Resultate zeigen zuallererst, dass das nichtthermische ortho-para-Verhältnis von H_2 eine erhebliche Begrenzung für die Deuteriumanreicherung darstellt und somit ein wichtiger charakteristischer Parameter für kalte Wolken ist.

Résumé français

Les nuages moléculaires denses, reconnus comme pépinières d'étoiles, sont la scène d'une deutération moléculaire extrême. Malgré le rapport cosmique D/H de $\sim 10^{-5}$, les espèces moléculaires qui sont observées dans les noyaux préstellaires contiennent presque autant de deutérium que d'hydrogène. Cet enrichissement stupéfiant en deutérium promu par les basses températures (~ 10 K) est l'oeuvre de H_3^+. C'est l'espèce clé qui libère le deutérium de son réservoir HD, par le biais de réactions du type $H_3^+ + HD \rightleftharpoons H_2D^+ + H_2$, puis le transfert à d'autres espèces lors de réactions successives. De ce fait le système isotopique $H_3^+ + H_2$ est de première importance pour l'astrochimie des milieux froids. Pourtant sa compréhension est aujourd'hui incomplète et insuffisante.

Cette thèse focalise donc sur le système isotopique $H_3^+ + H_2$ depuis des points de vue théorique, expérimental et astronomique avec une attention particulière pour le rôle des spins nucléaires.

En premier lieu, les règles de sélection de spins nucléaires lors de collisions associatives, dissociatives et réactives sont examinées. Cette étude théorique zoome sur les fonctions d'onde de spin nucléaire démontrant ainsi que leur représentation de symétrie de permutation est nécessaire et suffisante, contrairement à leur représentation de moment angulaire. De plus, une nouvelle interprétation déterministe des spins nucleaires pour les réactions chimiques est proposée.

Sur la base de ces considérations, un jeu complet de vitesses de réaction d'état-à-état pour toutes les variantes isotopiques $H_3^+ + H_2$ est calculé d'après un modèle microcanonique reposant sur la théorie de l'espace des phases. Parallèlement, une étude expérimentale est conduite avec un piège à ions à 22 pôles afin d'inspecter les influences de la température et du rapport *ortho*/*para* de H_2. Le bon accord entre résultats théoriques et expérimentaux soutient la validité et l'utilité du jeu de coefficients calculé. Par ailleurs, le potentiel du dispositif expérimental est étendu avec la technique de *Reaction Induite par Laser* appliquée a notre système d'intérêt, réalisant ainsi de la spectroscopie vibrationnelle de H_2D^+ et D_2H^+ avec des lasers de type diode ou OPO.

En dernier lieu, les implications astronomiques sont déclinées sur une base observationnelle du noyau préstellaire L183 en utilisant des modèles chimiques simples qui tiennent compte du caractère *ortho*, *meta* ou *para* des isotopologues de H_3^+ et H_2 et faisant usage des vitesses de réactions calculées dans cette thèse. Les résultats montrent que le rapport *ortho*/*para* de H_2 étant loin de l'équilibre thermique, il est un facteur limitant sérieux pour le fractionnement deutéré de H_3^+. C'est donc un paramètre de premier ordre pour l'astrochimie des milieux froids.

Contents

List of Figures

List of Tables

CHAPTER 1

Introduction

"Progress isn't made by early risers. Its made by lazy men trying to find easier ways to do something."

Robert A. Heinlein, American science-fiction Writer (1907–1988)

According to this quote, astronomy is certainly the biggest progress in History since astronomers keep exploring remote corners of the universe from the earth, just by sitting in a chair all nights long, going to bed when the sun rises. This shortcut doesn't say that, once collected with telescopes, electromagnetic radiations which emanated from space must be quantitatively (flux) and qualitatively (spectral) analysed in order to extract informations on their origin and path. From these astronomical observations spanning from the radio to the X-ray spectral domain, one can identify many classes of objects of different scales, ages, structures and physical conditions. One very efficient tool to investigate objects, in particular in the Milky Way, is to use gas phase molecular species as proxies by tracing local temperatures, densities, electromagnetic fields or dynamics with their characteristic spectra. This technique boomed in the late 60's thanks to the advent of major technical developments in radio astronomy. With this new possibility to probe pure rotational transitions and cool media, the molecular zoo of space had been unveiled and the interstellar medium which was considered as chemically sterile during the first mid-20$^{\text{th}}$ was about to become a new topic of great interest.

As of November 2008, most of the 230 detected species[1] have been identified beyond doubts by means of their rotational spectra, essentially in the interstellar medium. The majority are neutral molecules, some common on earth like H_2O, NH_3, $NaCl$ or CO_2 and some more exotic like OH, CH or NH_2 radicals as well as carbon chains like l-C_3H_2, c-H_2C_3O, C_5 or $HC_{11}N$ which can be linear or cyclic, saturated or unsaturated. Complex organic molecules such as hydrocarbons (CH_2CHCH_3), alcohols (CH_3OH, CH_2CHOH), carboxylic acids (CH_3COOH), aldehydes (CH_3CH_2CHO), sugars (CH_2OHCHO), amides (CH_3CONH_2) and amines (NH_2CH_2CN)

---

[1]including isotopologues and isotopomers. See http://astrochemistry.net and http://www.astrochymist.org and references therein.

1

are also found suggesting the presence of prebiotic molecules although species larger than 10 nuclei are still rare. About 30 cations like N_2H^+, HCO^+ or HCS^+ and recently 5 anions similar to C_6H^- and C_5N^- have also been identified. This hunt for new species is fruitful every year thanks to combined efforts in characterising their spectra in the laboratories and developing more powerful and sensitive observation facilities, not to forget the necessary softwares and databases to handle the enormous quantities of produced data.

Detecting and determining the abundance of molecular species in space is by itself a big deal but explaining these abundances and their evolution is another story. This is where astrochemistry begins.

1.1 ASTROCHEMISTRY

1.1.1 Chemical networks

The number density of a species depends on the processes which lead to its production and destruction. In the gas phase, regarding the low densities of the interstellar medium, only binary processes involving atoms, molecules, ions, electrons and photons play a significant role. The main processes which modify the bonds between nuclei and electrons are

- Ion–neutral reaction $\qquad XY^+ + Z \quad \longrightarrow \quad X + YZ^+$
- Neutral–neutral reaction $\qquad XY + Z \quad \longrightarrow \quad X + YZ$
- Collisional dissociation $\qquad XY + Z \quad \longrightarrow \quad X + Y + Z$
- Charge–transfer reaction $\qquad X^+ + Y \quad \longrightarrow \quad X + Y^+$
- Associative detachment $\qquad X^- + Y \quad \longrightarrow \quad XY + e^-$
- Radiative association $\qquad X^+ + Y \quad \longrightarrow \quad XY^+ + h\nu$
- Dissociative recombination $\qquad XY^+ + e^- \quad \longrightarrow \quad X + Y$
- Radiative attachement $\qquad X + e^- \quad \longrightarrow \quad X^- + h\nu$
- Photoionisation $\qquad X + h\nu \quad \longrightarrow \quad X^+ + e^-$
- Photodissociation $\qquad XY + h\nu \quad \longrightarrow \quad X + Y$

collisional processes being described with rate coefficients in units of $\mathrm{cm^3 s^{-1}}$ and photo-processes with rates in $\mathrm{s^{-1}}$.

The load of species are interconnected by a plethora of reactions forming a chemical network. The two largest databases for astrochemistry are *UDFA* [1] and *OSU*[2] both containing ~ 4500 gas-phase reactions among ~ 450 species. About half of these databases concern ion–neutral reactions which are of central importance despite the low abundance of ions because they are barrierless in most cases hence very efficient. Astrochemical models are usually run by

---

[2]available at http://www.udfa.net/ and http://www.physics.ohio-state.edu/ eric/research.html

plugging these rates into systems of ordinary differential equations supplied with initial abundances and physical conditions like temperature, density and radiation field in order to obtain species' steady–state or time–dependant number densities. One of the models' Achilles heel is the uncertainty which lies in the rate coefficients of poorly understood and critical reactions [2] often due to a lack of experimental measurements.

Generally talking, the faster its production paths and the slower its destruction paths, the more abundant the species. Conversely, a species will be almost inexistent if its productions are inefficient and destructions efficient. Nevertheless, species which are non-abundant because transient can still be important nodes in a chemical network. That said, the abundance of species depend first of all on the abundance of their building blocks : the nuclei.

1.1.2 Hydrogen, the ubiquitous nucleus

Nuclei are essentially synthesised in three distinct mechanisms, namely the Big Bang, stellar and explosive nucleosynthesis.

In the Big Bang scenario, the known universe started from a singularity with quasi–infinite temperature and density and cooled during rapid expansion. In a nutshell, few minutes after the beginning, the universe had cooled down sufficiently ($\sim 10^9$ K) to freeze out the primordial quark–gluon plasma into stable protons and neutrons (baryogenesis) which then started to fuse to form heavier nuclides (nucleogenesis). Some ten minutes later, the temperature and density of the universe fell below that which is required for thermonuclear fusion. The brevity of nucleogenesis prevented nuclides heavier than beryllium from forming resulting in the approximative primeval abundances [3]

$$
\begin{array}{ll}
^1\mathrm{H} & 1 \\
^4\mathrm{He} & 1.10^{-1} \\
^2\mathrm{H} & 3.10^{-5} \\
^3\mathrm{He} & 1.10^{-5} \\
\mathrm{Li} + \mathrm{Be} & < 10^{-9}
\end{array}
$$

Heavier elements[3] like C, N and O did not exist until stellar nucleosynthesis began. Stars arise from the interstellar medium, they are nuclear furnaces ($> 10^7$ K) which burn their reservoir of ^{1}H and eventually ^{4}He generating heavier elements from carbon to iron through a complex chain of nuclear fusion processes. The nucleosynthesis during their evolution as well as the death of a star strongly depends on its mass. Lower mass stars usually end as red giants blowing a significant fraction of their mass in strong stellar winds relatively rich in heavy elements created within the star. Higher mass stars tend to explode in intense bursts when their nuclear fuel runs out. These powerful explosions like supernovae also produce traces of nuclides heavier than iron. In any case, instantly or gradually, stars inseminate the interstellar medium with

---

[3]Astronomers call them "metals".
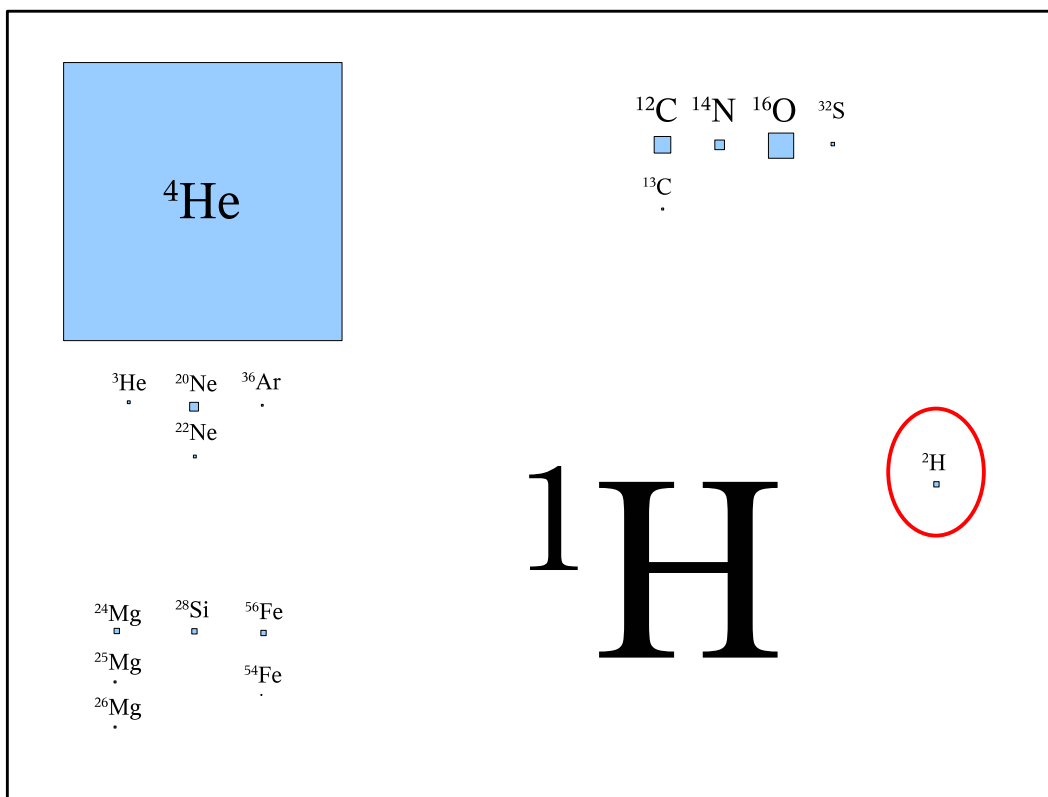
Figure 1.1: Most abundant chemical elements in our solar system [4]. The shaded squares represent their abundances with respect to ^{1}H (the full rectangle). Elements with abundances $< 10^{-5}$ are not shown.

elements heavier than helium. This permanent transformation of cosmic material in successive star factories is known as *astration*.

Although the relative abundances of elements can vary through the Milky Way, the abundances found in the solar system are well representative. As may be seen in figure 1.1, hydrogen is obviously ubiquitous, including in the astrochemical network.

1.1.3 Trihydrogen cation H_3^+

H_3^+ was first discovered by Thomson [5] in 1911 using plasma discharges and an early form of mass spectrometry. In 1961, Martin et al. [6] first suggested that H_3^+ may be present in the interstellar medium given the overwhelming abundance of hydrogen. It took 27 years and the particular perseverance of Takeshi Oka to confirm this hypothesis. As may be inferred from

its symmetry[4], the rotational spectrum of H_3^+ is forbidden due to lack of a permanent dipole moment therefore this species should be detected through vibrational transitions. The first laboratory detection occurred in 1980 and the complete spectrum is by now well characterised [7]. After several unfruitful attempts, H_3^+ was finally spotted in the Jovian ionosphere in 1989 [8] and in the interstellar medium in 1996 [9].

In 1973, Herbst and Klemperer [10] as well as Watson [11] suggested that H_3^+ might be responsible for the formation of many molecular ions. Indeed, the pivotal role of H_3^+ in the gas-phase chemistry of the interstellar medium is unparallelled by any other molecular ion. It can be summarised briefly in the following way: Cosmic rays[5] ionise molecular hydrogen which yields a trihydrogen cation upon an exothermic reaction with the next colliding molecular hydrogen

$$H_2 \; + \; \zeta \quad \rightarrow \quad H_2^+ \; + \; e^- \tag{1.1}$$

$$H_2^+ \; + \; H_2 \quad \rightarrow \quad H_3^+ \; + \; H \; + \; 1.5 \; eV \tag{1.2}$$
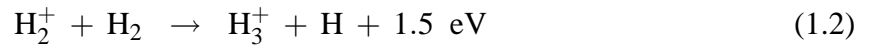
The trihydrogen cation is stable upon collisions with molecular hydrogen as well as atomic hydrogen and helium. However, given the low proton affinity of molecular hydrogen, it will often transfer a proton to other species

$$H_3^+ \; + \; H_2 \quad \rightarrow \quad H_3^+ \quad + \; H_2 \tag{1.3}$$

$$H_3^+ \; + \; X \quad \rightarrow \quad XH^+ \; + \; H_2 \; + \; \Delta E \tag{1.4}$$

Most of the ion-neutral chemistry which is triggered by cosmic ray ionisation goes through the H_3^+ cation according to this simple scheme. This justifies why the *protonated molecular hydrogen* is sometimes referred to as the *universal protonator*. As will be shown shortly, its role is even more critical when it comes to deuterium astrochemistry.

1.2 DEUTERIUM ASTROCHEMISTRY

The deuterium abundance relative to hydrogen (see Fig. 1.1) is $D/H = 1.5 \times 10^{-5}$ in the ~ 100 parsec *Local Bubble* surrounding the solar system but significant variations are found throughout the Milky Way [12]. The depletion with respect to the primeval abundance – the *astration factor* – reflects the past stellar activity which does not produce deuterium and consumes it preferentially because of its low fusion temperature (5×10^6 K).

The proto–solar D/H ratio derived from measurements of Jupiter's and Saturn's atmospheres [13] is comparable to that of the Local Bubble. However, the D/H ratio is not constant throughout the solar system. For example, the terrestrial D/H ratio derived from the ocean's water

---

[4]The three nuclei form an equilateral triangle held together by two delocalised electrons

[5]Cosmic rays are highly energetic particles ($^1H^+$, $^4_2He^{2+}$, e^- or photons) travelling through the interstellar medium and whose origin is still unclear.

is 1.6×10^{-4}. A D/H ratio of 3×10^{-4} has been observed in 3 comets' water [14], 1.3×10^{-4} in Titan's methane [15] and $\sim 6 \times 10^{-5}$ in Uranus' and Neptune's methane and molecular hydrogen [13]. These local D/H ratios are all inferred from the deuterium fractionation of observed molecular species according to the simple statistical relation

$$\frac{XH_nD_m}{XH_{n+m}} = C_{n+m}^m \left(\frac{D}{H}\right)^m \tag{1.5}$$

where XH_{n+m} is the fully hydrogenated species, XH_nD_m its m–times deuterated isotopologue and C_{n+m}^m the binomial coefficient.

It is clear that the inhomogeneous enhancement of deuterium among solar orbiting objects can only be the indirect consequence of the D/H mass ratio of 2. Physical processes such as thermal evaporation, diffusion and gravitational escape can in principle contribute to the segregation of the heavier isotopologues toward these objects, particularly during their formation epoch [16]. But the prime origin of their deuterium enhancement lies in the chemistry of the pre– and proto–solar nebula before these objects started to form; that is during early stages of solar formation when planetary science and cosmochemistry meets with astrochemistry of star forming regions.

1.2.1   Cold space and star formation

Star formation occurs in molecular clouds which are the coldest and densest regions of our galaxy (see Table 1.1). Eventhough they represent a small fractional volume of the Milky Way, the overall mass they represent is very significant. These extended structures, sometimes called *stellar nurseries* are inhomogeneous presenting clumpy substructures of higher densities and lower temperatures ($n_H \approx 10^6$ cm^{-3}, T $\leq$ 10 K). Such dense cold and optically thick cores give birth to stars according to the scenario described in Fig. 1.2 . The reader is also urged to a thorough review on the early physical and chemical conditions of star forming regions [18].

Table 1.1: Classes of environments in the interstellar medium [17]

Environment	Fractional volume	Scale height (pc[a])	Temperature (K)	Density (atoms/cm^3)	State of hydrogen
Molecular clouds	< 1 %	70	$10 - 20$	$10^2 - 10^6$	molecular
Cold neutral medium	$1 - 5$ %	$100 - 300$	$50 - 100$	$20 - 50$	neutral atomic
Warm neutral medium	$10 - 20$ %	$300 - 400$	$6000 - 10000$	$0.2 - 0.5$	neutral atomic
Warm ionised medium	$20 - 50$ %	1000	8000	$0.2 - 0.5$	ionised
Hot ionised medium	$30 - 70$ %	$1000 - 3000$	$10^6 - 10^7$	$10^{-4} - 10^{-2}$	ionised

[a]pc = parsec, astronomical length unit of approximatively 3×10^{13} km, 3.26 light years or 2×10^5 AU.
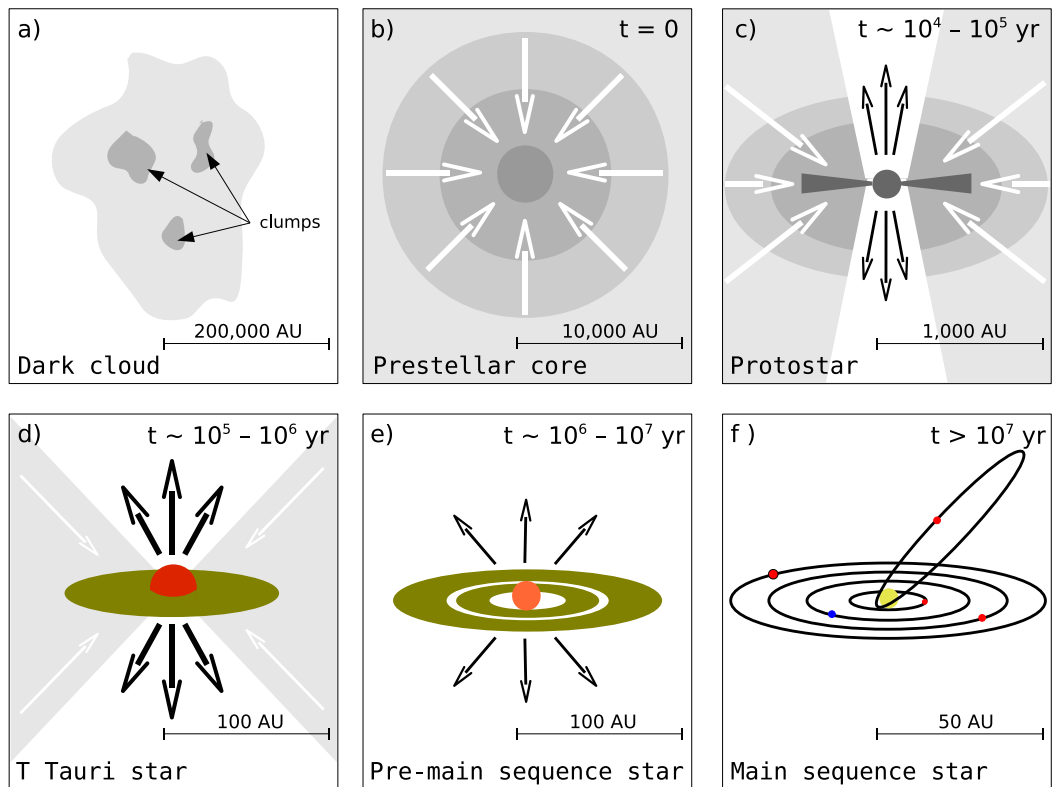
Figure 1.2: The birth of a Sun-like star can be described in a series of stages that span more than 50 million years (after [19, 20]). **(a)** Star formation begins inside dark interstellar clouds containing high-density regions **(b)** which become gravitationally unstable and collapse under their own weight. **(c)** The collapsing core forms a protostar and a circumstellar disk rapidly accreting mass from the surrounding envelope of gas and dust, relieving the build-up of angular momentum in bipolar outflows. **(d)** As the dusty envelope dissipates, the object powered by gravitational energy becomes a T Tauri star visible at optical wavelengths for the first time. These objects can often be recognised in telescopic images by the presence of a protoplanetary disk. **(e)** After a few million years the dusty disk dissipates, leaving a bare pre-main-sequence star at its centre. In some instances, a remnant disk with debris and planetesimals may continue to orbit the star. **(f)** The star continues its gravitational collapse to the point where its core temperature becomes hot enough for nuclear fusion, and the object becomes a main-sequence star with an eventual planetary system. (AU = astronomical unit, the average distance between the Sun and the Earth.)
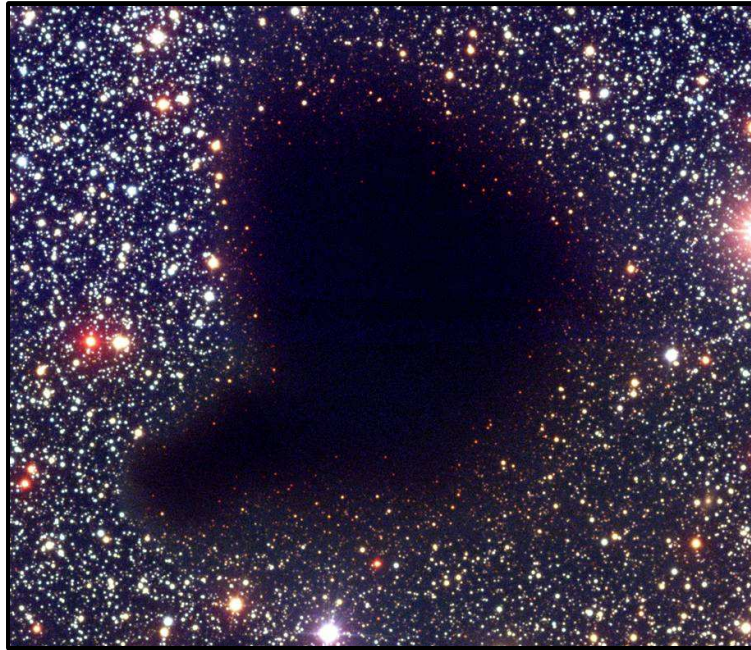
Figure 1.3: The dense molecular cloud Barnard 68, a prestellar core probably in its early phase of collapse. The dust and molecular gas at high concentration absorb practically all the visible light emitted from background stars. Distance $\sim$ 100–150 pc, diameter $\sim$ 0.2 pc, temperature $\sim$ 10 K, H_2 central density $\sim 2 \times 10^5$ cm^{-3}.

Molecular clouds form from the mild temperature neutral medium thanks to the radiative cooling induced by spontaneous emission of its atomic and molecular material. As suggested by their appellation, the hydrogen there is essentially in its most stable form *i.e.* molecular. The H_2 formation by radiative association of atomic hydrogen in binary collisions is extremely inefficient because of the very low quadrupole spontaneous emission probabilities from the molecule's continuum into stable vibrational levels during its short lifetime. H_2 formation thus requires a third body to release the excess energy in order to stabilise, and this role is played by grains

$$H + H \quad\quad \rightarrow \quad H_2^* \quad\quad \nrightarrow H_2 + h\nu \quad (\leq 4.48\text{eV}) \quad\quad\quad (1.6)$$

$$H + H + \text{grain} \rightarrow H_2^* + \text{grain} \rightarrow H_2 + \text{grain}^* \quad\quad\quad (1.7)$$
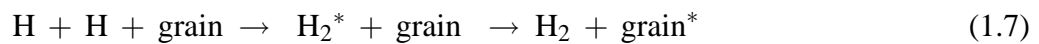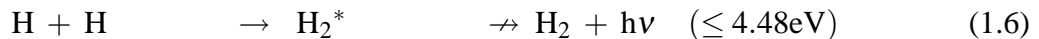
Interstellar grains are mainly carbonaceous and siliceous submicrometric aggregates, hence the term interstellar *dust*. Their presence in the interstellar medium has strong implications on radiative transfer and thermal balance as well as on chemistry. Toward low temperatures, gas phase species freeze onto the grains forming a layer of ice. In extremely dense and cold cores, depletion of gas phase metallic species can be very important and icy grains can be as large as few $\sim 0.1\mu$m in radius and represent up to 1% of the mass [21]. Chemisorbed or physisorbed

species, especially the light and small hydrogen and deuterium atoms, can diffuse on ice surfaces or to a lesser extent into their mantle and find reactant partners. Since the interaction timescales of the reactants are dramatically increased as compared to the gas phase, some reactions are far more probable on grains, in particular associative reactions regarding their ternary character as illustrated in Eq. 1.7 . Interstellar dust thus act as a catalyst by opening new reaction paths, extending the chemical network to larger molecules that otherwise cannot form in the gas phase. Complex organic molecules which are synthesised on grains eventually desorb into the gas phase upon exoergic formation, photo–induced desorption or thermal evaporation. Unfortunately, besides their porous structure and inhomogeneous chemical composition, most of the grain and ice processes as those put forward are still poorly understood. Grain–ice chemistry is probably the greatest weakness of astrochemical models and it is the subject of many research projects (see *e.g.* [22–25]).

Nevertheless, it is clear that cold quiescent icy regions are favourable for rich chemistry in contrast to warmer, ionised, photo–dominated or shocked environments where molecular species are exposed to harsh conditions. More surprisingly, these cold regions are also the scene of an extraordinarily rich deuterium chemistry.

1.2.2   Extreme deuteration

Equation 1.5 is based on the assumption that hydrogen and deuterium are equiprobably assimilated in molecular species. Singly, doubly and triply deuterated molecules are thus expected to be fairly, very and extremely rare, respectively. However, about 20 singly, 6 doubly and even 2 triply deuterated species have been observed mostly in prestellar cores and young protostellar objects with deuterium fractionations as large as

$$\frac{XH_nD_m}{XH_{n+m}} \geq C_{n+m}^m \ (0.1)^m \tag{1.8}$$

Comparing Eq. 1.8 to Eq. 1.5 shows that the incorporation of deuterium in molecular species is favoured by ~ 4 orders of magnitude with respect to hydrogen. It appears very likely that the deuterium enhancements found in sun–orbiting objects are the inheritage of an extreme molecular deuteration during early phases of solar formation, but this early deuteration still needs to be explained.

The D/H mass ratio of 2 reduces the frequencies of the vibrational modes involving a deuterium nucleus by a factor of $\sim \sqrt{2}$ with respect to their hydrogenated analogs. Therefore, Zero–Point Vibrational Energies (ZPVE[6]) for deuterated molecular species are lower than their hydrogenated isotopologues. Moreover, larger molecular species tend to a larger isotopic ZPVE differences since a given H or D nucleus is involved in more vibrational modes. We thus have the isotope exchange reactions

$$XH + YD \rightleftharpoons XD + YH + \Delta E \tag{1.9}$$

---

[6]The ZPVE consists of half quantum residual energy in each vibrational mode

9

where the reactions' ZPVE differences ΔE are usually positive when X is larger than Y. It is important to note that ΔE is (i) substantial when the reaction involves molecular hydrogen *i.e.* Y = H and (ii) very important with atomic hydrogen *i.e.* Y = $\emptyset$. Given the Boltzmann behaviour of the reaction's equilibrium constant K [26]

$$K(T) = \frac{[XD][YH]}{[XH][YD]} \propto \exp\left(\frac{\Delta E}{kT}\right) \tag{1.10}$$

it becomes clear that a severe chemical isotopic segregation in favour of the large deuterated molecular species appears for temperatures lower than the activation energy

$$kT < \Delta E \quad \Rightarrow \quad \frac{[XD]}{[XH]} \gg \frac{[YD]}{[YH]} \tag{1.11}$$

The question that persits is how do such deuterium enhancements occur. What are the main routes of the deuterium chemical network ?

1.2.3 H_3^+ isotopologues

The starting point is molecular hydrogen with $HD/H_2 = 3 \times 10^{-5}$ where most of the deuterium of molecular clouds is locked. The H_3^+ cation is the key species which unlocks this deuterium reservoir via three isotope exchange reactions.

$$H_3^+ \;\; + HD \;\; \rightleftharpoons \;\; H_2D^+ \; + \; H_2 \; + \; \Delta E \tag{1.12}$$
$$H_2D^+ \; + HD \;\; \rightleftharpoons \;\; D_2H^+ \; + \; H_2 \; + \; \Delta E \tag{1.13}$$
$$D_2H^+ \; + HD \;\; \rightleftharpoons \;\; D_3^+ \;\; + \; H_2 \; + \; \Delta E \tag{1.14}$$
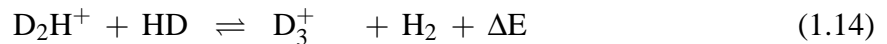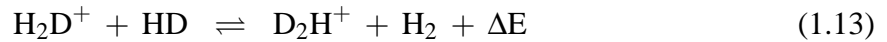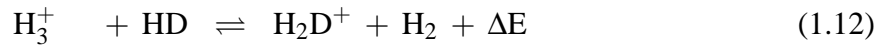
with ΔE = 232, 187 and 234 K respectively. At temperatures as low as 10 K, the equilibria are dramatically shifted in the forward directions corresponding to fast exothermic deuteration reactions with HD and extremely slow endothermic backward reactions with H_2. At such temperatures, D_3^+ can in principle become more abundant than H_3^+. The H_3^+ isotopologues are then destroyed (i) by metallic species in proton (deuteron) transfer reactions (see Eq. 1.4) or (ii) by electrons in dissociative recombination like

$$D_3^+ + e^- \;\; \rightarrow \;\; D + D + D \tag{1.15}$$
$$\rightarrow \;\; D_2 + D \tag{1.16}$$

In the former case (i), the H_3^+ isotopologues pass on directly their deuterium fractionation to other metallic species and in the latter (ii), they enrich the medium with free deuterons both according to

$$\frac{[D]}{[H]} \approx \frac{[XD^+]}{[XH^+]} \approx \frac{[H_2D^+] + 2[D_2H^+] + 3[D_3^+]}{3[H_3^+] + 2[H_2D^+] + [D_2H^+]} \tag{1.17}$$

The atomic deuterium fractionation is spread further on ice surfaces to the complex organic species via association or isotope exchange reactions [27, 28] like

$$CO \xrightarrow{D} DCO \xrightarrow{H} HDCO \xrightarrow{D} CD_2HO \xrightarrow{H} \quad CD_2HOH + H \nrightarrow CH_2DOH + D \qquad (1.18)$$
$$CD_2HOH + D \rightarrow CD_3OH \quad + H + \Delta E$$
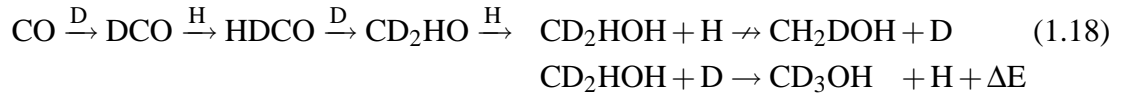
1.2.4 *ortho* and *para*

The H_3^+ cation is thus at the origin of a rich deuterium chemical network. However this digest is somewhat too simple because it should account for the nuclear spins.

Molecular hydrogen is referred as *ortho* or *para* whether his nuclear spins are symmetric or antisymmetric, respectively, with degeneracies of 3 and 1. The same appellations are given to the H_3^+ isotopologues with respect to their indistinguishable hydrogen or deuterium nuclei. According to the molecular symmetry selection rules, the rotational ground states of p–H_2 and o–H_2 are J=0 and J=1, respectively, with an energy difference of 170 K. The thermal *ortho*–to–*para* ratio of H_2 is 3 at high temperature[7] and $9 \times \exp(-170/T)$ at low temperature corresponding to quasi–pure p–H_2 with less than 1 ppm of o–H_2 at 10 K. However, it is unlikely that such purities are reached in molecular clouds since the continuous H_2 formation on grains (see Eq. 1.7) refills the gas phase with an o/p ratio of 3. The dominant relaxation mechanisms for H_2 are proton exchange reactions [29, 30] like

$$o\text{--}H_2 + \quad \tilde{H}^+ \qquad \longrightarrow \quad p\text{--}H\tilde{H} + \quad H^+ \quad + 170 \text{ K} \qquad (1.19)$$
$$o\text{--}H_2 + p\text{--}\tilde{H}_2D^+ \quad \longrightarrow \quad p\text{--}H\tilde{H} + o\text{--}\tilde{H}HD^+ + 84 \text{ K} \qquad (1.20)$$
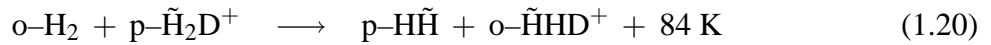
but their efficiency which depend on the abundance of free protons and the H_3^+ isotopologues is not certain and the o/p ratio of H_2 is suspected to be non–thermal in dense cores. These overabundant traces of o–H_2 are probably very important since their 170 K internal energy helps overcoming the endothermicities of reactions 1.12 to 1.14 and shifts the equilibrium back to the purely hydrogenated H_3^+. Moreover, the o/p ratio of H_2 appears to have an influence on the o/p ratios of H_3^+ and H_2D^+ as illustrated in reaction 1.20.

---

[7]H_2 with an *ortho*–to–*para* ratio of 3 is called normal–H_2, abbreviated n–H_2

1.3 THIS THESIS

1.3.1 Aim

Regarding that H_3^+ is a pivotal species in the astrochemical network and that its isotoplogues are at the origin of extreme deuterium fractionations in dense molecular clouds, the $H_3^+ + H_2$ isotopic system appears to be of paramount importance for astrochemical models yet it is only partially understood.

This thesis thus aims at clarifying the connections between the nuclear spins and the deuterium fractionation of the H_3^+ and H_2 isotopologues. The problem is tackled from all three theoretical, experimental and astronomical points of view.

1.3.2 Outline

Chapter 2

We first investigate the role of nuclear spins in associative, dissociative and reactive processes in the *frozen nuclear spin* approximation. This purely theoretical study zooms into the details of the nuclear spin wavefunctions considering their angular momentum and permutation symmetry representations. Pure nuclear spin statistics are dissected among different reaction mechanisms. The symmetry viewpoint is shown to be robust while the angular momentum viewpoint reveals weaknesses and even leads to interpretational paradoxes. A new deterministic Bohmian–like interpretation of nuclear spins which appears better suited for chemical reactions is also proposed.

Chapter 3

Based on these results, focus is set on the rate coefficients of the $H_3^+ + H_2$ isotopic variants at temperatures of astronomical interest (< 50 K) considering the role of nuclear spins and the reaction mechanisms at play. A complete set of state–to–state rate coefficients for the whole $H_3^+ + H_2$ isotopic system is calculated using a microcanonical model based on the conservation of isotopes, nuclear spins, energies and rotational angular momenta. Measurements of this system are carried out in parallel with a 22–pole ion trap apparatus inspecting the influences of temperature and H_2 *ortho*–to–*para* ratio. The rate coefficients and steady–state isotopic fractionations which are obtained support the full-scrambling hypothesis assumed for the calculations at low temperatures and suggest more direct reaction mechanisms toward higher temperatures. The successful comparison between experimental and theoretical results comforts the validity and utility of the calculated set of rate coefficients.

Chapter 4

The potentiality of the 22–pole ion trap apparatus are carried on further by applying the Laser Induced Reaction (LIR) technique to our system of interest in prospect for future measurements of state–specific rate coefficients. H_2D^+ is probed via the LIR scheme

$$
\begin{aligned}
H_2D^+ + H_2 \quad &\nrightarrow \quad H_3^+ + HD \\
\downarrow h\nu \qquad\qquad &\nearrow \\
H_2D^{+*} + H_2 &
\end{aligned}
\tag{1.21}
$$
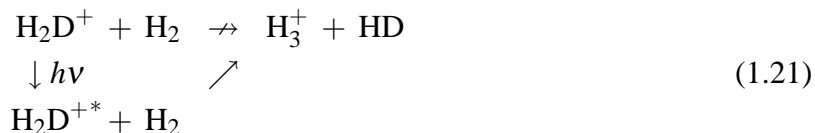
and D_2H^+ via an analogous scheme. Overtone, combination or simple vibrational spectroscopy of H_2D^+ and D_2H^+ in the wavenumber domain $2900 - 3100$ and $6100 - 7300$ cm^{-1} is achieved at high resolution using a cw–OPO and diode lasers. Experimental results are compared to *ab initio* predictions [31]. The LIR technique also serves as a diagnostic tool for the temperature of the ions revealing imperfections of the trap.

Chapter 5

Finally, astronomical implications are explored through the case of L183, a typical prestellar core with a central density of 2×10^6 cm^{-3} and a temperature of 7 K. A steady–state and a time–dependent simple chemical model for prestellar cores are presented. Their chemical network account for the nuclear spin symmetries of the H_3^+ and H_2 isotopologues integrating the rate coefficients calculated in chapter 3 as well as new dissociative recombination rate coefficients. Several parameters of the models are constrained by fitting the observed N_2H^+ deuterium fractionation and o–H_2D^+ abundance of L183. As a result, the prestellar core is estimated to be $\sim$1.5–2$\times10^5$ years old and its H_2 *ortho*–to–*para* ratio is evaluated at 0.05 in its outer layer down to 0.004 in its innermost part. This non-thermal o/p ratio of H_2 is identified as a dominant limiting factor for the H_3^+ deuterium fractionation.

1.3.3 Prospects

Even though the symmetry viewpoint of nuclear spins is sufficient to describe associative, dissociative and reactive processes, the evidenced failure of the angular momentum viewpoint is unsatisfactory and leaves us with an open question calling for further investigations. The deterministic interpretation of nuclear spins proposed here also deserves deeper considerations beyond its counter mainstream character. The sparse literature dedicated to the stringent role of nuclear spins in reactions, an aspect which is often ignored, could be completed following these leads.

Regarding the more specific $H_3^+ + H_2$ isotopic system, the phase space statistical treatment accomplished in this thesis represents a significant theoretical breakthrough. Nevertheless, on the condition that the nuclear spins are well considered, scattering calculations on the potential

13

energy surface would be beneficial. However, the full quantum mechanical level of theory appears difficult given the large size of the system.

The experimental lag with respect to theory can be recovered with state–specific kinetic studies in the laboratory which are in principle feasible with the state selective Laser Induced Reaction technique (LIR). The pure rotational LIR of H_2D^+ and D_2H^+ recently performed in Köln [32] expands the possibilities to two–laser schemes *e.g.* microwave and mid-infrared. In any case, a proper thermalization inside the ion trap will be necessary in order to obtain meaningful and accurate measurements below 20 K where the temperature becomes the most critical parameter.

The astronomical study conducted in this thesis demonstrates for the first time on an observational basis that the non–thermal *ortho*–to–*para* ratio of H_2 is a first–class parameter for the astrochemistry of very cold environments. This brings a new problematic, namely the quantum relaxation of o–H_2 during early phases of stellar formation. Answers will hardly come from the sole L183 prestellar core, a survey of the o/p ratio of H_2 in a sample of prestellar cores using the H_3^+ isotopologues as tracers is highly desirable. Such survey would greatly benefit from the next generation of observational facilities – ALMA, Herschel and SOFIA – which will improve the detection limits of H_2D^+ and D_2H^+ and their spatial resolution.

REFERENCES

[1] J. Woodall, M. Agúndez, A. J. Markwick-Kemper, and T. J. Millar, Astron. Astrophys. **466**, 1197 (2007).

[2] V. Wakelam, E. Herbst, and F. Selsis, Astron. Astrophys. **451**, 551 (2006).

[3] F. Iocco, G. Mangano, G. Miele, O. Pisanti, and P. D. Serpico, ArXiv e-prints (2008), `0809.0631`.

[4] A. G. W. Cameron, Space Science Reviews **15**, 121 (1973).

[5] J. Thomson, Philos. Mag. **21**, 225 (1911).

[6] D. W. Martin, E. W. McDaniel, and M. L. Meeks, Astrophys. J. **134**, 1012 (1961).

[7] B. J. McCall, Ph.D. thesis, AA(Department of Chemistry and Department of Astronomy and Astrophysics, University of Chicago, 5735 S. Ellis Ave., Chicago, IL 60637) (2001).

[8] P. Drossart, J.-P. Maillard, J. Caldwell, S. J. Kim, J. K. G. Watson, W. A. Majewski, J. Tennyson, S. Miller, S. K. Atreya, J. T. Clarke, et al., Nature **340**, 539 (1989).

[9] T. R. Geballe and T. Oka, Nature **384**, 334 (1996).

[10] E. Herbst and W. Klemperer, Astrophys. J. **185**, 505 (1973).

[11] W. D. Watson, Astrophys. J. Lett. **183**, L17 (1973).

[12] J. L. Linsky, ArXiv Astrophysics e-prints (2003), `arXiv:astro-ph/0309255`.

[13] T. Owen and T. Encrenaz, Space Science Reviews **106**, 121 (2003).

[14] H. A. Weaver, M. F. A'Hearn, C. Arpigny, M. R. Combi, P. D. Feldman, G.-P. Tozzi, N. Dello Russo, and M. C. Festou, LPI Contributions **1405**, 8216 (2008).

[15] D. Cordier, O. Mousis, J. I. Lunine, A. Moudens, and V. Vuitton, Astrophys. J. Lett. **689**, L61 (2008).

[16] J. Horner, O. Mousis, Y. Alibert, J. I. Lunine, and M. Blanc, Planet. Space Sci. **56**, 1585 (2008).

[17] K. M. Ferrière, Reviews of Modern Physics **73**, 1031 (2001).

[18] E. A. Bergin and M. Tafalla, Ann. Rev. Astron. Astrophys. **45**, 339 (2007).

[19] M. Hogerheijde, Ph.D. thesis, Dept. of Astronomy, University of California, Campbell Hall, Berkeley, CA 94720, USA (1998).

[20] T. Greene, American Scientist **89**, 316 (2001).

[21] C. M. Walmsley, D. R. Flower, and G. Pineau des Forêts, Astron. Astrophys. **418**, 1035 (2004).

[22] R. T. Garrod, S. L. W. Weaver, and E. Herbst, Astrophys. J. **682**, 283 (2008).

[23] E. Matar, E. Congiu, F. Dulieu, A. Momeni, and J. L. Lemaire, Astron. Astrophys. **492**, L17 (2008).

[24] S. Andersson and E. F. van Dishoeck, Astron. Astrophys. **491**, 907 (2008).

[25] S. Ioppolo, H. M. Cuppen, C. Romanzin, E. F. van Dishoeck, and H. Linnartz, Astrophys. J. **686**, 1474 (2008).

[26] E. Herbst, Astron. Astrophys. **111**, 76 (1982).

[27] N. Watanabe, H. Hidaka, A. Nagaoka, and A. Kouchi, in *Molecules in Space and Laboratory* (2007).

[28] B. Parise, C. Ceccarelli, A. G. G. M. Tielens, A. Castets, E. Caux, B. Lefloch, and S. Maret, Astron. Astrophys. **453**, 949 (2006).

[29] J. Le Bourlot, Astron. Astrophys. **242**, 235 (1991).

[30] D. R. Flower, G. Pineau Des Forêts, and C. M. Walmsley, Astron. Astrophys. **449**, 621 (2006).

[31] O. L. Polyansky and J. Tennyson, J. Chem. Phys. **110**, 5056 (1999).

[32] O. Asvany, O. Ricken, H. S. P. Müller, M. C. Wiedner, T. F. Giesen, and S. Schlemmer, Phys. Rev. Lett. **100**, 233004 (2008).

CHAPTER 2

Nuclear spins in reactive collisions

E. Hugo, S. Schlemmer and P. Jensen

In preparation

T he permutation symmetry algebra reported by Quack [1] and the angular momentum algebra reported by Oka [2] to derive nuclear spin selection rules and statistics for reactives collisions are revisited by working on the wavefunctions using permutation projectors and Clebsch–Gordan coefficients respectively. Both methods are merged to access the complete detail of information and applied to systems up to 5 identical nuclei of spin 1/2, 1 or 3/2. A detailed study of the D_3 system shows that the two algebras are generally inconsistent and that the permutation symmetry informations cannot be neglected, contrary to the angular momentum informations. Finally, we propose a deterministic interpretation of nuclear spin systems and discuss its physical implications.

2.1 INTRODUCTION

The symmetrisation postulate states that the total wavefunction of a system must be symmetric or anti-symmetric upon permutation of two identical bosons or fermions, respectively. It is a stringent selection rule which endows nuclear spins with a very peculiar role in molecular physics. Because of the weakness of hyperfine interactions, one can assume the internal wavefunction of a molecule as the product of a nuclear spin wavefunction and a rovibronic–electron spin wavefunction.

$$\Phi_{\text{tot}} = \Phi_{\text{nspin}} \left(\Phi_{\text{rot}} \Phi_{\text{vib}} \Phi_{\text{elec}} \Phi_{\text{espin}} \right) \tag{2.1}$$

According to the symmetrisation postulate, a symmetrised nuclear spin wavefunction cannot support all symmetrised rovibronic–electron spin wavefunctions which means that the nuclear spin permutation symmetry (*eq.* modification) constrains the accessible sets of rovibronic quantum numbers and energy levels. These nuclear spin symmetries for a molecule are commonly named with the Greek terms *ortho*, *meta* and *para*.

The weak hyperfine interactions can be translated as the *frozen nuclear spin* approximation. In this approximation, the magnetic coupling between nuclear spins and intra– or extra–molecular magnetic fields are neglectable such that the magnetic moment of each nucleus is frozen, *i.e.* its quantised values is strictly conserved and cannot flip to another value. The nuclear spin wavefunction of a given set of nuclei is thereby frozen and its total nuclear spin permutation symmetry, angular momentum and magnetic moment are conserved (*eq.* good) quantum informations or numbers.

It obviously results that whenever sets of nuclei are conserved (*e.g.* spectroscopy and non-reactive collisions), conversions between nuclear spin modifications are strictly forbidden [3–6]:

$$para-\text{NH}_3 \quad + \quad h\nu \quad \quad \nrightarrow \quad ortho-\text{NH}_3 \tag{2.2}$$

$$para-\text{H}_2 \quad + \quad para-\text{H}_2\text{O} \quad \nrightarrow \quad para-\text{H}_2 \quad + \quad ortho-\text{H}_2\text{O} \tag{2.3}$$
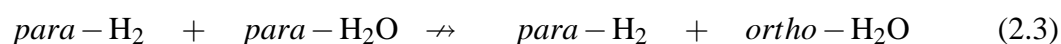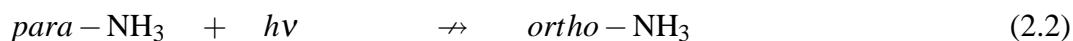
Whereas if the sets of nuclei are rearranged (*e.g.* reactive collisions, radiative associations and dissociative recombinations), new products are formed with their nuclear spin modifications. However, some modifications can be strictly forbidden by the *frozen nuclear spin* approximation.

$$para-\text{NH}_2^+ \quad + \quad para-\text{H}_2 \quad \rightarrow \quad para-\text{NH}_3^+ \quad + \quad \text{H} \tag{2.4}$$

$$\nrightarrow \quad ortho-\text{NH}_3^+ \quad + \quad \text{H} \tag{2.5}$$

$$para-\text{CH}_3^+ \quad + \quad ortho-\text{H}_2 \quad \rightarrow \quad meta-\text{CH}_5^+ \quad + \quad h\nu \tag{2.6}$$

$$\nrightarrow \quad ortho-\text{CH}_5^+ \quad + \quad h\nu \tag{2.7}$$

$$ortho-\text{H}_3\text{O}^+ \quad + \quad \text{e}^- \quad \rightarrow \quad ortho-\text{H}_2\text{O} \quad + \quad \text{H} \tag{2.8}$$

$$\nrightarrow \quad para-\text{H}_2\text{O} \quad + \quad \text{H} \tag{2.9}$$
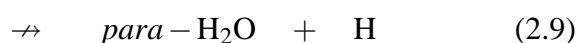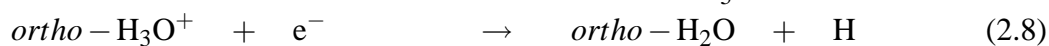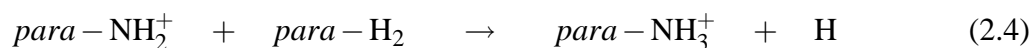
As for homonuclear exchange reactions, although they seem non-reactive, they can eventually lead to the apparent conversion of nuclear spin modifications, but some of them are strictly forbidden by the *frozen nuclear spin* approximation [7].

$$
\begin{aligned}
para-\mathrm{H_2D^+} \;+\; para-\tilde{\mathrm{H}}_2 \quad &\rightarrow \quad ortho-\tilde{\mathrm{H}}\mathrm{HD^+} \;+\; ortho-\tilde{\mathrm{H}}\mathrm{H} &(2.10)\\
&\rightarrow \quad para-\tilde{\mathrm{H}}\mathrm{HD^+} \;+\; para-\tilde{\mathrm{H}}\mathrm{H} &(2.11)\\
&\nrightarrow \quad para-\tilde{\mathrm{H}}\mathrm{HD^+} \;+\; ortho-\tilde{\mathrm{H}}\mathrm{H} &(2.12)\\
&\nrightarrow \quad ortho-\tilde{\mathrm{H}}\mathrm{HD^+} \;+\; para-\tilde{\mathrm{H}}\mathrm{H} &(2.13)
\end{aligned}
$$
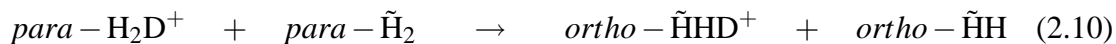
Nuclear spins are strongly coupled to the rovibronics by the symmetrisation postulate. Nevertheless, due to the frozen nuclear spin approximation, the nuclear spin degree of freedom is quasi–unperturbed by all other degrees of freedom *e.g.* rotation, vibration, electronic, kinetic, radiative, *etc*. Indeed, it is common to observe species in space whose nuclear spin modifications are not properly thermalized with their environment. The species can conserve through time and temperature their initial nuclear spin modifications since the "conventional" mechanisms that affect a molecule, *i.e.* radiative transitions and non-reactive collisions, are extremely ineffective conversion mechanisms. The only mechanisms that effectively affect the ortho/(meta)/para ratio of a species are its production, destruction and conversion in associative, dissociative or reactive collisions which all consist in rearrangement of sets of nuclei.

The first work on this subject was established by Quack in 1977 [1]. In his contribution, he reported nuclear spin selection rules using the permutation-inversion group algebra and the way to insert nuclear spin statistics in statistical scattering theories according to symmetry representations. More recently, Oka [2] reformulated the selection rules using the angular momentum algebra and derived nuclear spin statistics according to angular momentum representations of the K(spatial) rotation group.

In this contribution, we revisit those two complementary viewpoints by working on the wavefunctions themselves using the bracket formalism. We shall only focus on the nuclear spin wavefunction since it can be treated separately from the rovibronic wavefunction in accordance with the *frozen nuclear spin* approximation. Molecules are thus considered as boxes containing nuclei which are distinguished by sets regardless of the geometry of the molecule. Such incomplete description of reactive processes is a prerequisite before merging with the rovibronic wavefunctions and its energetics also at play. Moreover, we can focus on systems of identical nuclei only since the nuclear spin wavefunctions of different kinds of nuclei can be treated separately given that they are necessarily distinguishable.

The paper is organised as follow. In section 2.2, the angular momentum viewpoint only is developed using Clebsch-Gordan coefficients. In section 2.3, the permutation symmetry viewpoint only is developed using permutation symmetry projectors. In section 2.4, both methods are merged in order to access the full detail of information. We then apply these tools to the 3–spin 1 system in section 2.5 to show that the angular momentum and permutation symmetry

algebras are inconsistent and that, contrary to the angular momentum information, the symmetry information is necessary and should not be neglected. In addition, a more controversial yet interesting deterministic interpretation of the nuclear spin statistics is also proposed in section 2.6. Results of this work are summarised in section 2.7 and outlooks discussed.

2.2 THE ANGULAR MOMENTUM VIEWPOINT

2.2.1 Elementary Spins and the uncoupled basis set

From a physical viewpoint, spins give rise to magnetic moments. The projection of a spin I along a reference axis in space can adopt quantised magnetic moments i in the range $-I$, $-I+1$, $\cdots$, $I-1$, I and its state is noted $|I,i\rangle$. A spin I thus represents a multiplet of (2I+1) degenerate states. From a mathematical viewpoint, spins can be described as angular momenta or vectors represented in the K(spatial) rotation group [8, 9]. The representation of a spin I in this group is conventionally labelled $\mathscr{D}_I$ and has a dimension of (2I+1).

A deuterium nucleus or an ortho–H_2 molecule both have a spin of 1 however the latter is a composite spin which can be divided in several spins and the former is an elementary spin *i.e.* indivisible. The statistical weight of an elementary spin in the state $|I,i\rangle$ is $W_{I,i} = 1$ and the statistical weight of an elementary spin I is $W_I = 2I+1$, its multiplet degeneracy or its representation dimension. Note that throughout this chapter, the term "statistical weight" can be systematically replaced by "number of possible states".

The combination of n identical nuclei of spin I can be represented in the uncoupled basis set consisting of $(2I+1)^n$ pure states. Individual pure states correspond to a complete knowledge of the system where all nuclei are distinguished and each magnetic moment known. Indexing the nuclei and their spins with Latin letters, the states should be noted $|I_a,i_a,I_b,i_b,I_c,i_c\cdots\rangle$ but the spins I are often dropped down from the ket notation since they are a constant of the problem. Those pure states fulfil the orthonormality relation

$$|\langle i'_a,i'_b,i'_c\ldots|i_a,i_b,i_c\ldots\rangle|^2 = \delta_{i_a i'_a}\delta_{i_b i'_b}\delta_{i_c i'_c}\ldots \tag{2.14}$$

and the closure relation verifies

$$\sum_{i_a=-I}^{+I}\sum_{i_b=-I}^{+I}\sum_{i_b=-I}^{+I}\ldots|\langle i_a,i_b,i_c\ldots|i_a,i_b,i_c\ldots\rangle|^2 = (2I+1)^n \tag{2.15}$$

which we contract as

$$\sum_{i_a,i_b,i_c\ldots}|\langle i_a,i_b,i_c\ldots|i_a,i_b,i_c\ldots\rangle|^2 = W_{tot} \tag{2.16}$$

with $W_{tot} = (2I+1)^n$ the total weight of the system.
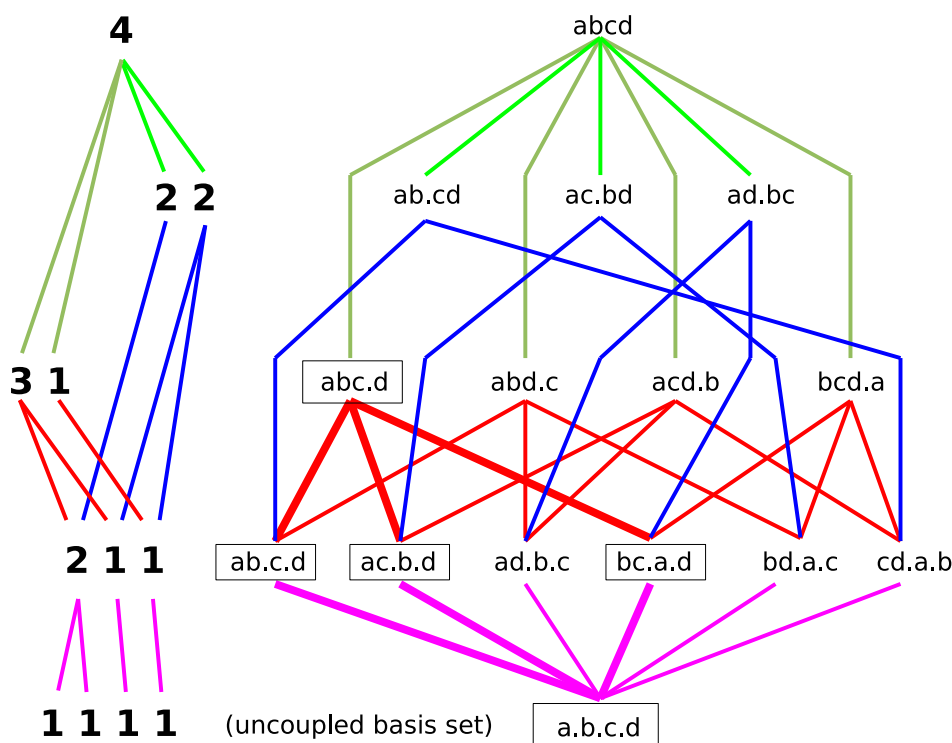
Figure 2.1: Mapping of the 4–nuclei system. **Left map**: The 5 classes of partitioning for 4 nuclei. **Right map**: The nuclei are distinguished and labeled *a, b, c, d.* The connections represent an addition of two subsets of nuclei. The 3–nuclei sub-system (abc) is emphasised.

2.2.2 Addition of elementary spins

A pure state is rarely representative of our knowledge of a system of nuclei (*e.g.* a molecule, a molecular complex or a colliding system) since we cannot distinguish and measure all its nuclei. Nevertheless, we can in principle measure the spin and the magnetic moment of the complete set of nuclei and/or some subsets of nuclei, *i.e.* the *total* and/or *local* spins and magnetic moments. In order to build nuclear spin wavefunctions which represent the system with specific total and local nuclear spin angular momenta, we build linear combinations of pure states, so–called *mixed* states, using Clebsch-Gordan coefficients. Since Clebsch-Gordan coefficients work on the addition of two angular momenta only, it is necessary to add the local elementary and/or composite spins two by two, stepwise, until the total spin is formed. As illustrated in Fig. 2.1 for the 4–nuclei system, there are several ways to add nuclei two by two in order to obtain the complete set of nuclei. These bottom–up paths or addition schemes are referred as *induction schemes* and they are representative of complex formation and associative processes. We illustrate the method through the 4–nuclei system.

The addition of 4 identical nuclei a, b, c and d of spin $I_a = I_b = I_c = I_d$ can be done according to two class of induction schemes[1] (see Fig. 2.1):

- $((I_a \otimes I_b) \otimes (I_c \otimes I_d)) \uparrow (I_{ab} \otimes I_{cd}) \uparrow I_{abcd}$

- $(((I_a \otimes I_b) \otimes I_c) \otimes I_d) \uparrow ((I_{ab} \otimes I_c) \otimes I_d) \uparrow (I_{abc} \otimes I_d) \uparrow I_{abcd}$

respectively describing complex formations of the type

- $(a + b) + (c + d) \rightarrow ab + cd \rightarrow abcd$

- $\big((a + b) + c\big) + d \rightarrow \big(ab + c\big) + d \rightarrow abc + d \rightarrow abcd$

Regarding the latter induction scheme, the nuclear spin wavefunction of the total state $|I_{abcd}, i_{abcd}\rangle$ induced via local spins I_{abc} and I_{ab} is given by

$$|I_{abcd}, i_{abcd}, I_{abc}, I_{ab}\rangle = \sum_{i_a, i_b, i_c, i_d} \langle I_a, i_a, I_b, i_b | I_{ab}, i_{ab}\rangle \times \langle I_{ab}, i_{ab}, I_c, i_c | I_{abc}, i_{abc}\rangle$$

$$\times \langle I_{abc}, i_{abc}, I_d, i_d | I_{abcd}, i_{abcd}\rangle \times |i_a, i_b, i_c, i_d\rangle \qquad (2.17)$$

with $i_{ab} = i_a + i_b$ and $i_{abc} = i_a + i_b + i_c$. The statistical weight of the total spin I_{abcd} induced via the local spins I_{abc} and I_{ab} is thus

$$W_{(I_a \otimes I_b \otimes I_c \otimes I_d) \uparrow (I_{ab} \otimes I_c \otimes I_d) \uparrow (I_{abc} \otimes I_d) \uparrow I_{abcd}} = \sum_{i_{abcd}} |\langle I_{abcd}, i_{abcd}, I_{abc}, I_{ab} | I_{abcd}, i_{abcd}, I_{abc}, I_{ab}\rangle|^2$$

$$= (2I_{abcd} + 1) \qquad (2.18)$$

By summing the previous induction scheme over all possible local spins I_{ab}, we obtain the induction scheme describing the complex formations of the type $(a + b + c) + d \rightarrow abc + d \rightarrow abcd$:

$$((I_a \otimes I_b \otimes I_c) \otimes I_d) \uparrow (I_{abc} \otimes I_d) \uparrow I_{abcd}$$

$$= \sum_{I_{ab} = |I_a - I_b|}^{I_a + I_b} (((I_a \otimes I_b) \otimes I_c) \otimes I_d) \uparrow ((I_{ab} \otimes I_c) \otimes I_d) \uparrow (I_{abc} \otimes I_d) \uparrow I_{abcd} \quad (2.19)$$

Correspondingly, the statistical weight of the total spin I_{abcd} induced via the local spin I_{abc} irrespective of the local spin I_{ab} is obtained by summing over all possible local spins I_{ab}:

$$W_{(I_a \otimes I_b \otimes I_c \otimes I_d) \uparrow (I_{abc} \otimes I_d) \uparrow I_{abcd}} = \sum_{I_{ab} = |I_a - I_b|}^{I_a + I_b} W_{(I_a \otimes I_b \otimes I_c \otimes I_d) \uparrow (I_{ab} \otimes I_c \otimes I_d) \uparrow (I_{abc} \otimes I_d) \uparrow I_{abcd}}$$

$$= f_{(I_a \otimes I_b \otimes I_c) \uparrow I_{abc}} \times (2I_{abcd} + 1) \qquad (2.20)$$

---

[1] The direct product $\otimes$ in the K(spatial) rotation group correspond to the vectorial sum of angular momenta.

where $f_{(I_a \otimes I_b \otimes I_c) \uparrow I_{abc}}$ is the frequency of the representation $\mathscr{D}_{I_{abc}}$ induced by the direct product $\mathscr{D}_{I_a} \otimes \mathscr{D}_{I_b} \otimes \mathscr{D}_{I_c}$.

We can also obtain the weight of the total spin I_{abcd} irrespective of local spins I_{abc} and I_{ab} by summing further over all possible local spins I_{abc} :

$$
\begin{aligned}
W_{(I_a \otimes I_b \otimes I_c \otimes I_d) \uparrow I_{abcd}} &= \sum_{I_{abc} = |I_{abcd} - I_d|}^{I_{abcd} + I_d} W_{(I_a \otimes I_b \otimes I_c \otimes I_d) \uparrow (I_{abc} \otimes I_d) \uparrow I_{abcd}} \\
&= f_{(I_a \otimes I_b \otimes I_c \otimes I_d) \uparrow I_{abcd}} \times (2 I_{abcd} + 1)
\end{aligned}
\tag{2.21}
$$

This equation can be generalised to any (sub)system of n nuclei with spins I by stating that the statistical weight of a total spin I_{tot} irrespective of local spins is given by

$$
W(I_{tot}) = f(I_{tot}) \times dim(I_{tot})
\tag{2.22}
$$

with $dim(I_{tot}) = 2 I_{tot} + 1$ the dimension of the represention $\mathscr{D}_{I_{tot}}$ and $f(I_{tot})$ its frequency in the complete representation of the system $\bigotimes^{n} \mathscr{D}_I$.

2.2.3 Division of spins

Divisions of composite spins into several spins are the reciprocal of the additions and thus represent complex decay and dissociative processes. As illustrated in Fig. 2.1, a division corresponds to a top–down path and consists in subducing direct products of representations from irreducible representations. A division scheme is therefore referred as a *subduction scheme*. In terms of braket notation, it results in inverting the reciprocal induction formula, *i.e.* exchanging the bras and kets.

Considering the subduction scheme $I_{abcd} \downarrow (I_{abc} \otimes I_d) \downarrow ((I_{ab} \otimes I_c) \otimes I_d) \downarrow (((I_a \otimes I_b) \otimes I_c) \otimes I_d)$ of the 4–nuclei system, the statistical weight of a total spin I_{abcd} subducing 4 elementary spins I_a, I_b, I_c and I_d via local spins I_{abc} and I_{ab} is

$$
\begin{aligned}
W_{I_{abcd} \downarrow (I_{abc} \otimes I_d) \downarrow (I_{ab} \otimes I_c \otimes I_d) \downarrow (I_a \otimes I_b \otimes I_c \otimes I_d)} &= \sum_{i_{abcd}} |\langle I_{abcd}, i_{abcd}, I_{abc}, I_{ab} | I_{abcd}, i_{abcd}, I_{abc}, I_{ab} \rangle|^2 \\
&= W_{(I_a \otimes I_b \otimes I_c \otimes I_d) \uparrow (I_{ab} \otimes I_c \otimes I_d) \uparrow (I_{abc} \otimes I_d) \uparrow I_{abcd}} \\
&= (2 I_{abcd} + 1)
\end{aligned}
\tag{2.23}
$$

This equation shows that the weight of a subduction scheme is equal to the weight of its reciprocal induction scheme as may be generally inferred from the Frobenius reciprocity theorem.

2.2.4 Reaction statistics

A reactive process is a rearrangement of nuclei. It can be described by (i) the addition of two or several reactants forming of an intermediate complex which can be long– or short–lived, tight or loose, followed by (ii) the division of this complex into two or several products. Correspondingly, a reactive process can be described by an induction scheme followed by a subduction scheme.

In the example of the 4–nuclei system, reactions of the type $X_2 + X_2 \rightarrow X_4 \rightarrow X_3 + X$ can be decomposed in 4 equivalent transfer reaction mechanisms:

$$ab + cd \rightarrow abcd \rightarrow abc + d \tag{2.24}$$
$$\rightarrow abd + c \tag{2.25}$$
$$\rightarrow acd + b \tag{2.26}$$
$$\rightarrow bcd + a \tag{2.27}$$

The transfer of the "c" nucleus (Eq. 2.24) corresponds to the induction–subduction scheme $(I_a \otimes I_b \otimes I_c \otimes I_d) \uparrow (I_{ab} \otimes I_{cd}) \uparrow I_{abcd} \downarrow (I_{abc} \otimes I_d) \downarrow (I_a \otimes I_b \otimes I_c \otimes I_d)$. Its statistical weights are given by

$$
\begin{aligned}
W_{(I_a \otimes I_b \otimes I_c \otimes I_d)\uparrow(I_{ab}\otimes I_{cd})\uparrow I_{abcd}\downarrow(I_{abc}\otimes I_d)\downarrow(I_a\otimes I_b\otimes I_c\otimes I_d)} \\
= \sum_{i_{abcd}} |\langle I_{abcd}, i_{abcd}, I_{ab}, I_{cd} | I_{abcd}, i_{abcd}, I_{abc}, I_{ab}\rangle|^2
\end{aligned} \tag{2.28}
$$

Equivalently, the statistical weights for each reaction mechanism can be determined with the proper induction–subduction scheme.

In the full–scrambling limit, all nuclei of the complex are completely mixed such that the 4 possible outcomes are equiprobable (Eqs. 2.24 to 2.27). Therefore, the statistical weights for the full-scrambling reaction $X_2 + X_2 \rightarrow X_4 \xrightarrow{FS} X_3 + X$ correspond to the average of the statistical weights of the individual reaction mechanisms.

The full–scrambling of the nuclei within the complex can also be interpreted as the lost of their initial informations, *i.e.* labels and arrangements, except the total nuclear spin which is implicitly conserved since it includes all the nuclei. We can thus express the statistical weights for the full-scrambling by reseting the nuclei labels between the complex formation and decay:

$$
\begin{aligned}
W_{(I_a \otimes I_b \otimes I_c \otimes I_d)\uparrow(I_{ab}\otimes I_{cd})\uparrow I_{abcd}\xrightarrow{FS} I_{a'b'c'd'}\downarrow(I_{a'b'c'}\otimes I_{d'})\downarrow(I_{a'}\otimes I_{b'}\otimes I_{c'}\otimes I_{d'})} \\
= W_{(I_a \otimes I_b \otimes I_c \otimes I_d)\uparrow(I_{ab}\otimes I_{cd})\uparrow I_{abcd}} \times \frac{W_{I_{a'b'c'd'}\downarrow(I_{a'b'c'}\otimes I_{d'})\downarrow(I_{a'}\otimes I_{b'}\otimes I_{c'}\otimes I_{d'})}}{W_{I_{a'b'c'd'}}}
\end{aligned} \tag{2.29}
$$

with $I_{abcd} = I_{a'b'c'd'}$. With this equation, statistical weights for the full–scrambling collision scheme is easily derived from the sole induction(subduction) statistical weights. Furthermore,

the overall statistics for the reaction $X_2 + X_2 \overset{FS}{\leftrightharpoons} X_3 + X$ are obtained by summing Eq. 2.29 over all total nuclear spins.

2.3 THE SYMMETRY VIEWPOINT

2.3.1 Permutation groups and symmetrised states

One can represent a system of n identical nuclei in a permutation group according to how well he can distinguish its nuclei. For example, when the nuclei are completely indistinguishable, any transposition or permutation operation in the complete set of nuclei keeps the system unchanged thus corresponding to the complete permutation group S_n. If the nuclei are partionned in k distinguishable subsets of $n_1, n_2 \cdots n_k$ indistinguishable nuclei with $\sum_{i=1}^{k} n_i = n$, only those permutations within these subsets keep the system unchanged thereby corresponding to the permutation group $S_{n_1, n_2 \cdots n_k} = S_{n_1} \otimes S_{n_2} \times \ldots \otimes S_{n_k}$ which is a subgroup of S_n. Ultimately, if all the nuclei of the system are perfectly distinguished (*eq.* localised), the system is represented by the uncoupled basis set or the $(S_1)^n = \overset{n}{\bigotimes} S_1$ group since no permutation is possible.

In order to represent the system in a permutation group, we build symmetrised wavefunctions $P_{\Gamma_i} |i_a, i_b, i_c \ldots\rangle$ by applying projectors P_{Γ_i} of the symmetry representations Γ_i on the pure states of the uncoupled basis set. The symmetry projectors P_{Γ_i} of a permutation group are defined as

$$P_{\Gamma_i} = \frac{1}{h} \sum_R \chi_{\Gamma_i}[R] \times R \tag{2.30}$$

with h the order of the group, R the permutation operations of the group and $\chi_{\Gamma_i}[R]$ the character of the representation Γ_i under the permutation R. Thorough description of permutation groups, symmetry representations and projectors can also be found in Bunker and Jensen [8; 9] and character tables for permutation groups containing up to 5 nuclei are given in appendix 2.A as supplementary material.

The statistical weight of a symmetry representation Γ_i from a permutation group is given by its dimension $dim(\Gamma_i)$ and the sum of square of its projector's elements according to Born's rule:

$$W_{\Gamma_i} = dim(\Gamma_i)^2 \times \sum_{i_a, i_b, i_c \cdots i_{d'}, i_{b'}, i_{c'} \cdots} \sum |\langle i_{a'}, i_{b'}, i_{c'} \cdots |P_{\Gamma_i}|i_a, i_b, i_c \cdots\rangle|^2 \tag{2.31}$$

As in Eq. 2.22 for the angular momentum representations, the statistical weight of a symmetry representation Γ_i is also given by the algebraic formula:

$$W_{\Gamma_i} = dim(\Gamma_i) \times f(\Gamma_i) \tag{2.32}$$

with $f(\Gamma_i)$ the frequency of Γ_i in the complete symmetry representation of the system.

2.3.2 Induction statistics

It is possible to represent simultaneously different local symmetries of a system using symmetry projectors of different permutation subgroups. As an example, the statistical weight of a 5–nuclei system with local symmetries Γ_{abc} and Γ_{de} inducing a total symmetry Γ_{abcde} according to the induction scheme $S_{a,b,c,d,e} \uparrow S_{abc,de} \uparrow S_{abcde}$ is

$$
W_{\Gamma_{a,b,c,d,e} \uparrow \Gamma_{abc,de} \uparrow \Gamma_{abcde}} = dim(\Gamma_{abc,de})^2 \times dim(\Gamma_{abcde})^2 \times \tag{2.33}
$$
$$
\sum_{i_a,i_b,i_c,i_d,i_e} \sum_{i_{a'},i_{b'},i_{c'},i_{d'},i_{e'}} |\langle i_{a'},i_{b'},i_{c'},i_{d'},i_{e'}|P_{\Gamma_{abcde}}P_{\Gamma_{abc,de}}|i_a,i_b,i_c,i_d,i_e\rangle|^2
$$

Equivalently, the notations $\Gamma_{abc,de}$ corresponds to $\Gamma_{abc} \otimes \Gamma_{de}$ and we have

$$
dim(\Gamma_{abc,de}) = dim(\Gamma_{abc}) \times dim(\Gamma_{de}) \tag{2.34}
$$
$$
P_{\Gamma_{abc,de}} = P_{\Gamma_{abc}}P_{\Gamma_{de}} \tag{2.35}
$$

2.3.3 Subduction statistics

In the bracket formalism, a subduction scheme is related to its reciprocal induction scheme by inverting the formula that is to exchange the bras into kets, the kets into bras and the operators P_{Γ_i} into dagger operators $P_{\Gamma_i}{}^\dagger$. Since (i) the dagger operator is the Hermitian conjugate of an operator which is the transpose conjugate in terms of matrices operators and (ii) the symmetry projector matrices are real and diagonal symmetric, we have $P_{\Gamma_i}{}^\dagger = P_{\Gamma_i}$. Moreover, the projector operators are commutative. Therefore, the statistical weight of a 5–nuclei system with a total symmetry Γ_{abcde} subducing local symmetries Γ_{abc} and Γ_{de} according to the subduction scheme $S_{abcde} \downarrow S_{abc,de} \downarrow S_{a,b,c,d,e}$ is

$$
W_{\Gamma_{abcde} \downarrow \Gamma_{abc,de} \downarrow \Gamma_{a,b,c,d,e}} = dim(\Gamma_{abc,de})^2 \times dim(\Gamma_{abcde})^2
$$
$$
\times \sum_{i_{a'},i_{b'},i_{c'},i_{d'},i_{e'}} \sum_{i_a,i_b,i_c,i_d,i_e} |\langle i_a,i_b,i_c,i_d,i_e|P_{\Gamma_{abc,de}}^\dagger P_{\Gamma_{abcde}}^\dagger|i_{a'},i_{b'},i_{c'},i_{d'},i_{e'}\rangle|^2
$$
$$
= dim(\Gamma_{abc,de})^2 \times dim(\Gamma_{abcde})^2
$$
$$
\times \sum_{i_a,i_b,i_c,i_d,i_e} \sum_{i_{a'},i_{b'},i_{c'},i_{d'},i_{e'}} |\langle i_{a'},i_{b'},i_{c'},i_{d'},i_{e'}|P_{\Gamma_{abcde}}P_{\Gamma_{abc,de}}|i_a,i_b,i_c,i_d,i_e\rangle|^2
$$
$$
= W_{\Gamma_{a,b,c,d,e} \uparrow \Gamma_{abc,de} \uparrow \Gamma_{abcde}} \tag{2.36}
$$

As for the angular momentum viewpoint (Eq. 2.23) and accordingly to the Frobenius reciprocity theorem, the statistical weight of a subduction scheme is equal to the statistical weight of its reciprocal induction scheme.

2.3.4   Reaction statistics

Similarly to Sec. 2.2.4, statistical weights for reaction schemes can be obtained by corre-lating the symmetrised states of the induction scheme (complex formation) with the sym-metrised states of the subduction scheme (complex decay). In the example of the reaction $X_2 + X_2 \to X_4 \to X_3 + X$, the "c" nucleus transfer (Eq. 2.24) correspond to the induction–subduction scheme $S_{a,b,c,d} \uparrow S_{ab,cd} \uparrow S_{abcd} \downarrow S_{abc,d} \downarrow S_{a,b,c,d}$. The statistical weight of local sym-metries Γ_{ab} and Γ_{cd} correlated with Γ_{abc} via a total symmetry Γ_{abcd} is

$$
\begin{aligned}
&W_{\Gamma_{a,b,c,d}\uparrow\Gamma_{ab,de}\uparrow\Gamma_{abcd}\downarrow\Gamma_{abc,d}\downarrow\Gamma_{a,b,c,d}} \\
&= dim(\Gamma_{ab,cd})^2 \times dim(\Gamma_{abcd})^4 \times dim(\Gamma_{abc,d})^2 \\
&\times \sum_{i_a,i_b,i_c,i_d}\sum_{i_{a'},i_{b'},i_{c'},i_{d'}} |\langle i_{a'},i_{b'},i_{c'},i_{d'}|P_{\Gamma_{ab,cd}}P_{\Gamma_{abcd}}P_{\Gamma_{abcd}}P_{\Gamma_{abc,d}}|i_a,i_b,i_c,i_d\rangle|^2 \quad (2.37)
\end{aligned}
$$

Following the argumentation of Sec. 2.2.4, the symmetry statistical weights for the full–scrambling collisions $X_2 + X_2 \to X_4 \xrightarrow{FS} X_3 + X$ is the average of the statistical weights of the individual reaction mechanisms. The symmetry statistical weights for the full–scrambling can also be obtained from the sole induction statistical weights as in Eq. 2.29 by reseting the nuclei labels between the complex formation and decay:

$$
\begin{aligned}
&W_{\Gamma_{a,b,c,d}\uparrow\Gamma_{ab,cd}\uparrow\Gamma_{abcd}\xrightarrow{FS}\Gamma_{a'b'c'd'}\downarrow\Gamma_{a'b'c',d'}\downarrow\Gamma_{a',b',c',d'}} \\
&= W_{\Gamma_{a,b,c,d}\uparrow\Gamma_{ab,cd}\uparrow\Gamma_{abcd}} \times \frac{W_{\Gamma_{a'b'c'd'}\downarrow\Gamma_{a'b'c',d'}\downarrow\Gamma_{a',b',c',d'}}}{W_{\Gamma_{a'b'c'd'}}} \quad (2.38)
\end{aligned}
$$

with $\Gamma_{abcd} = \Gamma_{a'b'c'd'}$. Further summation over all possible total symmetries yields the overall symmetry statistics for the $X_2 + X_2 \overset{FS}{\leftrightharpoons} X_3 + X$ reaction.

2.4   MERGING BOTH VIEWPOINTS

2.4.1   Induction and subduction statistics

Angular momentum and symmetry informations can be accessed simultaneously by projecting the angular momentum wavefunctions on the different representations of the permutation sub-groups.

Considering the angular momentum and symmetry viewpoints of the induction scheme

$$\big((a+b)+c\big)+d \quad \rightarrow \quad \big(ab+c\big)+d \quad \rightarrow \quad abc+d \quad \rightarrow \quad abcd$$

$$\big((I_a \otimes I_b) \otimes I_c\big) \otimes I_d \quad \uparrow \quad \big(I_{ab} \otimes I_c\big) \otimes I_d \quad \uparrow \quad I_{abc} \otimes I_d \quad \uparrow \quad I_{abcd}$$

$$\big((S_a \otimes S_b) \otimes S_c\big) \otimes S_d \quad \uparrow \quad \big(S_{ab} \otimes S_c\big) \otimes S_d \quad \uparrow \quad S_{abc} \otimes S_d \quad \uparrow \quad S_{abcd}$$

the state with a total spin I_{abcd}, a total magnetic moment i_{abcd} and a total symmetry Γ_{abcd} induced via local spins I_{abc} and I_{ab} with local symmetries Γ_{abc} and Γ_{ab} is

$$|I_{abcd}, i_{abcd}, \Gamma_{abcd}, I_{abc}, \Gamma_{abc}, I_{ab}, \Gamma_{ab}\rangle = P_{\Gamma_{abcd}} P_{\Gamma_{abc,d}} P_{\Gamma_{ab,c,d}} |I_{abcd}, i_{abcd}, I_{abc}, I_{ab}\rangle \tag{2.39}$$

with $i_{ab} = i_a + i_b$ and $i_{abc} = i_a + i_b + i_c$, and its statistical weight is

$$W^{(I_a \otimes I_b \otimes I_c \otimes I_d) \ \uparrow (I_{ab} \otimes I_c \otimes I_d) \ \uparrow (I_{abc} \otimes I_d) \ \uparrow I_{abcd}}_{(\Gamma_a \otimes \Gamma_b \otimes \Gamma_c \otimes \Gamma_d) \uparrow (\Gamma_{ab} \otimes \Gamma_c \otimes \Gamma_d) \uparrow (\Gamma_{abc} \otimes \Gamma_d) \uparrow \Gamma_{abcd}} \tag{2.40}$$

$$= \ dim(\Gamma_{abcd})^4 \times dim(\Gamma_{abc,d})^4 \times dim(\Gamma_{ab,c,d})^4$$

$$\times \ \sum_{i_{abcd}} |\langle I_{abcd}, i_{abcd}, \Gamma_{abcd}, I_{abc}, \Gamma_{abc}, I_{ab}, \Gamma_{ab} | I_{abcd}, i_{abcd}, \Gamma_{abcd}, I_{abc}, \Gamma_{abc}, I_{ab}, \Gamma_{ab}\rangle|^2$$

Accordingly to the Frobenius reciprocity principle, the angular momentum–symmetry statistical weight of a subduction scheme and its reciprocal induction scheme are equal as demonstrated in Eqs. 2.23 and 2.36 for the angular momentum and the symmetry viewpoints, respectively.

The total angular momentum–symmetry statistical weights for systems of 3, 4 or 5 particles of spins 1/2, 1 or 3/2 are given in Table 2.13 and their detailed statistical weights for bimolecular induction (*eq.* subduction) schemes are given in Tables 2.14, 2.15 and 2.16.

2.4.2 Reaction statistics

As in sections 2.2.4 and 2.3.4, the statistical weights for induction–subduction schemes are obtained by correlating the induced states (complex formation) with the subduced states (complex decay).

In the example of the induction–subduction scheme

$$(a+b)+(c+d) \rightarrow ab+cd \rightarrow abcd \rightarrow abc+d \rightarrow (ab+c)+d \rightarrow \big((a+b)+c\big)+d$$

representing the "c" nucleus transfer reaction mechanism, the statistical weight of local spins I_{ab} and I_{cd} with local symmetries Γ_{ab} and Γ_{cd} correlated with a local spin I_{abc} with local symmetry

Γ_{abc} via a total spin I_{abcd} with a total symmetry Γ_{abcd} is

$$
\begin{aligned}
& W^{(I_a\otimes I_b\otimes I_c\otimes I_d)\ \uparrow(I_{ab}\otimes I_{cd})\ \uparrow I_{abcd}\downarrow(I_{abc}\otimes I_d)\ \downarrow(I_{ab}\otimes I_c\otimes I_d)\ \downarrow(I_a\otimes I_b\otimes I_c\otimes I_d)}_{(\Gamma_a\otimes\Gamma_b\otimes\Gamma_c\otimes\Gamma_d)\uparrow(\Gamma_{ab}\otimes\Gamma_{cd})\uparrow\Gamma_{abcd}\downarrow(\Gamma_{abc}\otimes\Gamma_d)\downarrow(\Gamma_{ab}\otimes\Gamma_c\otimes\Gamma_d)\downarrow(\Gamma_a\otimes\Gamma_b\otimes\Gamma_c\otimes\Gamma_d)} \qquad (2.41)\\
& = \ dim(\Gamma_{ab,cd})^2 \times dim(\Gamma_{abcd})^4 \times dim(\Gamma_{abc,d})^2 \times dim(\Gamma_{ab,c,d})^2 \\
& \times \ \sum_{i_{abcd}} |\langle I_{abcd},i_{abcd},\Gamma_{abcd},I_{abc},\Gamma_{abc},I_{ab},\Gamma_{ab}|I_{abcd},i_{abcd},\Gamma_{abcd},I_{ab},\Gamma_{ab},I_{cd},\Gamma_{cd}\rangle|^2
\end{aligned}
$$

Detailed angular momentum–symmetry statistical weights for each reaction mechanism can be determined with the corresponding induction–subduction scheme as in Eq. 2.41. Repeating sections 2.2.4 and 2.3.4, the detailed statistical weights for the full-scrambling reaction can be obtained by averaging the detailed statistical weights of the individual reaction mechanisms. They can also be obtained as in Eqs. 2.29 and 2.38 using the induction detailed statistical weights from Tables 2.14, 2.15 or 2.16.

2.5 ANALYSIS OF THE D_3 SYSTEM

For systems of spin 1/2 particles, there is a one-to-one corelation between the angular momentum and the symmetry representations[2] (see Table 2.13). The total spin information thus implicitly gives the symmetry information and vice-versa such that, separately or combined, the angular momentum and symmetry viewpoints yield identical statistics. The system of three particles of spin 1 is therefore interesting because it is the smallest and simplest system where the isomorphism between angular momentum and symmetry representations breaks down. Table 2.13 shows indeed that for the 3–spin 1 system, a total spin of 1 can be either of A_1 or E symmetry and that the total symmetries A_1 and E can have total spins 1 or 3 and 1 or 2, respectively. To study this system, we shall focus on the reaction $D_2 + D \rightarrow D_3 \rightarrow D_2 + D$.

2.5.1 Full-scrambling statistics

The statistics for the $D_2 + D \rightarrow D_3$ induction scheme can be derived either from the angular momentum viewpoint (Table 2.2a), the symmetry viewpoint (Table 2.2c) or both simultaneously (Table 2.2b). Note that Tables 2.2a and 2.2c can also be obtained by rebinning the statistical weights from Table 2.2b according to angular momentum or symmetry informations.

As in equation 2.29 and 2.38, the full–scrambling statistics can be calculated directly from these induction statistics considering angular momentum, symmetry informations or both. The overall statistics of the $D_2 + D \overset{FS}{\rightleftharpoons} D_2 + D$ reaction, *i.e.* summed over the total spins and/or symmetries of the intermediate complex, are given in tables 2.3a, 2.3b and 2.3c depending on the

---

[2]We could not find a mathematical proof of this statement but verified it for systems up to at least 6 particles.

Table 2.1: $D_2 + D \rightleftharpoons D_3$ induction (subduction) statistical weights.

(a) Angular momentum

	$0(A_2)$	$1(A_1,E)$	$2(E)$	$3(A_1)$	sum
$2(A) \otimes 1(A)$	0	3	5	7	15
$1(B) \otimes 1(A)$	1	3	5	0	9
$0(A) \otimes 1(A)$	0	3	0	0	3
sum	1	9	10	7	$27=3^3$

(b) Angular momentum and symmetry

	$0\,A_2$	$1\,A_1$	$1\,E$	$2\,E$	$3\,A_1$	sum
$2,A \otimes 1,A$	0	4/3	5/3	5	7	15
$1,B \otimes 1,A$	1	0	3	5	0	9
$0,A \otimes 1,A$	0	5/3	4/3	0	0	3
sum	1	3	6	10	7	$27=3^3$

(c) Symmetry

	$A_1(1,3)$	$A_2(0)$	$E(1,2)$	sum
$A(0,2) \otimes A(1)$	10	0	8	18
$B(1) \quad \otimes A(1)$	0	1	8	9
sum	10	1	16	$27=3^3$

viewpoint(s) considered.

The striking result is that contrary to the statistics derived with the symmetry information only, the statistics derived with the angular momentum information only are inconsistent with those derived with both angular momentum and symmetry informations. Indeed, rebinning the statistical weights from table 2.3b with respect to the angular information does not yield table 2.3a while rebinning them with respect to the symmetry information does yield table 2.3c. Such result can also be observed for systems of 4 nuclei of spin 1 and 3 nuclei of spin 3/2. By extent, it will be true for any system where the isomorphism between its angular momentum and symmetry representations is not true.

Table 2.2: $D_2 + D \xrightarrow{FS} D_2 + D$ full–scrambling statistical weights.

(a) Angular momentum

	2(A) ⊗ 1(A)	1(B) ⊗ 1(A)	0(A) ⊗ 1(A)	sum
2(A) ⊗ 1(A)	21/2	7/2	1	15
1(B) ⊗ 1(A)	7/2	9/2	1	9
0(A) ⊗ 1(A)	1	1	1	3
sum	15	9	3	27=3³

(b) Angular momentum and symmetry

	2,A ⊗ 1,A	1,B ⊗ 1,A	0,A ⊗ 1,A	sum
2,A ⊗ 1,A	95/9	30/9	10/9	15
1,B ⊗ 1,A	30/9	5	6/9	9
0,A ⊗ 1,A	10/9	6/9	11/9	3
sum	15	9	3	27=3³

(c) Symmetry

	A(0,2) ⊗ A(1)	B(1) ⊗ A(1)	sum
A(0,2) ⊗ A(1)	14	4	18
B(1) ⊗ A(1)	4	5	9
sum	18	9	27=3³

We thus observe that the permutation symmetry algebra [1] and the angular momentum algebra [2] are inconsistent when describing reaction (induction–subduction) schemes. The angular momentum informations (total and local spins) are good[3] quantum numbers to describe molecules (the complete permutation group), associations (induction schemes) or dissociations (subduction schemes) but they seem to be "bad" quantum numbers to describe reactions (induction–subduction schemes). This result is embarrassing and counter–intuitive as one would expect it feasible to derive good statistics from the sole angular momentum viewpoint, yet we must conclude that the angular momentum information is insufficient and that the symmetry information is essential. The necessity of the symmetry informations is also motivated by the symmetrisation postulate (a postulate of quantum mechanics) since the symmetries of

---

[3]in its literal sens and the sens of "conserved in time"

the reactants' and products' nuclear spin wavefunctions are required to tell which rovibronic wavefunctions and energetics are accessible.

2.5.2 Detailed reaction mechanisms statistics

Once the weakness of the angular momentum viewpoint has been evidenced, we shall try to explain it by focusing on finer details. The statistics found in Table 2.2 are (i) summed over the total symmetries and/or angular momenta and (ii) correspond to the full–scrambling which is the average of all reaction mechanisms. We will now derive the detailed angular momentum–symmetry statistics (i) for a total angular momentum of 1 with E total symmetry and (ii) for each reaction mechanism. To do that, we can use two methods either starting from the full-scrambling statistics and ending by the reaction mechanisms statistics or vice–versa.

Decomposition method

This method described by Oka in the frame of the angular momentum algebra [see 2, sec. 3.2] is shown in Table 2.4 . The *full-scrambling* statistical weights (Table 2.4a) are first derived as in Eqs. 2.29 and 2.38 using the induction (subduction) statistical weights from Table 2.2b . The *Identity* statistical weights (Table 2.4b) are then inferred from the strict conservation of local spins and symmetries. Finally, the *Transfer* statistical weights (Table 2.4c) are derived from the *full-scrambling* and *Identity* statistical weights since, as illustrated in Table 2.3 , the full-scrambling consists in 3 equiprobable reaction mechanisms : 1 *Identity* and 2 equivalent *Transfer*.

Recomposition method

We directly calculate the *Identity* and *Transfer* statistical weights (Tables 2.5a and 2.5b) as in Eq. 2.41 and recompose the *full–scrambling* statistical weights (Table 2.5c) according to Table 2.3 .

Table 2.3: Mechanisms for the $D_2 + D \rightarrow D_2 + D$ reaction.

ab	+	c	$\rightarrow$	abc	$\rightarrow$	ab	+	c		1/3	Identity
					$\rightarrow$	ac	+	b	+	1/3	'a'–Transfer
					$\rightarrow$	bc	+	a	+	1/3	'b'–Transfer
D_2	+	D	$\rightarrow$	D_3	$\rightarrow$	D_2	+	D		=	Full–scrambling

Comparison and analysis

Surprisingly, the decomposition method results in negative weights (see Table 2.4c) which have no physical meaning. Its reasoning thus holds an error which is revealed by the *Identity* statistical weights from the recomposition method (Table 2.5a) where we see that the local angular momentum of a D$_2$ with local symmetry A is a 4/9 : 5/9 mixture of spins 0 and 2. Note that this ratio also appears in the column "1 E" of Table 2.2b. We must conclude that local nuclear spin angular momenta are not strictly conserved as assumed for the inference of the *Identity* statistical weights in the decomposition method (Table 2.4b). In other words, local and composite nuclear spin angular momenta are not *good* quantum numbers.

This observation raises questioning since for an isolated *ortho*–D$_2$ molecule, *i.e.* a complete system with A symmetry, its total nuclear spin angular momentum of 0 or 2 ought to be strictly conserved. However, considering this same molecule with another distant D atom, *i.e.* as a subsystem, its nuclear spin angular momentum turns out *local* hence not strictly conserved. We evidence a paradox regarding the conservation of nuclear spin angular momenta based on their *total* or *local* properties. This interpretational dilemma is unsatisfactory and needs to be solved.

It it also interesting to note that in Table 2.5, for all reaction mechanisms, the symmetry reaction probabilities are independent of the local angular momenta. Comparing with the statistical weights for a total angular momentum of 2 and the E total symmetry (Table 2.6), we can also conclude that the symmetry reaction probabilities are independent of the total nuclear spin angular momentum. This confirms the conclusion from section 2.5.1: Contrarily to the symmetry informations, the angular momentum informations are not sufficient nor necessary.

Finally, Table 2.6 can also be derived with the decomposition method since the total nuclear spin angular momenta correlates with a single total symmetry. The decomposition method thus works systematically for spin 1/2 systems.

Table 2.4: $D_2 + D \rightarrow D_2 + D$ statistics with $I_{tot} = 1$ and $\Gamma_{tot} = E$: Decomposition method.

(a) Full–scrambling

	2,A $\otimes$ 1,A	1,B $\otimes$ 1,A	0,A $\otimes$ 1,A	sum
2,A $\otimes$ 1,A	25/54	45/54	20/54	5/3
1,B $\otimes$ 1,A	45/54	81/54	36/54	3
0,A $\otimes$ 1,A	20/54	36/54	16/54	4/3
sum	5/3	3	4/3	6

(b) Identity reaction mechanism

	2,A $\otimes$ 1,A	1,B $\otimes$ 1,A	0,A $\otimes$ 1,A	sum
2,A $\otimes$ 1,A	5/3	0	0	5/3
1,B $\otimes$ 1,A	0	3	0	3
0,A $\otimes$ 1,A	0	0	4/3	4/3
sum	5/3	3	4/3	6

$$- \quad \frac{1}{3}$$

(c) Transfer reaction mechanism

	2,A $\otimes$ 1,A	1,B $\otimes$ 1,A	0,A $\otimes$ 1,A	sum
2,A $\otimes$ 1,A	**-5/36**	45/36	20/36	5/3
1,B $\otimes$ 1,A	45/36	27/36	36/36	3
0,A $\otimes$ 1,A	20/36	36/36	**-8/36**	4/3
sum	5/3	3	4/3	6

$$= \quad \frac{2}{3}$$

Table 2.5: D$_2$ + D $\rightarrow$ D$_2$ + D statistics with $I_{tot} = 1$ and $\Gamma_{tot} = E$: Recomposition method.

(a) Identity reaction mechanism

	2,A $\otimes$ 1,A	1,B $\otimes$ 1,A	0,A $\otimes$ 1,A	sum
2,A $\otimes$ 1,A	25/27	0	20/27	5/3
1,B $\otimes$ 1,A	0	3	0	3
0,A $\otimes$ 1,A	20/27	0	16/27	4/3
sum	5/3	3	4/3	6

(b) Transfer reaction mechanism

	2,A $\otimes$ 1,A	1,B $\otimes$ 1,A	0,A $\otimes$ 1,A	sum
2,A $\otimes$ 1,A	25/108	45/36	20/108	5/3
1,B $\otimes$ 1,A	45/36	27/36	36/36	3
0,A $\otimes$ 1,A	20/108	36/36	16/108	4/3
sum	5/3	3	4/3	6

(c) Full–scrambling

	2,A $\otimes$ 1,A	1,B $\otimes$ 1,A	0,A $\otimes$ 1,A	sum
2,A $\otimes$ 1,A	25/54	45/54	20/54	5/3
1,B $\otimes$ 1,A	45/54	81/54	36/54	3
0,A $\otimes$ 1,A	20/54	36/54	16/54	4/3
sum	5/3	3	4/3	6

$$\frac{1}{3}$$

$$+ \quad \frac{2}{3}$$

$$=$$

Table 2.6: $D_2 + D \rightarrow D_2 + D$ statistics with $I_{tot} = 2$ and $\Gamma_{tot} = E$

(a) Identity reaction mechanism

	2,A $\otimes$ 1,A	1,B $\otimes$ 1,A	0,A $\otimes$ 1,A	sum
2,A $\otimes$ 1,A	5	0	0	5
1,B $\otimes$ 1,A	0	5	0	5
0,A $\otimes$ 1,A	0	0	0	0
sum	5	5	0	10

(b) Transfer reaction mechanism

	2,A $\otimes$ 1,A	1,B $\otimes$ 1,A	0,A $\otimes$ 1,A	sum
2,A $\otimes$ 1,A	5/4	15/4	0	5
1,B $\otimes$ 1,A	15/4	5/4	0	5
0,A $\otimes$ 1,A	0	0	0	0
sum	5	5	0	10

(c) Full–scrambling

	2,A $\otimes$ 1,A	1,B $\otimes$ 1,A	0,A $\otimes$ 1,A	sum
2,A $\otimes$ 1,A	5/2	5/2	0	5
1,B $\otimes$ 1,A	5/2	5/2	0	5
0,A $\otimes$ 1,A	0	0	0	0
sum	5	5	0	10

2.6 BOHMIAN INTERPRETATION OF NUCLEAR SPINS

Note: This section will not be part of the expected publication.

What is the nature of a wavefunction and its mathematical representation ? Is a wavefunction a true description of reality or is it an observer's mind construction ? How determined is the state of a system and can a wavefunction faithfully transcribe this state ? Do nuclei entities which are indistinguishable to an observer loose their individualities ? Are they really delocalised ? Here are few foundational questions which can be answered firmly according to dogmata or cautiously according to various schools of thought.

In this section, we question the interpretation of the informations and statistical weights gathered with the wavefunctions in the previous sections by reconsidering nuclear spin systems in line with the Bohmian interpretation of quantum mechanics. We propose a formalism to extract hidden variables of the systems. This incomplete attempt is a constructive challenge to the commonly accepted Copenhagen interpretation.

In section 2.6.1 , we will remind some differences between the Copenhagen and Bohmian interpretations of quantum mechanics and project these interpretations to our systems of interest. In section 2.6.2 , a formalism necessary for the Bohmian interpretation of nuclear spin systems is described. In section 2.6.3 , this formalism is applied to the H_3 system in order to derive statistical weights for the Bohmian informations. Physical implications are then discussed in section 2.6.4 .

2.6.1 Quantum determinacy or indeterminacy

A wavefunction can be interpreted according to the Copenhagen (indeterministic) or the Bohmian (deterministic) interpretation but before applying those semantics to nuclear spin systems, we shall briefly remind their differences through the Schroedinger's cat example.

Schroedinger's cat

A Cat can be in a living or dead state which we write $|alive\rangle$ and $|dead\rangle$. A living cat is enclosed in a box and asked to toss a quantum coin[4] which triggers a device that release hydrocyanic acid in the box if the result is head. The probabilities that the cat is alive or dead after the coin event and before the box is opened are 1/2. The wavefunction assigned to the cat entity is therefore $\left(1/\sqrt{2}\,|alive\rangle + 1/\sqrt{2}\,|dead\rangle\right)$. The $1/\sqrt{2}$ amplitudes are determined according to Born's rule and the signs of the two coefficients are irrelevant in this case because there are no symmetry implications.

---

[4]The original setup consist of a Geiger counter with a little bit of radioactive substance

The fundamental difference between the Copenhagen and the Bohmian interpretation lies in the interpretation of the mixing of the pure states. In the Copenhagen interpretation, the mixing is apparented to the "AND" logic operator or equivalently the intersection "∩" set operator meaning that the cat (the reality) is undetermined since both states $(\ |alive\rangle$ AND $|dead\rangle\ )$ are coexisting[5]. Only when the box is opened, the wavefunction collapses to one or the other state, *i.e.* the measurement action unfolds a degenerate reality. In the Bohmian interpretation, the mixing is apparented to the "exclusive–OR" logic operator or "exclusive disjunction" set operator meaning that the cat can be only in one single state at a time, even if the observer does not know it. Contrary to the Copenhagen interpretation, the Bohmian interpretation is deterministic nevertheless it can be undetermined from the observer's viewpoint which explains the mixing construction.

multi–spin system

According to the Copenhagen interpretation, we could measure the total symmetry, total spin and total magnetic moment for all subsets of nuclei of a given system in order to fully determine the system (*eq.* collapse the states). However, according to the frozen nuclear spin approximation which implies their time conservation, these quantum informations must have been the same before the measurement action meaning that the system was necessarily determined before the measurement. Therefore, the only fact that we can measure those quantum informations in the future implies that they are determined at anytime : the system is fully determined irrespective whether a measurement was performed or not. This argument known as "counterfactual definiteness" invalidates the Copenhagen interpretation since mixed states do not really exist nor do wavefunction collapse really occur. All the informations of the system already exist but the observer simply ignores them, which is why this interpretation belongs to the family of "hidden variable theories".

Taking for instance two molecules H_aH_b and H_cH_d far from each other and non-interacting, the symmetries of all the nuclei sets, *e.g.* Γ_{ad} or Γ_{bcd}, are already determined.

2.6.2   Formalism of the Bohmian interpretation

The formalism and the method will be illustrated through the most simple example, the 3–spin 1/2 system, *e.g.* H_3. The symmetry and angular momentum representations of this system as those of its subsystems are equivalent so we may only work from the symmetry viewpoint.

---

[5]If it were the "OR" logical operator or equivalently the union "∪" set operator, the state of the cat is even more undetermined since it is $(\ |alive\rangle$ OR $|dead\rangle$ OR $(\ |alive\rangle$ AND $|dead\rangle\ )\ )$.

Complete representation space

The representation space of the S_3 permutation group is $\{A_1, A_2, E\}$ and the representation space of each of the three $S_{2,1}$ permutation groups is $\{A, B\}$. Based on the previous argumentation, the symmetry information for all (sub)sets of nuclei is determined. Let this be the **complete state** of information. The complete states represent the map of permutation groups (see Fig. 2.1) and belong to the direct product of the representation spaces of all permutation groups. It implies not only the **total state** of symmetry but also all the **local states** of symmetry. The complete state of the 3–Hydrogen system $H_a H_b H_c$ thus belongs to the representation space of $S_{abc} \otimes S_{ab,c} \otimes S_{ac,b} \otimes S_{bc,a}$ which is $\{A_1, A_2, E\}_{abc} \otimes \{A, B\}_{ab,c} \otimes \{A, B\}_{ac,b} \otimes \{A, B\}_{bc,a}$ [6]. Let this be the **complete representation space**. The complete symmetry states which form the basis set of the complete representation space are written $(\Gamma_{abc} \otimes \Gamma_{ab,c} \otimes \Gamma_{ac,b} \otimes \Gamma_{bc,a})$ but for brevity, we will drop the $\otimes$ operators.

It is important to mention that the map of permutation groups does not have a group structure. Therefore the complete states are not classic group representations. This category of mathematical object with a higher order structure should be treated in the topos of the finite permutation groups using category theory. However, this paper aims for physical rather than mathematical implications so only the necessary tools are developed.

We can organise the complete states in classes where the localisation of the information is lost. We write those classes as $[\Gamma_{S_3} \Gamma_{S_2} \Gamma_{S_2} \Gamma_{S_2}]$. For example, the class of partition $[EAAB]$ written $[EA^2B]$ corresponds to $(EAAB) \oplus (EABA) \oplus (EBAA)$.

We also define for each permutation group the undetermined state u as $u = \bigcup_i \Gamma_i$, the union set operator $\cup$ being equivalent to the direct sum operator $\oplus$. The undetermined state in S_3 and S_2 permutation groups are $u = A_1 \oplus A_2 \oplus E$ and $u = A \oplus B$, respectively. Using the undetermined states of the permutation groups, we can express the **partial states** as sets (direct sums) of complete states. The direct sum operator being distributive, we have for example:

$$
\begin{align}
(EAuB) &= (E \otimes A \otimes u \otimes B) \tag{2.42} \\
&= (E \otimes A \otimes (A \oplus B) \otimes B) \tag{2.43} \\
&= (E \otimes A \otimes A \otimes B) \oplus (E \otimes A \otimes B \otimes B) \tag{2.44} \\
&= (EAAB) \oplus (EABB) \tag{2.45}
\end{align}
$$

This partial states considers $\Gamma_{ac,b}$ as undetermined corresponding to the induction–subduction scheme $S_{a,b,c} \uparrow S_{ab,c} \uparrow S_{abc} \downarrow S_{a,bc} \downarrow S_{a,b,c}$ which does not consider $S_{ac,b}$. The induction-subduction schemes employed in previous sections concern the representations in at most two different paths with their permutation groups, irrespective of the representations in the other permutation

---

[6] the subscripts are here to distinguish the permutation subgroups

groups. Their corresponding partial states are thus incomplete informations representative of the Copenhagen interpretation which consider as coexisting and undetermined all the possible states in some permutation groups. In the Bohmian interpretation, the partial states as unions (or direct sums) of complete states reflect an observer's construction due to his lack of knowledge of the system.

The direct product operator $\otimes$ is equivalent to the intersection set operator in the complete representation space. In the Bohmian interpretation, the direct product reflects the reality. Working between representations of the same permutation group, the direct product gives:

$$\Gamma_i \otimes \emptyset = \emptyset \tag{2.46}$$

$$\Gamma_i \otimes \Gamma_i = \Gamma_i \tag{2.47}$$

$$\Gamma_i \otimes \Gamma_j = \emptyset \tag{2.48}$$

$$\Gamma_i \otimes u = \Gamma_i \tag{2.49}$$

Working between representations of two distinct permutation groups, the direct product gives:

$$\Gamma_i \otimes \emptyset = \emptyset \tag{2.50}$$

$$\Gamma_i \otimes \Gamma_j = \Gamma_i \otimes \Gamma_j \tag{2.51}$$

$$\Gamma_i \otimes u = \Gamma_i \otimes u \tag{2.52}$$

From these properties, we can show that complete states are necessarily orthogonal since they do not share a common space in the complete representation space. For example, we have

$$
\begin{aligned}
(EAAB) \otimes (EABB) &= ((E \otimes E) \otimes (A \otimes A) \otimes (A \otimes B) \otimes (B \otimes B)) \tag{2.53}\\
&= (E \otimes A \otimes \emptyset \otimes B) \tag{2.54}\\
&= \emptyset \tag{2.55}
\end{aligned}
$$

which translates the fact that a system cannot have the complete symmetries (EAAB) and (EABB) at the same time since it cannot be both of A and B symmetry in the $S_{ac,b}$ permutation group. However, partial states may be non–orthogonal and overlap. For example, we have

$$
\begin{aligned}
(uAuB) \otimes (EAuB) &= ((u \otimes E) \otimes (A \otimes A) \otimes (u \otimes u) \otimes (B \otimes B)) \tag{2.56}\\
&= (E \otimes A \otimes u \otimes B) \tag{2.57}\\
&= (E \otimes A \otimes (A \oplus B) \otimes B) \tag{2.58}\\
&= (EAAB) \oplus (EABB) \tag{2.59}
\end{aligned}
$$

Causal Bayesian network

Consider now that the complete representation space forms a causal Bayesian network where the weights and probabilities of its elements are related.

We define the conditional weights $W_{(Y|X)}$ and probabilities (likelihoods) $P_{(Y|X)}$ as

$$W_{(Y|X)} \quad = \quad W_{(X \cap Y|X)} \quad = \quad W_{(X \cap Y)} \tag{2.60}$$

$$P_{(Y|X)} \quad = \quad P_{(X \cap Y|X)} \quad = \quad W_{(X \cap Y)}/W_{(X)} \tag{2.61}$$

X and Y being the observer's prior and posterior informations, respectively. In this study, they are symmetry representations of the permutation groups. The unconditional weights $W_{(X|u)}$ correspond to the absence of prior condition and we simply write them $W_{(X)}$. The weight of the no–information information corresponds to the total weight of the system, *i.e.* $W_{(u)} = W_{TOT} = (2I+1)^n$. The unconditional probabilities $P_{(X|u)}$ which we simply write $P_{(X)}$ are thus $P_{(X)} = W_{(X)}/W_{TOT}$.

Some important properties of the statistical weights are:

$$W_{(Y \cup X)} \quad = \quad W_{(X)} + W_{(Y)} - W_{(X \cap Y)} \tag{2.62}$$

$$W_{(Y \cap X)} \quad = \quad 0 \quad \text{if} \quad X \cap Y = \emptyset \tag{2.63}$$

$$W_{(Y|X)} \quad = \quad W_{(X|Y)} \tag{2.64}$$

Note that "$\cup$" is equivalent to "$\oplus$" and "$\cap$" is equivalent to "$\otimes$" in the complete space. The "$|$" is also equivalent to "$\otimes$" with the extra–characteristic that it delimits the observer's prior and posterior informations.

Equation 2.64 states that a conditional weight and its reciprocal are equal. This was interpreted as an equivalence to the Frobenius reciprocity principle in the previous sections (see Eqs. 2.23 and 2.36) and we see here that this principle also applies to the complete representation space. It implies that all the weight–tables of this paper are transposable by exchanging the prior and posterior property of the informations, *e.g.* switching an induction into its reciprocal subduction and vice–versa.

2.6.3 Derivation of the Bohmian informations

Unconditional weights of the Copenhagen informations

All the statistical weights of the H_3 system derived as in previous sections are given in Table 2.7 according to total and local symmetries and reaction mechanisms. They correspond to Copenhagen informations since the symmetry information in some permutation groups is undetermined. They can be translated in the Bohmian interpretation as unconditional weights for partial states. Their transcription into the Bohmian formalism is found in Table 2.8.

Unconditional weights of the Bohmian informations

The aim is now to access the unconditional weights of all the complete states from the unconditional weights of the partial states using Bayes inference.

Table 2.7: $H_2 + H \rightarrow H_2 + H$ statistical weights from the Copenhagen interpretation.

S_3		S_2		Id		Trans		FS	
				A	B	A	B	A	B
Total	8	A	6	6	0	9/2	3/2	5	1
		B	2	0	2	3/2	1/2	1	1
A_1	4	A	4	4	0	4	0	4	0
		B	0	0	0	0	0	0	0
A_2	0	A	0	0	0	0	0	0	0
		B	0	0	0	0	0	0	0
E	4	A	2	2	0	1/2	3/2	1	1
		B	2	0	2	3/2	1/2	1	1

Regarding the A_1 total symmetry, we find:

$$
\begin{aligned}
W_{(A_1AAA)} &= W_{(A_1AAu)} - W_{(A_1AAB)} & (2.65) \\
&= W_{(A_1AAu)} - P_{(A_1AAB|A_1uAB)} \times W_{(A_1uAB)} & (2.66) \\
&= W_{(A_1AAu)} & (2.67) \\
&= 4 & (2.68)
\end{aligned}
$$

since $W_{(A_1uAB)} = 0$. Furthermore, it is straightforward to derive that all the complete states of the classes $[A_1A^2B]$, $[A_1AB^2]$ and $[A_1B^3]$ have statistical weights of 0 since the partial states of the classes $[A_1ABu]$ and $[A_1B^2u]$ have weights of 0.

We thus have the likelihood $P_{(A_1AAA|A_1uuu)} = W_{(A_1AAA)}/W_{(A_1uuu)} = 1$ meaning that all the subsets of a totally symmetric set are necessarily symmetric. Equivalently for the 3–deuterium system, we would derive $P_{(A_2BBB|A_2uuu)} = 1$ meaning that all the subsets of a totally antisymmetric set are necessarily antisymmetric.

We can then put forward the causality principle to state that: Since a totally symmetric (A_1uuu) set of nuclei necessarily subduces symmetric subsets ($uAAA$), reciprocally, completely symmetric subsets ($uAAA$) must necessarily induce a totally symmetric set (A_1uuu). The same causality stands for antisymmetric representations strictly correlating A_2 with ($uBBB$). It fol-

Table 2.8: H_3 unconditional weight of the partial states corresponding to Copenhagen informations.

Class	Partial states						Weight
$[uu^3]$	(uuuu)						8
$[uAu^2]$	(uAuu)	(uuAu)	(uuuA)				6
$[uBu^2]$	(uBuu)	(uuBu)	(uuuB)				2
$[uA^2u]$	(uAAu)	(uAuA)	(uuAA)				9/2
$[uB^2u]$	(uBBu)	(uBuB)	(uuBB)				1/2
$[uABu]$	(uABu)	(uBAu)	(uAuB)	(uBuA)	(uuAB)	(uuBA)	3/2
$[A_1u^3]$	(A_1uuu)						4
$[A_1Au^2]$	(A_1Auu)	(A_1uAu)	(A_1uuA)				4
$[A_1Bu^2]$	(A_1Buu)	(A_1uBu)	(A_1uuB)				0
$[A_1A^2u]$	(A_1AAu)	(A_1AuA)	(A_1uAA)				4
$[A_1B^2u]$	(A_1BBu)	(A_1BuB)	(A_1uBB)				0
$[A_1ABu]$	(A_1ABu)	(A_1BAu)	(A_1AuB)	(A_1BuA)	(A_1uAB)	(A_1uBA)	0
$[A_2u^3]$	(A_2uuu)						0
$[A_2Au^2]$	(A_2Auu)	(A_2uAu)	(A_2uuA)				0
$[A_2Bu^2]$	(A_2Buu)	(A_2uBu)	(A_2uuB)				0
$[A_2A^2u]$	(A_2AAu)	(A_2AuA)	(A_2uAA)				0
$[A_2B^2u]$	(A_2BBu)	(A_2BuB)	(A_2uBB)				0
$[A_2ABu]$	(A_2ABu)	(A_2BAu)	(A_2AuB)	(A_2BuA)	(A_2uAB)	(A_2uBA)	0
$[Eu^3]$	(Euuu)						4
$[EAu^2]$	(EAuu)	(EuAu)	(EuuA)				2
$[EBu^2]$	(EBuu)	(EuBu)	(EuuB)				2
$[EA^2u]$	(EAAu)	(EAuA)	(EuAA)				1/2
$[EB^2u]$	(EBBu)	(EBuB)	(EuBB)				1/2
$[EABu]$	(EABu)	(EBAu)	(EAuB)	(EBuA)	(EuAB)	(EuBA)	3/2

lows that the (*uAAA*) and (*uBBB*) completely symmetric and antisymmetric subsets cannot correlate with the total symmetry (*Euuu*). Therefore, the complete states (*EAAA*) and (*EBBB*) cannot exist and we have

$$W_{(EAAA)} \;=\; W_{(EBBB)} \;=\; 0 \tag{2.69}$$

Looking now at the E total symmetry, we have the relations

$$W_{(EAuu)} = W_{(EAAA)} + W_{(EAAB)} + W_{(EABA)} + W_{(EABB)} = 2 \tag{2.70}$$
$$W_{(EuuB)} = W_{(EBBB)} + W_{(EAAB)} + W_{(EBAB)} + W_{(EABB)} = 2 \tag{2.71}$$

Subtracting Eq. 2.71 from Eq. 2.70 and using Eq. 2.69, we find that

$$W_{(EABA)} = W_{(EBAB)} \tag{2.72}$$

By permutation of the $S_{2,1}$ subgroups is Eqs. 2.70 and 2.71, we can establish that all the complete states of the classes $[EA^2B]$ and $[EAB^2]$ have the same weights. Regarding that

$$W_{(Euuu)} = W_{(EAAB)} + W_{(EABA)} + W_{(EBAA)} + W_{(EABB)} + W_{(EBAB)} + W_{(EBBA)} = 4 \tag{2.73}$$

we get

$$W_{(EAAB)} = W_{(EABA)} = W_{(EBAA)} = W_{(EABB)} = W_{(EBAB)} = W_{(EBBA)} = 2/3 \tag{2.74}$$

and

$$W_{[EA^2B]} = W_{(EAAB)} + W_{(EABA)} + W_{(EBAA)} = 2 \tag{2.75}$$
$$W_{[EAB^2]} = W_{(EABB)} + W_{(EBAB)} + W_{(EBBA)} = 2 \tag{2.76}$$

Note that the unconditional weights of the complete states implies that we don't have any prior informations on the subsets of nuclei. Since there is no prior localisation in the system, the unconditional complete informations are *a posteriori* delocalised.

Conditional weights of the localised Bohmian informations

Consider now a $H_aH_b + H_c$ collision with the prior information $\Gamma_{ab,c} = B$, that is $(uBuu)$. Using the unconditional weights we just determined and the definition of the conditional weights (Eq. 2.60), we find

$$
\begin{aligned}
W_{(EBuu|uBuu)} &= W_{(EBuu)} &= 2 & \tag{2.77} \\
W_{(EBAu|uBuu)} &= W_{(EBAu)} &= 3/2 & \tag{2.78} \\
W_{(EBuA|uBuu)} &= W_{(EBuA)} &= 3/2 & \tag{2.79} \\
W_{(EBBu|uBuu)} &= W_{(EBBu)} &= 1/2 & \tag{2.80} \\
W_{(EBuB|uBuu)} &= W_{(EBuB)} &= 1/2 & \tag{2.81}
\end{aligned}
$$

Given the relations

$$W_{(EBBA|uBuu)} + W_{(EBBB|uBuu)} = W_{(EBBu|uBuu)} = 1/2 \tag{2.82}$$
$$W_{(EBAB|uBuu)} + W_{(EBBB|uBuu)} = W_{(EBuB|uBuu)} = 1/2 \tag{2.83}$$
$$W_{(EBAA|uBuu)} + W_{(EBAB|uBuu)} = W_{(EBAu|uBuu)} = 3/2 \tag{2.84}$$

and Eq. 2.69 , we have

$$
\begin{aligned}
W_{(EBBA|uBuu)} &= 1/2 & \tag{2.85} \\
W_{(EBAB|uBuu)} &= 1/2 & \tag{2.86} \\
W_{(EBAA|uBuu)} &= 1 & \tag{2.87}
\end{aligned}
$$

Table 2.9: Conditional weights of the localised Bohmian informations for the 3 spin–1/2 system. The induction weights are equivalent to the subduction weights since it consists in exchanging the prior and posterior properties of the informations. Note that the no-information (uuuu) prior information implies that the posterior informations are delocalised.

$S_{ab,c}$	$S_{ac,b}$	$S_{bc,a}$	A_1 [A^3] AAA	E [A^2B] AAB	ABA	BAA	[AB^2] BBA	BAB	ABB	A_2 [B^3] BBB	Sum
u	u	u	4	2/3	2/3	2/3	2/3	2/3	2/3	0	8
A	u	u	4	1/2	1/2	0	0	0	1	0	6
B	u	u	0	0	0	1	1/2	1/2	0	0	2
A	A	u	4	1/2	0	0	0	0	0	0	9/2
A	B	u	0	0	1/2	0	0	0	1	0	3/2
B	A	u	0	0	0	1	0	1/2	0	0	3/2
B	B	u	0	0	0	0	1/2	0	0	0	1/2
A	A	A	4	0	0	0	0	0	0	0	4
A	A	B	0	1/2	0	0	0	0	0	0	1/2
A	B	A	0	0	1/2	0	0	0	0	0	1/2
B	A	A	0	0	0	1	0	0	0	0	1
B	B	A	0	0	0	0	1/2	0	0	0	1/2
B	A	B	0	0	0	0	0	1/2	0	0	1/2
A	B	B	0	0	0	0	0	0	1	0	1
B	B	B	0	0	0	0	0	0	0	0	0
Sum			4	1/2	1/2	1	1/2	1/2	1	0	8=2^3
					2			2			

Moreover, the prior condition $(uBuu)$ forces to 0 the conditional weights of the partial states and complete states with $\Gamma_{ab,c} = A$.

By applying the same method to any prior localised information(s), we obtain all the conditional weights of localised Bohmian informations for the H_3 system as given in Table 2.9.

Conditional weights of the delocalised Bohmian informations

It is also possible to extract conditional weights for delocalised prior and posterior informations using the conditional weights of the localised informations just calculated. For this purpose, we use the classes as defined in section 2.6.2.

For example, let our only prior information be "*there is at least one pair of nuclei with B symmetry*" corresponding to $[uBu^2] = (uBuu) \oplus (uuBu) \oplus (uuuB)$. Since the unconditional weights of those partial states are equal, *i.e.* $W_{(uBuu)} = W_{(uuBu)} = W_{(uuuB)}$, we find that each localised partial state is equiprobable:

$$P_{(uBuu|[uBu^2])} = P_{(uuBu|[uBu^2])} = P_{(uuuB|[uBu^2])} = 1/3 \tag{2.88}$$

In other terms, the identified (but not localised) pair of nuclei with B symmetry is equaly likely to be one of the three pairs.

Using the fact that

$$W_{(X|Z)} = \sum_Y W_{(X|Y)} \times P_{(Y|Z)} \tag{2.89}$$

we can derive the conditional weight of the class $[EA^2B]$ composed of (EAAB), (EABA) and (EBAA):

$$
\begin{aligned}
W_{([EA^2B]|[uBu^2])} &= W_{(EAAB|[uBu^2])} + W_{(EABA|[uBu^2])} + W_{(EBAA|[uBu^2])} \\
&= \left(W_{(EAAB|uBuu)} + W_{(EABA|uBuu)} + W_{(EBAA|uBuu)}\right) \times P_{(uBuu|[uBu^2])} \\
&\quad + \left(W_{(EAAB|uuBu)} + W_{(EABA|uuBu)} + W_{(EBAA|uuBu)}\right) \times P_{(uuBu|[uBu^2])} \\
&\quad + \left(W_{(EAAB|uuuB)} + W_{(EABA|uuuB)} + W_{(EBAA|uuuB)}\right) \times P_{(uuuB|[uBu^2])} \\
&= (0+0+1) \times 1/3 \\
&\quad + (0+1/2+0) \times 1/3 \\
&\quad + (1/2+0+0) \times 1/3 \\
&= 2/3 \tag{2.90}
\end{aligned}
$$

and the conditional weight of the class $[EAB^2]$ composed of (EABB), (EBAB) and (EBBA):

$$
\begin{aligned}
W_{([EAB^2]|[uBu^2])} &= W_{(EBBA|[uBu^2])} + W_{(EBAB|[uBu^2])} + W_{(EABB|[uBu^2])} \\
&= \left(W_{(EBBA|uBuu)} + W_{(EBAB|uBuu)} + W_{(EABB|uBuu)} \right) \times P_{(uBuu|[uBu^2])} \\
&\quad + \left(W_{(EBBA|uuBu)} + W_{(EBAB|uuBu)} + W_{(EABB|uuBu)} \right) \times P_{(uuBu|[uBu^2])} \\
&\quad + \left(W_{(EBBA|uuuB)} + W_{(EBAB|uuuB)} + W_{(EABB|uuuB)} \right) \times P_{(uuuB|[uBu^2])} \\
&= \left(1/2 + 1/2 + 0 \right) \times 1/3 \\
&\quad + \left(1/2 + 0 + 1 \right) \times 1/3 \\
&\quad + \left(0 + 1/2 + 1 \right) \times 1/3 \\
&= 4/3
\end{aligned}
\tag{2.91}
$$

By applying the same method to any prior delocalised information(s), we obtain all the conditional weights of localised Bohmian informations for the H_3 system as given in Table 2.10.

Table 2.10: Conditional weights of the delocalised Bohmian informations for the 3 spin–1/2 system. The induction weights are equivalent to the subduction weights since it consists in exchanging the prior and posterior properties of the informations.

S_3 $[S_{2,1}{}^3]$	A_1 $[A^3]$	E $[A^2B]$	$[AB^2]$	A_2 $[B^3]$	Sum
$[u^3]$	4	2	2	0	8
$[Au^2]$	4	4/3	2/3	0	6
$[Bu^2]$	0	2/3	4/3	0	2
$[A^2u]$	4	2/3	0	0	14/3
$[ABu]$	0	4/3	4/3	0	8/3
$[B^2u]$	0	0	2/3	0	2/3
$[A^3]$	4	0	0	0	4
$[A^2B]$	0	2	0	0	2
$[AB^2]$	0	0	2	0	2
$[B^3]$	0	0	0	0	0

2.6.4 Physical implications

Theories with their formalism, objects, classes, semantic, logic, attributes, relations, laws and so forth represent interpretations of reality and conversely. Two different interpretations can thus lead to different theoretical predictions. We will dicuss few examples which highlight the differences between the Copenhagen and the Bohmian interpretations.

3–proton Gedankenexperiment

The protocole of the thought experiment is:

> *Let a p–H_2 molecule collide with an H^+ cation in order to obtain an H_3^+ complex with E total symmetry. Then repeat infinitely the following procedure: Randomly pick one H_2 molecule from the H_3^+ complex and measure the symmetry of its nuclear spin wavefunction, e.g. by spectroscopic means[7]. Reassemble the H_3^+ complex.*
>
> *What should the A:B ratio of the measured symmetries converge to ?*

The Copenhagen interpretation only considers one type of E total symmetry which correlates with A and B local symmetries evenly. As shown in table 2.7, the probabilities that a randomly picked H_2 molecule has A or B symmetry will always be 1/2 and 1/2. Therefore, any experiment should converge to the A:B ratio of 1:1.

The Bohmain interpretation distinguishes two types of E total symmetries: those from the complete symmetry class [EA^{2}B] and those from the class [EAB^2]. According to table 2.9, with the B symmetry of the initial H_2 molecule as a prior localised information, the probabilities to form a complexes with a complete symmetry from the class [EA^{2}B] and [EAB^2] are 1/2 and 1/2. Once the complex is formed, the localisation of the informations is lost since we cannot distinguish the two nuclei of the initial H_2 molecule. According to table 2.10, the probabilities to pick randomly an H_2 molecule with A or B symmetry are 2/3 and 1/3 for a [EA^{2}B] complex and 1/3 and 2/3 for a [EAB^2] complex. Therefore, half of the experiments will converge to a A:B ratio of 2:1 and the other half will converge to 1:2.

Note that if the 3–proton system is renewed after each random pick and symmetry measurement of an H_2 molecule, *e.g.* using molecular beams, the Bohmian interpretation yields probabilities of $1/2 \times 2/3 + 1/2 \times 1/3 = 1/2$ for A and B symmetries like the Copenhagen interpretation. It is thus essential to carry out the experiment with the same 3–protons in order

---

[7]which have the advantage to conserve the nuclear spin symmetries

to expect differences.

The fact that an A or B symmetry is preferentially picked will bias the expected results in both interpretations. Nevertheless, it will remain that (i) all the experiments will have the same A:B ratio according to the Copenhagen interpretation while (ii) two different A:B ratios will be evenly observed for the Bohmian interpretation. Consequently, the complete randomness of the pick of the H_2 molecule is not a critical element of the experiment.

Scattering theories

In statistical scattering theories such as Phase Space Theory (PST), nuclear spin selection rules can be (i) simply neglected or (ii) considered in accordance with the Copenhagen interpretation or (iii) the Bohmian interpretation.

Consider for instance the following collision at low kinetic energy ($\sim$10 K):

$$o–H_2 \text{ (J=1)} + H^+ + 10\,K \longrightarrow o–H_2 \text{ (J=1)} + H^+ + 10\,K \qquad (2.92)$$
$$\longrightarrow p–H_2 \text{ (J=0)} + H^+ + 180\,K \qquad (2.93)$$
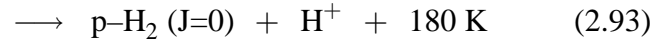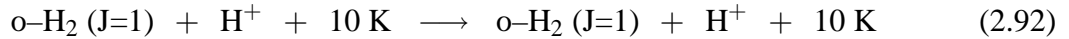
The two only energetically accessible channels are the entrance channel and the channel $p–H_2(J=0) + H^+$ that we label α and β, respectively. In the high orbital angular momentum limit, we have $W_\alpha = 3W_\beta$ because of the channels' angular momentum degeneracies (2J+1).

When neglecting the nuclear spins, irrespective of the feasible reaction mechanisms, the inelastic transition probability is:

$$
\begin{aligned}
P_{(\beta|\alpha,E_{col}=10K)} &= \frac{W_\beta}{W_\beta + W_\alpha} \\
&= 1/4
\end{aligned}
\qquad (2.94)
$$

In the Copenhagen interpretation (see Table 2.7), a system has only one total symmetry. The scatering quantities (probabilities, cross sections, *etc*) are thus calculated separately for each total symmetry and then summed according to their respective weights. Assuming full–scrambling of the H_3^+ intermediate complex, the inelastic transition probability is:

$$
\begin{aligned}
P_{(\beta|\alpha,E_{col}=10K)} &= P_{(A_1|A)} \times \frac{P^*_{(B|A_1)} \times W_\beta}{P^*_{(A|A_1)} \times W_\alpha + P^*_{(B|A_1)} \times W_\beta} \\
&\quad + P_{(E|A)} \times \frac{P^*_{(B|E)} \times W_\beta}{P^*_{(A|E)} \times W_\alpha + P^*_{(B|E)} \times W_\beta} \\
&= 4/6 \times \frac{0 \times 1}{1 \times 3 + 0 \times 1} + 2/6 \times \frac{1/2 \times 1}{1/2 \times 3 + 1/2 \times 1} \\
&= 1/12
\end{aligned}
\qquad (2.95)
$$

The corrected decay probabilities P^* are defined as $P^*_{(\Gamma_2|\Gamma_3)} = P_{(\Gamma_2|\Gamma_3)}/dim(\Gamma_2)$ [see 10]. Since the dimensions of the A and B symmetries of $S_{2,1}$ are unity, this correction does not affect the results of a 3–nuclei system.

In the Bohmian interpretation (see Tables 2.9 and 2.10), a system belongs to only one class of complete symmetry. The scaterring quantities are thus calculated separately for each class of complete symmetry and then summed according to their respective conditional weights. Assuming full–scrambling of the H_3^+ intermediate complex, the inelastic transition probability is:

$$
\begin{aligned}
P_{(\beta|\alpha,E_{col}=10K)} &= P_{([A_1AAA]|uAuu)} \times \frac{P^*_{([uBuu]|[A_1AAA])} \times W_\beta}{P^*_{([uAuu]|[A_1AAA])} \times W_\alpha + P^*_{([uBuu]|[A_1AAA])} \times W_\beta} \\
&+ P_{([EA^2B]|uAuu)} \times \frac{P^*_{([uBuu]|[EA^2B])} \times W_\beta}{P^*_{([uAuu]|[EA^2B])} \times W_\alpha + P^*_{([uBuu]|[EA^2B])} \times W_\beta} \\
&+ P_{([EAB^2]|uAuu)} \times \frac{P^*_{([uBuu]|[EAB^2])} \times W_\beta}{P^*_{([uAuu]|[EAB^2])} \times W_\alpha + P^*_{([uBuu]|[EAB^2])} \times W_\beta} \\
&= 4/6 \times \frac{0 \times 1}{1 \times 3 + 0 \times 1} \\
&+ 1/6 \times \frac{1/3 \times 1}{2/3 \times 3 + 1/3 \times 1} \\
&+ 1/6 \times \frac{2/3 \times 1}{1/3 \times 3 + 2/3 \times 1} \\
&= 19/210
\end{aligned}
\tag{2.96}
$$

As illustrated by the Gedenkenexperiment, the Copenhagen and Bohmian interpretations lead to the different theoretical expectations of 35/420 and 38/420, respectively.

Statistical scattering theories account for nuclear spins do it according to the Copenhagen interpretation only [1, 10–12]. We could not clarify yet how full–quantum scattering theories (time–dependant or time–independent) could treat the nuclear spin degree of freedom and its statistics nor if they could go beyond the frozen nuclear spin approximation. It is also unfortunate that some studies still do not consider at all the nuclear selection rules at risk for important errors, *e.g.* a factor of ~ 3 in the example presented.

Regarding the symmetrisation postulate of quantum mechanics, the full-dimensional symmetry information of a colliding system is necessary to tell which rovibronic channels are accessible at each dissociative asymptote. Rejecting[8] the superposition of symmetries of any subset of nuclei or dissociative asymptote, the complete state of symmetry and the Bohmian interpretation of nuclear spins appear imperative.

---

[8]See the counterfactual argumentation in Sec. 2.6.1

Spectroscopy

New spectroscopic implications would also be expected with the Bohmian interpretation. For example, para-H_3^+ molecules which have a E total nuclear spin symmetry and a total nuclear spin angular momentum of 1/2 would split in two classes: the $[EA^2B]$ and the $[EAB^2]$ complete symmetry classes corresponding to the $[1/2,1^2,0]$ and the $[1/2,1,0^2]$ complete angular momentum classes. According to the frozen nuclear spin approximation, the transition from one class to another would be extremely unlikely although not impossible considering very small internal nuclear spin interactions. Such interactions should lead to off–diagonal terms in the total Hamiltonian and extremely–fine splitting, probably finer than the hyperfine splitting.

To reach that point, molecular quantum mechanics ought to be re–interpreted according to the Bohmian viewpoint by generalising the symmetrisation postulate from the total symmetry to the complete symmetry, *i.e.* from the complete nuclear permutation group to the complete map of nuclear permutation groups (see Fig. 2.1). Moreover, like the nuclear spin degree of freedom, the rotational, vibrational and electronic degrees of freedom also need to be re-interpreted in the complete symmetry space.

2.6.5   Conclusion of the Bohmian section

The "counterfactual definiteness" of the nuclear spin symmetries supports the deterministic Bohmian interpretation and invalidates the indeterministic Copenhagen interpretation.

The statistics of the Bohmian informations are fully consistent (*i.e.* not contradictory) with the statistics of the Copenhagen interpretation since the latter are inferred from the former using the causality principle and Bayesian inference. In fact, the Bohmian informations which are based on the constraining determinacy property contain extra informations which can be regarded as hidden variables, *i.e.* informations which are real but unknown to the observer. Bohmian (complete states) statistics can be summed to recover the Copenhagen (partial states) statistics. Furthermore, it is possible to infer statistics for delocalised Bohmian informations from the statistics of the localised Bohmian informations. Great care must be taken with the concept of prior, posterior, localised, delocalised and undetermined informations from the observer's viewpoint. These apparently simple concepts can be misleading.

The Bohmian interpretation has been applied to the 3–spin 1/2 system and it can be applied to any system. However, comparing the 3–nuclei and the 4–nuclei systems in Fig. 2.1, it is clear that the number of permutation groups and subgroups and the complexity of a system increases dramatically with its number of nuclei. Like the system presently studied, spin 1/2 systems are the most simple because their complete symmetry and complete angular momentum spaces are isomorphic. Therefore, regarding the conclusions of Sec. 2.5, it would be interesting to apply this interpretation to the 3–spin 1 system and the complete symmetry–angular momentum space $[A_1, A_2, E]_{abc} \otimes [\mathscr{D}_0, \mathscr{D}_1, \mathscr{D}_2, \mathscr{D}_3]_{abc} \otimes [A, B]_{ab,c} \otimes [\mathscr{D}_0, \mathscr{D}_1, \mathscr{D}_2]_{ab,c} \otimes [A, B]_{ac,b} \otimes [\mathscr{D}_0, \mathscr{D}_1, \mathscr{D}_2]_{ac,b} \otimes [A, B]_{bc,a} \otimes [\mathscr{D}_0, \mathscr{D}_1, \mathscr{D}_2]_{bc,a}$.

The 3–proton Gedankenexperiment and the o–H_2 + H^+ scaterring examples were developed to illustrate the differences in predictions between the Copenhagen and the Bohmian interpretations of nuclear spins. These two examples are probably the "worst" cases but for most of the systems, the two interpretations could lead to extremely faint differences probably beyond most instrumental limits.

2.7 CONCLUSIONS

We described in details nuclear spin wavefunctions according to the angular momentum and/or symmetry viewpoints. Using these wavefunctions, a method to derive the nuclear spin statistics rising from the frozen nuclear spin approximation in associative, dissociative or reactive processes was developed. This method is in agreement with the permutation symmetry and angular momentum algebra from Quack [1] and Oka [2], respectively.

A detailed analysis of the D_3 system revealed weaknesses in the angular momentum viewpoint and supports the necessity of the permutation symmetry viewpoint. The problems and paradox encountered for the angular momentum viewpoint are mostly intriguing and need an explanation which lies either in the interpretation itself or in its mathematical transcription.

Additionally, a new deterministic interpretation of nuclear spins in molecular physics is proposed. This interpretation in the line of the Bohmian school of thought seems better suited for scattering theories than the indeterministic Copenhagen interpretation but its extension to the field of spectroscopy appears difficult.

Regarding the symmetrisation postulate of quantum mechanics, the nuclear spin degree of freedom has an essential role in molecular physics and particularly scattering theories, nevertheless, it is clear that its understanding can be improved and its weak dedicated literature completed.

REFERENCES

[1] M. Quack, Mol. Phys. **34**, 477 (1977).

[2] T. Oka, J. Mol. Spec. **228**, 635 (2004).

[3] P. L. Chapovsky, Phys. Rev. A **43**, 3624 (1991).

[4] P. Chapovsky, J. Mol. Struc. **599**, 337 (2001).

[5] P. L. Chapovsky and L. J. F. Hermans, ArXiv Physics e-prints (2002), `arXiv:physics/0204036`.

[6] M. Tudorie, P. Cacciani, J. Cosléou, F. Herlemont, M. Khelkhal, C. Puzzarini, S. Maret, and C. Kahane, Astron. Astrophys. **453**, 755 (2006).

[7] M. Cordonnier, D. Uy, R. M. Dickson, K. E. Kerr, Y. Zhang, and T. Oka, J. Chem. Phys. **113**, 3181 (2000).

[8] P. Bunker and P. Jensen, *Molecular symmetry and spectroscopy* (NRC Research Press, Ottawa, 1998).

[9] P. Bunker and P. Jensen, *Fundatamentals of molecular symmetry* (Institute of Physics Publishers, Bristol and Philadelphia, 2004).

[10] K. Park and J. C. Light, J. Chem. Phys. **127**, 224101 (2007).

[11] D. Gerlich, J. Chem. Phys. **92**, 2377 (1990).

[12] K. Park and J. C. Light, J. Chem. Phys. **126**, 044305 (2007).

APPENDICES

2.A CHARACTER AND CORRELATION TABLES

S₂		
class	$[1^2]$	$[2]$
partition	1	1
A	1	1
B	1	-1

S₅							
class	$[1^5]$	$[21^3]$	$[2^21]$	$[31^2]$	$[32]$	$[41]$	$[5]$
partition	1	10	15	20	20	30	24
A_1	1	1	1	1	1	1	1
A_2	1	-1	1	1	-1	-1	1
G_1	4	2	0	1	-1	0	-1
G_2	4	-2	0	1	1	0	-1
H_1	5	1	1	-1	1	-1	0
H_2	5	-1	1	-1	-1	1	0
I	6	0	-2	0	0	0	1

S₃			
class	$[1^3]$	$[21]$	$[3]$
partition	1	3	2
A_1	1	1	1
A_2	1	-1	1
E	2	0	-1

$S_3\otimes S_2$						
S₃ class	$[1^3]$	$[21]$	$[3]$	$[1^3]$	$[21]$	$[3]$
S₂ class	$[1^2]$	$[1^2]$	$[1^2]$	$[2]$	$[2]$	$[2]$
partition	1	3	2	1	3	2
(A_1,A)	1	1	1	1	1	1
(A_1,B)	1	1	1	-1	-1	-1
(A_2,A)	1	-1	1	1	-1	1
(A_2,B)	1	-1	1	-1	1	-1
(E,A)	2	0	-1	2	0	-1
(E,B)	2	0	-1	-2	0	1

S₄					
class	$[1^4]$	$[21^2]$	$[2^2]$	$[31]$	$[4]$
partition	1	6	3	8	6
A_1	1	1	1	1	1
A_2	1	-1	1	1	-1
E	2	0	2	-1	0
F_1	3	1	-1	0	-1
F_2	3	-1	-1	0	1

$^\diamond S_2\otimes{}^\bullet S_2$				
$^\diamond$S₂ class	$[1^2]$	$[2]$	$[1^2]$	$[2]$
$^\bullet$S₂ class	$[1^2]$	$[1^2]$	$[2]$	$[2]$
partition	1	1	1	1
$(^\diamond A,{}^\bullet A)$	1	1	1	1
$(^\diamond A,{}^\bullet B)$	1	1	-1	-1
$(^\diamond B,{}^\bullet A)$	1	-1	1	-1
$(^\diamond B,{}^\bullet B)$	1	-1	-1	1

Table 2.11: Character tables

S_3	$S_2 \otimes S_1$
A_1	(A,A)
A_2	(B,A)
E	(A,A) + (B,A)

$S_2 \otimes S_1$	S_3
(A,A)	A_1 + E
(B,A)	A_2 + E

S_4	$S_3 \otimes S_1$	$S_2 \otimes S_2$
A_1	(A_1,A)	(A,A)
A_2	(A_2,A)	(B,B)
E	(E,A)	(A,A) + (B,B)
F_1	$(A_1,A) + (E,A)$	(A,A) + (A,B) + (B,A)
F_2	$(A_2,A) + (E,A)$	(A,B) + (B,A) + (B,B)

$S_2 \otimes S_2$	S_4
(A,A)	A_1 + E + F_1
(A,B)	F_1 + F_2
(B,A)	F_1 + F_2
(B,B)	A_2 + E + F_2

$S_3 \otimes S_1$	S_4
(A_1,A)	A_1 + F_1
(A_2,A)	A_2 + F_2
(E,A)	E + F_1 + F_2

S_5	$S_4 \otimes S_1$	$S_3 \otimes S_2$
A_1	(A_1,A)	(A_1,A)
A_2	(A_2,A)	(A_2,B)
G_1	$(A_1,A)+(F_1,A)$	$(A_1,A)+(A_1,B)+(E,A)$
G_2	$(A_2,A)+(F_2,A)$	$(A_2,A)+(A_2,B)+(E,B)$
H_1	$(E,A)+(F_1,A)$	$(A_1,A)+(E,A)+(E,B)$
H_2	$(E,A)+(F_2,A)$	$(A_2,A)+(E,A)+(E,B)$
I	$(F_1,A)+(F_2,A)$	$(A_1,B)+(A_2,A)+(E,A)+(E,B)$

$S_4 \otimes S_1$	S_5
(A_1,A)	A_1 + G_1
(A_2,A)	A_2 + G_2
(E,A)	H_1 + H_2
(F_1,A)	G_1 + H_1
(F_2,A)	G_2 + H_2

$S_3 \otimes S_2$	S_5
(A_1,A)	A_1 + G_1 + H_1
(A_1,B)	G_1 + I
(A_2,A)	G_2 + I
(A_2,B)	A_2 + G_2 + H_2
(E,A)	G_1 + H_1 + H_1
(E,B)	G_2 + H_1 + H_1

Table 2.12: Correlation tables

2.B NUCLEAR SPIN STATISTICS

Table 2.13: Total angular momentum and total symmetry representations of several systems.

System	Total Spin	Frequency[a]	Degeneracy[b]	Symmetry	Weight
$(\mathscr{D}_{1/2})^2$	0	1	1	B	1
	1	1	3	A	3
	$\mathscr{D}_0 \oplus \mathscr{D}_1$		$3A \oplus B$		$\Sigma = 2^2$
$(\mathscr{D}_{1/2})^3$	1/2	2	2	E	4
	3/2	1	4	A_1	4
	$2\mathscr{D}_{1/2} \oplus \mathscr{D}_{3/2}$		$4A_1 \oplus 2E$		$\Sigma = 2^3$
$(\mathscr{D}_{1/2})^4$	0	2	1	E	2
	1	3	3	F_1	9
	2	1	5	A_1	5
	$2\mathscr{D}_0 \oplus 3\mathscr{D}_1 \oplus \mathscr{D}_2$		$5A_1 \oplus E \oplus 3F_1$		$\Sigma = 2^4$
$(\mathscr{D}_{1/2})^5$	1/2	5	2	H_1	10
	3/2	4	4	G_1	16
	5/2	1	6	A_1	6
	$5\mathscr{D}_{1/2} \oplus 4\mathscr{D}_{3/2} \oplus \mathscr{D}_{5/2}$		$6A_1 \oplus 4G_1 \oplus 2H_1$		$\Sigma = 2^5$
$(\mathscr{D}_1)^2$	0	1	1	A	1
	1	1	3	B	3
	2	1	5	A	5
	$\mathscr{D}_0 \oplus \mathscr{D}_1 \oplus \mathscr{D}_2$		$6A \oplus 3B$		$\Sigma = 3^2$
$(\mathscr{D}_1)^3$	0	1	1	A_2	1
	1	1 + 2	3	$A_1 + E$	9
	2	2	5	E	10
	3	1	7	A_1	8
	$\mathscr{D}_0 \oplus 3\mathscr{D}_1 \oplus 2\mathscr{D}_2 \oplus \mathscr{D}_3$		$10A_1 \oplus A_2 \oplus 8E$		$\Sigma = 3^3$
$(\mathscr{D}_1)^4$	0	1 + 2	1	$A_1 + E$	3
	1	3 + 3	3	$F_1 + F_2$	18
	2	1 + 2 + 3	5	$A_1 + E + F_1$	30
	3	3	7	F_1	21
	4	1	9	A_1	9
	$3\mathscr{D}_0 \oplus 6\mathscr{D}_1 \oplus 6\mathscr{D}_2 \oplus 3\mathscr{D}_3 \oplus \mathscr{D}_4$		$15A_1 \oplus 6E \oplus 15F_1 \oplus 3F_2$		$\Sigma = 3^4$
$(\mathscr{D}_1)^5$	0	6	1	I	6
	1	1 + 4 + 5 + 5	3	$A_1 + G_1 + H_1 + H_2$	45
	2	4 + 5 + 6	5	$G_1 + H_1 + I$	75
	3	1 + 4 + 5	7	$A_1 + G_1 + H_1$	70
	4	4	9	G_1	36
	5	1	11	A_1	11
	$6\mathscr{D}_0 \oplus 15\mathscr{D}_1 \oplus 15\mathscr{D}_2 \oplus 10\mathscr{D}_3 \oplus 4\mathscr{D}_4 \oplus \mathscr{D}_5$		$21A_1 \oplus 24G_1 \oplus 15H_1 \oplus 3H_2 \oplus 6I$		$\Sigma = 3^5$
$(\mathscr{D}_{3/2})^2$	0	1	1	A	1
	1	1	3	B	3
	2	1	5	A	5
	3	1	7	B	7
	$\mathscr{D}_0 \oplus \mathscr{D}_1 \oplus \mathscr{D}_2 \oplus \mathscr{D}_3$		$10A \oplus 6B$		$\Sigma = 4^2$
$(\mathscr{D}_{3/2})^3$	1/2	2	2	E	4
	3/2	1 + 1 + 2	4	$A_1 + A_2 + E$	16
	5/2	1 + 2	6	$A_1 + E$	18
	7/2	2	8	E	16
	9/2	1	10	A_1	10
	$2\mathscr{D}_{1/2} \oplus 4\mathscr{D}_{3/2} \oplus 3\mathscr{D}_{5/2} \oplus 2\mathscr{D}_{7/2} \oplus \mathscr{D}_{9/2}$		$20A_1 \oplus 4A_2 \oplus 20E$		$\Sigma = 4^3$

[a]Frequency of the angular momentum representation *eq.* Dimensions of the symmetry representations
56 [b]Dimension of the angular momentum representation *eq.* Frequency of the symmetry representations

Table 2.14: Spin 1/2 sytems (*e.g.* H, ^{3}He, ^{13}C, ^{15}N ...). Bimolecular induction (subduction) statistics with angular momentum and symmetry details.

$$(\mathscr{D}_{1/2})^2 \otimes \mathscr{D}_{1/2} \uparrow\downarrow (\mathscr{D}_{1/2})^3$$

		1/2(E)	3/2(A$_1$)	sum
1(A)	1/2(A)	2	4	6
0(B)	1/2(A)	2	0	2
sum		4	4	$8=2^3$

$$(\mathscr{D}_{1/2})^2 \otimes (\mathscr{D}_{1/2})^2 \uparrow (\mathscr{D}_{1/2})^4$$

		0(E)	1(F$_1$)	2(A$_1$)	sum
1(A)	1(A)	1	3	5	9
1(A)	0(B)	0	3	0	3
0(B)	1(A)	0	3	0	3
0(B)	0(B)	1	0	0	1
sum		2	9	5	$16=2^4$

$$(\mathscr{D}_{1/2})^3 \otimes \mathscr{D}_{1/2} \uparrow\downarrow (\mathscr{D}_{1/2})^4$$

		0(E)	1(F$_1$)	2(A$_1$)	sum
3/2(A$_1$)	1/2(A)	0	3	5	8
1/2(E)	1/2(A)	2	6	0	8
sum		2	9	5	$16=2^4$

$$(\mathscr{D}_{1/2})^4 \otimes \mathscr{D}_{1/2} \uparrow\downarrow (\mathscr{D}_{1/2})^5$$

		1/2(H$_1$)	3/2(G$_1$)	5/2(A$_1$)	sum
2(A$_1$)	1/2(A)	0	4	6	10
1(F$_1$)	1/2(A)	6	12	0	18
0(E)	1/2(A)	4	0	0	4
sum		10	16	6	$32=2^5$

$$(\mathscr{D}_{1/2})^3 \otimes (\mathscr{D}_{1/2})^2 \uparrow (\mathscr{D}_{1/2})^5$$

		1/2(H$_1$)	3/2(G$_1$)	5/2(A$_1$)	sum
3/2(A$_1$)	1(A)	2	4	6	12
1/2(E)	1(A)	4	8	0	12
3/2(A$_1$)	0(B)	0	4	0	4
1/2(E)	0(B)	4	0	0	4
sum		10	16	6	$32=2^5$

Table 2.15: Spin 1 systems (*e.g.* D, ^{6}Li, ^{14}N ...). Bimolecular induction (subduction) statistics with angular momentum and symmetry details.

$$(\mathscr{D}_1)^2 \otimes \mathscr{D}_1 \uparrow (\mathscr{D}_1)^3$$

		$0(A_2)$	$1(A_1)$	$1(E)$	$2(E)$	$3(A_1)$	sum
2(A)	1(A)	0	4/3	5/3	5	7	15
1(B)	1(A)	1	0	3	5	0	9
0(A)	1(A)	0	5/3	4/3	0	0	1
sum		1	3	6	10	7	$27=3^3$

$$(\mathscr{D}_1)^3 \otimes \mathscr{D}_1 \uparrow (\mathscr{D}_1)^4$$

		$0(A_1)$	$0(E)$	$1(F_1)$	$1(F_2)$	$2(A_1)$	$2(E)$	$2(F_1)$	$3(F_1)$	$4(A_1)$	sum
$3(A_1)$	1(A)	0	0	0	0	3/2	0	7/2	7	9	21
2(E)	1(A)	0	0	9/4	15/4	0	15/2	5/2	14	0	30
$1(A_1)$	1(A)	1	0	3	0	7/2	0	3/2	0	0	9
1(E)	1(A)	0	2	15/4	9/4	0	5/2	15/2	0	0	18
$0(A_2)$	1(A)	0	0	0	0	0	0		0	0	3
sum		1	2	9	9	5	10	15	21	9	$81=3^4$

$$(\mathscr{D}_1)^2 \otimes (\mathscr{D}_1)^2 \uparrow (\mathscr{D}_1)^4$$

		$0(A_1)$	$0(E)$	$1(F_1)$	$1(F_2)$	$2(A_1)$	$2(E)$	$2(F_1)$	$3(F_1)$	$4(A_1)$	sum
2(A)	2(A)	4/9	5/9	3	0	10/9	35/9	0	7	9	25
2(A)	1(B)	0	0	1/2	5/2	0	0	5	7	0	15
1(B)	2(A)	0	0	1/2	5/2	0	0	5	7	0	15
2(A)	0(A)	0	0	0	0	35/18	5/9	5/2	0	0	5
0(A)	2(A)	0	0	0	0	35/18	5/9	5/2	0	0	5
1(B)	1(B)	0	1	0	3	0	5	0	0	0	9
1(B)	0(A)	0	0	5/2	1/2	0	0	0	0	0	3
0(A)	1(B)	0	0	5/2	1/2	0	0	0	0	0	3
0(A)	0(A)	5/9	4/9	0	0	0	0	0	0	0	1
sum		1	2	9	9	5	10	15	21	9	$81=3^4$

$$(\mathscr{D}_1)^4 \otimes \mathscr{D}_1 \uparrow (\mathscr{D}_1)^5$$

		0(I)	1(A$_1$)	1(G$_1$)	1(H$_1$)	1(H$_2$)	2(G$_1$)	2(H$_1$)	2(I)	3(A$_1$)	3(G$_1$)	3(H$_1$)	4(G$_1$)	5(A$_1$)	sum
4(A$_1$)	1(A)	0	0	0	0	0	0	0	0	8/5	27/5	0	9	11	27
3(F$_1$)	1(A)	0	0	0	0	0	64/15	7/3	42/5	0	7/3	56/3	27	0	63
2(A$_1$)	1(A)	0	8/5	7/5	0	0	5	0	0	27/5	8/5	0	0	0	15
2(E)	1(A)	0	0	0	1	5	0	10	0	0	0	14	0	0	30
2(F$_1$)	1(A)	0	0	3	6	0	7/3	20/3	6	0	56/3	7/3	0	0	45
1(F$_1$)	1(A)	3	0	6	3	0	42/5	6	3/5	0	0	0	0	0	27
1(F$_2$)	1(A)	3	0	0	0	9	0	0	15	0	0	0	0	0	27
0(A$_1$)	1(A)	0	7/5	8/5	0	0	0	0	0	0	0	0	0	0	3
0(E)	1(A)	0	0	0	5	1	0	0	0	0	0	0	0	0	6
sum		6	3	12	15	15	20	25	30	7	28	35	36	11	243=3^5

		0(I)	1(A$_1$)	1(G$_1$)	1(H$_1$)	1(H$_2$)	2(G$_1$)	2(H$_1$)	2(I)	3(A$_1$)	3(G$_1$)	3(H$_1$)	4(G$_1$)	5(A$_1$)	sum
3(A$_1$)	2(A)	0	12/25	28/25	7/5	0	8/3	7/3	0	28/25	7/25	28/5	9	11	35
3(A$_1$)	1(B)	0	0	0	0	0	4/5	0	21/5	0	7	0	9	0	21
3(A$_1$)	0(A)	0	0	0	0	0	0	0	0	21/10	56/15	7/6	0	0	7
2(E)	2(A)	2	0	2	1/2	15/4	2/3	70/12	7/2	0	14/3	28/3	18	0	50
2(E)	1(B)	0	0	0	9/4	15/4	0	5/2	15/2	0	0	14	0	0	30
2(E)	0(A)	0	0	0	0	0	14/3	10/3	2	0	0	0	0	0	10
1(A$_1$)	2(A)	0	28/25	121/75	4/15	0	7/3	8/3	0	189/50	224/75	7/30	0	0	15
1(A$_1$)	1(B)	1	0	3	0	0	21/5	0	4/5	0	0	0	0	0	9
1(A$_1$)	0(A)	0	7/5	4/15	4/3	0	0	0	0	0	0	0	0	0	3
1(E)	2(A)	0	0	2/3	49/12	5/4	14/3	5/6	9/2	0	28/3	14/3	0	0	30
1(E)	1(B)	2	0	0	15/4	9/4	0	15/2	5/2	0	0	0	0	0	18
1(E)	0(A)	0	0	10/3	5/3	1	0	0	0	0	0	0	0	0	6
0(A$_2$)	2(A)	0	0	0	0	0	0	0	5	0	0	0	0	0	5
0(A$_2$)	1(B)	0	0	0	0	3	0	0	0	0	0	0	0	0	3
0(A$_2$)	0(A)	1	0	0	0	0	0	0	0	0	0	0	0	0	1
sum		6	3	12	15	15	20	25	30	7	28	35	36	11	243=3^5

$$(\mathscr{D}_1)^3 \otimes (\mathscr{D}_1)^2 \uparrow (\mathscr{D}_1)^5$$

Table 2.16: 3–Spin 3/2 system (*e.g.* ^{7}Li, ^{35}Cl, ^{37}Cl ...). Bimolecular induction (subduction) statistics with angular momentum and symmetry details.

$$(\mathscr{D}_{3/2})^2 \otimes \mathscr{D}_{3/2} \uparrow (\mathscr{D}_{3/2})^3$$

		1/2(E)	3/2(A$_1$)	3/2(A$_2$)	3/2(E)	5/2(A$_1$)	5/2(E)	7/2(E)	9/2(A$_1$)	sum
3(A)	3/2(A)	0	6/5	0	14/5	14/5	16/5	8	10	28
2(B)	3/2(A)	2	0	10/3	2/3	0	6	8	0	20
1(A)	3/2(A)	2	14/5	0	6/5	16/5	14/5	0	0	12
0(B)	3/2(A)	0	0	2/3	10/3	0	0	0	0	4
sum		4	4	4	8	6	12	8	10	64=4^3

CHAPTER 3

The H_3^+ + H_2 isotopic system at low temperatures : Microcanonical model and experimental study

E. Hugo, O. Asvany and S. Schlemmer

S tate–to–state thermal rate coefficients for reactions of all H_3^+ + H_2 isotopic variants are derived and compared to new experimental data. The theoretical data are also sought for astrochemical modelling of cold environments (<50K). The rates are calculated on the basis of a microcanonical approach using the Langevin model and the conservation laws of mass, energy, angular momentum and nuclear spin. Full scrambling of all five nuclei during the collision is assumed for the calculations and alternatively partial dynamical restrictions are considered. The ergodic principle of the collision is employed in two limiting cases, neglecting (weak ergodic limit) or accounting for explicit degeneracies of the reaction mechanisms (strong ergodic limit). The resulting sets of rate coefficients are shown to be consistent with the detailed balance and thermodynamical equilibrium constants. Rate coefficients, k(T), for the deuteration chain of H_3^+ with HD as well as H_2D^+/H_3^+ equilibrium ratios have been measured in a variable temperature 22–pole ion trap. In particular, the experimental results indicate a change in reaction mechanism when going to higher temperatures. The good overall agreement between experiment and theory encourages the use of the theoretical predictions for astrophysical modelling.

3.1 INTRODUCTION

Deuterium in cold environments like dense molecular clouds, prestellar or protostellar objects is essentially locked in molecular HD. Yet, many species are observed with deuterium enhancements of several orders of magnitude with respect to the cosmic D/H ratio of 1.5×10^{-5} [1]. Even triply–deuterated species are observed [2, 3].

Isotopic substitution , *e.g.* X–H versus X–D, is promoted by differences in zero–point vibrational energies (ZPVE) which can be larger than typical collision energies, $E \sim kT$, thereby favoring the incorporation of deuterium atoms in larger and heavier species. H_3^+ has been identified to play a dominant role in this interstellar relevant isotopic fractionation. H_3^+ originates from cosmic ray ionisation of H_2 and a fast exoergic proton transfer reaction with another H_2:

$$\begin{aligned} H_2 + \zeta &\rightarrow H_2^+ + e^- & (3.1) \\ H_2^+ + H_2 &\rightarrow H_3^+ + H & (3.2) \end{aligned}$$

It can quickly deuterate in succesive steps via exchange or transfer reactions with HD

$$\begin{aligned} H_3^+ + HD &\rightleftharpoons H_2D^+ + H_2 + \Delta E & (3.3) \\ H_2D^+ + HD &\rightleftharpoons D_2H^+ + H_2 + \Delta E & (3.4) \\ D_2H^+ + HD &\rightleftharpoons D_3^+ + H_2 + \Delta E & (3.5) \end{aligned}$$
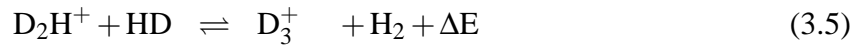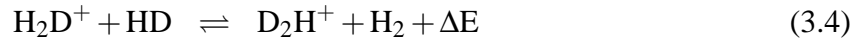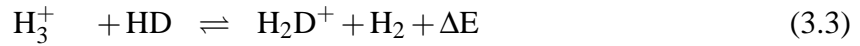
with ΔE = 232, 187 and 234 K for reactions 3.3, 3.4 and 3.5, respectively. One of its deuterium nuclei can then be transfered to "metallic" species via direct reactions such as

$$D_2H^+ + X \rightarrow X\text{–}D^+ + HD \qquad (3.6)$$

with X = N_2, CO, *etc*. Else, it recombines with a free electron and enriches the medium with free deuterons in reactions like

$$\begin{aligned} D_3^+ + e^- &\rightarrow D_2 + D & (3.7) \\ &\rightarrow D + D + D & (3.8) \end{aligned}$$

This may trigger a deuterium–rich ice chemistry after the free deuteron's accretion onto icy grains [4–6]. In this scenario, the H_3^+ cation acts as a vector dragging the deuterium from its reservoir and spreading it further, directly or indirectly, to other species. This pivotal role in the deuterium chemical network is by now well established.

The growing interest of the astronomical community in deuterium chemistry and its H_3^+ parents has been stimulated by numerous detections of deuterated H_3^+ [7–9] leading to ever more complex astrochemical models [10–16]. We now understand that high deuterium fractionations of the H_3^+ cations need not only very low temperatures to occur but also significant depletion of heavy–element–bearing species (CO, N_2) onto the grains and sufficiently low electron abundances. The H_2 *ortho/para* (hereafter o/p) ratio which is thought to be not fully thermalised in

dense molecular clouds [17] has also been identified as a limiting factor to the level of deuteration of H_3^+ [10, 18] since *e.g.* the 170 K internal energy of o–H_2 (J=1) helps to overcome the endothermicity of reactions 3.3 to 3.5 in the reverse direction.

Regarding theory, the potential energy surface (PES) of the H_5^+ system was first characterized by Yamaguchi et al. [19] and has now been explored in greater detail also for its isotopic variants [20, 21]. Much of the theoretical work has been concerned with the bond energies and structure of this elusive molecule. Recently, the determination of the vibrational spectrum of H_5^+ is also subject to a number of theoretical work [22, 23].

However, quantum scattering calculations for the H_3^+ + H_2 system calculating reactive or inelastic cross sections or rate coefficients are missing to date. Nevertheless, Oka and Epp [24] proposed a simple formulation for the inelastic rate coefficients but their statistical approximation suffers a proper normalisation and neglects nuclear spin constraints. More recently, state–to–state rate coefficients including *ortho–para* conversions of the purely hydrogenated system were derived by Park and Light [25] on the basis of a microcanonical statistical approach. Essentially, the present theoretical treatment employs the same statistical approach, where the reaction probability is calculated on the basis of a capture model for the collision considering the cumulative reaction probability (CRP). Complex formation and conservation of the total energy, the total rotational angular momentum as well as total nuclear spin are used to determine the CRP. In the present study, not only inelastic collisions but in particular isotopic reactions are considered.

Prior to the derivation of rate coefficients for the H_3^+ + H_2 collision, Quack [26] had most imposingly settled the stringent nuclear spin constraints which are at play in reactive collisions. Later, Oka [27] gave an elegant reformulation of those selection rules and Park and Light [28] carried on those aspects to greater details.

In the laboratory, the rate coefficients for all isotopic reactions were first measured with a VT–SIFT apparatus in the temperature range 80–300 K [29, 30] using normal–H_2 and normal–D_2 *i.e.* o/p=3 and 2 respectively. Later, Cordonnier et al. [31] employed spectroscopical means to analyse nuclear spin reactions of the purely hydrogenated system at temperatures of ~ 400 K relating *ortho–para* conversion probabilities with reaction mechanisms. More recently, Gerlich et al. [18] used a 22–pole ion trap apparatus at 10 K to measure the rate coefficients for reactions 3.3 to 3.5 in the forward direction and inferred the speed of reaction 3.3 in the backward direction by equilibrium measurements in n–H_2 and p–H_2 containing natural impurities of HD. This experimental study demonstrated the detrimental effect of o-H_2 on deuteration for the first time. Nevertheless, the low value for the forward rate coefficients caused a lot of discussion and showed the need for temperature-dependent measurements and theoretical predictions in the low temperature domain. A recent summary of some of the most important $H_mD_n^+$ collision systems is given in [32]. The branching ratios for some of these systems pose very critical tests to current experimental and theoretical work. In addition, a critical discussion of the in-situ calibration of HD and the o/p ratio of H_2 and other experimental considerations is given therein.

The H_3^+ + H_2 isotopic system represented in Fig. 3.1 consists in 8 reactions when considering the isotopic exchange between the ionic and neutral collision partner as well as 168

Complex	H_3^+		H_2D^+		D_2H^+		D_3^+				
H_5^+	ortho	para	ortho	para	para	ortho	para	ortho	meta		ΔZPE > 0
H_4D^+	33	**0**	87	**0**	50	**0**	63	43	**0**	para	H_2
$H_3D_2^+$	203	170	257	170	220	170	233	213	170	ortho	
$D_3H_2^+$	265	232	273	187	284	234	63	43	**0**		HD
D_4H^+	372	339	428	341	205	155	63	43	**0**	ortho	D_2
D_5^+	457	424	513	426	290	240	148	128	85	para	

Figure 3.1: The $H_3^+ + H_2$ isotopic system with nuclear spin details. All reactions within a given isotopic complex (color shades) are possible (i) if allowed by the feasible reaction mechanisms and (ii) if not strictly forbidden by nuclear spin selection rules. The numbers are the channel's zero-point energies (ΔE/k in Kelvin) relative to their complex' most exoergic channel. The reactions are globally favored in the top right direction.

reactions when considering nuclear spin symmetries. Among those reactions, 73 are strictly forbidden assuming nuclear spin conservation (frozen nuclear spin approximation). Despite the several advances in both theoretical and experimental fields, a complete set of rate coefficients in order to model the interaction of the H_3^+ and H_2 isotopologues in interstellar conditions is still missing and we would like to address this problem here.

The paper is organized as follows. In section 3.2, the microcanonical model to calculate thermal state–to–state rate coefficients of the $H_3^+ + H_2$ isotopic system is given. The incorporation of the reaction mechanisms during the complex's lifetime and the ergodic limits are described. The results are presented and analysed in section 3.3. In section 3.4, new measurements performed with a 22–pole ion trap apparatus are presented, experimental and theoretical results being compared. Limitations of the current theoretical as well as experimental approach are discussed in the section 3.5. Finally, section 3.6 summarizes the work and draws several conclusions.

3.2 MICROCANONICAL MODEL

The model is based on phase space theory (PST). It describes the collisions at low temperatures (<50K) of state specific H_3^+ and H_2 isotopologues. The phase space and the conservation laws are first introduced in section 3.2.1 by settling the nomenclature and presenting the H_3^+ and H_2 isotopologues. In section 3.2.2, we describe the complex formation with the Langevin

model and derive statistical weights for nuclear spins and rotational angular momenta from which we obtain reactants-to-complex state–detailed probabilities. Equivalently, the complex decay is treated in section 3.2.3 specifying statistical weights for mass, nuclear spin, energy and rotational angular momentum conservation from which complex-to-products state–detailed probabilities are derived. State-to-state cross sections are obtained in section 3.2.4 by distributing the **capture cross section** on the basis of the complex formation and decay state–detailed probabilities. State-to-state thermal rate coefficients are derived by integrating the state-to-state cross sections over the Maxwellian collision energy distribution.

3.2.1 Phase space and conservation laws

Micro states and phase space

The reaction process is decomposed in the entrance channel ($\mathscr{I}\mathscr{N}\mathscr{M}$), the complex channel $\mathscr{C}$ and the exit channel ($\mathscr{I}'\mathscr{N}'\mathscr{M}'$). The internal states (microstates) of the reactants, intermediate complexes and products are expressed in the phase space consisting of mass and energy scalars as well as rotational angular momentum and nuclear spin vectors. The entrance channel consists in an ion $\mathscr{I}$, a neutral $\mathscr{N}$ and their relative motional channel $\mathscr{M}$. An ion $\mathscr{I}$ or a neutral $\mathscr{N}$ is defined by its degree of isotopic substitution determining its mass m and zero–point vibrational energy E^v, its nuclear spin symmetries for hydrogen nuclei Γ^H and deuterium nuclei Γ^D and its rotational state described by rotational quantum number(s) – among which the rotational angular momentum J – determining its rotational energy E^r. The charge of the ion, q_i, and the isotropic polarizability of the neutral α_n. The subscripts i and n are used to define the quantities of the ion and the neutral, respectively. A relative motion $\mathscr{M}$ is described by the collision energy E_{col} and the quantum orbital angular momentum l. The reduced mass of two species is denoted as μ. The exit channel ($\mathscr{I}'\mathscr{N}'\mathscr{M}'$) and its quantities are defined identically and referred to with a prime. The intermediate complex channel $\mathscr{C}$ is defined by its total mass m_{tot}, total energy E_{tot}, total rotational angular momentum J_{tot} and the total nuclear spin symmetries for hydrogen nuclei Γ^H_{tot} and deuterium nuclei Γ^D_{tot}. Table 3.1 summarizes the quantities used in this paper.

Table 3.2 details the channels for the ions and the neutrals which were considered in the following calculations. The rotational states of the species correlate with the nuclear spin symmetry representations according to the symmetrisation postulate [33]. As first introduced by Maue [34] for methane, the greek appellations *ortho*, *meta* and *para* for the different nuclear spin symmetry representations Γ_i (*eq.* modifications) of an isotopologue are assigned in decreasing order of their high–temperature ($T \to \infty$) statistical weights $W^\infty_{(\Gamma_i)}$ which is simply their high–temperature populations. The $W^\infty_{(\Gamma_i)}$'s are thus proportional to their total number of rovibronic states $N_{rve}(\Gamma_i)$ and the nuclear spin degeneracy of their rovibronic states $g(\Gamma_i)$:

$$W^\infty_{(\Gamma_i)} = g(\Gamma_i) \times N_{rve}(\Gamma_i) \tag{3.9}$$

Table 3.1: Nomenclature of the quantities considered. See the text for detailed explanations.

	Reactants		Complex	Products	
	Ion	Neutral Motion		Ion	Neutral Motion
Channel	$\mathscr{I}$ $\mathscr{M}$	$\mathscr{N}$	$\mathscr{C}$	$\mathscr{I}'$ $\mathscr{M}'$	$\mathscr{N}'$
Mass	m_i μ	m_n	m_{tot}	$m_{i'}$ μ'	$m_{n'}$
Energy	E_i^v E_i^r E_{col}	E_n^v E_n^r	E_{tot}	$E_{i'}^v$ $E_{i'}^r$ $E_{col'}$	$E_{n'}^v$ $E_{n'}^r$
Rotational ang. mom.	J_i l	J_n	J_{tot}	$J_{i'}$ l'	$J_{n'}$
Nuclear spin symmetry	Γ_i^H Γ_i^D	Γ_n^H Γ_n^D	Γ_{tot}^H Γ_{tot}^D	$\Gamma_{i'}^H$ $\Gamma_{i'}^D$	$\Gamma_{n'}^H$ $\Gamma_{n'}^D$
Polarizability and Charge	q_i	α_n		$q_{i'}$	$\alpha_{n'}$

Since $g(\Gamma_i)$ is the frequency of the representation, $f(\Gamma_i)$, and $N_{rve}(\Gamma_i)$ is proportional to its dimension $\dim(\Gamma_i)$

$$g(\Gamma_i) = f(\Gamma_i) \tag{3.10}$$

$$\frac{N_{rve}(\Gamma_i)}{\dim(\Gamma_i)} = \frac{N_{rve}(\Gamma_j)}{\dim(\Gamma_j)} \tag{3.11}$$

the high–temperature statistical weight of a nuclear spin symmetry representation is proportional to its frequency and its dimension *i.e.* its pure nuclear spin statistical weight

$$\frac{W_{(\Gamma_i)}^\infty}{W_{(\Gamma_j)}^\infty} = \frac{f(\Gamma_i) \times \dim(\Gamma_i)}{f(\Gamma_j) \times \dim(\Gamma_j)} \tag{3.12}$$

It is noteworthy that in the literature, the appellations for the nuclear spin modifications are often misassigned in decreasing order of the rovibronic state's nuclear spin degeneracy $g(\Gamma_i)$ only, neglecting the nuclear spin representation's total number of rovibronic states $N_{rve}(\Gamma_i)$. This results in the exchange of *ortho* and *meta* appellations for D_3^+ [15, 35, 36] and could lead to confusions and errors.

The zero–point vibrational energies [37, 38] in Table 3.2 are expressed relative to D_3^+ for the ions and D_2 for the neutrals. Only the vibronic ground states were considered according to the low temperatures of interest. The rotational energies of H_2, HD and D_2 were calculated according to Ramanlal and Tennyson [38]. The rotational energies of H_3^+ were taken from Lindsay and McCall [39], those of H_2D^+ and D_2H^+ were taken from Tennyson [40]. For the D_3^+ rotational levels, we used the parameters for the Watson Hamiltonian given by Miller and Tennyson [41]. All energies were rounded with 0.1 Kelvin accuracy. In order to avoid errors due to energy truncation for the low–lying states of interest, we systematically included the 9 and 4 lowest levels of each H_3^+ and H_2 isotopologue and modification. The isotropic polarizability of H_2, HD and D_2 was taken as 0.79Å^3[42].

Conservation laws

The phase space volume in which a given microstate can evolve is restricted by the conservation of the total mass, total energy, total rotational angular momentum and the hydrogen and deuterium total nuclear spin symmetries:

$$m_i + m_n = m_{tot} = m_{i'} + m_{n'} \tag{3.13}$$

$$E_i^v + E_i^r + E_n^v + E_n^r + E_{col} = E_{tot} = E_{i'}^v + E_{i'}^r + E_{n'}^v + E_{n'}^r + E_{col'} \tag{3.14}$$

$$J_i \otimes J_n \otimes l \uparrow J_{tot} \downarrow J_{i'} \otimes J_{n'} \otimes l' \tag{3.15}$$

$$\Gamma_i^H \otimes \Gamma_n^H \uparrow \Gamma_{tot}^H \downarrow \Gamma_{i'}^H \otimes \Gamma_{n'}^H \tag{3.16}$$

$$\Gamma_i^D \otimes \Gamma_n^D \uparrow \Gamma_{tot}^D \downarrow \Gamma_{i'}^D \otimes \Gamma_{n'}^D \tag{3.17}$$

Equation 3.13 is equivalent to the conservation of the hydrogen and deuterium nuclei. The $\otimes$ operators in Eq. 3.15 and 3.16, 3.17 are the direct products for the K spatial rotation group (*i.e.* vectorial sum of angular momenta) and the nuclear permutation groups, respectively. The $\uparrow$ and $\downarrow$ operators correspond to inductions and subductions of the representations in the groups of concern [26, 28]. The nuclear spins are treated as completely decoupled from the other degrees of freedom considering the lack of significant magnetic couplings during the collision process [27, 43]. The nuclear spins are thus assumed to be frozen, resulting in the strict conservation of the total spin angular momenta, symmetries and magnetic moments. The constraints and statistics rising from this *frozen–nuclear spin* approximation have already been discussed in the literature regarding symmetry [26], angular momentum [27] or both [28]. Regarding the symmetrisation postulate, the nuclear spin symmetry representations must be considered contrarily to their angular momentum representations.

Transition probabilities of the microstates are assumed to fulfill the equiprobability principle according to the ergodic principle and the full-scrambling hypothesis inferred from the topology of the H_5^+ PES (see Sec. 3.2.5). Throughout this paper, the weights and probabilities derived according to those conservation laws will be written with the general form $W_{(\beta|\alpha)}$ and $P_{(\beta|\alpha)}$ with α and β being the prior and posterior informations.

Table 3.2: H_3^+ and H_2 isotopologues: mass, zero–point vibrational energy, nuclear spin symmetries and lowest rotational levels.

Isotopologue	H_2D^+		D_2H^+		$D_3{}^+$		
Mass (a.m.u.)	4		5		6		
ZPVE[a] (K)	1245.8		646.2		0		
Modification[b]	ortho (9)	para (3)	ortho (12)	para (6)	ortho (16)	meta (10)	para(1)
H symmetry[c]	$3\,A$ (1)	$1\,B$ (1)	$2\,A$ (1)	$2\,A$ (1)			
D symmetry[c]	$3\,A$ (1)	$3\,A$ (1)	$6\,A$ (1)	$3\,B$ (1)	$8\,E$ (2)	$10\,A_1$ (1)	$1\,A_2$ (1)
Selection rules[d]	K_a odd	K_a even	K_a+K_c even	K_a+K_c odd	$K=3n\pm1$	$K=0$, J even or $K=3n$	$K=0$, J odd or $K=3n$
	86.4 (1_{11})	0.0 (0_{00})	0.0 (0_{00})	50.2 (1_{01})	46.5 (1_1)	0.0 (0_0)	62.7 (1_0)
	104.2 (1_{10})	65.8 (1_{01})	70.9 (1_{11})	83.4 (1_{10})	123.2 (2_2)	187.9 (2_0)	230.0 (3_3)
	199.8 (2_{12})	189.4 (2_{02})	146.3 (2_{02})	158.6 (2_{12})	171.7 (2_1)	230.0 (3_3)	374.7 (3_0)
Rotational	253.1 (2_{11})	314.6 (2_{21})	196.2 (2_{11})	257.8 (2_{21})	310.6 (3_2)	622.3 (4_0)	730.6 (6_6)
levels[e]	365.5 (3_{13})	322.1 (2_{20})	262.0 (2_{20})	282.1 (3_{03})	358.7 (3_1)	730.6 (6_6)	788.4 (5_3)
	469.3 (3_{12})	361.7 (3_{03})	287.8 (3_{13})	361.6 (3_{12})	366.9 (4_4)	788.4 (5_3)	929.1 (5_0)
	580.7 (4_{14})	510.4 (3_{22})	407.7 (3_{22})	426.0 (3_{21})	533.8 (5_5)	1155.6 (6_3)	1155.6 (6_3)
	659.5 (3_{31})	541.5 (3_{21})	454.3 (4_{04})	456.4 (4_{14})	559.0 (4_2)	1163.1 (7_6)	1163.1 (7_6)
	661.6 (3_{30})	579.6 (4_{04})	542.6 (3_{31})	543.5 (3_{30})	606.5 (4_1)	1293.5 (6_0)	1499.0 (9_9)

Isotopologue	H_3^+		H_2		HD	D_2	
Mass (a.m.u)	3		2		3	4	
ZPVE[a] (K)	1797.7		903.6		491.2	0	
Modification[b]	ortho (4)	para (4)	ortho (3)	para (1)	(6)	ortho (6)	para (3)
H symmetry[c]	$4\,A_1$ (1)	$2\,E$ (2)	$3\,A$ (1)	$1\,B$ (1)	$2\,A$ (1)		
D symmetry[c]					$3\,A$ (1)	$6\,A$ (1)	$3\,B$ (1)
Selection rules[d]	K=0, J odd or K=3n	K=3n$\pm$1	J odd	J even		J even	J odd
Rotational levels[e]	125.1 (1_0)	92.3 (1_1)	170.4 (1)	0.0 (0)	0.0 (0)	0.0 (0)	85.9 (1)
	453.7 (3_3)	243.6 (2_2)	1014.5 (3)	509.7 (2)	128.4 (1)	257.6 (2)	513.9 (3)
	743.7 (3_0)	341.5 (2_1)	2499.6 (5)	1679.9 (4)	384.2 (2)	853.9 (4)	1276.0 (5)
	947.7 (4_3)	615.8 (3_2)	4567.2 (7)	3465.3 (6)	765.7 (3)	1778.1 (6)	2357.9 (7)
	1432.8 (6_6)	711.8 (3_1)					
	1554.5 (5_3)	722.3 (4_4)					
	1829.0 (5_0)	1048.9 (5_5)					
	2269.4 (6_3)	1105.6 (4_2)					
	2282.7 (7_6)	1199.3 (4_1)					

[a]relative to the zero–point vibrational energy of D_3^+ and D_2 [37, 38]

[b]The integer in parenthesis represents the high–temperature statistical weight, *eq.* the pure nuclear spin statistical weight, as defined in Eq. 3.12.

[c]Symmetry representation in the appropriate permutation group. The first integer is the frequency of the representation, *eq.* the nuclear spin degeneracy of the rovibronic states, and the integer in parenthesis is the dimension, *eq.* the density of rovibronic states.

[d]Rotational selection rules for the vibronic ground states according to the symmetrisation postulate.

[e]Energies in Kelvin and quantum numbers in parenthesis: J for H_2, HD and D_2, J_K for H_3^+ and D_3^+, $J_{K_a K_c}$ for H_2D^+ and D_2H^+.

3.2.2 Complex formation

Consider a given entrance channel ($\mathscr{I}\mathscr{N}$) representing two H_3^+ and H_2 isotopologues with specific internal states.

Langevin Model

Let the two reactants be on a trajectory with a collision energy E_{col} and an impact parameter b corresponding to a motional channel $\mathscr{M}$. The reduced mass of the ion-neutral reacting system is

$$\mu = \frac{m_i \times m_n}{m_i + m_n} \tag{3.18}$$

Their relative motion may be described by the classical Langevin model. Considering the charge-induced dipole interaction and the centrifugal energy of the orbital motion, the long–range effective potential between the reactants in Joules is

$$V_{eff}(r) = -\frac{1}{2}\frac{1}{4\pi\varepsilon_0}\frac{q_i^2\alpha_n}{r^4} + E_{col}\left(\frac{b}{r}\right)^2 \tag{3.19}$$

r being the distance between the reactants in meters, q the charge of the ion in Coulombs, α the isotropic polarizability of the neutral in m^3, E$_{col}$ the collision energy in Joules and b the impact parameter in meters. Taking as a capture criterium the condition that the collision energy overcomes the barrier of the effective potential, ($E_{col} > V_{eff}^{max}$), leads to a critical impact parameter b_c given by

$$b_c{}^2 = \sqrt{\frac{q_i^2\alpha_n}{2\pi\varepsilon_0 E_{col}}} \tag{3.20}$$

and the Langevin capture cross section

$$\sigma_c(E_{col}) = \pi b_c{}^2 \tag{3.21}$$

For a given collision energy, it is assumed that a complex with a finite lifetime is formed if the impact parameter is below this critical value, else no complex is formed. The complex lifetimes are considered to be much longer than any period of an internal motion. This is taken as a justification to use a phase space approach for calculating the reaction probabilities and subsequently also the cross sections. In contrast, direct transitions [44] which might result from distant trajectories ($b > b_c$) are neglected as well as radiative association processes.

The classical orbital angular momentum L of the collision is given by $L^2 = 2\mu b^2 E_{col}$ and is related to the quantum orbital angular momentum l by $L^2 = l(l+1)\hbar^2$. The maximum classical orbital angular momentum L_{max} and the maximum quantum orbital angular momentum l_{max} for the formation of a complex are thus given by

$$2\mu b_c{}^2 E_{col} = L_{max}{}^2 \equiv l_{max}(l_{max}+1)\hbar^2 \tag{3.22}$$

$$l_{max}(l_{max}+1) \leq \frac{L_{max}{}^2}{\hbar^2} \leq (l_{max}+1)(l_{max}+2) \tag{3.23}$$

Equation 3.23 discretises the classical picture. It results that the quantum orbital angular momentum l for a given collision energy E_{col} can have equiprobable values in the range $0 \leq l \leq l_{max}$, that is

$$W_{(l|\mu,E_{col})} = \begin{cases} 1 & \text{if } l \leq l_{max} \\ 0 & \text{if } l > l_{max} \end{cases} \tag{3.24}$$

The charge of the ion and the polarizability of the neutral are not explicited here since they are the same for all isotoplogues but they are implicitely contained in l_{max}. This equation corresponds to the heavyside transmission function of Park and Light [see 25, Eq. 43] where the transmission between a complex and reactants with a given orbital angular momentum is constrained by the minimum collision energy necessary *i.e.* $E_{col} > V_{eff}^{max}$, while in our case, the transmission between a complex and reactants with a given collision energy is constrained by the maximum orbital angular momentum feasible defined with the condition $V_{eff}^{max} < E_{col}$.

Angular momentum conservation

The vectorial sum of the three rotational angular momenta J_i, J_n and l induces a total rotational angular momentum J_{tot} as decribed by the first part of Eq. 3.15. Its statistical weight, as derived with angular momentum algebra, is

$$W_{(J_{tot}|J_i,J_n,l)} = (2J_{tot}+1) \sum_{J_{in}=|J_i-J_n|}^{J_i+J_n} \sum_{J_{inl}=|J_{in}-l|}^{J_{in}+l} \delta_{J_{tot}J_{inl}} \tag{3.25}$$

$\delta_{J_{tot}J_{inl}}$ being the Kronecker delta. Given a collision energy, the statistical weight of a total rotational angular momentum is the sum of the previous weight over all possible motional channels $\mathcal{M}$, *i.e.* orbital angular momenta:

$$\begin{aligned} W_{(J_{tot}|J_i,J_n,\mu,E_{col})} &= \sum_{l=0}^{\infty} W_{(J_{tot}|J_i,J_n,l)} \times W_{(l|\mu,E_{col})} \\ &= \sum_{l=0}^{l_{max}} W_{(J_{tot}|J_i,J_n,l)} \end{aligned} \tag{3.26}$$

l_{max} being the maximum orbital angular momentum defined in Eq. 3.23.

Nuclear Spin conservation

The hydrogen and deuterium nuclei must be considered separately since they are distinguishable. The direct product of the local nuclear spin symmetries Γ_i and Γ_n induces a total nuclear spin symmetry Γ_{tot} as described by the first part of Eq. 3.16 and 3.17 for hydrogen and deuterium nuclei, and their pure nuclear spin statistical weights are given in tables 3.3 and 3.4,

Table 3.3: Pure nuclear spin symmetry induction and subduction statistical weights, $W_{(\Gamma_i \otimes \Gamma_n \uparrow \Gamma_{tot})} = W_{(\Gamma_{tot} \downarrow \Gamma_i \otimes \Gamma_n)}$, for several hydrogen systems

$H + H \rightarrow H_2$

		A	B	total
A	A	3	1	4
total		3	1	$4=2^2$

$H_2 + H \rightarrow H_3$

		A_1	A_2	E	total
A	A	4	0	2	6
B	A	0	0	2	2
total		4	0	4	$8=2^3$

$H_3 + H \rightarrow H_4$

		A_1	A_2	E	F_1	F_2	total
A_1	A	5	0	0	3	0	8
A_2	A	0	0	0	0	0	0
E	A	0	0	2	6	0	8
total		5	0	2	9	0	$16=2^4$

$H_2 + H_2 \rightarrow H_4$

		A_1	A_2	E	F_1	F_2	total
A	A	5	0	1	3	0	8
A	B	0	0	0	3	0	0
B	A	0	0	0	3	0	8
B	B	0	0	1	0	0	8
total		5	0	2	9	0	$16=2^4$

$H_3 + H_2 \rightarrow H_5$

		A_1	A_2	G_1	G_2	H_1	H_2	I	total
A_1	A	6	0	4	0	2	0	0	12
A_1	B	0	0	4	0	0	0	0	4
A_2	A	0	0	0	0	0	0	0	0
A_2	B	0	0	0	0	0	0	0	0
E	A	0	0	8	0	4	0	0	12
E	B	0	0	0	0	4	0	0	4
total		6	0	16	0	10	0	0	$32=2^5$

Table 3.4: Pure nuclear spin symmetry induction and subduction statistical weights, $W_{(\Gamma_i \otimes \Gamma_n \uparrow \Gamma_{tot})} = W_{(\Gamma_{tot} \downarrow \Gamma_i \otimes \Gamma_n)}$, for several deuterium systems

$D + D \rightarrow D_2$

		A	B	total
A	A	6	3	9
total		6	3	$9 = 3^2$

$D_2 + D \rightarrow D_3$

		A_1	A_2	E	total
A	A	10	0	8	18
B	A	0	1	8	9
total		10	1	16	$27 = 3^3$

$D_3 + D \rightarrow D_4$

		A_1	A_2	E	F_1	F_2	total
A_1	A	15	0	0	15	0	30
A_2	A	0	0	0	0	3	3
E	A	0	0	12	30	6	48
total		15	0	12	45	9	$81 = 3^4$

$D_2 + D_2 \rightarrow D_4$

		A_1	A_2	E	F_1	F_2	total
A	A	15	0	6	15	0	36
A	B	0	0	0	15	3	18
B	A	0	0	0	15	3	18
B	B	0	0	6	0	3	9
total		15	0	12	45	9	$81 = 3^4$

$D_3 + D_2 \rightarrow D_5$

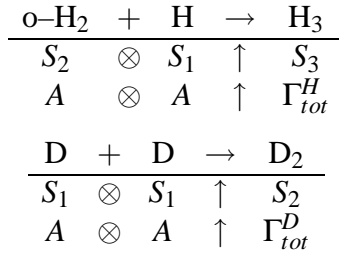|		A_1	A_2	G_1	G_2	H_1	H_2	I	total
A_1	A	21	0	24	0	15	0	0	60
A_1	B	0	0	24	0	0	0	6	30
A_2	A	0	0	0	0	0	0	6	6
A_2	B	0	0	0	0	0	3	0	3
E	A	0	0	48	0	30	6	12	96
E	B	0	0	0	0	30	6	12	48
total		21	0	96	0	75	15	36	$243 = 3^5$

respectively. These weights are directly used in the microcanonical model.

$$W_{(\Gamma_{tot}|\Gamma_i,\Gamma_n)} = W_{(\Gamma_i\otimes\Gamma_n\uparrow\Gamma_{tot})} \tag{3.27}$$

It is noteworthy that, according to the Frobenius reciprocity principle, the statistical weight of an induction and its reciprocal subduction are equal.

$$W_{(\Gamma_i\otimes\Gamma_n\uparrow\Gamma_{tot})} = W_{(\Gamma_{tot}\downarrow\Gamma_i\otimes\Gamma_n)} \tag{3.28}$$

In the case of an o–$H_2D^+ + HD \to H_3D_2^+$ collision, the hydrogen and deuterium components are

o–H_2	$+$	H	$\to$	H_3
S_2	$\otimes$ S_1	$\uparrow$	S_3
A	$\otimes$ A	$\uparrow$	Γ_{tot}^H

D	$+$	D	$\to$	D_2
S_1	$\otimes$ S_1	$\uparrow$	S_2
A	$\otimes$ A	$\uparrow$	Γ_{tot}^D

S_n being the permutation group of n identical nuclei. The statistical weights for Γ_{tot}^H and Γ_{tot}^D are

$$W_{(\Gamma_{tot}^H|\Gamma_i^H=A,\Gamma_n^H=A)} = \begin{cases} 4 & \text{for} \quad \Gamma_{tot}^H = A_1 \\ 2 & \text{for} \quad \Gamma_{tot}^H = E \end{cases} \tag{3.29}$$

$$W_{(\Gamma_{tot}^D|\Gamma_i^D=A,\Gamma_n^D=A)} = \begin{cases} 6 & \text{for} \quad \Gamma_{tot}^D = A \\ 3 & \text{for} \quad \Gamma_{tot}^D = B \end{cases} \tag{3.30}$$

In the case of a m–$D_3^+ + p$–$H_2 \to D_3H_2^+$ collision, the total hydrogen and deuterium symmetries are simply the local symmetries of the neutral and ion reactants with statistical weights

$$W_{(\Gamma_{tot}^H=B|\Gamma_i^H=\emptyset,\Gamma_n^H=B)} = 1 \tag{3.31}$$

$$W_{(\Gamma_{tot}^D=A_1|\Gamma_i^D=A_1,\Gamma_n^D=\emptyset)} = 10 \tag{3.32}$$

Overall Complex formation probability

The total mass m_{tot} and total energy E_{tot} of the formed complex are given by the first parts of Eq. 3.13 and 3.14. For the total rotational angular momentum J_{tot} and the total hydrogen and deuterium nuclear spin symetries Γ_{tot}^H and Γ_{tot}^D, the overall weight of a complex channel $\mathscr{C}$ given a reactant channel $(\mathscr{I}\mathscr{N})$ and a collision energy E_{col} is

$$\begin{aligned} W_{(\mathscr{C}|\mathscr{I},\mathscr{N},E_{col})} = &\; W_{(J_{tot}|J_i,J_n,\mu,E_{col})} \\ &\times W_{(\Gamma_{tot}^H|\Gamma_i^H,\Gamma_n^H)} \\ &\times W_{(\Gamma_{tot}^D|\Gamma_i^D,\Gamma_n^D)} \end{aligned} \tag{3.33}$$

and its overall probability is

$$P_{(\mathscr{C}|\mathscr{I},\mathscr{N},E_{col})} = \frac{W_{(\mathscr{C}|\mathscr{I},\mathscr{N},E_{col})}}{\sum\limits_{\mathscr{C}} W_{(\mathscr{C}|\mathscr{I},\mathscr{N},E_{col})}} \tag{3.34}$$
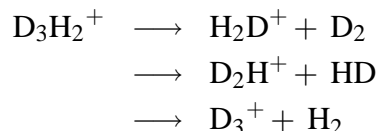
3.2.3 Complex decay

Consider a given complex channel $\mathscr{C}$ with a total mass m_{tot}, total energy E_{tot}, total rotational angular momentum J_{tot} and total nuclear spin symmetries Γ_{tot}^H and Γ_{tot}^D for its hydrogen and deuterium nuclei.

Mass conservation

The accessible isotopic channels $(m_{i'}, m_{n'})$ are constrained by the second equality of Eq. 3.13 and the feasible reaction mechanisms. In the most simple approach corresponding to the full–scrambling hypothesis and the weak ergodic limit (see Sec. 3.2.5 and Table 3.5), the weights are

$$W_{(m_{i'},m_{n'}|m_{tot})} = \begin{cases} 1 & \text{if} \quad m_{i'} + m_{n'} = m_{tot} \\ 0 & \text{else} \end{cases} \tag{3.35}$$

As an example, a $D_3H_2^+$ complex can decay to the following isotopic channels

$$\begin{aligned} D_3H_2^+ \quad &\longrightarrow \quad H_2D^+ + D_2 \\ &\longrightarrow \quad D_2H^+ + HD \\ &\longrightarrow \quad D_3^+ + H_2 \end{aligned}$$

According to equation 3.35, all possible isotopic channels are considered with equal probability. However, as will be discussed below, different weights may be introduced accounting for accessible and inaccessible dissociative asymptotes of the different product isotopologues. Therefore reaction mechanism degeneracies have to be accounted for. The introduction of these weights is moved to the end of this section in order to proceed with the overall derivation of the desired state–to–state rate coefficients.

Nuclear spin conservation

Within a given isotopic channel, the accessible nuclear spin channels are constrained by the subduction parts of Eq. 3.16 and 3.17 and the feasible reaction mechanisms [28]. According to the Frobenius reciprocity principle, the statistical weights for the induction and subduction of a total symmetry Γ_{tot} for both hydrogen and deuterium nuclei are equal as stated in Eq. 3.28. However, since the rotational states correlate with the nuclear spin symmetries as pointed out

in section 3.2.1, the full-scrambling statistical weight of the products' local symmetries $\Gamma_{i'}$ and $\Gamma_{n'}$ emerging from a total symmetry Γ_{tot} for both hydrogen and deuterium nuclei are taken as

$$W_{(\Gamma_{i'},\Gamma_{n'}|\Gamma_{tot})} = \frac{W_{(\Gamma_{tot}\downarrow\Gamma_{i'}\otimes\Gamma_{n'})}}{dim(\Gamma_{i'}) \times dim(\Gamma_{n'})} \tag{3.36}$$

where the numerator is the pure nuclear spin subduction statistical weight given in Tables 3.3 and 3.4 and the denominators are the dimensions of the products' nuclear spin representations given in Table 3.2.

In the case of a D_4H^+ complex with $\Gamma_{tot}^D = F_2$, the accessible and inaccessible isotopic and nuclear spin channels are

$$
\begin{aligned}
D_4H^+(\Gamma_{tot}^D = F_2) \quad &\rightarrow \quad o\text{--}D_2H^+ + p\text{--}D_2 \\
& \quad p\text{--}D_2H^+ + o\text{--}D_2 \\
& \quad p\text{--}D_2H^+ + p\text{--}D_2 \\
&\nrightarrow \quad o\text{--}D_2H^+ + o\text{--}D_2 \\
&\rightarrow \quad o\text{--}D_3^+ + HD \\
& \quad p\text{--}D_3^+ + HD \\
&\nrightarrow \quad m\text{--}D_3^+ + HD
\end{aligned}
$$
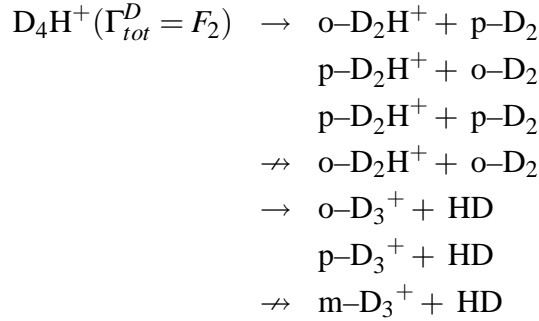
with the deuterium nuclear spin statistical weights of $e.g.$ the $D_3^+ + HD$ isotopic channel

$$W_{(E,A|F_2)} = 3 \tag{3.37}$$
$$W_{(A_2,A|F_2)} = 3 \tag{3.38}$$
$$W_{(A_1,A|F_2)} = 0 \tag{3.39}$$

Note that Eq. 3.36 ensures that the high–temperature statistics are consistent with the pure nuclear spin statistics. Indeed, in the high–temperature limit ($eq.$ infinite energy and orbital angular momentum), all the internal states of an isotopic channel are accessible irrespective of their energy and rotational angular momentum such that

$$
\begin{aligned}
W_{(\Gamma_{i'},\Gamma_{n'}|\Gamma_{tot})}^{\infty} \quad &\propto \quad \sum_{\mathscr{I}'\in\Gamma_{i'}}\sum_{\mathscr{N}'\in\Gamma_{n'}} W_{(\Gamma_{i'},\Gamma_{n'}|\Gamma_{tot})} \\
&\propto \quad N_{rve}(\Gamma_{i'}) \times N_{rve}(\Gamma_{n'}) \times W_{(\Gamma_{i'},\Gamma_{n'}|\Gamma_{tot})}
\end{aligned}
\tag{3.40}
$$

and given Eq. 3.11, we find

$$
\begin{aligned}
W_{(\Gamma_{i'},\Gamma_{n'}|\Gamma_{tot})}^{\infty} \quad &\propto \quad dim(\Gamma_{i'}) \times dim(\Gamma_{n'}) \times W_{(\Gamma_{i'},\Gamma_{n'}|\Gamma_{tot})} \\
&\propto \quad W_{(\Gamma_{tot}\downarrow\Gamma_{i'}\otimes\Gamma_{n'})}
\end{aligned}
\tag{3.41}
$$

Regarding the previous example, the ratios of the high–temperature statistical weights of the nuclear spin channels of $D_3^+ + HD$ are

$$W_{(A_1|F_2)}^{\infty} : W_{(A_2|F_2)}^{\infty} : W_{(E|F_2)}^{\infty} = 0 : 3 : 6 \tag{3.42}$$

which agrees as expected with the deuterium statistical weights of $D_3^+ + D$ emerging from $\Gamma_{tot}^D = F_2$ (see Table 3.4).

Energy conservation

Within a given isotopic and nuclear spin channel, the accessible rotational channels are constrained by the second equality of Eq. 3.14. A rotational channel with its vibrational and rotational energies $E_{i'}^v$, $E_{i'}^r$, $E_{n'}^v$ and $E_{n'}^r$ may only be accessed if the complex has enough total energy which we can translate with the energy statistical weight [45]

$$W_{(E_{i'}^v,E_{i'}^r,E_{n'}^v,E_{n'}^r|E_{tot})} = \begin{cases} 1 & \text{if} \quad E_{col'} \geq 0 \\ 0 & \text{else} \end{cases} \tag{3.43}$$

with $E_{col'} = E_{tot} - E_{i'}^v + E_{i'}^r + E_{n'}^v + E_{n'}^r$ the relative kinetic energy of the products' motional channel.

Angular Momentum conservation

Moreover, only the motional channels $\mathcal{M}'$ whose kinetic energy is superior to the maximum of the effective potential of the exit channel are accessible. Conversely, the barrier of the effective potential should be lower than the products' relative kinetic energy ($V_{eff'}^{max} < E_{col'}$). As developed in Sec. 3.2.2, this condition leads to the statistical weight

$$W_{(l'|\mu',E_{col'})} = \begin{cases} 1 & \text{if} \quad l' \leq l'_{max} \\ 0 & \text{if} \quad l' > l'_{max} \end{cases} \tag{3.44}$$

with l'_{max} defined as in Eq. 3.23.

The rotational angular momentum statistical weight of a product channel $(\mathcal{I}'\mathcal{N}')$ is obtained by summing over all accessible motional channels $\mathcal{M}'$, i.e. orbital angular momenta l':

$$W_{(J_{i'},J_{n'},\mu',E_{col'}|J_{tot})} = \sum_{l'=0}^{l'_{max}} W_{(J_{i'},J_{n'},l'|J_{tot})} \tag{3.45}$$

where $W_{(J_{i'},J_{n'},l'|J_{tot})}$ is the statistical weight of an angular momentum channel $(J_{i'},J_{n'},l')$ given a total rotational angular momentum J_{tot}. This weight describing the subduction part of Eq. 3.15 can be straightforwardly inferred from its reciprocal induction (Eq. 3.25) using the Frobenius reciprocity principle:

$$W_{(J_{i'},J_{n'},l'|J_{tot})} = W_{(J_{tot}|J_{i'},J_{n'},l')} \tag{3.46}$$

Overall decay probability

The overall weight of a product channel $(\mathscr{I}'\mathscr{N}')$ given a complex channel $\mathscr{C}$ is

$$
\begin{aligned}
W_{(\mathscr{I}',\mathscr{N}'|\mathscr{C})} &= W_{(m_{i'},m_{n'}|m_{tot})} \\
&\times W_{(\Gamma_{i'}^H,\Gamma_{n'}^H|\Gamma_{tot}^H)} \\
&\times W_{(\Gamma_{i'}^D,\Gamma_{n'}^D|\Gamma_{tot}^D)} \\
&\times W_{(E_{i'}^v,E_{i'}^r,E_{n'}^v,E_{n'}^r|E_{tot})} \\
&\times W_{(J_{i'},J_{n'},\mu',E_{col'}|J_{tot})}
\end{aligned}
\tag{3.47}
$$

and its probability is

$$
P_{(\mathscr{I}',\mathscr{N}'|\mathscr{C})} = \frac{W_{(\mathscr{I}',\mathscr{N}'|\mathscr{C})}}{\sum\limits_{\mathscr{I}',\mathscr{N}'} W_{(\mathscr{I}',\mathscr{N}'|\mathscr{C})}}
\tag{3.48}
$$

3.2.4 State-to-state cross sections and thermal rate coefficients

The state-to-state cross sections for a given collision energy E_{col} are obtained by distributing the Langevin cross section (Eq. 3.21) among the product channels according to

$$
\sigma_{\mathscr{I}\mathscr{N}\to\mathscr{I}'\mathscr{N}'}(E_{col}) = \sigma_c(E_{col}) \times P_{(\mathscr{I}',\mathscr{N}'|\mathscr{I},\mathscr{N},E_{col})}
\tag{3.49}
$$

where the state–to–state reaction probabilities are obtained from the reactants-to-complex and complex-to-products state–detailed probabilities summed over all intermediate complex channels:

$$
P_{(\mathscr{I}',\mathscr{N}'|\mathscr{I},\mathscr{N},E_{col})} = \sum_{\mathscr{C}} P_{(\mathscr{I}',\mathscr{N}'|\mathscr{C})} \times P_{(\mathscr{C}|\mathscr{I},\mathscr{N},E_{col})}
\tag{3.50}
$$

Eqs. 3.34 and 3.48 show that the normalisation $\sum\limits_{\mathscr{I}'\mathscr{N}'} P_{(\mathscr{I}',\mathscr{N}'|\mathscr{I},\mathscr{N},E_{col})} = 1$ is automatically fulfilled.

In thermal environments, the motions of the reactants, $\mathscr{I}$ and $\mathscr{N}$, in the laboratory frame exhibit Maxwell-Boltzmann velocity and energy distributions. Based on the properties of the Gaussian distributions representing the reactants in the laboratory frame, the distributions of the relative velocity v_{col} and energy E_{col} in the center-of-mass frame are also Maxwell-Boltzmann with the reduced mass μ

$$
P_{(v_{col}|T)} = 4\pi \left(\frac{\mu}{2\pi kT}\right)^{3/2} v_{col}^2 \, e^{-\mu v_{col}^2/2kT}
\tag{3.51}
$$

$$
P_{(E_{col}|T)} = 4\pi \left(\frac{\mu}{2\pi kT}\right)^{3/2} \frac{2E_{col}}{\mu} \, e^{-E_{col}/kT}
\tag{3.52}
$$

The reaction probabilities have been calculated in the center-of-mass frame. The state-to-state thermal rate coefficients are obtained from the definition $k = \int v_{col} \cdot \sigma(v_{col}) \cdot P(v_{col}) \cdot dv_{col}$, and in the energy domain using the substitutions $v_{col} = \sqrt{2E_{col}/\mu}$ and $dv_{col}/dE_{col} = (2\mu E_{col})^{-1/2}$. As a result the thermal state-to-state rate coefficients, $k_{\mathscr{I}\mathscr{N} \to \mathscr{I}'\mathscr{N}'}(T)$ are given by

$$
\begin{aligned}
&k_{\mathscr{I}\mathscr{N} \to \mathscr{I}'\mathscr{N}'}(T) \\
&= \int_{v_{col}=0}^{\infty} v_{col} \times \sigma_{\mathscr{I}\mathscr{N} \to \mathscr{I}'\mathscr{N}'}(v_{col}) \times P_{(v_{col}|T)} \times dv_{col} \\
&= \int_{E_{col}=0}^{\infty} \sqrt{\frac{2E_{col}}{\mu}} \times \sigma_c(E_{col}) \times P_{(\mathscr{I}',\mathscr{N}'|\mathscr{I},\mathscr{N},E_{col})} \times P_{(E_{col}|T)} \times \frac{dv_{col}}{dE_{col}} \times dE_{col} \\
&= \int_{E_{col}=0}^{\infty} \sqrt{\frac{2E_{col}}{\mu}} \times \pi \sqrt{\frac{\alpha q^2}{2\pi\varepsilon_0 E_{col}}} \times P_{(\mathscr{I}',\mathscr{N}'|\mathscr{I},\mathscr{N},E_{col})} \times 4\pi \left(\frac{\mu}{2\pi kT}\right)^{3/2} \frac{2E_{col}}{\mu} e^{-E_{col}/kT} \\
&\hspace{8cm} \times \frac{1}{\sqrt{2\mu E_{col}}} \times dE_{col} \\
&= k_L \times \int_{E_{col}=0}^{\infty} P_{(\mathscr{I}',\mathscr{N}'|\mathscr{I},\mathscr{N},E_{col})} \times \frac{2}{\sqrt{\pi(kT)^3}} \sqrt{E_{col}} e^{-E_{col}/kT} dE_{col}
\end{aligned}
$$

with the Langevin rate coefficient being:

$$
k_L = \sqrt{\frac{\pi\alpha q^2}{\mu\varepsilon_0}} \tag{3.53}
$$

The state-to-state thermal rate coefficients are properly normalized since they verify

$$
k_{\mathscr{I}\mathscr{N}}(T) = \sum_{\mathscr{I}'\mathscr{N}'} k_{\mathscr{I}\mathscr{N} \to \mathscr{I}'\mathscr{N}'}(T) = k_L \tag{3.54}
$$

Based on the above described procedure, state–to–state rate coefficients have been calculated for simulating low temperature laboratory experiments as discussed below and for simulating H_3^+ and its isotopologues in interstellar environments [36]. As pointed out above in subsection 3.2.3, the possible reaction mechanisms as well as the proper implementation of the ergodic principle will influence the results. Therefore a set of different approaches are discussed prior to applications of the microcanonical rate coefficients.

3.2.5 Ergodic principle and reaction mechanisms

Phase Space Theory is based on the equiprobability principle, it is a simple thus convenient theory to describe systems but it is only a good approximation in the ergodic limit which considers the microcanonical population as fully relaxed to an equilibrium state in the complexes' potential energy surface (PES). As a consequence, a complex channel forgets its history and the decay
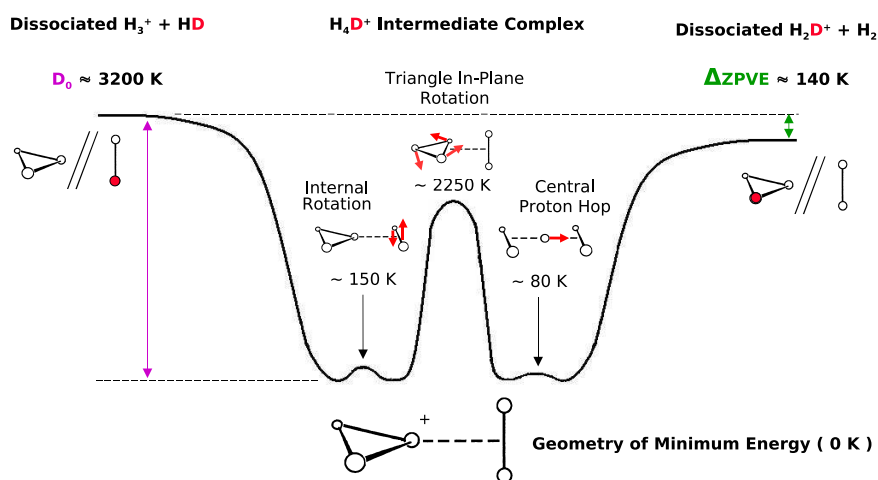
Figure 3.2: Schematic of the H_4D^+ PES according to calculations on H_5^+ [19–21]. The minimum energy configuration consist of an H_3^+ triangle entity and an H_2 entity, the charge being localised on the central nucleus. Saddle points for three internal motions are represented as well as the asymptotes for the two isotopic channels. They differ in energy because of zero-point rotational and vibrational energies.

probabilities are independent of the reactants' channels. Such collision process can therefore be described microscopically as a memoryless Markov chain $(\mathscr{I}\mathscr{N}\mathscr{M}) \rightarrow \mathscr{C} \rightarrow (\mathscr{I}'\mathscr{N}'\mathscr{M}')$ and be decomposed in the complex formation and complex decay as done here. In this statistical approach, a weight has to be assigned to each isotopic channel. If nothing is known on the number of possible pathways to link a reactant channel with a product channel, a statistical weight of 1 may be associated to an accessible isotopic channel while a weight of 0 is associated with an inaccessible isotopic channel. This implementation of the ergodic principle is called the *weak* ergodic limit. In the *strong* ergodic limit, the statistical weight of an isotopic channel is given by its number of accessible dissociative asymptotes *eq.* the degeneracy of reaction mechanisms leading to this isotopic channel. The statistical weights introduced in Sec. 3.2.3, and consequently the microcanonical rate coefficients derived above for the H_5^+ isotopic system will thus depend on (i) the *weak* or *strong* ergodic limit considered as well as on (ii) the feasible reaction mechanisms constrained by the PES.

The H_5^+ considered here is a peculiar system because on the sole consideration of its potential energy surface (PES), any entrance channel can potentially access all $5!/3!2! = 10$ dissociative asymptotes. Its configuration of minimum energy on the PES consists of a H_3 and a H_2 moiety with the charge localised on the central nucleus (see Fig. 3.2). The two relevant internal motions for nuclear rearrangement are the central nucleus hop with an extremely shallow barrier and the in–plane rotation of the H_3 moiety with a more consequent yet submerged saddle point.
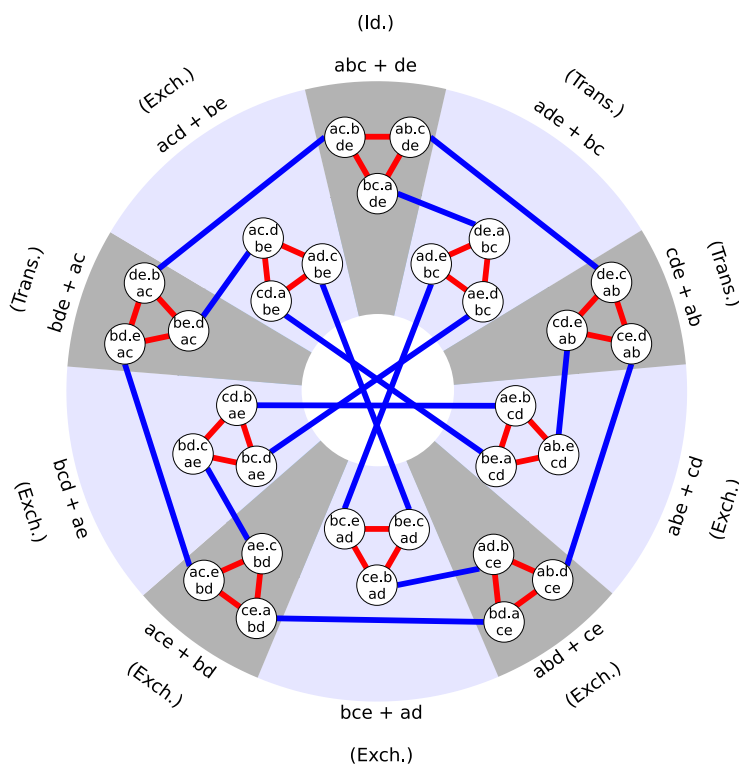
Figure 3.3: Map of minimum energy arrangements of a H_5^+ isotopic complex. A quartet of arrangements is labelled as *ab.c/de* with *a* and *b* the two outer nuclei of the H_3 moiety, *c* the central nucleus belonging to the H_3 moiety, *d* and *e* the two nuclei of the H_2 moiety. The 30 quartets of arrangements are interconnected by the H_3 moieties' in–plane rotation (red lines) and the central nucleus hop (blue lines) internal motions. Each of the 10 dissociative asymptotes (shades) is connected to three quartets of arrangements. The one identity, three transfer and six exchange reaction mechanisms are attributed to the dissociative asymptotes assuming $(abc+de)$ is the entrance channel.

Upon the internal rotation, also shown in Fig. 3.2, the positions of the two outer nuclei of the H_3 moiety or those of the H_2 moiety are rearranged. This internal motion cannot promote any modification of the H_3 and H_2 moieties therefore it can be ignored in the current treatment and the $5! = 120$ different minimum energy arrangements are grouped by $2!2! = 4$ into 30 quartets. As depicted in Fig. 3.3, the 30 quartets of arrangements are connected to the 10 dissociative asymptotes and interconnected by the two relevant internal motions, forming a map in which the microcanonical population can evolve. We discuss two limiting cases to which we refer as (i) *full–scrambling* and (ii) *hop*, neglecting possible centrifugal distortion of the PES and the fact that isotopic substitution in H_5^+ breaks the symmetry of the PES [21], potentially favoring some particular arrangements.

Table 3.5: Microcanonical isotopic statistical weights of H_2D^+ + HD collisions for the full–scrambling and hop limits as used in section 3.2.3. The accessible dissociative asymptotes correspond to reaction mechanisms for which the hydrogen and/or deuterium nuclei involved are specified.

Isotopic channel			Reaction mechanisms			
			Id	Trans	Exch	Total[a]
Full–scramling limit						
H_3^+	+	D_2	0	0	1 D–H	1 (1)
H_2D^+	+	HD	1	2 H	2 H–H 1 D–D	6 (1)
D_2H^+	+	H_2	0	1 D	2 H–D	3 (1)
	Total		1	3	6	10
Hop limit						
H nucleus locked in the center: probability 2/3						
H_3^+	+	D_2	0	0	0	0 (0)
H_2D^+	+	HD	1	1 H	0	2 (1)
D_2H^+	+	H_2	0	0	0	0 (0)
	Total		1	1	0	2
D nucleus locked in the center: probability 1/3						
H_3^+	+	D_2	0	0	0	0 (0)
H_2D^+	+	HD	1	0	0	1 (1)
D_2H^+	+	H_2	0	1 D	0	1 (1)
	Total		1	1	0	2

[a]Isotopic statistical weight for the strong ergodic limit. The number in parenthesis corresponds to the weak ergodic limit which only accounts for the accessibility of the channel.

(i) If both internal motions (hop and in–plane rotation) can proceed efficiently with respect to the dissociation events, the microcanonical population will visit all 120 minimum energy arrangements of the PES corresponding to the full–scrambling limit. Consequently, the complex can probe equally all 10 dissociative asymptotes, depicted in Fig. 3.3. These asymptotes are denoted as 1 identity, 3 transfer and 6 exchange reaction mechanisms, when entering as reactants (abc+de) at the top of Fig. 3.3.

(ii) If the rotation of the H_3 moiety is dynamically hindered and only the central nucleus hop can proceed efficiently during the complex lifetime, the central nucleus is locked and the microcanonical population will be equally distributed in two local wells of the PES corresponding to the entrance arrangement (abc+de) and its arrangement connected by the central nucleus hop. In this hop limit, the complex can probe only 2 dissociative asymptotes corresponding to 1 identity and 1 transfer but no exchange reaction mechanism.

As an example, the microcanonical isotopic statistical weights introduced in section 3.2.3 are given in Table 3.5 for the H_2D^+ + HD collision for the two limiting cases of full scrambling and hop. In case of full scrambling, e.g., the product channel H_3^+ + D_2 is accessible via one exchange reaction, the H_2D^+ + HD channel occurs on 6 accessible assymptotes, and the D_2H^+ + H_2 channel has 3 possibilities. Correspondingly, the statistical weights in the *strong* ergodic limit are 1:6:3 (see right side of table) and in the *weak* ergodic limit they are 1:1:1. In the following sections, the *strong* ergodic limit is considered if not stated otherwise. Comparison of the full scrambling and the hop limits to experimental data will give some first semi-quantitative insight into the role of dynamical restrictions and reaction mechanisms.

3.3 RESULTS

3.3.1 Thermal rate coefficients

The outcome of the calculation is a set of several thousands of state–to–state thermal rate coefficients, at present in the temperature range 5–50 K. An example is given in Fig. 3.4 illustrating an Arrhenius plot of the main state–to–state rate coefficients for p–H_2D^+($J_{K_aK_c}= 0_{00}$) + o–H_2(J=1) collisions. Elastic, inelastic as well as reactive collisions are accounted for. Collisions accessing endoergic states show an Arrhenius behaviour with an activation energy very close to the endoergicity while reactions to exoergic states are quasi temperature independent. Based on the observed temperature dependence it is well justified to parameterize the rate coefficient as $k = \alpha \cdot e^{-\beta/T}$. Such temperature behaviours are also found for the inelastic state-to-state rate coefficients for the *para* and *ortho* ground transitions of H_2D^+ and D_2H^+ in collsions with *para* and *ortho* H_2 given in Table 3.6. These rate coefficients are of particular interest for the modelling of astronomical observations.

We note that our results agree with the ground state–to–nuclear spin species thermal rate coefficients of the H_3^+ + H_2 system at 10 K calculated by Park and Light [25] within 3 % of their given accuracy. These rates are defined according to

$$k_{\mathscr{I}\mathscr{N}\rightarrow\Gamma_{i'}\Gamma_{n'}}(T) = \sum_{\mathscr{I}'\in\Gamma_{i'}}\sum_{\mathscr{N}'\in\Gamma_{n'}} k_{\mathscr{I}\mathscr{N}\rightarrow\mathscr{I}'\mathscr{N}'}(T) \tag{3.55}$$

Regarding the greater details they accounted for, we conclude that in this temperature range, spectroscopic accuracy of the energy levels, charge–dipole and charge–quadrupole interactions [46], tunneling and above–barrier reflections do not affect the rate coefficients significantly and can thus be safely neglected.

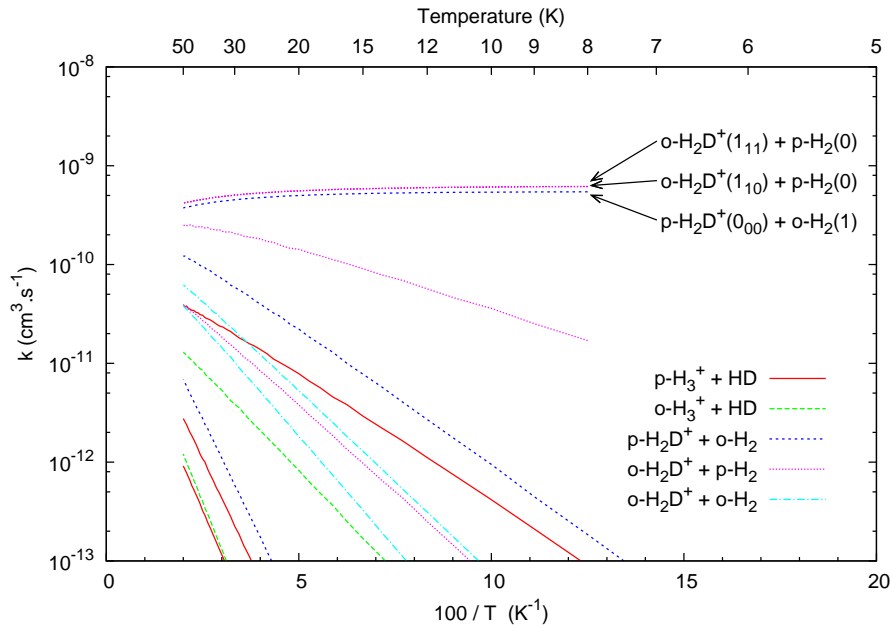**Figure 3.4:** Main state-to-state thermal rate coefficients for p–H_2D^+($J_{K_aK_c}= 0_{00}$) + o–H_2(J=1) collisions. The product channels are represented with different lines according to their isotopic–nuclear spin modifications. Rates for endoergic channels show an Arrhenius behaviour while those for exoergic channels are quasi temperature independant.

Table 3.6: Inelastic state-to-state rate coefficients for the *ortho* and *para* ground transitions of H_2D^+ and D_2H^+ in collisions with *para* and *ortho* H_2 according to strong ergodicity. The rates are given in the form $k = \alpha\, e^{-\beta/T}$. The α ($cm^3 s^{-1}$) and β (Kelvin) coefficients were fitted in the temperature range 5–15 K. The Einstein coefficients for spontaneous emission A_{ul} (s^{-1}) [38] and the critical densities $n_c = A_{ul}/k_{ul}$ (cm^{-3}) of the transitions for p–H_2 dominated environments are also given.

Reactants		Products		ΔE^a	Rate coefficient	
ion	H_2	ion	H_2		α^b	β

p–H_2D^+ ($0_{00} \leftrightarrow 1_{01}$) at 1.370 THz

ion	H_2	ion	H_2	ΔE^a	α^b	β
p–0_{00}	p–0	p–1_{01}	p–0	- 66	1.48(-9)	65.24
p–0_{00}	o–1	p–1_{01}	o–1	- 66	5.35(-10)	63.43
p–1_{01}	p–0	p–0_{00}	p–0	+ 66	4.91(-10)	-0.24
p–1_{01}	o–1	p–0_{00}	o–1	+ 66	1.96(-10)	-0.93

A = 4.0397×10^{-3} $n_c \approx 8 \times 10^6$

o–H_2D^+ ($1_{11} \leftrightarrow 1_{10}$) at 372 GHz

ion	H_2	ion	H_2	ΔE^a	α^b	β
o–1_{11}	p–0	o–1_{10}	p–0	- 18	9.41(-10)	17.68
			o–1	- 188	3.20(-10)	186.80
o–1_{11}	o–1	o–1_{10}	p–0	+ 152	4.36(-11)	-0.56
			o–1	- 18	6.47(-10)	17.66
o–1_{10}	p–0	o–1_{11}	p–0	+ 18	9.36(-10)	-0.17
			o–1	- 152	3.69(-10)	150.74
o–1_{10}	o–1	o–1_{11}	p–0	+ 188	3.71(-11)	-0.03
			o–1	+ 18	6.43(-10)	-0.21

A = 1.2186×10^{-4} $n_c \approx 1.3 \times 10^5$

p–D_2H^+ ($1_{01} \leftrightarrow 1_{10}$) at 692 GHz

ion	H_2	ion	H_2	ΔE^a	α^b	β
p–1_{01}	p–0	p–1_{10}	p–0	- 33	9.13(-10)	33.07
			o–1	- 203	2.89(-10)	198.35
p–1_{01}	o–1	p–1_{10}	p–0	+ 137	6.89(-11)	-1.43
			o–1	- 33	6.35(-10)	31.69
p–1_{10}	p–0	p–1_{01}	p–0	+ 33	9.07(-10)	-0.14
			o–1	- 137	5.72(-10)	133.26
p–1_{10}	o–1	p–1_{01}	p–0	+ 203	4.05(-11)	-0.81
			o–1	+ 33	6.70(-10)	-0.84

A = 5.0911×10^{-4} $n_c \approx 5.6 \times 10^5$

o–D_2H^+ ($0_{00} \leftrightarrow 1_{11}$) at 1.476 THz

ion	H_2	ion	H_2	ΔE^a	α^b	β
o–0_{00}	p–0	o–1_{11}	p–0	- 71	1.32(-9)	69.44
			o–1	- 241	3.25(-10)	232.39
o–0_{00}	o–1	o–1_{11}	p–0	+ 99	1.21(-10)	-1.25
			o–1	- 71	9.51(-10)	68.06
o–1_{11}	p–0	o–0_{00}	p–0	+ 71	4.72(-10)	-0.24
			o–1	- 99	3.84(-10)	98.17
o–1_{11}	o–1	o–0_{00}	p–0	+ 241	1.78(-11)	-1.04
			o–1	+ 71	3.66(-10)	-0.73

A = 3.3031×10^{-3} $n_c \approx 7 \times 10^6$

[a]Internal energy difference in Kelvin.
[b]The format a(-b) represents a×10^{-b}.

3.3.2 Microcanonical and Canonical approach

In order to test the microcanonical model, we compared the calculated set of state–to–state thermal rate coefficients to thermodynamical equations by the intermediate of a state–detailed master equation.

State–detailed master equation

Consider an ensemble of H_3^+ isotopologues in a given H_2 isotopic environment with respective state populations $[\mathscr{I}]$ and $[\mathscr{N}]$ in cm^{-3}. The fluxes of populations can be described by a set of differential equations corresponding to a state-detailed chemical master equation. Within the dilute limit, *i.e.* the assumption that the ions are much less abundant than the neutrals ($\sum\limits_{\mathscr{I}}[\mathscr{I}] \ll \sum\limits_{\mathscr{N}}[\mathscr{N}]$), the populations of the H_3^+ isotopologues evolve on a much shorter timescale than the neutral environment's populations hence the populations of the neutrals are almost unaffected by the ionic ensemble. Consequently, the master equation can be decomposed in (i) an ionic part assuming a static environment and (ii) a neutral part considering the ionic ensemble in pseudo–equilibrium with the environment itself.

The master equation describing the fluxes of populations of the ionic ensemble is defined by

$$\frac{d[\mathscr{I}]}{dt} = \sum_{\mathscr{I}'} [\mathscr{I}'] R_{\mathscr{I}' \to \mathscr{I}} - [\mathscr{I}] \sum_{\mathscr{I}'} R_{\mathscr{I} \to \mathscr{I}'} \tag{3.56}$$

the first and second terms respectively representing the inflow and outflows of the ion state $\mathscr{I}$ from/to the other ion states $\mathscr{I}'$. The elements $R_{\mathscr{I} \to \mathscr{I}'}$ of the $\mathbf{R}_{\mathscr{I}}$ matrix are conversion rates in s^{-1} defined as

$$R_{\mathscr{I} \to \mathscr{I}'} = \sum_{\mathscr{N}} \sum_{\mathscr{N}'} [\mathscr{N}] \, k_{\mathscr{I}\mathscr{N} \to \mathscr{I}'\mathscr{N}'}(T) \tag{3.57}$$

with $[\mathscr{N}]$ the neutral states' populations here considered as constant. They correspond to given isotopic enrichments $[HD]/[H_2]$ and $[D_2]/[H_2]$, o/p ratios of H_2 and D_2 and a rotational temperature T_{rot}. Only bimolecular processes with $\mathscr{N}$ as a collision partner are considered. The state–to–state thermal rate coefficients are those corresponding to the kinetic temperature of the neutral environment T_{kin}. Contrarily to the nuclear spins (o/p ratios), the rotational and kinetic degrees of freedom are often very well thermalised therefore we considered a single temperature, T.

The steady–state populations $[\mathscr{I}]_{ss}$ of the H_3^+ isotopologues which are solution to the set of equations $d[\mathscr{I}]/dt=0$ can be easily obtained through diagonalisation of the $\mathbf{R}_{\mathscr{I}}$ matrix. Furthermore, the master equation describing the population fluxes of the neutral environment is defined by

$$\frac{d[\mathscr{N}]}{dt} = \sum_{\mathscr{N}'} [\mathscr{N}'] R_{\mathscr{N}' \to \mathscr{N}} - [\mathscr{N}] \sum_{\mathscr{N}'} R_{\mathscr{N} \to \mathscr{N}'} \tag{3.58}$$

with the conversion rates $R_{\mathcal{N} \to \mathcal{N}'}$ of the $\mathbf{R}_{\mathcal{N}}$ matrix defined as

$$R_{\mathcal{N} \to \mathcal{N}'} = \sum_{\mathcal{I}} \sum_{\mathcal{I}'} [\mathcal{I}]_{ss} \, k_{\mathcal{I} \mathcal{N} \to \mathcal{I}' \mathcal{N}'}(T) \tag{3.59}$$

Thermal equilibrium

Consider the following exothermic reaction with forward and backward rate coefficients k_f and k_b

$$A + B \underset{k_b}{\overset{k_f}{\rightleftharpoons}} C + D + \Delta E_0 \tag{3.60}$$

The canonical equilibrium constant K at a temperature T given by statistical mechanics [30, 47, 48] is

$$K(T) = \frac{k_f}{k_b} = \frac{g'}{g} \left(\frac{\mu'}{\mu} \right)^{\frac{3}{2}} \frac{Q_C \, Q_D}{Q_A \, Q_B} \, exp\left(\frac{-\Delta E_0}{kT} \right) \tag{3.61}$$

where μ and μ' are the reduced masses of A+B and C+D respectively and ΔE_0 is the zero–point energy difference. The terms g and g' were added with respect to prior publications. These canonical isotopic statistical weights correspond to the degeneracies of the backward and forward reaction mechanisms. They are a consequence of the statistical weights used in the microcanonical description. These weights are given in Table 3.7. It is for example obvious that for the $H_3^+ + D_2 \rightleftharpoons D_2H^+ + H_2$ reaction the $g : g'$ ratio is 1:3 in the *strong* ergodic and full scrambling limit, because there are three ways to pick a H from three H's but only one to form $H_3^+ + D_2$.

The Q's in Eq. 3.61 are the partition functions of the species at the temperature T defined by

$$Q_A(T) = \sum_i N_{A_i}(T) \tag{3.62}$$

$$N_{A_i}(T) = g_i \, exp(-E_i/kT) \tag{3.63}$$

with N_{A_i} the population of the ith state of species A, g_i its nuclear spin and rotational degeneracy and E_i its energy. It should be reminded that Eq. 3.61 describes thermal equilibrium only, when all the species are effectively internally and kinetically Boltzmann distributed. The equilibrium constants of the 8 isotopic reactions are plotted in Fig. 3.5 using the strong ergodicity principle and the full–scrambling hypothesis. It is noteworthy that every equilibrium constant seems to converge to unity at infinite temperature. Moreover, on the whole temperature range 5–300 K, *i.e.* from the low toward the high temperature limit [48], we observe the strict equalities

$$\frac{K_1}{K_2} = \frac{K_3}{K_4} = \frac{K_6}{K_7} \quad \text{and} \quad \frac{K_3}{K_6} = \frac{K_5}{K_8} \tag{3.64}$$

with K_i the equilibrium constant of reaction i (i as in Fig. 3.5). Those unexpected relations might be explained by symmetric isotopic substitutions yet they are non–intuitive since they

Table 3.7: Canonical isotopic statistical weights $g:g'$ of the 8 isotopic reactions for the Full–Scrambling (FS) and the Hop limits used in Eq. 3.61. In the weak (W) ergodic limit, the only accessibility of an isotopic channel is accounted for. In the strong (S) ergodic limit, the dissociative asymptotes are counted.

Reactants		$\rightleftharpoons$	Products		FS		Hop	
					S	W	S^a	W
H_2D^+	D_2		D_3^+	H_2	3:1	1:1	3:1	1:1
H_3^+	D_2		D_2H^+	H_2	1:3	1:1	1:3	1:1
D_2H^+	HD		D_3^+	H_2	6:1	1:1	0:0	0:0
H_3^+	HD		H_2D^+	H_2	4:6	1:1	2:3	1:1
H_2D^+	HD		D_2H^+	H_2	6:3	1:1	2:1	1:1
D_2H^+	D_2		D_3^+	HD	6:4	1:1	3:2	1:1
H_3^+	D_2		H_2D^+	HD	1:6	1:1	0:0	0:0
H_2D^+	D_2		D_2H^+	HD	3:6	1:1	1:2	1:1

[a] Averaged values assuming the 3 nuclei of the H_3^+ isotopologue can equiprobably lock in the center of the complex.
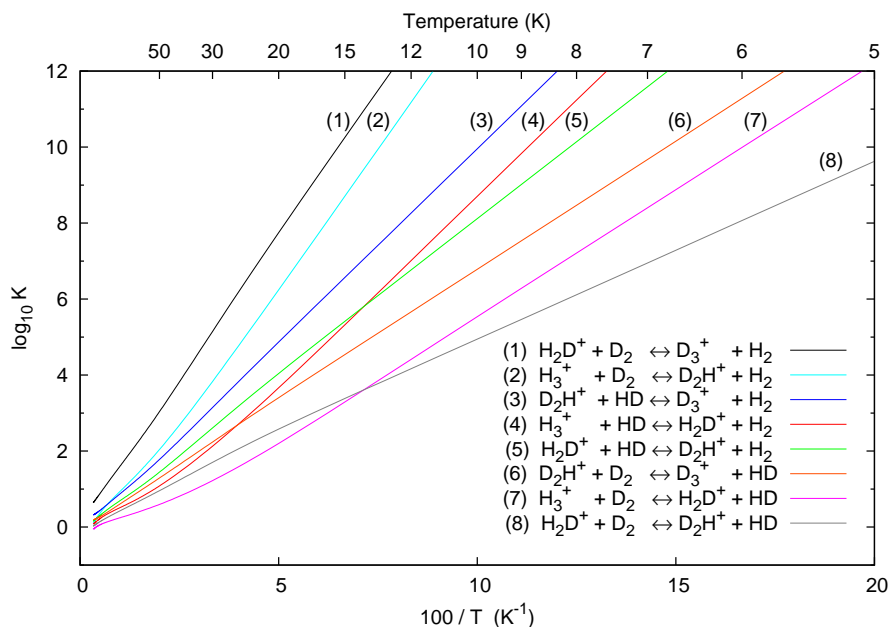

Figure 3.5: Equilibrium constants (Eq.3.61) of the 8 isotopic reactions with the full-scrambling limit and the strong ergodicity principle.

involve vibrational energies, rotational constants and densities of states as well as nuclear spin selection rules and degeneracies.

The canonical equilibrium constant is also related to the chemical equilibrium (steady–state populations or number densities) by

$$K(T) = \frac{[C]_{ss}\,[D]_{ss}}{[A]_{ss}\,[B]_{ss}} \tag{3.65}$$

The canonical balance corresponding to Eq. 3.61 and 3.65 can be transposed to specific internal states of the species resulting in the detailed balance. Although it also holds for reactive collisions, this principle is mostly known for non-reactive, inelastic collisions *i.e.* with (A,B)=(C,D), $\Delta E_0 = 0$, $\mu = \mu'$ and $g = g'$:

$$A_i + B_j \underset{k_b}{\overset{k_f}{\rightleftharpoons}} A_{i'} + B_{j'} \tag{3.66}$$

$$K(T) = \frac{k_f}{k_b} = \frac{N_{A_i}\,N_{B_j}}{N_{A_{i'}}\,N_{B_{j'}}} \tag{3.67}$$

$$= \frac{[A_{i'}]_{ss}\,[B_{j'}]_{ss}}{[A_i]_{ss}\,[B_j]_{ss}} \tag{3.68}$$

Comparison and analysis

Steady–state populations of the H_3^+ isotopologues were obtained by solving the master equation for various thermal and non-thermal neutral environments (Eq. 3.56 and 3.57). These populations are compared to thermal populations derived according to the canonical balance (Eq. 3.61 and 3.65) and the detailed balance (Eq. 3.67 and 3.68). We present here a sample of results.

The purely hydrogenated and deuterated systems were first simulated by employing a pure thermal H_2 or D_2 environment at various temperatures. As shown in Fig. 3.6 for the purely deuterated system, $D_3^+ + D_2$, the master equation renders thermalised D_3^+ steady–state populations thereby confirming that the set of state–to–state thermal rate coefficients fulfills the isotopically non-reactive detailed balance (Eq. 3.67). Note that an isotopically non-reactive collision can still be reactive in the sense of *homonuclear exchange*.

We also simulated environments at different temperatures with terrestrial and cosmic deuterium abundances, *i.e.* $HD/H_2 = 3.2\times10^{-4}$ and 3.2×10^{-5} respectively, neglecting D_2. The o/p ratio of H_2 was set as thermal or fixed between its high temperature limit of 3 down to 10^{-7}. As an example, the steady–state H_2D^+/H_3^+ isotopic ratio is shown in Fig. 3.7. The H_2D^+/H_3^+ as well as the D_2H^+/H_2D^+ and D_3^+/D_2H^+ (the latter two not shown in Fig. 3.7) steady–state ratios in the thermal o/p–H_2 environment are all consistent with the canonical equilibrium constants
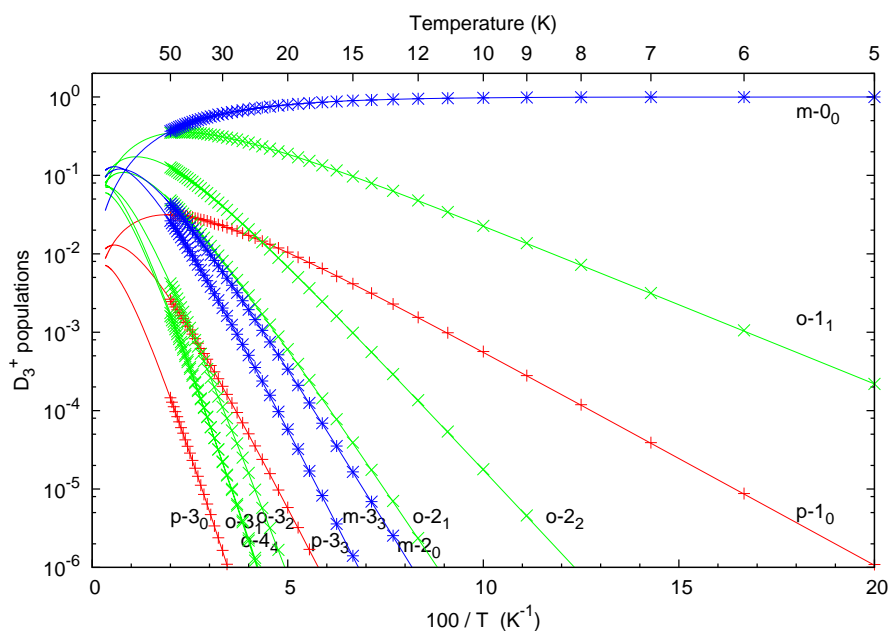
Figure 3.6: Populations of the 12 lowest rotational levels of D_3^+. Solid lines are thermal populations and crosses are the steady-state populations in a thermal D_2 environment derived from the master equation using the set of state–to–state rate coefficients.

of reactions (4), (5) and (3) in Fig. 3.5 respectively. Moreover, each H_3^+ isotopologue is well thermalised internally.

We thereby show that the calculated state–to–state thermal rate coefficients fullfill the canonical and detailed balance within few ‰. These results, which are observed for the weak and strong ergodic limits, demonstrate that the microcanonical model is consistent with the canonical description. While this result is gratifying, simulating experimental results or astrophysical observations with the state–to–state rate coefficients is posing a more serious test to the microcanonical model.

3.4 EXPERIMENTAL SECTION

3.4.1 22–pole ion trap apparatus

To study the H_3^+ + H_2 isotopic system, we extended the measurements described by Gerlich et al. [18] using the same apparatus depicted in Fig. 3.8.

The core of the setup, the temperature variable 22–pole ion trap, has been described in detail
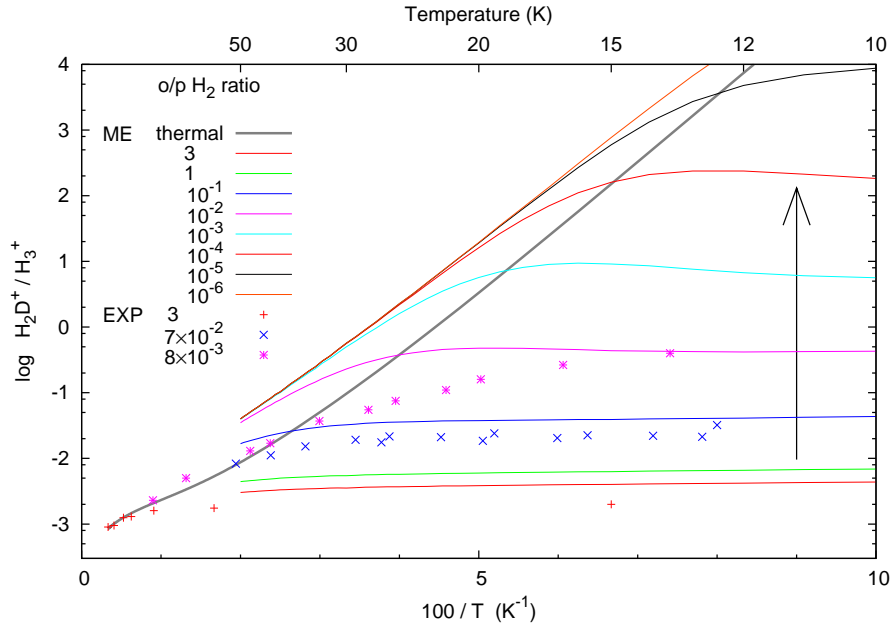
Figure 3.7: Steady–state H_2D^+/H_3^+ isotopic fractionation in a H_2 environment with terrestrial deuterium abundance ($HD/H_2 = 3.2 \times 10^{-4}$). The solid lines are results of the master equation using the strong ergodicity principle for various o/p ratios of H_2 (no D_2 is considered). The arrow indicates a decreasing o/p ratio of H_2. The points are experimental results for o/p–$H_2 = 3$, 7×10^{-2} and 8×10^{-3} (see Sec. 3.4.3).

elsewhere [49, 50]. It is enclosed in stainless steel walls which are mounted on a closed cycle helium refrigerator. The temperature of these walls, monitored by two silicon diodes, can range from ∼300 K down to 13.0±0.5 K.

H_3^+ parent ions are produced in a storage ion source by electron bombardment of n-H_2 and pulsed via a first quadrupole mass filter into the 22–pole ion trap. There, the ion cloud is exposed to a constant density of reactant gas (HD or H_2 with natural traces of HD) thermalised to the surrounding walls. Additionally, pulsed or constant He gas can be admitted to the trap. The gas number densities were accurately determined with a pressure ion gauge calibrated against a spinning rotor gauge prior to the measurements, and were kept below 10^{13} cm^{-3} in order to avoid ternary association [51]. After a storage period of 10 to 1000 ms, the ions are extracted, mass selected in the second quadrupole mass filter and counted in a Daly–type ion detector.

The storage cycle is repeated for several trapping times counting the H_3^+, H_2D^+, D_2H^+ or D_3^+ products. As illustrated in Fig. 3.9, we obtain the time evolution and steady–state populations of each isotopologue from which we can fit reaction rate coefficients using a standard system of differential equations.

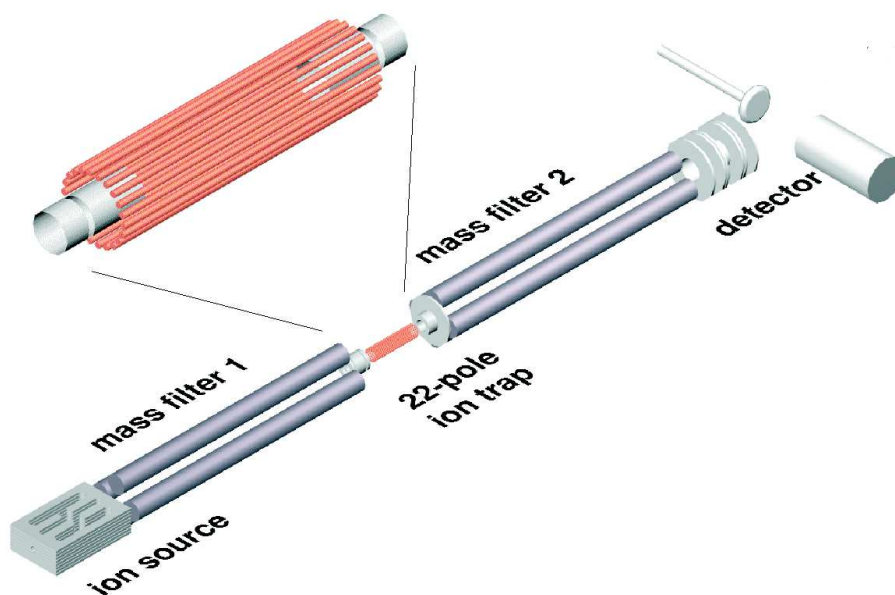Prior to its introduction into the trap, the H_2 reactant gas could be flown through a p–H_2

Figure 3.8: Schematic of the trapping apparatus. The H_3^+ ions are produced in the storage ion source and pulsed through the quadrupole mass filter 1 into the 22–pole ion trap. This trap, consisting of 22 electrodes forming a cylindrical structure, is mounted on a closed cycle helium refrigerator. On entrance, the ions are cooled down to the ambient temperature by a short intense pulse of He atoms. During the storage period of 10 to 1000 ms, the ions are subject to a constant density of H_2 or HD reactant gas. The result of the interaction is detected by extracting the stored ion cloud through the quadrupole mass filter 2 and counting the number of product ions in the detector.

generator in order to catalyse the conversion of *ortho*-H_2 into *para*–H_2. This converter contains a para-magnetic compound (Fe_2O_3 powder) confined in a copper block mounted onto a closed cycle helium refrigerator. The temperature of the catalyst was measured by a silicon diode mounted on the copper block and could be tuned in the range 11–50 K in order to vary the o/p ratio of the outflowing H_2 down to 8×10^{-3}. The o/p ratio was calibrated with an accuracy of 20% in the 22–pole ion trap using the proton abstraction reaction $N^+ + H_2 \rightarrow NH^+ + H$ as described in Ref. [52]. We also monitored *in situ* the HD content of natural H_2 using a H_2O^+ beam and the proton (deuteron) abstraction reactions

$$
\begin{array}{rcll}
H_2O^+ + H_2 & \rightarrow & H_3O^+ + H & \quad\quad (3.69) \\
H_2O^+ + HD & \rightarrow & H_3O^+ + D \quad 0.57 & \quad\quad (3.70) \\
& \rightarrow & H_2DO^+ + H \quad 0.43 & \quad\quad (3.71)
\end{array}
$$

with the given branching ratios determined *in situ* using pure HD target gas. In experiments with unprocessed n–H_2, we obtain the product ratio $H_2DO^+/H_3O^+ = 1.1 \times 10^{-4}$. Assuming that
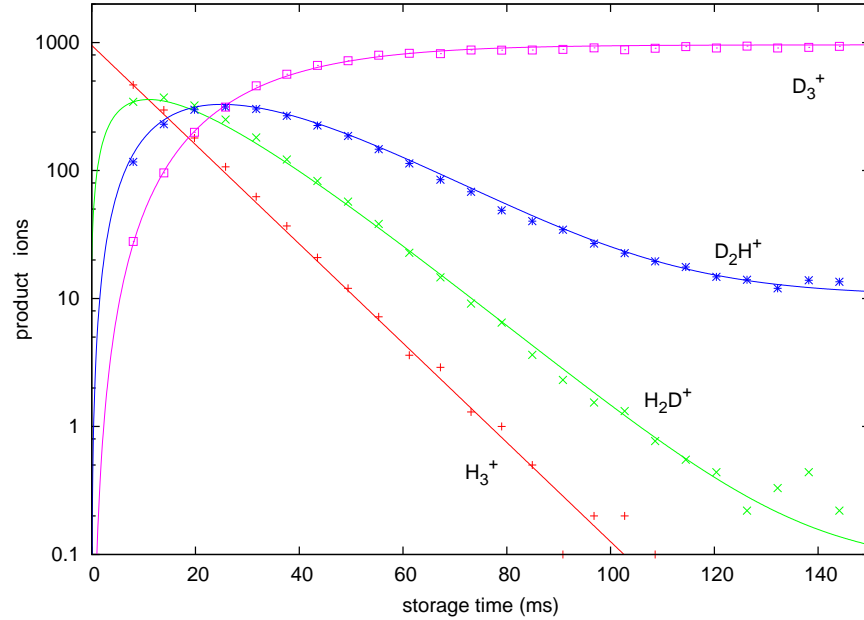
Figure 3.9: Sequential deuteration of H_3^+ in HD with a number density of 6.3×10^{10} cm^{-3} at a nominal temperature of 13.5 K. Due to the exothermicity of the reaction chain, a constant number density of about 6×10^{12} cm^{-3} He has been applied to ensure full thermalization of all reactants. The lines are the solutions of a rate equation system fitted to the experimental data yielding rates of 1.30×10^{-9}, 1.30×10^{-9} and 1.05×10^{-9} cm^{3}s^{-1} for the deuteration of H_3^+, H_2D^+ and D_2H^+, respectively.

both reactions with H_2 and HD proceed with the Langevin rate, that is

$$\frac{k_{H_2O^+ + HD}}{k_{H_2O^+ + H_2}} = \sqrt{\frac{\mu_{H_2O^+ + H_2}}{\mu_{H_2O^+ + HD}}} = 0.837 \tag{3.72}$$

we derive a HD fraction of 3.1×10^{-4} which corresponds to the expected terrestrial deuterium abundance. However, when starting the converter, the HD content of the processed H_2 was depleted by about one order of magnitude caused apparently by isotopic preferential freezing on the cold catalyst [53]. After some hours of operation, the terrestrial fraction was approched again. Therefore, to ensure the terrestrial HD fraction in the outflowing p-H_2, the converter was run one day prior to the experiments. In summary, great care has been taken to accurately determine the number densities of the neutral reaction partners as has been pointed out by Gerlich et al. [32].

3.4.2 Deuteration rates with HD

We measured the deuteration rate coefficients of H_3^+, H_2D^+ and D_2H^+ with HD between 13 and 210 K in the presence of Helium buffer gas ([He]$\gg$[HD]). The target gas HD has been purchased from Cambridge Isotope Laboratories, Inc., who specify the purity of the deuterium hydride to be 97 %, the rest mainly being H_2 and D_2. The results are compiled in Fig. 3.10 together with previously published values. Our results are in good agreement with Adams and Smith [29] and Giles et al. [30] showing systematic temperature dependencies overlapping in the common temperature range. The low temperature rate coefficients from Gerlich et al. [18] are systematically lower than ours by a factor of ~ 4. This important difference needs some special attention later.

All the rate coefficients approach the Langevin value at low temperature. At 300 K, (i) the deuteration rate coefficient of H_3^+ is still very fast, (ii) the deuteration rate coefficient of H_2D^+ + HD drops by a factor of 2 to 3 between 10 and 300 K and (iii) the deuteration rate coefficient of D_2H^+ + HD drops by one order of magnitude over the same temperature range. Contributions from D_2 contaminations (~ 1.5 %) in HD do not change these findings. These trends are all consistent with the departure from the full–scrambling to the hop limit toward high temperatures. Indeed, in the hop limit when one nucleus of the H_3^+ isotopologue locks in the center of the complex, (i) the deuteration of H_3^+ can still proceed on every collision, (ii) the deuteration of H_2D^+ can only proceed when the deuterium nucleus is locked in the center, *i.e.* with an upper limit for the rate coefficient of $\sim k_L/3$ and (iii) the deuteration of D_2H^+ would be unfeasible under these circumstances, *i.e.* the rate coefficient would practically approach zero. However, direct mechanisms without complex formation may have to be considered at higher energies. This interpretation of the current observation is in qualitative agreement with the experimental results from Cordonnier et al. [31] on the $H_3^+ + H_2$ system at ~ 400 K also showing an incomplete scrambling. They derived statistical weights for the transfer:exchange reaction mechanisms of 2.4:1 which are in between the full scrambling and hop limits with statistical weights for the identity:transfer:exchange reaction mechanisms of 1:3:6 and 1:1:0 respectively.

The presented experiments yield species–to–species rate coefficients without any information on the internal state distributions of the H_3^+ isotopologues. In order to compare them with theory, we overlaid in Fig. 3.10 the calculated state–to–species rate coefficients from the ground state of HD and the three lowest rotational states of each H_3^+ isotopologues' *para* and *ortho* nuclear spin modifications, corresponding to six curves. Both sets of rates according to the weak and strong ergodic limits are shown in this case. The deuteration rate coefficients of H_3^+ and H_2D^+ are more or less state–independent and they are in very good agreement with the measured rates irrespective of the ergodic limit used. The same observation holds for the deuteration rate coefficients of D_2H^+ based on the weak ergodic limit. However, those based on the strong ergodic limit are significantly lower than the experimental rates for the high–lying reactant states. Nevertheless, at low temperatures the thermalisation with the dominant Helium buffer gas populates essentially the D_2H^+ reactants in their lowest *para* and *ortho* ground
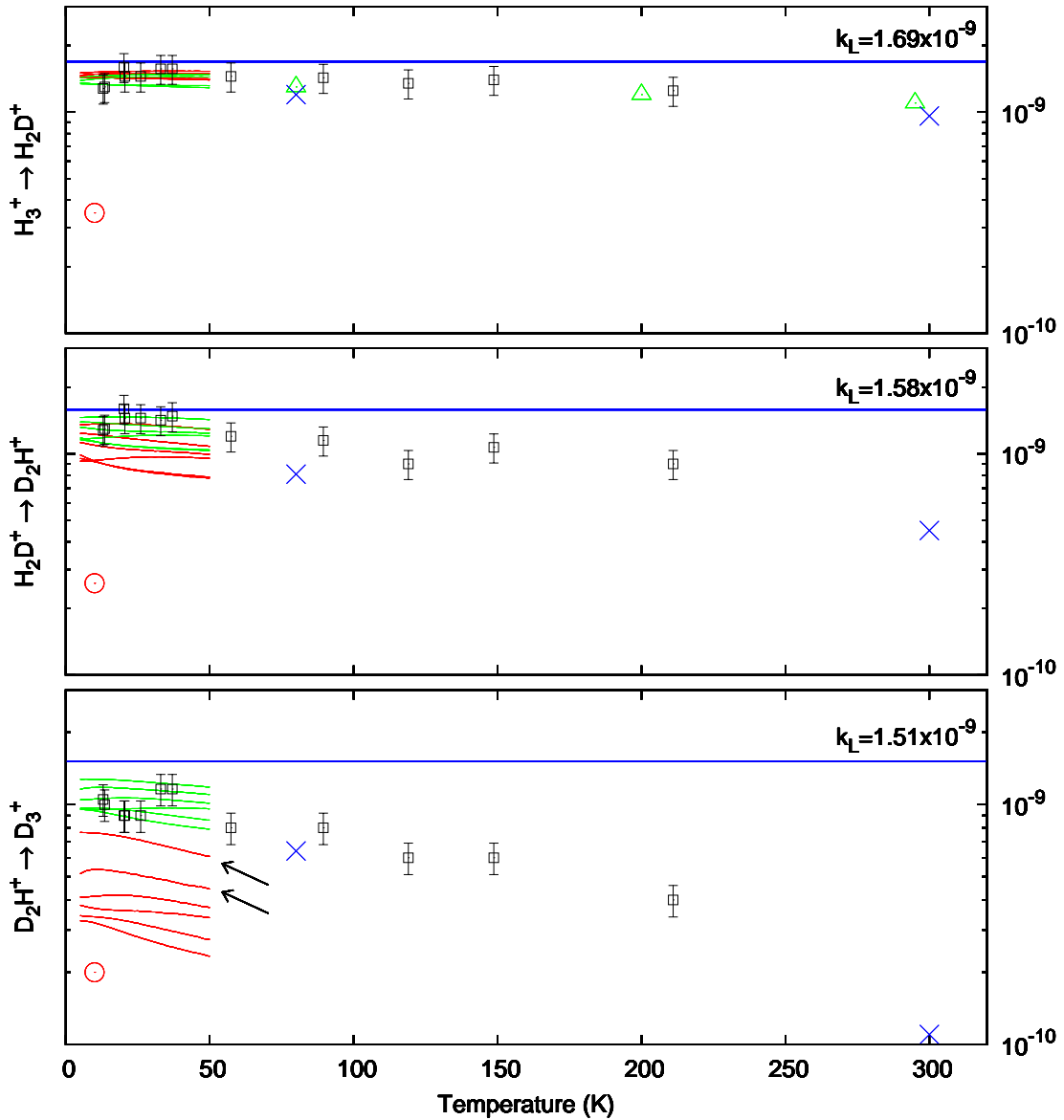
Figure 3.10: Deuteration rate coefficients of H_3^+, H_2D^+ and D_2H^+ with HD. The data points are experimental values corresponding to Gerlich et al. [18] (circles), Adams and Smith [29] (triangles), Giles et al. [30] (crosses) and this work (squares). The upmost lines show the Langevin limits. The short lines are the state-to-species rate coefficients from the ground state of HD and the lowest rotational states of the H_3^+ isotopologues' *para* and *ortho* modifications calculated with the full–scrambling hypothesis for the weak (green) and strong (red) ergodicity principles.

95

states corresponding to the two uppermost red lines in Fig. 3.10 (indicated by arrows). As a result, the calculations based on the strong ergodic limit also compare reasonably well with the experimental results.

3.4.3 Steady-state in H_2(HD)

Another critical test for any theoretical determination of state–to–state rate coefficients is the steady–state isotopic fractionation of H_3^+. It is also a crucial parameter for the deuterium astro-chemistry in cold molecular environments [10, 15, 36] which can be derived from astronomical observations. As a result, it can be considered a benchmark for comparison between theory, experiment and observation.

The steady–state H_2D^+/H_3^+ ratio has been measured in H_2 with terrestrial abundance of HD for o/p ratios of 8×10^{-3}, 7×10^{-2} and 3 with the temperature of the 22–pole ion trap ranging from 13 to 50 K. Results are shown in Fig. 3.7 together with theoretical values from the master equation based on the strong ergodic limit. Results at the lowest temperatures are in good agreement with Gerlich et al. [18]. Following their description, our forward rate coefficient being higher by a factor of ~ 4 together with an even equilibrium constant point at backward rate coefficients also a factor of ~ 4 higher. Indeed, a value in the range of 2×10^{-10} cm^{3}s^{-1} for the backward rate coefficient has also been measured directly by injecting H_2D^+ ions into n-H_2 target gas.

Our theoretical and experimental results shown in Fig. 3.7 are in reasonable agreement presenting similar trends. However, significant differences are found for the experiment at an H_2 o/p ratio of 0.8×10^{-2} in comparison to the theoretical curve for 10^{-2}. The discrepancy is likely due to an improper thermalisation of the ions to the trap's walls. Previous detailed spectroscopic studies of H_2D^+ and D_2H^+ ions showed an ion kinetic temperature of 27 K when the nominal temperature of the trap's walls was 17 K. Reasons for this discrepancy are discussed in Refs. [54–56] and improvements to the ion thermalisation at the lowest wall temperatures are currently explored. Despite these difficulties, the general trend of the H_2D^+/H_3^+ ratio as a function of temperature and o/p ratio of H_2 agree very well but follow up experiments at fully thermalized conditions will pose a more quantitative test for the current and future theoretical work.

The agreement with the experimental H_2D^+/H_3^+ ratio is better for the predictions based on the weak ergodic limit (not shown in Fig. 3.7) as compared to the strong ergodic limit results presented in Fig. 3.7. The former values are lower by a factor of $\sim 6/4$ as can be inferred from Table 3.7.

3.5 DISCUSSION

Despite the subtle discrepancies between experiment and theory the general trends are well re-produced. Therefore this work clearly demonstrates the utility of the microcanonical model. In

fact the agreement between the two supports the assumption of full scrambling in H_5^+ at low temperatures with an increasing influence of dynamical restrictions perhaps to the limit of a non-ergodic behavior at higher energies and temperatures. In any case, the rate coefficients of this study might serve as a test to compare any new experiment, astrophysical modelling or to a more realistic theoretical approach like scattering calculations which should be feasible for this five, light nuclei system even at a full quantum level when comparing to similar systems of current research [57]. Regardless of these future developements some other aspects deserve attention.

Regarding the complexity of state–detailed chemical models, a reduced model neglecting the rotational states and considering only the nuclear spin modification of the isotopologues may be preferred [10, 15, 36]. For this purpose, one can use (i) ground state–to–species rate coefficients (see Eq. 3.55 and appendix) on the basis that for low temperatures or for low H_2 densities, only the ground state of each isotope–nuclear spin species is significantly populated or (ii) thermal species–to–species (*eq.* canonical) rate coefficients by considering each isotope–nuclear spin species as internally thermalised. Such reduced models can account for the efficient pumping from p–H_2D^+ to H_3^+ via o–H_2D^+ in collisions with the energetic o–H_2 as well as non-thermal *ortho–(meta)–para* ratios. However, it cannot account for collisional pumping within the rotational ladder of each isotope–nuclear spin species as it cannot account for radiative cooling. This limitation may result in the overestimation or underestimation of the isotopic fractionation of H_3^+ in astrochemical modeling.

A principle limitation to the use of the microcanonical approach appears for non–thermal environments. State–to–state or species–to–species *thermal* rate coefficients are based on the fact that all internal states are kinetically thermalised. Using *thermal* rate coefficients in a time dependent or steady–state model thus implies that the kinetic degrees of freedom of all internal states are thermalised at all times. However, this assumption can be wrong in environments far from thermal equilibrium since the exchange of energy between the different degrees of freedom can lead to kinetic heating (or cooling). As an example, in an environment very far from equilibrium like H_2 at $T_{kin}=T_{rot}=10$ K with o/p=3, the H_3^+ ions would be frequently colliding with o–H_2. Since the rotational and kinetic degrees of freedom completely mix their energies during the collision process and that o–H_2 can relax to p–H_2 by exchanging a proton, the H_3^+ ions would keep absorbing a significant fraction of the 170 K internal energy of o–H_2 thereby exciting their rotational and kinetic degrees of freedom to mean energies much higher than the initial 10 K. The H_3^+ ions would be kinetically heated. Thermal rate coefficients are thus incorrect for such environments.
The master equation based on thermal state-to-state rate coefficients presented in section 3.3.2 works on the internal phase space only and implicitly forces the kinetic degree of freedom to be thermally distributed. Therefore, it cannot account for kinetic heating just as it violates the first law of thermodynamics in non–thermal environments. The steady-state and time dependent populations which follow from it are therefore biased. In order to mend this statistical mechan-

ical problem, a stochastic method working in the full phase space was proposed [35] but it has not yet been applied to the $H_3^+ + H_2$ system. Note that this kinetic heating effect applies to all species which can exchange a proton with H_2, thus also to CH_3^+, $C_2H_2^+$ and their isotopologues and particularly the light H^+.

3.6 CONCLUSIONS

A microcanonical model used to calculate thermal state-to-state rate coefficients for all $H_3^+ + H_2$ isotopic variants in the temperature range 5–50 K has been derived. Full–scrambling of the nuclei during the intermediate complex lifetime was assumed. In addition, both weak and strong ergodic limits, respectively neglecting and accounting for the degeneracies of the reaction mechanisms, were tested. In both cases, the resulting set of rate coefficients were successfully compared to the corresponding canonical approach by the intermediate of a state–detailed master equation. Such microcanonical model can be straightforwardly applied to other scrambling isotopic systems like $CH_3^+ + H_2$.

Extended measurements with a 22–pole ion trap were performed studying in particular the deuteration chain of H_3^+ with HD at low temperatures. In general, agreement between experiment and microcanoncical model was found. The temperature dependence of the experiment also agrees with previous experiments at higher temperatures [29, 30]. However, the deuteration rate coefficient at the lowest temperature is faster than previously reported by Gerlich et al. [18]. This is a very surprising result as the measurements have been conducted in the same setup but with a different trap. Recent spectroscopic investigations show that the ion temperature is of concern. However, similar steady–state H_2D^+ to H_3^+ ratios in the different experiments hint at similar trap temperatures. Still, it is quite possible that lower temperatures were reached in the previous study. But it is questionable whether the rate coefficient will show a drastic drop over a temperature range of 5-10 K. Therefore more systematic studies under conditions of proper thermalization are needed. Technical improvements of the current trap setup are underway.

The agreement between our experimental and theoretical results supports the full-scrambling hypothesis assumed for the calculations. Toward higher temperatures, experimental results suggest partial scrambling in favor of the transfer reaction mechanism. State specific experimental rate coefficients which could be obtained with spectroscopic tools [54, 55] would serve as a more stringent test for theory.

State–to–state and state–to–nuclear spin species rate coefficients based on the weak and strong ergodic limits as well as equilibrium constants and partition functions are available online as supplementary material. Regarding the underlying physical interpretation, we recommend to use the rate coefficients based on the strong rather than the weak ergodicity principle although our current experimental results tend to partially support the latter.

State–detailed astrochemical models of the H_3^+ isotopologues are now accessible despite their greater complexity. With the advent of a new generation of telescopes and observation facilities [58, see Table 3], the detection limits and spatial resolutions of o–H_2D^+ and p–D_2H^+
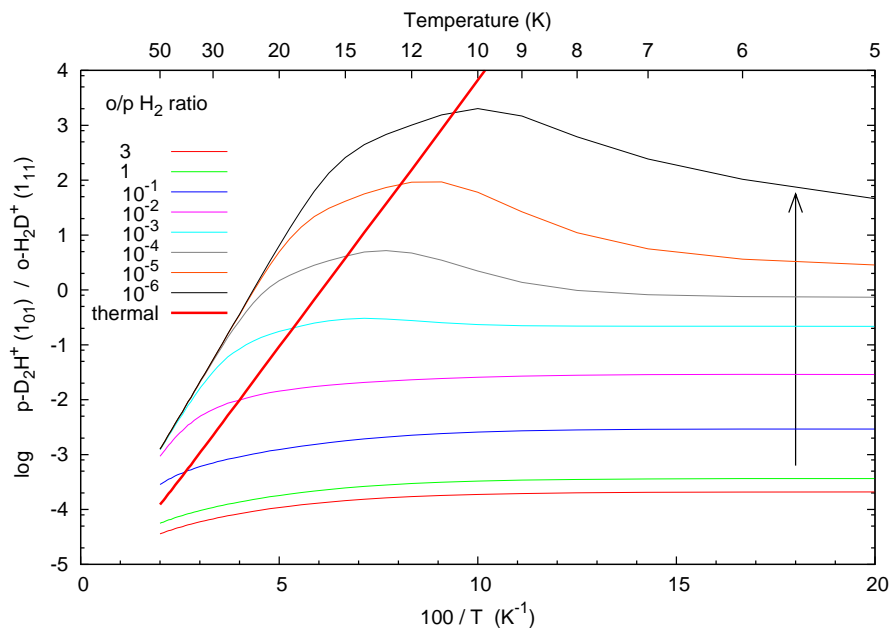
Figure 3.11: The p–$D_2H^+(1_{01})$ / o–$H_2D^+(1_{11})$ steady-state ratio as a function of temperature for pure molecular hydrogen environments with deuterium cosmic abundance (HD/H_2=3.2×10^{-5}) and various o/p-H_2 ratios. The arrow indicates a decreasing o/p ratio of H_2. Radiative processes are not considered here.

ground state transitions will be significantly improved and those of p–H_2D^+ and o–D_2H^+ will become accessible. Since their critical number densities (see Table 3.6) are in the typical range of prestellar cores and protostellar objects, coupling between radiative and collisional processes ought to be considered for a good interpretation of the astronomical observations and exact chemical modelling.

The H_3^+ isotopologues are greatly entangled with their H_2 environment, namely the HD/H_2 ratio, the temperature and the influential H_2 *ortho*–to–*para* ratio. The latter can be a serious limiting factor for the H_3^+ deuterium fractionation which is a cornerstone of the coolest astrochemistry. The H_2 o/p ratio thus has to be considered in models of cold environments ($\sim$ 10 K) where extreme molecular deuteration can occur. For the same reason, the H_3^+ isotopologues are likely the ideal tracers for the H_2 o/p ratio as illustrated in Fig. 3.11. We hope that the new tools developed here will shed light on the non–thermal o/p ratio of H_2 and its relaxation during stellar formation [16, 17, 36].

Acknowledgments

REFERENCES

[1] G. Steigman, D. Romano, and M. Tosi, Mon. Not. Astron. Soc. **378**, 576 (2007).

[2] B. Parise, A. Castets, E. Herbst, E. Caux, C. Ceccarelli, I. Mukhopadhyay, and A. G. G. M. Tielens, Astron. Astrophys. **416**, 159 (2004).

[3] E. Roueff, D. C. Lis, F. F. S. van der Tak, M. Gerin, and P. F. Goldsmith, Astron. Astrophys. **438**, 585 (2005).

[4] A. G. G. M. Tielens, Astron. Astrophys. **119**, 177 (1983).

[5] B. Parise, C. Ceccarelli, A. G. G. M. Tielens, A. Castets, E. Caux, B. Lefloch, and S. Maret, Astron. Astrophys. **453**, 949 (2006).

[6] C. Ceccarelli, P. Caselli, E. Herbst, A. G. G. M. Tielens, and E. Caux, in *Protostars and Planets V*, edited by B. Reipurth, D. Jewitt, and K. Keil (2007), pp. 47–62.

[7] R. Stark, F. van der Tak, and E. van Dishoeck, Astrophys. J. **521**, L67 (1999).

[8] P. Caselli, F. F. S. van der Tak, C. Ceccarelli, and A. Bacmann, Astron. Astrophys. **403**, L37 (2003).

[9] C. Vastel, T. Phillips, and H. Yoshida, Astrophys. J. **606**, L127 (2004).

[10] L. Pagani, M. Salez, and P. G. Wannier, Astron. Astrophys. **258**, 479 (1992).

[11] H. Roberts, E. Herbst, and T. J. Millar, Mon. Not. Astron. Soc. **336**, 283 (2002).

[12] H. Roberts, E. Herbst, and T. J. Millar, Astrophys. J. **591**, L41 (2003).

[13] H. Roberts, E. Herbst, and T. J. Millar, Astron. Astrophys. **424**, 905 (2004).

[14] C. M. Walmsley, D. R. Flower, and G. Pineau des Forêts, Astron. Astrophys. **418**, 1035 (2004).

[15] D. R. Flower, G. Pineau des Forêts, and C. M. Walmsley, Astron. Astrophys. **427**, 887 (2004).

[16] D. R. Flower, G. Pineau Des Forêts, and C. M. Walmsley, Astron. Astrophys. **449**, 621 (2006).

[17] J. Le Bourlot, Astron. Astrophys. **242**, 235 (1991).

[18] D. Gerlich, E. Herbst, and E. Roueff, Planet. Space Sci. **50**, 1275 (2002).

[19] Y. Yamaguchi, J. F. Gaw, R. B. Remington, and H. F. Schaefer, III, J. Chem. Phys. **86**, 5072 (1987).

[20] Z. Xie, B. J. Braams, and J. M. Bowman, J. Chem. Phys. **122**, 224307 (2005).

[21] P. H. Acioli, Z. Xie, B. J. Braams, and J. M. Bowman, J. Chem. Phys. **128**, 104318 (2008).

[22] G. M. e Silva, R. Gargano, W. B. da Silva, L. F. Roncaratti, and P. H. Acioli, Int. J. Quantum Chem. **108**, 2318 (2008).

[23] M. Barbatti and M. A. C. Nascimento, J. Chem. Phys. **119**, 5444 (2003).

[24] T. Oka and E. Epp, Astrophys. J. **613**, 349 (2004).

[25] K. Park and J. C. Light, J. Chem. Phys. **126**, 044305 (2007).

[26] M. Quack, Mol. Phys. **34**, 477 (1977).

[27] T. Oka, J. Mol. Spec. **228**, 635 (2004).

[28] K. Park and J. C. Light, J. Chem. Phys. **127**, 224101 (2007).

[29] N. Adams and D. Smith, Astrophys. J. **248**, 373 (1981).

[30] K. Giles, N. Adams, and D. Smith, J. Phys. Chem. **96**, 7645 (1992).

[31] M. Cordonnier, D. Uy, R. M. Dickson, K. E. Kerr, Y. Zhang, and T. Oka, J. Chem. Phys. **113**, 3181 (2000).

[32] D. Gerlich, F. Windisch, P. Hlavenka, R. Plašil, and J. Glosik, Phil. Trans. Royal Soc. London. Series A **364**, 3007 (2006).

[33] A. M. Messiah and O. W. Greenberg, Phys. Rev. **136**, 248 (1964).

[34] A.-W. Maue, Annalen der Physik **422**, 555 (1937).

[35] E. Hugo, O. Asvany, J. Harju, and S. Schlemmer, in *Molecules in Space and Laboratory* (2007).

[36] L. Pagani, C. Vastel, E. Hugo, V. Kokoouline, C. Greene, A. Bacmann, E. Bayet, C. Ceccarelli, R. Peng, and S. Schlemmer, Astron. Astrophys. (2008), accepted.

[37] J. Ramanlal, O. L. Polyansky, and J. Tennyson, Astron. Astrophys. **406**, 383 (2003).

[38] J. Ramanlal and J. Tennyson, Mon. Not. Astron. Soc. **354**, 161 (2004).

[39] C. M. Lindsay and B. J. McCall, J. Mol. Spec. **210**, 60 (2001).

[40] J. Tennyson (2005), list of calculated H_3^+, H_2D^+ and D_2H^+ transitions, private communication.

[41] S. Miller and J. Tennyson, J. Mol. Spec. **126**, 183 (1987).

[42] W. Kołos and L. Wolniewicz, J. Chem. Phys. **46**, 1426 (1967).

[43] D. Gerlich, J. Chem. Phys. **92**, 2377 (1990).

[44] W. H. Miller, J. Chem. Phys. **52**, 543 (1970).

[45] J. Hirschfelder, C. Curtiss, and R. Bird, *Molecular theory of gases and liquids* (Wiley, 1966), chapter 2.1.

[46] E. I. Dashevskaya, I. Litvin, E. E. Nikitin, and J. Troe, J. Chem. Phys. **122**, 184311 (2005).

[47] T. Hill, *An introduction to statistical thermodynamics* (Dover Publications, 1960).

[48] E. Herbst, Astron. Astrophys. **111**, 76 (1982).

[49] D. Gerlich, in *Adv. Chem. Phys.: State-Selected and State-to-State Ion-Molecule Reaction Dynamics*, edited by C.-Y. Ng and A. C. P. Michael Baer (1992), vol. LXXXII, pp. 1–176.

[50] D. Gerlich, Phys. Scripta **T59**, 256 (1995).

[51] W. Paul, B. Lücke, S. Schlemmer, and D. Gerlich, J. Mass Spectrom. Ion Processes **150**, 373 (1995).

[52] D. Gerlich, J. Chem. Soc. Faraday Trans. **89**, 2199 (1993).

[53] L. Amiaud, Ph.D. thesis, University of Cergy–Pontoise (2006).

[54] O. Asvany, E. Hugo, F. Müller, F. Kühnemann, S. Schiller, J. Tennyson, and S. Schlemmer, J. Chem. Phys. **127**, 154317 (2007).

[55] O. Asvany, O. Ricken, H. S. P. Müller, M. C. Wiedner, T. F. Giesen, and S. Schlemmer, Phys. Rev. Lett. **100**, 233004 (2008).

[56] O. Asvany and S. Schlemmer, Int. J. Mass Spectrom. (2008), in press.

[57] T. Wu, H. Werner, and U. Manthe, Science **306**, 2227 (2004).

[58] C. Vastel, P. Caselli, C. Ceccarelli, T. Phillips, M. C. Wiedner, R. Peng, M. Houde, and C. Dominik, Astrophys. J. **645**, 1198 (2006).

APPENDICES

3.A RATE COEFFICIENTS

Table 3.8: Ground state–to–species rate coefficients with nuclear spin modification details (see Eq. 3.55) according to the full–scrambling hypothesis and the strong ergodicity principle. The rows are the ground state reactants and the columns are the product species. The rates are given in the form $k = \alpha \, e^{-\beta/T}$. The α (cm^{3}s^{-1}) and β (Kelvin) coefficients were fitted in the temperature range 5–20 K if the rates were higher than 10^{-17} cm^3.s^{-1}, else up to 50 K. The α coefficients are given with the format a(-b) representing a$\times 10^{-b}$. The F's refer to reactions strictly forbidden by nuclear spins.

5 H system		p–H$_3^+$ p–H$_2$	p–H$_3^+$ o–H$_2$	o–H$_3^+$ p–H$_2$	o–H$_3^+$ o–H$_2$
p–H$_3^+$	p–H$_2$	1.89(-9) 0.00	8.16(-10) 164.9	F	5.88(-10) 198.2
p–H$_3^+$	o–H$_2$	2.98(-10) -0.69	1.13(-9) -0.19	3.46(-10) -0.69	8.03(-10) 32.6
o–H$_3^+$	p–H$_2$	F	1.50(-9) 136.2	1.84(-9) -0.26	8.84(-9) 170.0
o–H$_3^+$	o–H$_2$	1.04(-10) 0.00	4.00(-10) -0.19	9.67(-11) -0.14	1.29(-9) 0.07

4 H – 1 D system		p–H$_3^+$ HD	o–H$_3^+$ HD	p–H$_2$D$^+$ p–H$_2$	p–H$_2$D$^+$ o–H$_2$	o–H$_2$D$^+$ p–H$_2$	o–H$_2$D$^+$ o–H$_2$
p–H$_3^+$	HD	1.55(-10) -1.05	5.71(-11) 32.25	3.11(-10) -0.71	4.93(-10) 0.95	6.08(-10) -1.08	5.71(-10) 25.8
o–H$_3^+$	HD	2.87(-11) -0.38	1.62(-10) -0.94	F	1.70(-10) -0.44	2.22(-10) -0.47	1.11(-9) 0.35
p–H$_2$D$^+$	p–H$_2$	2.46(-10) 226.5	F	1.79(-9) -0.01	F	F	1.02(-9) 256.1
p–H$_2$D$^+$	o–H$_2$	1.48(-10) 58.8	9.32(-9) 94.6	F	5.29(-10) -0.18	1.26(-9) 0.06	6.04(-10) 88.8
o–H$_2$D$^+$	p–H$_2$	1.31(-10) 140.4	9.49(-11) 178.9	F	5.58(-10) 82.7	1.79(-9) -0.02	6.54(-10) 174.0
o–H$_2$D$^+$	o–H$_2$	4.67(-11) -0.82	1.64(-10) 6.31	8.31(-11) -0.92	1.68(-10) -0.77	2.19(-10) -0.72	1.14(-9) -0.06

3 H – 2 D system		$p–H_3^+$ $p–D_2$	$p–H_3^+$ $o–D_2$	$o–H_3^+$ $p–D_2$	$o–H_3^+$ $o–D_2$	$p–H_2D^+$ HD	$o–H_2D^+$ HD	$p–D_2H^+$ $p–H_2$	$p–D_2H^+$ $o–H_2$	$o–D_2H^+$ $p–H_2$	$o–D_2H^+$ $o–H_2$
$p–H_3^+$	$p–D_2$	2.21(-11) -0.20	F	F	F	3.50(-9) -0.41	5.08(-9) -0.08	3.02(-10) -0.12	4.03(-10) 0.62	F	F
$p–H_3^+$	$o–D_2$	F	1.73(-11) -0.29	F	F	3.06(-10) 0.59	2.42(-10) 0.08	F	F	4.81(-10) -0.42	5.39(-10) 0.06
$o–H_3^+$	$p–D_2$	F	F	3.14(-11) 0.29	F	F	8.02(-10) 0.09	F	7.50(-10) -0.10	F	F
$o–H_3^+$	$o–D_2$	F	F	F	2.38(-11) -0.63	F	5.59(-10) 2.49	F	F	F	1.03(-9) -0.86
$p–H_2D^+$	HD	7.83(-12) 237.8	9.48(-12) 146.6	F	F	2.08(-10) -0.50	2.84(-10) 88.5	4.12(-10) -0.50	1.89(-10) 33.1	7.32(-10) 0.30	1.93(-10) -0.64
$o–H_2D^+$	HD	2.52(-12) 150.1	3.88(-12) 65.1	6.80(-12) 181.7	1.03(-10) 96.8	8.64(-11) -0.38	4.66(-10) 1.38	6.41(-11) 0.22	3.02(-10) -0.60	1.49(-10) -0.9	5.24(-10) -0.56
$p–D_2H^+$	$p–H_2$	2.02(-10) 355.0	F	F	F	3.26(-10) 137.3	4.49(-10) 231.4	1.73(-9) -0.01	7.09(-10) 168.8	F	F
$p–D_2H^+$	$o–H_2$	F	F	2.65(-11) 233.9	F	7.33(-11) 1.58	5.94(-10) 54.6	2.84(-10) -0.58	1.35(-9) -0.10	F	F
$o–D_2H^+$	$p–H_2$	F	1.56(-11) 325.2	F	F	3.48(-10) 193.6	4.61(-10) 281.7	F	F	1.72(-9) -0.05	4.16(-10) 171.1
$o–D_2H^+$	$o–H_2$	F	8.35(-12) 171.1	F	1.65(-11) 194.6	8.15(-11) 15.6	6.82(-10) 103.4	F	F	4.17(-10) -0.36	1.27(-9) -0.08

2 H – 3 D system		p–H$_2$D$^+$ p–D$_2$	p–H$_2$D$^+$ o–D$_2$	o–H$_2$D$^+$ p–D$_2$	o–H$_2$D$^+$ o–D$_2$	p–D$_2$H$^+$ HD	o–D$_2$H$^+$ HD	p–D$_3^+$ p–H$_2$	p–D$_3^+$ o–H$_2$	m–D$_3^+$ p–H$_2$	m–D$_3^+$ o–H$_2$	o–D$_3^+$ p–H$_2$	o–D$_3^+$ o–H$_2$
p–H$_2$D$^+$	p–D$_2$	4.42(-11) -0.43	4.82(-11) -1.01	F	F	6.78(-10) -0.23	5.41(-10) 0.85	1.69(-11) -0.64	F	F	F	1.41(-10) -1.05	F
p–H$_2$D$^+$	o–D$_2$	2.07(-11) 86.3	7.62(-11) -0.65	F	F	2.57(-10) -0.55	7.49(-10) 0.60	F	F	2.27(-10) -0.86	F	1.60(-10) 0.11	F
o–H$_2$D$^+$	p–D$_2$	F	F	8.14(-11) 1.48	3.93(-11) 0.21	6.64(-10) 0.20	5.39(-10) -0.44	F	1.48(-11) -0.62	F	F	F	1.31(-10) 0.18
o–H$_2$D$^+$	o–D$_2$	F	F	3.95(-11) 88.5	8.52(-11) 1.73	2.74(-10) -0.36	8.75(-10) 0.53	F	F	F	1.63(-10) -1.57	F	8.01(-11) -0.94
p–D$_2$H$^+$	HD	1.54(-11) 145.5	1.17(-11) 57.0	9.47(-11) 237.3	4.68(-11) 146.2	6.53(-10) -0.73	3.36(-10) 1.80	1.45(-11) -0.69	4.09(-11) -0.71	F	F	1.09(-10) -0.78	3.70(-10) 0.52
o–D$_2$H$^+$	HD	7.83(-12) 202.2	2.12(-11) 107.6	3.59(-11) 285.1	7.79(-11) 196.7	2.90(-10) 48.3	7.54(-10) 0.04	F	F	1.36(-10) -0.15	2.07(-10) -0.10	1.10(-10) -0.27	2.84(-10) -0.38
p–D$_3^+$	p–H$_2$	2.21(-10) 379.2	F	F	F	1.77(-9) 225.2	F	1.69(-9) 0.00	F	F	F	F	F
p–D$_3^+$	o–H$_2$	F	F	3.00(-10) 286.7	F	1.69(-9) 52.3	F	F	1.59(-9) -0.41	F	F	F	F
m–D$_3^+$	p–H$_2$	F	1.65(-10) 344.9	F	F	F	9.57(-10) 239.3	F	F	1.69(-9) 0.00	F	F	F
m–D$_3^+$	o–H$_2$	F	F	F	1.90(-10) 262.7	F	1.53(-9) 65.6	F	F	F	1.68(-9) 0.00	F	F
o–D$_3^+$	p–H$_2$	1.07(-10) 393.9	7.85(-11) 296.9	F	F	9.43(-10) 237.4	6.89(-10) 189.7	F	F	F	F	1.69(-9) 0.00	F
o–D$_3^+$	o–H$_2$	F	F	1.53(-10) 303.8	9.60(-11) 213.6	9.06(-10) 66.2	7.70(-10) 17.0	F	F	F	F	F	1.30(-9) -1.47

1 H – 4 D system		p–D_2H^+ p–D_2	p–D_2H^+ o–D_2	o–D_2H^+ p–D_2	o–D_2H^+ o–D_2	p–D_3^+ HD	m–D_3^+ HD	o–D_3^+ HD
p–D_2H^+	p–D_2	2.45(-10) -0.19	5.16(-11) 0.10	4.36(-11) 3.11	1.42(-10) 1.31	8.94(-11) -1.00	F	8.23(-10) -0.13
p–D_2H^+	o–D_2	3.74(-11) 85.9	1.62(-10) 0.29	1.05(-10) 35.6	9.12(-11) 3.65	7.44(-11) 0.11	2.93(-10) 0.16	7.59(-10) -0.52
o–D_2H^+	p–D_2	3.64(-11) 50.0	1.92(-10) -0.70	9.40(-11) -0.33	1.11(-10) -0.50	6.87(-11) -0.85	2.77(-10) -0.76	6.52(-10) 0.90
o–D_2H^+	o–D_2	5.75(-11) 137.7	7.31(-11) 50.3	4.28(-11) 85.5	2.24(-10) -0.85	F	5.82(-10) -0.08	5.81(-10) 0.40
p–D_3^+	HD	2.77(-10) 229.7	2.24(-10) 144.8	1.50(-10) 182.0	F	6.91(-10) 0.00	F	7.75(-10) 0.00
m–D_3^+	HD	F	1.08(-10) 206.7	8.74(-11) 251.3	2.65(-10) 154.3	F	1.41(-9) -0.25	5.97(-10) 46.3
o–D_3^+	HD	1.40(-10) 247.4	1.63(-10) 160.5	1.08(-10) 198.4	1.20(-10) 105.2	9.16(-11) 15.5	2.46(-10) -0.23	1.17(-9) -0.18

5 D system		p–D_3^+ p–D_2	p–D_3^+ o–D_2	m–D_3^+ p–D_2	m–D_3^+ o–D_2	o–D_3^+ p–D_2	o–D_3^+ o–D_2
p–D_3^+	p–D_2	4.03(-10) -0.24	F	F	F	4.61(-10) -0.29	4.75(-10) 0.54
p–D_3^+	o–D_2	F	5.56(-10) -0.77	4.00(-10) 21.7	F	5.34(-10) 68.9	6.18(-10) -0.77
m–D_3^+	p–D_2	F	8.37(-11) -0.61	4.87(-10) -0.37	1.48(-10) -0.49	1.11(-10) 46.6	6.12(-10) 0.45
m–D_3^+	o–D_2	F	F	2.14(-10) 84.7	1.27(-9) -0.32	1.63(-10) 130.5	6.66(-10) 45.8
o–D_3^+	p–D_2	5.37(-11) 15.2	4.49(-11) -0.23	4.47(-11) -0.26	5.64(-11) 0.72	5.76(-10) -0.10	5.87(-10) -0.19
o–D_3^+	o–D_2	2.51(-11) 99.5	7.74(-11) 15.3	3.21(-10) 38.3	2.78(-10) -0.47	3.24(-10) 85.2	9.70(-10) -0.39

CHAPTER 4

Overtone spectroscopy of H_2D^+ and D_2H^+ using laser induced reactions

O. Asvany, E. Hugo, F. Müller, F. Kühnemann, S. Schiller, J. Tennyson and
S. Schlemmer

The method of laser induced reaction (LIR) is used to obtain high-resolution IR spectra of H_2D^+ and D_2H^+ in collision with n-H_2 at a nominal temperature of 17 K. For this purpose three cw-laser systems have been coupled to a 22-pole ion trap apparatus, two commercial diode laser systems in the range 6100-6600 cm^{-1} and 6760-7300 cm^{-1}, respectively, and a high power optical parametric oscillator (OPO) tunable in the range of 2600-3200 cm^{-1}. In total, 27 new overtone and combination transitions have been detected for H_2D^+ and D_2H^+, as well as a weak line in the ν_1 vibrational band of H_2D^+ ($2_{20} \leftarrow 1_{01}$) at 3164.118 cm^{-1}. The line positions are compared to high accuracy *ab initio* calculations, showing small but mode-dependent differences, being largest for three vibrational quanta in the ν_2 symmetric bending of H_2D^+. Within the experimental accuracy, the relative values of the *ab initio* predicted Einstein *B* coefficients are confirmed.

4.1 INTRODUCTION

The smallest polyatomic molecule, H_3^+, has since long fascinated chemical theorists, spectro-scopists and astronomers due to its apparent simplicity and importance in astrochemical environments. This molecule, in which the 3 protons are held together in a triangle by a distributed cloud of two electrons (three center-two electron bonding), has first been observed spectroscopically in the laboratory by Oka in 1980 [1], and since then a wealth of laboratory studies has been conducted, including fundamental, overtone, combination and hot bands [2].

For the investigation of cold interstellar clouds, the deuterated versions of H_3^+, H_2D^+ and D_2H^+, are of even greater importance, first because they are known to drive deuteration processes in these environments by ion-molecule exchange reactions [3], leading to a wealth of deuterated species [4]. Even multiply deuterated molecules have been discovered in prestellar cores (see for example [5–10]), suggesting the importance of D_3^+ in such environments [11]. Secondly, the H_2D^+ and D_2H^+ ions posses a permanent dipole moment and can thus be detected by their rotational lines. Although the 1_{10} - 1_{11} line of ortho-H_2D^+ was detected in the laboratory in 1984 [12–14], it took a longsome search until the H_2D^+ ion was observed 1999 in the interstellar medium [15], and five years later also the submillimeter detection of D_2H^+ was reported [16]. Since then, the 372 GHz-line of H_2D^+ has been used routinely to probe the conditions in cold clouds [17–19], whereas the D_2H^+ detection is the only one so far.

Owing to their fundamental importance, there is a 25 year history of laboratory infrared spectroscopy of H_2D^+ and D_2H^+. The first few fundamental lines of H_2D^+ were observed by Shy et al. [20] who used a Doppler-tuned fast ion beam method but gave no specific rotational assignments. Assignments were made as part of subsequent, more comprehensive cell discharge measurements of the ν_2 and ν_3 vibrational bands by Foster et al. [21], while the ν_1 band was measured by Amano and coworkers [22, 23]. The corresponding results for the D_2H^+ molecule were reported shortly thereafter [24, 25] by those two groups. The first detection of overtone and combination bands was reported by Fárník et al. [26] who detected the $2\nu_2$, $2\nu_3$ and $\nu_2 + \nu_3$ bands of H_2D^+ and D_2H^+ in a cold supersonic jet. As these light molecules cannot be described very well by the Born-Oppenheimer-approximation, and also due to strong Coriolis coupling in the D_2H^+ ion, that study was guided by and compared to high-level *ab initio* theoretical predictions.

Computational *ab initio* procedures have been developed in recent decades to provide highly accurate level predictions for few electron systems. For diatomics such as HD^+ the computations can reach an accuracy far better than 10^{-3} cm^{-1} [27, 28] and experiments using sympathetically cooled ions have been carried out to test those predictions [29, 30]. For the electronically simplest triatomic, H_3^+ and its isotopologues, the predictions reach 'only' near-spectroscopic accuracy of better than 0.1 cm^{-1} [26, 31]. This accuracy is still one order of magnitude better than can be obtained for a many-electron system such as water [32].

For triatomics the high-accuracy *ab initio* calculation of molecular vibration-rotation spectra involves the use of variational nuclear motion calculations [33] and a high accuracy potential energy surface. For the H_3^+ system, Cencek et al. [34] calculated a potential energy surface with

an absolute accuracy of 0.04 cm^{-1}. They also computed an electronic relativistic correction for this surface, although this only has a very minor influence on the spectrum. Of more significance are corrections due to failure of the Born-Oppenheimer approximation [35–37]. Polyansky and Tennyson [38] developed a high-accuracy model based on the *ab initio* calculations of Cencek et al., including in particular a refit of their adiabatic correction, and a model of non-adiabatic effects based on the use of the effective vibrational masses obtained by Moss for the H_2^+ system [39]. The predictive nature of this model has been tested by Fárník et al. [26] and, more recently, by Hlavenka et al. [40] for H_2D^+ and D_2H^+ ions, respectively. Given their greater sensitivity to corrections to the Born-Oppenheimer approximation [35, 36], the deuterated isotopologues provide a particularly stringent test of the theory.

For astronomical studies it is important to have accurate line positions as well as reliable transition intensities. Although such studies are based on experimental line positions (e.g. [41]), they have to rely on *ab initio* predictions of the transition strength (e.g. [42]). There is considerable indirect evidence that these transition strengths are indeed reliable, but the measurements by Fárník et al. [26] raised some doubts about this issue. Extensive tests on the theory [43] failed to identify any significant errors. Therefore, testing the reliability of the linestrength predictions is one of the objectives of the present study.

This work uses the technique of laser induced reactions (LIR) to obtain high-resolution overtone spectra of H_2D^+ and D_2H^+. In contrast to the direct absorption spectroscopy methods listed above, the transitions are detected by the action of the laser light on the ion species, as for example an induced chemical reaction with n-H_2 (see below). Several examples of the feasibility of this approach for H_3^+ isotopomers have already been published [44–46]. This work is organized as follows: The spectroscopic aspects of LIR are summarized and an introduction is given to the low-temperature 22-pole trapping apparatus, as well as the three laser systems used in this work. In the results section the measured overtone line positions are summarized for H_2D^+ and D_2H^+ and also some new data for the ν_1 transition of H_2D^+ are shown. These experimental results are then compared to the theoretical *ab initio* predictions, line positions as well as Einstein B coefficients. Furthermore, the measured Doppler widths and the influence of Coriolis coupling and Fermi resonances are discussed. The present work provides basic spectroscopic tools to probe the rotational level population of the presented ions, which will be the topic of a follow-up publication [47].

4.2 EXPERIMENTAL ASPECTS

4.2.1 Laser induced reactions (LIR) of H_2D^+ and D_2H^+

LIR belongs to the family of "action spectroscopy" methods where the influence of the laser light on the mass-selected ions investigated is monitored by detecting changes induced to the trapped ion cloud composition. Detection is usually achieved very efficiently using an ion counter. In the special case of LIR, changes of the rate of an endothermic ion-molecule reaction

serve to detect the excitation of the parent ionic species. This offers not only the possibility of doing very high sensitivity spectroscopy on transient ions (a number of only 1000 ions per trapping period is sufficient), but LIR can also yield, for example, information on state-selected reaction rate coefficients, inelastic collision rate coefficients, lifetimes of excited states, or the population of rotational states.

Recent examples of this method include the IR spectroscopy of the highly fluxional CH_5^+ molecule [48–50], the laser induced charge transfer in the system N_2^+ + Ar [51], and the spectroscopy of the infrared active stretching and bending motions [52–54] of $C_2H_2^+$ via the abstraction reaction $C_2H_2^+ + H_2 \rightarrow C_2H_3^+ + H$. In this latter scheme, the endothermicity of about 50 meV (= 403 cm^{-1}) is overcome by the rovibrational energy of the laser excited molecule. More recently, also the overtone spectroscopy and the corresponding population and temperature diagnostic has been demonstrated for H_3^+ in reaction with Ar atoms at a nominal temperature of 50 K [44], and a similar work has been carried out for D_2H^+ [45].

Here the lowest rotational states of H_2D^+ and D_2H^+ are probed by exciting their overtone and combination transitions and also using the v_1 band for H_2D^+. While the fundamental v_1 band is well studied [22, 23, 31, 55], and the states of H_3^+ have been explored up to high levels of excitation [2], the experimental search for overtone/combination rovibrational transitions of H_2D^+ and D_2H^+ has only recently started [26]. In the following, the basic processes of interest for the spectroscopic aspects of LIR are summarized with help of Figure 4.1 for H_2D^+, but are similar for D_2H^+. For LIR of H_2D^+, the exchange reaction

$$H_2D^+ + H_2 \xrightarrow{k} H_3^+ + HD \tag{4.1}$$

is used. This reaction is endothermic by about 232 K for H_2D^+ in the lowest rotational state 0_{00} and about 146 K for the the 1_{11} ortho state (see the dashed line in the Figure), and its overall rate coefficient k has been measured to be small at low temperatures. Adams and Smith [56] measured a value of 2.9×10^{-10} cm^{3}s^{-1} for the reaction with n-H_2 at 80 K, and Gerlich et al. [3] obtained a value of 4.9×10^{-11} cm^{3}s^{-1} at a nominal temperature of 10 K. The slowness of this reaction at low temperatures renders LIR-spectroscopy feasible by first exciting the ion (with rate R), starting from the ground vibrational level $(0,0,0)$

$$H_2D^+((0,0,0),J''K_a''K_c'') + \hbar\omega_1 \xrightarrow{R} H_2D^+((v_1',v_2',v_3'),J'K_a'K_c') \tag{4.2}$$
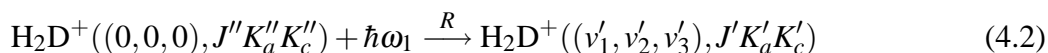
into a particular ro-vibrational level. Here, (v_1',v_2',v_3') indicate the quanta in the three vibrational modes of H_2D^+. Once excited, the H_2D^+ ion can react much faster with a H_2 target molecule (with rate coefficient $k^* > k$),

$$H_2D^+((v_1',v_2',v_3'),J'K_a'K_c') + H_2 \xrightarrow{k^*} H_3^+ + HD \ , \tag{4.3}$$
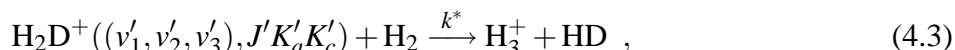
leading to an enhancement in the counts of H_3^+ product ions. Thus, by counting these product ions as a function of the laser wavelength, a LIR-spectrum is obtained. For maximal signal

counts in the L$_{IR}$-experiment, the collision rate with the neutral reaction partner H_2 should be similar to the decay rate A of the excited H_2D^+ ion:

$$k_c \cdot [H_2] \geq A \ . \tag{4.4}$$

In the above relation, $[H_2]$ is the number density of the neutral reaction partner (given in cm^{-3}). The rate coefficient k_c for the collision of H_2D^+ with H_2 can be assumed to be the Langevin rate coefficient k_L, which is calculated to be $k_c \approx k_L = 1.80 \times 10^{-9}$ $cm^3 s^{-1}$ (1.74×10^{-9} $cm^3 s^{-1}$ for D_2H^+).
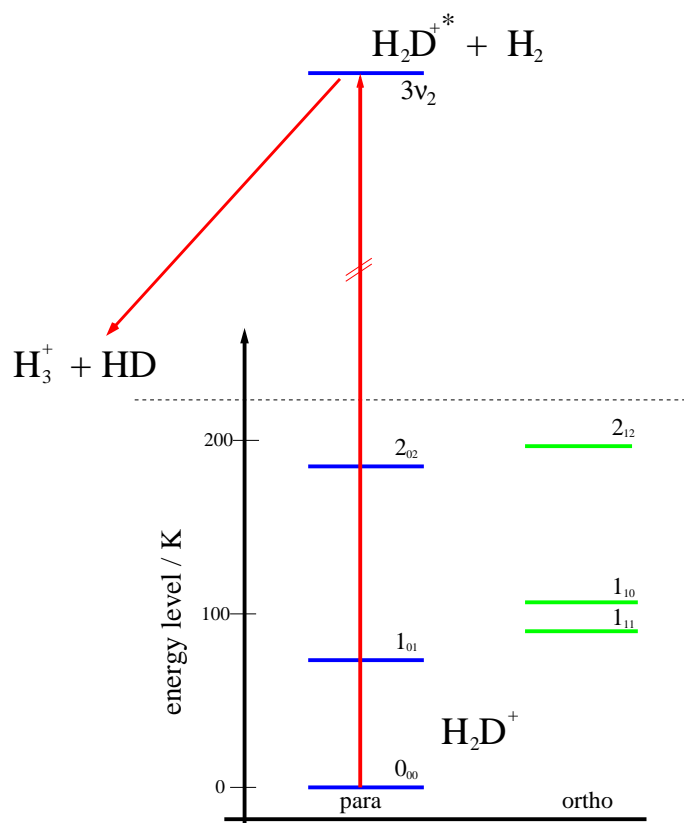
Figure 4.1: L$_{IR}$-spectroscopy exploits the change in speed of an ion-molecule reaction to detect the excitation of the ion involved. For the spectroscopy of H_2D^+ the collision with H_2, reaction (4.1), leading tho the ionic product H_3^+ is used. This reaction is endothermic by 232 K as indicated by the dashed line. As only the lowest rotational levels of H_2D^+ are populated at the low temperature of the experiment, the reaction is initially slow. Its speed can be substantially increased by exciting the ion prior to collision with the H_2 molecule.

4.2.2   22-pole ion trap apparatus

The experimental procedure is described using the setup shown in Fig. 4.2. The central part of this apparatus is a 22-pole ion trap which has been described in detail by Gerlich [57, 58]. The H_2D^+ parent ions are generated in the storage ion source by ionization of hydrogen gas containing D_2 admixtures of several percent (5-15%). All H_3^+ isotopologues are produced by reactions of the type $H_2^+ + H_2 \rightarrow H_3^+ + H$ and subsequent exchange reactions with the neutral gas. The ionization energy is kept at about 22 eV to allow for an efficient production of the parent ions. By trapping the ions in the source, the pressure of the precursor gas mixture can be kept below 10^{-5} mbar and the produced cations are cooled to the source temperature of 350 K by collisions. Low source pressures are essential for this type of experiment because gases leaking into the trap region would disturb the chemistry there.

The first mass filter is operated in a mode to admit only ions with masses greater than 3 u (i.e. H_2D^+, (D_2^+), D_2H^+ and D_3^+) into the 22-pole ion trap. This allows spectroscopy to be performed on all of the admitted ions simultaneously. D_2^+ impurities, with mass 4 u, react very fast to form H_3^+ isotopologues in the hydrogen environment of the trap. Usually the average number of H_2D^+ ions injected into the 22-pole trap is about 700. The trap is driven by a RF power of 17 MHz frequency and about $V_0 = 15$ V amplitude. In its field, the ion cloud is typically stored for 1 s embedded in a cold n-H_2 gas environment and exposed to the tunable IR light. The number density of H_2 (commercial grade 6.0) is about 5×10^{10} cm^{-3} to offer enough collision possibilities with the excited H_2D^+ within their lifetime. The trap temperature is kept at its lowest possible value. The closed cycle helium refrigerator to which the trap setup is mounted has a nominal temperature of 10 K at its tip. A temperature of (17 ± 1) K is measured with a silicon diode sensor at the trap housing on the opposite side of the cold head tip.

After the storage period, the content of the trap is extracted, mass selected in the second quadrupole mass filter and the ionic reaction product H_3^+ is counted in the Daly-type ion detector. The experiment is run in a shot-by-shot mode, i.e. the laser is tuned to the next frequency step and the process of *trapping/irradiation/reaction/detection* is repeated again, by which a spectrum is recorded. The shots can be repeated several times at the same frequency to improve the S/N ratio.

4.2.3   Laser systems

Two different laser systems have been used for the experiment. The first set of lasers were Agilent 8164A diode laser controllers with diode laser modules 81642A and 81480A operating in the frequency range of 6097 - 6622 cm^{-1} (1510-1640 nm) and 6757 - 7299 cm^{-1} (1370-1480 nm), respectively. The output power was varying over the frequency ranges with a maximum of about 5.5 mW. The diodes could be tuned and computer controlled with a precision of 0.0001 nm (i.e. about 0.0005 cm^{-1} = 15 MHz). The intrinsic linewidth of the lasers is specified to about 100 kHz, but exhibits broadening to several MHz due to frequency jitter.
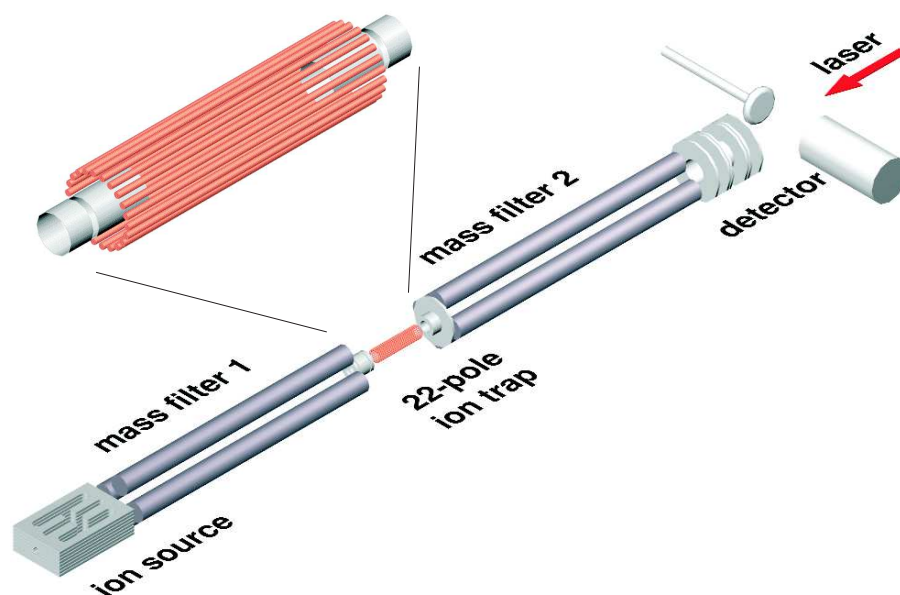
Figure 4.2: Schematic setup of the trapping apparatus as used for Laser Induced Reactions (LIR). The ions are generated and collected in the **storage ion source**, mass selected in the quadrupole **mass filter 1** and then stored in the **22-pole ion trap**. This trap, consisting of 22 RF-electrodes forming a cylindrical structure (see inset), is mounted on a closed cycle helium refrigerator. On entrance the ions are cooled down to the ambient cryogenic temperature by a short intense pulse of cold He atoms. During the storage period of typically one second, the ions are subject to reactant gas molecules and tunable **laser** light (coming from the right through the axially transparent setup). The result of this interaction is detected by extracting the stored ion cloud into **mass filter 2** and counting the number of product ions in the **detector**. By repeating this process while scanning the IR laser, an IR action spectrum of the stored parent ions is recorded.

The calibration of the diode lasers were first checked with two Burleigh wavemeters of the type WA-1500. As these calibrations turned out to be insufficient, the Agilent lasers have been compared to H_2O and CO_2 absorption lines which are tabulated with a precision better than 0.001 cm^{-1} in the HITRAN database [59]. In total, the laser line positions measured in this work are accurate within 0.002 cm^{-1}. The laser light was sent via an optic fiber to the laser table of the trapping machine, where it was steered via a collimator, a CaF_2 lens, a flip mirror and a differentially pumped vacuum window [60] into the 22-pole ion trap, see Fig. 4.3. No nitrogen flushing was necessary on the short path of the laser table, as the water absorptions in the investigated frequency regions are quite weak.

The second laser system used in the experiments was a optical parametric oscillator (OPO) operating in the 3 μm region. This OPO is a homemade high-power tunable cw system in
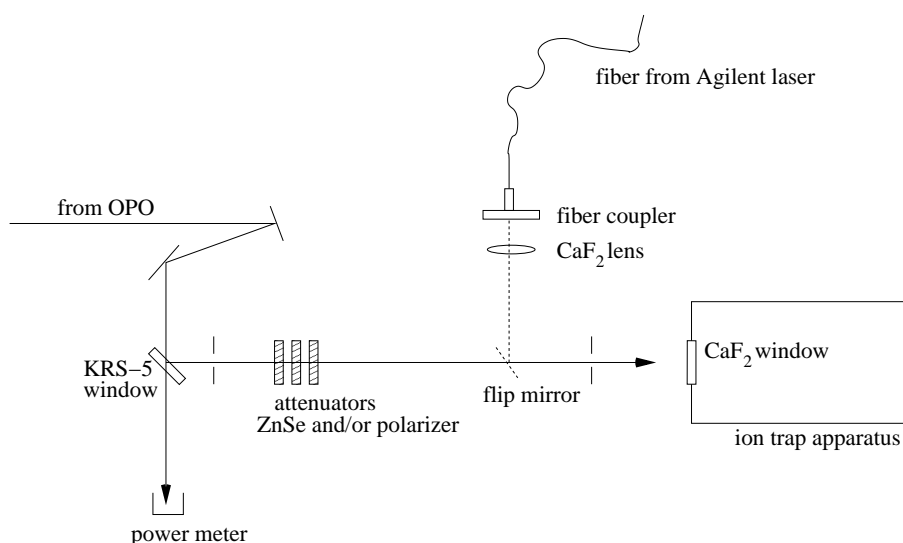
Figure 4.3: Setup of optical components on the laser table attached to the trapping machine. A flip mirror mount allowed to change between the laser light of the commercial Agilent diode lasers and the homemade OPO system. As the OPO power is quite high (up to 50 mW), several attenuators (ZnSe windows, a KRS-5 window and a polarizer) have been used to weaken the laser power to levels below 1 mW. By means of the KRS-5 window the beam is split and the relative power is measured.

which photons from a pump YAG-laser at about $\omega_p = 9394$ cm^{-1} (1064 nm) are split in a PPLN (periodically poled lithium niobate) crystal into signal and idler photons according to $\omega_s + \omega_i = \omega_p$ [61]. The idler beam of the OPO is tunable in the range 2600 - 3200 cm^{-1} and can reach a maximum power of 50 mW. For high precision determination of the lines two Burleigh wavemeters have been used to measure simultaneously the frequencies of the pump and signal beam, giving an accuracy of about 0.003 cm^{-1}. Where lower accuracy was required only one wavemeter was used to measure the signal beam, assuming the pump frequency did not vary appreciably. As shown in Fig. 4.3, a KRS-5 window was used as a beam splitter to send about 13% of the laser power to the 22-pole trapping apparatus and the remaining 87% into a power meter. The idler beam could be further attenuated to sub-mW power levels by additional beam inserts.

The OPO has a short-term intrinsic linewidth of some kHz and a stability of several MHz during the trapping time of 1 s [61], which is much smaller than the Doppler width $\sigma_D = 70$ MHz of the corresponding transitions (see following sections). Problems arose initially due to mode hops of the OPO system, rendering the spectroscopy difficult. This problem was solved by the data acquisition software, which rejected any data points when the wavemeters indicated frequency jumps during trapping time.

4.3 *Ab initio* PREDICTIONS

The line positions and corresponding wavefunctions were calculated using the model of Polyansky and Tennyson [38]. Nuclear motion calculations were performed in Jacobi coordinates with the DVR3D program suite [62] and used basis sets optimized for previous studies [43]. Einstein *A* coefficients were calculated using the *ab initio* dipole surfaces of Röhse et al. [37].

Variational nuclear motion calculations only use the rigorous quantum numbers of the system, for H_2D^+ and D_2H^+ these are the total rotational angular momentum J, parity p, and the nuclear spin state (ortho or para). Here approximate vibrational, (v_1, v_2, v_3), and rotational, (K_aK_c), quantum numbers were assigned by hand based on a simple analysis of the energy patterns in the two systems. This procedure is not general and can be hard to apply for H_2D^+ and D_2H^+ as they show strong Coriolis effects which leads to strong mixing between vibrational states. However, the present experiments were performed at very low temperatures meaning that only states starting from the $J = 0$, 1 and 2 states of the vibrational ground states needed to be considered. For these low-*J* states the sparsity of levels means that the assignments could be made unambiguously. The systematic errors shown by different bands which are discussed below (section 4.4.2) acts as confirmation that this assignment procedure is indeed correct.

4.4 RESULTS AND DISCUSSION

4.4.1 Detection of H_2D^+ and D_2H^+ transitions

Second overtone and combination bands

The H_2D^+ transitions were measured by applying LIR to reaction (4.1), while the laser excited D_2H^+ ions were detected by counting the same product ion (H_3^+) of the similar reaction

$$D_2H^+ + H_2 \rightarrow H_3^+ + D_2 \ , \tag{4.5}$$

in which the excited D_2H^+ ion transfers a proton to the hydrogen molecule. These LIR-schemes have proven to work well in a previous study in which the fundamental bands v_2 and v_3 of H_2D^+ and D_2H^+ have been excited by the powerful free-electron laser FELIX [46]. That the respective ions are indeed responsible for the increase of H_3^+ counts in their LIR-spectra has been checked by mass spectrometric means in selected cases. For the line detections the density of the H_2 reactant was about 4×10^{10} cm^{-3}, the trapping time was between 1 and 2 s, and the laser power varying from 1.5 to 5.5 mW. The trap was kept at its lowest nominal temperature of about 17 K. Therefore, only transitions starting from the lowest rotational levels of H_2D^+ (see Fig. 4.1) and D_2H^+ could be expected. The detections were guided by high accuracy *ab initio* calculations, from which the strongest transitions falling into the wavelength range of the lasers have been selected for the search. As an example, the strongest transitions detected for H_2D^+ ($(0,2,1)$ $1_{11} \leftarrow 0_{00}$) and one weak transition for D_2H^+ ($(1,1,1)$ $0_{00} \leftarrow 1_{01}$)
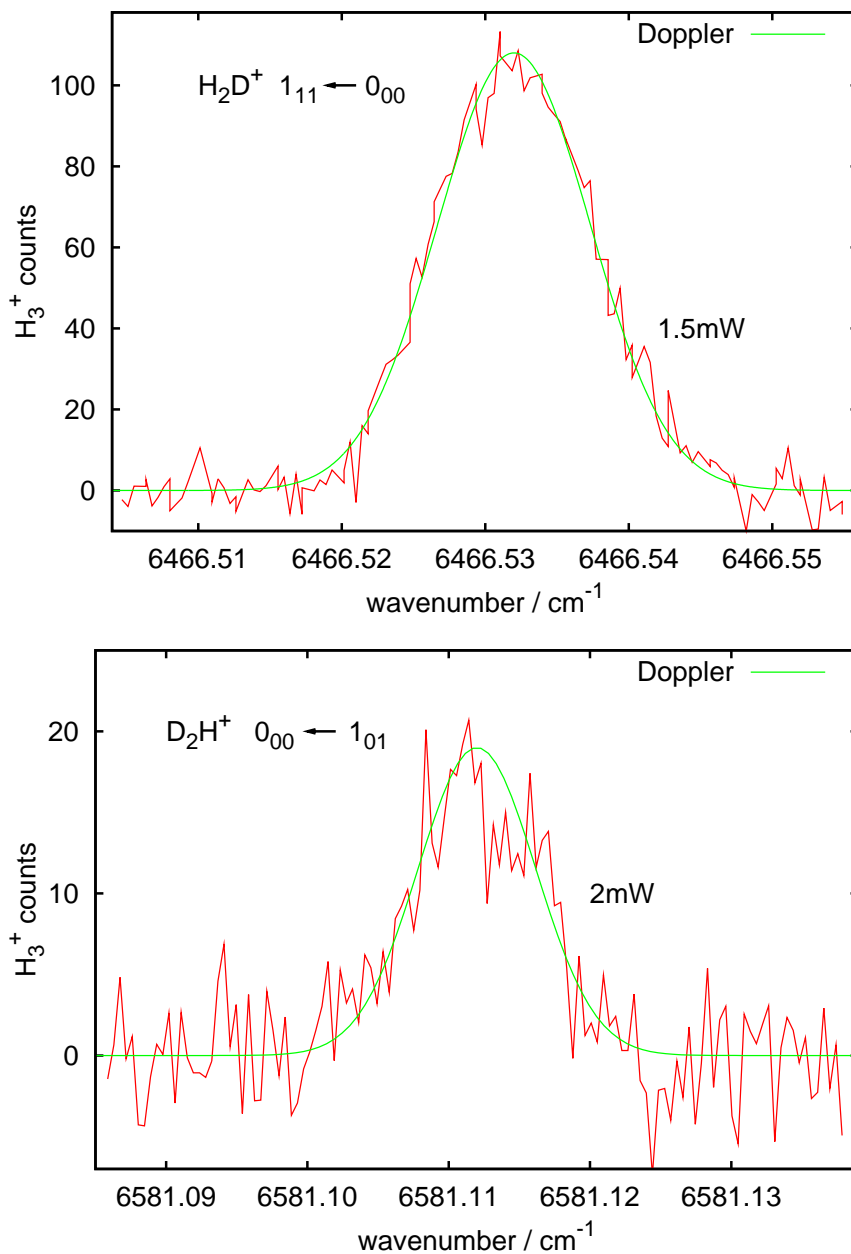
Figure 4.4: Two representative combination band transitions measured with the Agilent diode laser, the strongest peak for H_2D^+ at $6466.532\,\mathrm{cm^{-1}}$ ($(0,2,1)\ 1_{11} \leftarrow 0_{00}$), and one of the weakest peaks measured for D_2H^+ at $6581.112\,\mathrm{cm^{-1}}$ ($(1,1,1)\ 0_{00} \leftarrow 1_{01}$). The storage times were 1.5 and 2 s, respectively, and the laser power is indicated in the figures. The constant H_3^+ background count of several hundred ions per trap filling has been subtracted. The H_2D^+ peak shape follows a Doppler profile, yielding a fitted kinetic temperature of (27 ± 2) K.

Table 4.1: Second overtone and combination transitions of H_2D^+ (in cm^{-1}) detected with the diode laser systems. The overall experimental accuracy is about 0.002 cm^{-1}. The *ab initio* transition wavenumbers and Einstein A_{ul} coefficients (in s^{-1}) are taken from a line list [63] which was calculated according to the procedures described in [38]. From this list, the lifetimes of the upper states $\tau = 1/A_{tot}$ were determined. Also, the Einstein B_{lu} coefficients have been calculated from the A_{ul} according to equation (4.8) and normalized to the strongest transition at 6466.532 cm^{-1}.

transition		this work	calc	A_{ul}	A_{tot}	g_u/g_l	B_{lu}
(0,3,0)	$0_{00} \leftarrow 1_{01}$	6241.966	6242.121	7.08	154.7	1/3	0.21
(0,3,0)	$1_{11} \leftarrow 1_{10}$	6270.392	6270.544	2.13	156.9	3/3	0.19
(0,3,0)	$1_{10} \leftarrow 1_{11}$	6303.784	6303.941	3.36	154.5	3/3	0.29
(0,3,0)	$1_{01} \leftarrow 0_{00}$	6330.973	6331.127	1.21	158.7	3/1	0.31
(0,2,1)	$0_{00} \leftarrow 1_{11}$	6340.688	6340.778	9.36	268.1	1/3	0.27
(0,2,1)	$1_{01} \leftarrow 1_{10}$	6369.460	6369.557	6.04	267.4	3/3	0.51
(0,2,1)	$1_{10} \leftarrow 1_{01}$	6433.742	6433.833	4.64	270.3	3/3	0.38
(0,2,1)	$2_{02} \leftarrow 1_{11}$	6459.036	6459.133	2.47	269.8	5/3	0.34
(0,2,1)	$1_{11} \leftarrow 0_{00}$	6466.532	6466.635	4.10	271.6	3/1	1
(0,2,1)	$3_{03} \leftarrow 2_{12}$	6483.576	6483.681	3.86	282.7	7/5	0.44
(0,2,1)	$2_{12} \leftarrow 1_{01}$	6491.349	6491.451	4.49	266.8	5/3	0.60
(0,2,1)	$2_{21} \leftarrow 1_{10}$	6573.837	6573.925	3.64	280.7	5/3	0.47
(0,2,1)	$2_{20} \leftarrow 1_{11}$	6589.412	6589.505	2.49	280.9	5/3	0.32
(1,2,0)	$0_{00} \leftarrow 1_{01}$	6945.877	6945.868	10.25	105.2	1/3	0.22
(1,2,0)	$1_{11} \leftarrow 1_{10}$	6974.252	6974.253	5.54	117.0	3/3	0.36
(1,2,0)	$1_{10} \leftarrow 1_{11}$	7004.803	7004.794	5.10	105.5	3/3	0.33
(1,2,0)	$1_{01} \leftarrow 0_{00}$	7039.362	7039.366	3.72	121.4	3/1	0.70
(1,2,0)	$2_{12} \leftarrow 1_{11}$	7066.839	7066.878	3.60	191.0	5/3	0.37
(1,2,0)	$2_{02} \leftarrow 1_{01}$	7077.529	7077.560	4.05	170.9	5/3	0.42
(1,2,0)	$2_{11} \leftarrow 1_{10}$	7105.518	7105.505	3.38	129.9	5/3	0.35

Table 4.2: Second overtone and combination transitions of D_2H^+, for explanations see Table 4.1. For comparison, also two transitions measured by cw-CRDS [40, 45] are listed. The values of the Einstein A_{ul} coefficients given here are about three times smaller than those for H_2D^+, making the detection of D_2H^+ somewhat more difficult. The Einstein B_{lu} coefficients are given relative to the transition at 6536.319 cm^{-1}.

transition		this work	Ref [40]	calc	A_{ul}	A_{tot}	g_u/g_l	B_{lu}
(1,2,0)	$1_{01} \leftarrow 1_{10}$	6466.936		6466.916	2.41	160.9	3/3	0.49
(1,2,0)	$1_{11} \leftarrow 0_{00}$	6482.033		6482.011	0.53	149.6	3/1	0.32
(1,2,0)	$2_{20} \leftarrow 1_{11}$	6518.523		6518.511	1.88	151.1	5/3	0.62
(1,0,2)	$1_{10} \leftarrow 1_{01}$	6524.010		6523.987	1.27	165.2	3/3	0.25
(1,2,0)	$2_{12} \leftarrow 1_{01}$	6535.953	6535.950	6535.943	2.28	157.4	5/3	0.75
(1,0,2)	$1_{11} \leftarrow 0_{00}$	6536.319	6536.319	6536.301	1.68	171.1	3/1	1
(1,1,1)	$0_{00} \leftarrow 1_{01}$	6581.112		6581.141	4.35	255.1	1/3	0.28

are shown in Fig. 4.4. To increase the S/N ratio, the scan was repeated 10 times for the strong H_2D^+ signal, while averaging over 30 scans was necessary for the D_2H^+ peak shown. The background of H_3^+ ions has been subtracted in both cases. The good S/N ratio for most of the measured peaks allowed their relative positions to be determined to better than 10^{-3} cm^{-1}, but the total accuracy was limited by the calibration of the diode lasers with an accuracy better than 2×10^{-3} cm^{-1} (see experimental section). A total of 20 H_2D^+ and 7 D_2H^+ lines have been detected which are summarized in Tables 4.1 and 4.2 together with their assignments. Also given in the Tables are the *ab initio* computed transition wavenumbers and the Einstein A_{ul} coefficients (u=upper, l=lower) [63]. The total decay constants $A_{tot} = \sum_l A_{ul}$ of the upper states have also been calculated from a comprehensive list of such transitions. While A_{ul} characterizes the decay of the excited ion back into the specific state where it came from, A_{tot} gives the overall decay rate of the upper state. More interesting in the case of LIR is the effective decay constant A_{eff}, specifying the time the excited ion needs to cascade back into the ground vibrational state:

$$A_{ul} < A_{eff} < A_{tot} \ . \tag{4.6}$$

For the transitions summarized in Tables 4.1 and 4.2, the effective decay constants A_{eff} of the corresponding upper states have been calculated by solving a complete rate equation system including all relevant rovibrational energy levels. This procedure is similar to that described by Kreckel et al. [64]. By solving the rate equations, an effective decay constant A_{eff} between 25 and 35 s^{-1} has been determined for various upper levels of both species. This quantity is an important parameter in LIR as to guarantee that the excited ions meet a H_2 reaction partner before fluorescing back to the vibrational ground state, see relation (4.4). For example, a H_2

Table 4.3: Transitions (in cm^{-1}) of the (1,0,0) band of H_2D^+ detected with the OPO system, for further explanations see Table 4.1. The accuracy of the OPO-measurements using two wavemeters is 0.003 cm^{-1} and thus similar to the accuracy of Amano and coworkers [22, 23]. The *ab initio* calculated values [63] were published by Ramanlal and Tennyson [31].

transition	this work	Ref. [22]	calc	A_{ul}	A_{tot}	g_u/g_l	B_{lu}
$0_{00} \leftarrow 1_{01}$	2946.805	2946.802	2946.826	53.167	53.4	1/3	0.318
$1_{10} \leftarrow 1_{11}$	3003.279	3003.276	3003.304	27.509	53.4	3/3	0.466
$1_{01} \leftarrow 0_{00}$	3038.182	3038.177	3038.198	20.353	53.9	3/1	1
$2_{12} \leftarrow 1_{11}$	3068.850	3068.845	3068.860	20.088	54.3	5/3	0.532
$2_{02} \leftarrow 1_{01}$		3077.611	3077.626	24.757	54.8	5/3	0.650
$2_{11} \leftarrow 1_{10}$		3094.671	3094.690	19.302	54.6	5/3	0.64
$2_{20} \leftarrow 1_{01}$	3164.118		3164.149	1.5976	53.1	5/3	0.04

number density of at least 4×10^{10} cm^{-3} and a collision rate coefficient $k_c = 1.8 \times 10^{-9}$ $cm^3 s^{-1}$ for $H_2D^+ + H_2$, yields a collision rate of more than 72 s^{-1}, which is high enough to compete with the effective rate A_{eff} given above.

For H_2D^+, the measured transitions fall into three well separated vibrational overtone or combination bands, each of them containing at least two quanta in the ν_2 bending mode. It is interesting to note that the different character of these bands is mirrored in the decay constant A_{tot} (see the corresponding column in Table 4.1), as well as in the difference to the *ab initio* computed transition wavenumbers (section 4.4.2). The same is true for D_2H^+. The transition at 6581.112 cm^{-1}, the only one measured for the (1,1,1) band, has an upper level with a remarkably short lifetime, and it also exhibits a different offset to the calculated frequency values (see Fig. 4.6 lower) than the other D_2H^+ transitions. The rest of the D_2H^+ transitions belong to the (1,2,0) and (1,0,2) bands which are mixed by Fermi resonances (see section 4.4.3). Accordingly, their lifetimes A_{tot} show similar values.

ν_1 vibrational band

In a further series of experiments, the 3 μm cw-OPO laser system has been used for the spectroscopy of the ν_1 band of H_2D^+ and to evaluate the feasibility of probing the low-temperature rotational population. This band was detected 25 years ago by Amano and Watson [22, 23], and later partly reassigned by Kozin et al. [55]. Table 4.3 lists the 5 lines measured with the OPO laser and compares them to previous experimental and calculated values. The transitions from low rotational states presented here agree well with the results from Amano and Watson [22], while the calculated values from Ramanlal and Tennyson [31] seem to be systematically higher
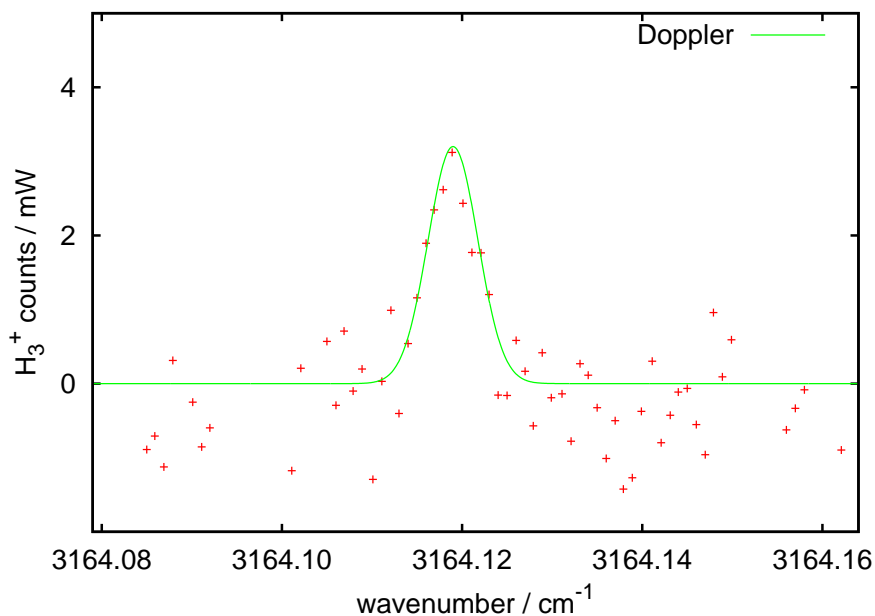
Figure 4.5: H_2D^+ transition in the ν_1 vibrational band ($2_{20} \leftarrow 1_{01}$) at 3164.118 cm^{-1} as measured with the OPO system. It was predicted by Ramanlal and Tennyson [31] to be at 3164.149 cm^{-1}. The detection of this weak transition was possible by exploiting the high cw-power of 24 mW at this frequency. The Doppler width of about σ_D=75 MHz confirms the low kinetic temperatures of the ions.

than the experimental values by about 0.02 cm^{-1} (see next subsection for a general comparison).

The fundamental band ν_1 of H_2D^+ is much stronger than the overtone and combination bands by a factor of about 50. This can be estimated by inserting some values of A_{ul} from Tables 4.1 and 4.2 in relation 4.8. Additionally, the Doppler width of a transition reduces as the frequency of a transition is lowered ($\sigma_D \sim \nu_0$). Therefore, only very low power was needed for the ν_1 band and the OPO power was therefore attenuated by several filters (see Fig. 4.3). For example, with an Einstein coefficient $B_{lu} = 1.3 \times 10^{17}$ m^3/(J·s^2) for the $1_{01} \leftarrow 0_{00}$ transition at 3038.182 cm^{-1}, a laser power of P=0.1 mW is sufficient to excite the cold ions (27 K) with a rate $R \approx 4.9$ s^{-1}. The full power capabilities of the OPO system could be demonstrated by a hitherto undetected line which was predicted by Ramanlal and Tennyson [31] at the position 3164.149 cm^{-1} with a very small Einstein A_{ul} coefficient of only 1.598 s^{-1} (Table 4.3). For the measurement of this line, all attenuators have been taken out of the beam line (Fig. 4.3) and a full idler power of about 24 mW at the corresponding laser frequency was directed to the ion trap. The $2_{20} \leftarrow 1_{01}$ line measured with the cw-OPO is depicted in Fig. 4.5, and its line position is determined to be at 3164.118 cm^{-1}. In the Figure, the H_3^+ signal counts were background corrected (about 500 background ions) and normalized to the measured laser power.

120

The Doppler width of this peak and all other transitions of the ν_1 band have measured values of about σ_D=75 MHz. Subtracting the slight broadenings caused by the two wavemeters and the jitter of the OPO on the timescale of 1 second leads to similar kinetic temperatures of the H_2D^+ ion as measured with the Agilent diode lasers at higher wavenumbers (see section 4.4.4).

4.4.2 Comparison of experimental to computed line positions

The experimental line positions compiled in Tables 4.1 through 4.3 are compared to the high accuracy *ab initio* calculations in Figure 4.6 together with other experimental work on fundamentals [21, 22, 24, 25] and overtone/combination bands [26] performed over the last 25 years. The previous experimental work on the fundamentals was carried out in discharge tubes and therefore the elevated ion temperatures allowed a wealth of lines to be detected, from which only the transitions from the 4 lowest rotational levels are depicted in Fig. 4.6 for simplicity.

As can be seen, the deviations between experiment and theory show a clear dependence on the specific vibrational band; a systematic dependence of the deviations on rotational quantum numbers could not be observed. Heavier molecules violate less the Born-Oppenheimer approximation, and indeed the differences between experiment and calculations are visibly smaller for the heavier D_2H^+ molecule, even though non-Born-Oppenheimer terms are included explicitly in the *ab initio* predictions. The greatest deviations between calculation and measurements are seen for the bending mode ν_2 in H_2D^+, and with three quanta in this mode the vibrational band (0,3,0) reaches a maximum deviation of 0.15 cm^{-1}. It has already been observed in cw-CRDS experiments [40], that the *ab initio* model developed by Polyansky and Tennyson [38] is better in predicting stretching frequencies (ν_1 and ν_3) than frequencies for the ν_2 bending motion. Furthermore, for H_2D^+ the ν_2 and ν_3, and the $2\nu_2$ and $2\nu_3$ states show an approximately equal and opposite error in the *ab initio* predictions. This is precisely the behavior expected from a less than complete treatment of Born-Oppenheimer failure [36]. This effect is less marked for D_2H^+ for which, in any case, the errors and Born-Oppenheimer correction terms are smaller.

In the (1,2,0) band of H_2D^+ there are two transitions at 7066.839 cm^{-1} and 7077.529 cm^{-1} which fall outside the band group in Fig. 4.6. These two transitions also show a higher A_{tot} in Table 4.1. The reason for this differing behavior is most probably that these levels are subject to Coriolis coupling (see next section) with rotational sublevels of the band (0,0,3) (which is not measured in this work). The magnitude of the C-axis Coriolis coupling is proportional to the quantum number K_c [26]. The strong deviation only for these two transitions thus relies on upper levels with $K_c = 2$ and apparently on near-accidental degeneracies.

4.4.3 Coriolis coupling and Fermi resonances

The spectroscopic assignments of the fundamental ν_2 and ν_3 vibrations of H_2D^+ and D_2H^+ were already hampered by the fact that these modes are coupled by the Coriolis interaction [21, 25]. Both H_2D^+ and D_2H^+ belong to the C_{2v} symmetry group and the bending mode ν_2

121
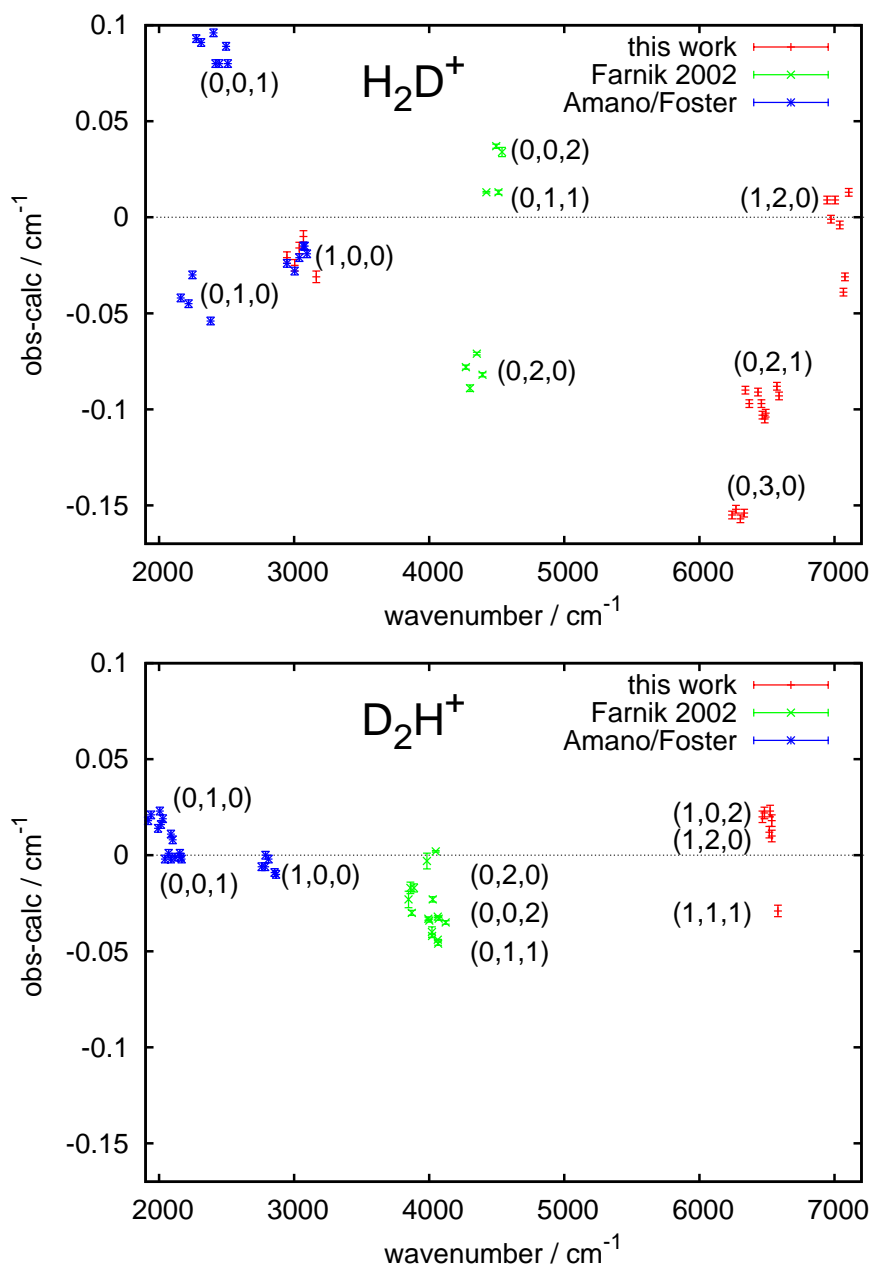
Figure 4.6: Comparison of experimentally determined fundamental, overtone and combination transitions of H_2D^+ and D_2H^+ to high accuracy *ab initio* calculations [31, 38]. The measured transitions comprise the fundamentals [21, 22, 24, 25], some first (Fárník et al. [26]) and some second overtone and combination transitions (this work). Experimental accuracies are marked by error bars. Although deviations from the Born-Oppenheimer approximation are explicitly included in the *ab initio* predictions, the deviations for H_2D^+ are visibly greater than for D_2H^+. For H_2D^+, the deviations depend on the specific vibrational band (v_1, v_2, v_3) and are greatest when there are 3 quanta in the bending mode v_2.

and the antisymmetric stretch ν_3 (with symmetries A_1 and B_2, respectively) can couple by a rotational motion with symmetry B_2, which is in fact the rotation about the out-of-plane C-axis. Fárník et al. [26] also observed strong Coriolis coupling between the combination band $(0,1,1)$ (symmetry B_2) and overtone $(0,0,2)$ (symmetry A_1) for both molecules. For D_2H^+, the small difference in band origins ($\Delta\nu_0 \approx 18$ cm^{-1}) leads to large shifts and in fact inverts the zeroth-order asymmetric top level structure in several instances.

Similar resonance effects can be expected for the second overtone and combination bands of H_2D^+ and D_2H^+ which are only qualitatively discussed here. From the detected H_2D^+ bands, $(0,2,1)$ (symmetry B_2) can couple to the other two bands $(0,3,0)$ and $(1,2,0)$ (both A_1) by C-axis Coriolis coupling, although the difference in band origins suggests that only $(0,3,0)$ and $(0,2,1)$ are substantially perturbed. These two bands are $\Delta\nu_0 \approx 113$ cm^{-1} apart, see the vertical arrow in Fig. 4.7 (upper), and therefore the level shifts have a relatively small magnitude, preserving the asymmetric top energy pattern.

For D_2H^+, both the $(1,2,0)$ and $(1,0,2)$ bands are close in energy ($\Delta\nu_0 \approx 67$ cm^{-1}) and have symmetry A_1. Thus they are mixed by Fermi resonances, and therefore the vibrational assignments given in Table 4.2 have to be taken as an approximation. Based on this approximative band assignment, the degree of perturbation is more pronounced than for H_2D^+, see Fig. 4.7 (lower). From the simple symmetry arguments, there is also Coriolis coupling between $(1,1,1)$ and the other two bands, although of small magnitude.

4.4.4 Kinetic temperature of ions

The stable and reliable operation of the commercial diode lasers permitted to measure spectroscopically several properties of the trapped ions, as for example their kinetic temperature. As indicated before, the measured Doppler temperature of the ions is higher than the nominal temperature of the trap. It is of special interest to determine the main influence on this discrepancy, as also discussed by Mikosch et al. [44]. In particular, the influence of hot gases leaking from the ion source, of the laser power and of the RF field have been tested. Applying the relation

$$\sigma_D = \sqrt{\frac{k_B T}{mc^2}}\, \nu_0 \,, \tag{4.7}$$

the kinetic temperature T of the ions has been calculated using the ion mass m and the fitted Doppler width σ_D. Under normal operating conditions, the ion temperature for H_2D^+ has been measured to be (27 ± 2) K (corresponding to $\sigma_D \approx 150$ MHz), using the trapping parameters V_0=15 V and f =17 MHz (see section 4.2.2), and moderate laser power of 2 mW (see Fig. 4.4). For D_2H^+, the measured Dopper temperature was determined to be lower by a few K. Allowing an excess of hot gas (300 K) from the source region to leak to the ion trap did not have a measurable impact on the ion temperature. This is probably due to the fact that the hot gases entering the ion trap are readily thermalized. Likewise, a pronounced heating of the ions by the laser could not be detected. A laser power in excess of 2 mW only pretended a heating
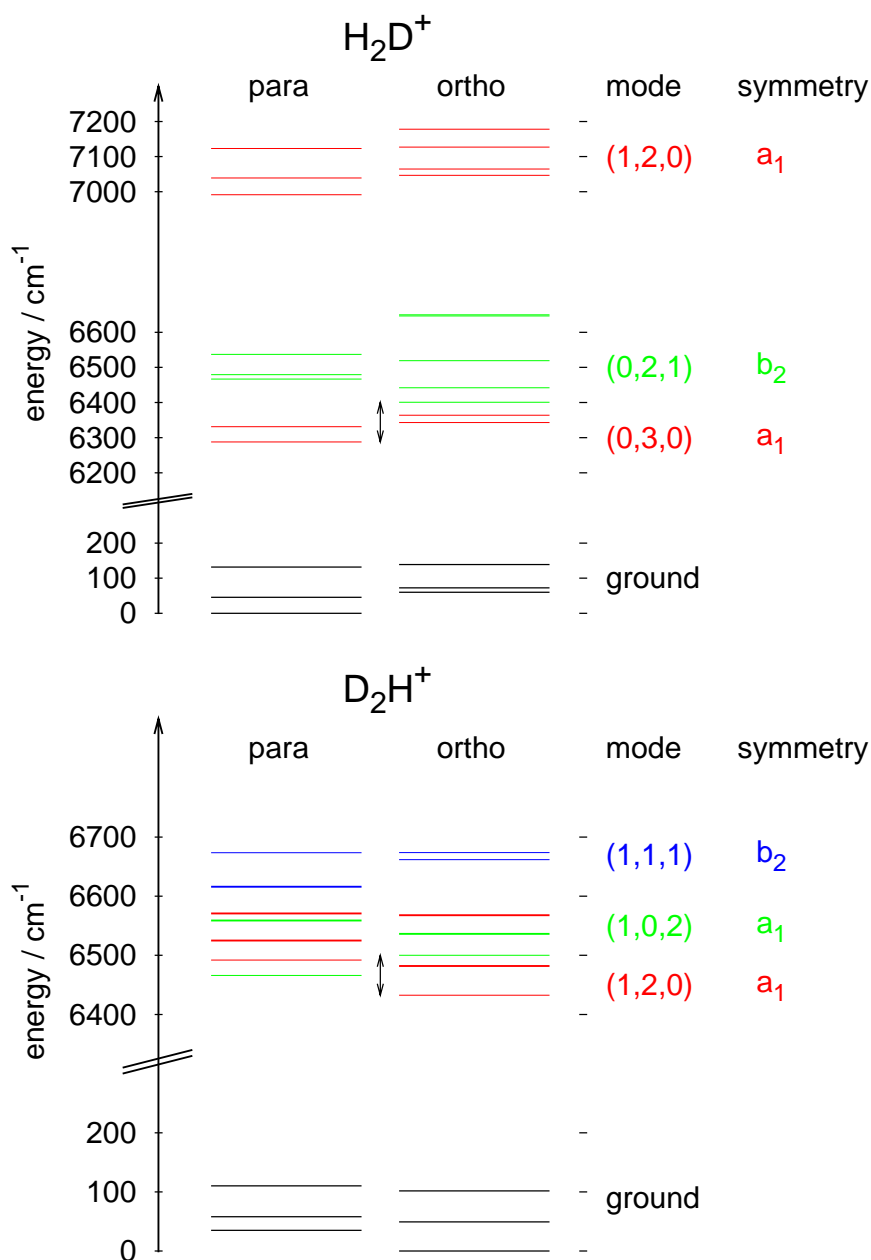
Figure 4.7: The lowest rotational levels of H_2D^+ (upper) and D_2H^+ (lower) for the bands of interest. The level positions are taken from the *ab initio* linelist [63] which was obtained using the methodology described in [31, 38]. For D_2H^+, the 7 levels actually probed by spectroscopy (see Table 4.2) are drawn thicker. Due to the difference in band origin of 113 cm^{-1} for H_2D^+ (vertical arrow), the (0,2,1) and (0,3,0) bands are only coupled by a small Coriolis effect, thus preserving the asymmetric top energy level patterns. For D_2H^+, the band origin difference for (1,0,2) and (1,2,0) is quite small (67 cm^{-1}), leading to strong mixing by Fermi resonances.

effect by saturating the peak maximum and thereby apparently broadening the measured peak, giving it a non-Doppler profile. For this reason, special care was used to employ low laser power when determining the Doppler temperature. The most noticeable effect on the kinetic ion temperature was caused by the amplitude of the RF voltage. It was easy to heat the ions by using RF voltage amplitudes beyond V_0=50 V. As an amplitude increase should not lead to higher ion temperatures in an ideal multipole trap, this effect can only be explained by imperfections (patch fields) or by a direct heating of the trap by the RF power. Still, it was difficult to obtain kinetic ion temperatures substantially below the above mentioned 27 K, even when approaching the lowest possible RF amplitudes of about V_0=10V. Thus, there is a discrepancy of about 10 K to the nominal trap temperature of 17 K.

Numerical 3D simulations of a single ion moving in the 22-pole trap were performed to attempt resolving this discrepancy. These computations take into account the combined effects of the elastic collisions with the He buffer gas, the perfect RF multipole field, as well as the electrostatic field of the endelectrodes [65]. Space charge effects were neglected due to the low number of stored ions. Similar calculations for other types of multipole traps have been presented by Gerlich [58]. As pointed out in that work, the RF field of a multipole trap conserves the energy of the ion after reflection from the effective RF walls, and it is only by including buffer gas collisions that heating effects occur. These heating effects depend on the trap geometry and multipolarity, the RF frequency, and also on the ion-neutral mass ratio. Preliminary results of our simulations thus show that a temperature increase of about 2 K can be explained by collisions of the H_2D^+ ions with the He buffer in the RF field, and a further 2 K increase can be expected when the influence of the electrostatic field of the endelectrodes (shown in the inset in Fig. 4.2) is included into the simulations. This relatively small heating effect is due to the favorable ion-neutral mass ratio, in contrast to an unfavorable case as for example H_3^+ + Ar, where a pronounced heating effect has been observed [44]. In summary, only about half of the temperature discrepancy of 10 K can be explained by the operation of a perfect ion trap, while the remaining temperature increase is probably caused by trap imperfections or potential distortion [44, 58], but also the kinetic energy release in exothermic exchange reactions with o-H_2 (or traces of HD or D_2) could play a role.

4.4.5 Measurement of relative Einstein B_{lu} coefficients

Tables 4.1 through 4.3 list the *ab initio* calculated coefficients A_{ul} for spontaneous emission for all transitions. In laser probe experiments like LIR, the quantity of interest is the coefficient for laser absorption, the Einstein B_{lu} coefficient, which can be obtained using

$$B_{lu} = \frac{g_u}{g_l} \frac{c^3 A_{ul}}{8\pi h \nu^3} \tag{4.8}$$

where g_u and g_l are the rotational degeneracies $g = (2J + 1)$ of the upper and lower states. These calculated B_{lu} coefficients are also included in the tables, and for simplicity they have been normalized to the respective strongest transitions for H_2D^+ and D_2H^+.

Table 4.4: Calculated and measured relative Einstein B_{lu} coefficients for several groups of transitions starting from the same rotational levels in H_2D^+ or D_2H^+.

transition		line position / cm^{-1}	laser power / mW	meas B_{lu}	calc B_{lu}
		H_2D^+			
(0,3,0)	$1_{01} \leftarrow 0_{00}$	6330.973	4.0	0.32 ± 0.02	0.31
(0,2,1)	$1_{11} \leftarrow 0_{00}$	6466.532	1.8	1	1
(0,3,0)	$1_{10} \leftarrow 1_{11}$	6303.784	5.0	0.29	0.29
(0,2,1)	$0_{00} \leftarrow 1_{11}$	6340.688	5.3	0.27 ± 0.03	0.27
(0,2,1)	$2_{02} \leftarrow 1_{11}$	6459.036	4.1	0.35 ± 0.04	0.34
		D_2H^+			
(1,2,0)	$1_{11} \leftarrow 0_{00}$	6482.033	3.8	0.33 ± 0.02	0.32
(1,0,2)	$1_{11} \leftarrow 0_{00}$	6536.319	1.6	1	1

If one wants to measure the rotational level population of a molecular species, it is important to know how reliable the predictions for the (relative) B_{lu} coefficients are. The simple fact that all *ab initio* predicted lines have been found in this search, gave us the confidence that the calculated B_{lu} coefficients are relatively correct within, say, a factor of 2. To get a more quantitative picture, relative B_{lu} coefficients have been measured using transitions in H_2D^+ and D_2H^+ starting from the same rotational level. Special care has been taken in these measurements not to saturate the signals by applying too much laser power, thereby probably skewing the ratios. Table 4.4 gives an overview of the measurements where groups of relatively strong transitions have been selected to compare the measured relative coefficient B_{lu} to the calculated ones. With the stable and computer-controlled diode lasers, these measurements could be done in an automated fashion: The laser was tuned iteratively to the maximum of the respective peaks, and the background-corrected counts divided by the laser power yielded the relative strength of the transition. If necessary, the slight difference in Doppler widths for distant peaks was accounted for (because it is the area, and not the maximum of the peak which matters).

As seen in Table 4.4, the applied experimental method is able to measure the relative B_{lu} coefficients within 10% of error, as determined from several automated runs. The agreement between experiment and calculations is surprisingly good, and the different strength of the three transitions starting at the 1_{11} rotational level in H_2D^+ is also well reproduced. A similar good agreement within overtone/combination bands of D_2H^+ has been reported by Fárník et al. (see their Fig. 7b), although statistically significant discrepancies have been found comparing the fundamental band ν_1 to overtone/combination bands in H_2D^+ and D_2H^+ [26]. Anyway, as the determination of rotational populations requires the B_{lu} coefficients to be relatively correct

within the applied band, the good agreement in Table 4.4 not only gives a solid basis for the determination of rotational populations [47], but also suggests that the overall reaction probability of the excited H_2D^+ or D_2H^+ ions with H_2 does not depend on the type of combination band or rotational state. This is astonishing, as it is known that different fundamental vibrational modes can have different reaction probabilities, as is for example the case for $C_2H_2^+ + H_2$ [52, 53]. One reason of this mode-independence is probably the fact that the excited states considered lie well above the reaction endothermicity of 170 cm^{-1}, and that the highly excited ions have several different possibilities to react in collisions with H_2 while decaying.

4.5 CONCLUSIONS AND FURTHER EXPERIMENTS

The initial motivation for this research is to understand the role of the nuclear spin in low-temperature ion-molecule collisions, and thereby explain the rotational populations of ions at cryogenic temperatures and its dependence on the o/p-ratio of the H_2 collision partner. Such information is crucial to fully understand the processes in low-temperature interstellar clouds, in particular deuteration processes.

The present work describes the spectroscopic tools needed to reach this final goal. Applying the method of laser induced reaction (LIR), several laser sources have been used to excite rovibrational transitions of H_2D^+ and D_2H^+ when embedded in cold n-H_2 gas. Of the hitherto used laser systems (free-electron laser FELIX [46, 66], OPO, Agilent commercial diode laser), the diode lasers are ideal to probe the level populations and to explore rate coefficients of the collision systems, due to their easy computer controlled operation and stability.

An excellent agreement between experiment and *ab initio* calculations has been observed for the line positions and (relative) Einstein *B* coefficients. Especially the latter fact is of paramount importance not only for the astronomical community, but also when reliable rotational populations have to be determined in laser probe experiments. Such experiments, accompanied by microcanonical simulations, are currently performed at the I. Physikalisches Institut in Köln, using n-H_2 and p-H_2 as low-temperature collision partners.

Acknowledgements

REFERENCES

[1] T. Oka, Physical Review Letters **45**, 531 (1980).

[2] C. M. Lindsay and B. J. McCall, J. Mol. Spec. **210**, 60 (2001).

[3] D. Gerlich, E. Herbst, and E. Roueff, Planet. Space Sci. **50**, 1275 (2002).

[4] T. Millar, Space Sci. Rev. **106**, 73 (2003).

[5] D. Lis, E. Roueff, M. Guerin, T. Phillips, L. Coudert, F. van der Tak, and P. Schilke, Astrophys. J. **571**, L55 (2002).

[6] F. F. S. van der Tak, P. Schilke, H. S. P. Müller, D. C. Lis, T. G. Phillips, M. Gerin, and E. Roueff, Astron. Astrophys. **388**, L53 (2002).

[7] B. Parise, C. Ceccarelli, A. G. G. M. Tielens, E. Herbst, B. Lefloch, E. Caux, A. Castets, I. Mukhopadhyay, L. Pagani, and L. Loinard, Astron. Astrophys. **393**, L49 (2002).

[8] B. Parise, A. Castets, E. Herbst, E. Caux, C. Ceccarelli, I. Mukhopadhyay, and A. G. G. M. Tielens, Astron. Astrophys. **416**, 159 (2004).

[9] C. Ceccarelli, C. Vastel, A. G. G. M. Tielens, A. Castets, A. C. A. Boogert, L. Loinard, and E. Caux, Astron. Astrophys. **381**, L17 (2002).

[10] A. Bacmann, B. Lefloch, C. Ceccarelli, J. Steinacker, A. Castets, and L. Loinard, Astrophys. J. Lett. **585**, L55 (2003).

[11] D. R. Flower, G. Pineau des Forêts, and C. M. Walmsley, Astron. Astrophys. **427**, 887 (2004).

[12] M. Bogey, C. Demuynck, M. Denis, J. L. Destombes, and B. Lemoine, Astron. Astrophys. **137**, L15+ (1984).

[13] H. E. Warner, W. T. Conner, R. H. Petrmichl, and R. C. Woods, J. Chem. Phys. **81**, 2514 (1984).

[14] T. Amano and T. Hirao, J. Mol. Spec. **233**, 7 (2005).

[15] R. Stark, F. van der Tak, and E. van Dishoeck, Astrophys. J. **521**, L67 (1999).

[16] C. Vastel, T. Phillips, and H. Yoshida, Astrophys. J. **606**, L127 (2004).

128

[17] C. Ceccarelli, C. Dominik, B. Lefloch, P. Caselli, and E. Caux, Astrophys. J. Lett. **607**, L51 (2004).

[18] P. Caselli, F. F. S. van der Tak, C. Ceccarelli, and A. Bacmann, Astron. Astrophys. **403**, L37 (2003).

[19] F. van der Tak, P. Caselli, C. M. Walmsley, C. Ceccarelli, A. Bacmann, and A. Crapsi, in *The Dense Interstellar Medium in Galaxies*, edited by S. Pfalzner, C. Kramer, C. Staubmeier, and A. Heithausen (2004), pp. 549–+.

[20] J.-T. Shy, J. W. Farley, and W. H. Wing, Phys. Rev. A **24**, 1146 (1981).

[21] S. C. Foster, A. R. W. McKellar, I. R. Peterkin, J. K. G. Watson, and F. S. Pan, J. Chem. Phys. **84**, 91 (1986).

[22] T. Amano and J. K. G. Watson, J. Chem. Phys. **81**, 2869 (1984).

[23] T. Amano, J. Opt. Soc. Am. B **2**, 790 (1985).

[24] K. G. Lubic and T. Amano, Can. J. Phys. **62**, 1886 (1984).

[25] S. C. Foster, A. R. W. McKellar, and J. K. G. Watson, J. Chem. Phys. **85**, 664 (1986).

[26] M. Fárník, S. Davis, M. A. Kostin, O. L. Polyansky, J. Tennyson, and D. J. Nesbitt, J. Chem. Phys. **116**, 6146 (2002).

[27] R. E. Moss, Mol. Phys. **78**, 371 (1993).

[28] V. I. Korobov, Phys. Rev. A **74**, 052506 (2006).

[29] B. Roth, J. C. J. Koelemeij, H. Daerr, and S. Schiller, Phys. Rev. A **74**, 040501 (2006).

[30] J. C. J. Koelemeij, B. Roth, A. Wicht, I. Ernsting, and S. Schiller, Phys. Rev. Lett. **98**, 173002 (2007).

[31] J. Ramanlal and J. Tennyson, Mon. Not. Astron. Soc. **354**, 161 (2004).

[32] O. L. Polyansky, A. G. Császár, S. V. Shirin, N. F. Zobov, P. Barletta, J. Tennyson, D. W. Schwenke, and P. J. Knowles, Science **299**, 539 (2003).

[33] J. Tennyson, P. Barletta, M. A. Kostin, O. L. Polyansky, and N. F. Zobov, Spectrochimica Acta A **58**, 663 (2002).

[34] W. Cencek, J. Rychlewski, R. Jaquet, and W. Kutzelnigg, J. Chem. Phys. **108**, 2831 (1998).

[35] J. Tennyson and O. L. Polyansky, Phys. Rev. A **50**, 314 (1994).

[36] B. M. Dinelli, C. R. Le Sueur, J. Tennyson, and R. D. Amos, Chem. Phys. Lett. **232**, 295 (1995).

[37] R. Röhse, W. Kutzelnigg, R. Jaquet, and W. Klopper, J. Chem. Phys. **101**, 2231 (1994).

[38] O. L. Polyansky and J. Tennyson, J. Chem. Phys. **110**, 5056 (1999).

[39] R. E. Moss, Mol. Phys. **89**, 195 (1996).

[40] P. Hlavenka, R. Plasil, G. Bano, I. Korolov, D. Gerlich, J. Ramanlal, J. Tennyson, and J. Glosik, International Journal of Mass Spectrometry, Vol. 255-256, No. , p. 170-176 **255**, 170 (2006).

[41] L. Kao, T. Oka, S. Miller, and J. Tennyson, Astrophys. J. Suppl. **77**, 317 (1991).

[42] L. Neale, S. Miller, and J. Tennyson, Astrophys. J. **464**, 516 (1996).

[43] J. Ramanlal, Ph.D. thesis, University of London (2004).

[44] J. Mikosch, H. Kreckel, R. Wester, R. Plašil, J. Glosík, D. Gerlich, D. Schwalm, and A. Wolf, J. Chem. Phys. **121**, 11030 (2004).

[45] J. Glosík, P. Hlavenka, R. Plašil, and et al., Phil. Trans. Royal Soc. London. Series A **364**, 2931 (2006).

[46] S. Schlemmer, O. Asvany, E. Hugo, and D. Gerlich, in *Astrochemistry: Recent Successes and Current Challenges*, edited by D. C. Lis, G. A. Blake, and E. Herbst (2005), vol. 231 of *IAU Symposium*, pp. 125–134.

[47] O. Asvany, E. Hugo, F. Müller, F. Kühnemann, S. Schiller, J. Tennyson, and S. Schlemmer, J. Chem. Phys. **127**, 154317 (2007).

[48] O. Asvany, P. K. P, B. Redlich, I. Hegemann, S. Schlemmer, and D. Marx, Science **309**, 1219 (2005).

[49] S. Schlemmer and O. Asvany, J. Phys. Conf. Series **4**, 134 (2005).

[50] S. Borman, Chem. & Eng. News **83**, 45 (2005).

[51] S. Schlemmer, T. Kuhn, E. Lescop, and D. Gerlich, Int. J. Mass Spectrom. **185**, 589 (1999).

[52] S. Schlemmer, E. Lescop, J. von Richthofen, D. Gerlich, and M. A. Smith, J. Chem. Phys. **117**, 2068 (2002).

[53] S. Schlemmer, O. Asvany, and T. Giesen, PCCP **7**, 1592 (2005).

[54] O. Asvany, T. Giesen, B. Redlich, and S. Schlemmer, Phys. Rev. Lett. **94**, 073001 (2005).

[55] I. N. Kozin, O. L. Polyansky, and N. F. Zobov, J. Mol. Spec. **128**, 126 (1988).

[56] N. Adams and D. Smith, Astrophys. J. **248**, 373 (1981).

[57] D. Gerlich, Phys. Scripta **T59**, 256 (1995).

[58] D. Gerlich, in *Adv. Chem. Phys.: State-Selected and State-to-State Ion-Molecule Reaction Dynamics*, edited by C.-Y. Ng and A. C. P. Michael Baer (1992), vol. LXXXII, pp. 1–176.

[59] L. S. Rothman, D. Jacquemart, A. Barbe, D. Chris Benner, M. Birk, L. R. Brown, M. R. Carleer, C. Chackerian, K. Chance, L. H. Coudert, et al., J. Quant. Spec. Rad. Trans. **96**, 139 (2005).

[60] O. Asvany, E. Hugo, and S. Schlemmer, J. Vac. Sci. Technol. A **25**, 628 (2007).

[61] F. Müller, G. von Basum, A. Popp, D. Halmer, P. Hering, M. Mürtz, F. Kühnemann, and S. Schiller, Appl. Phys. B **80**, 307 (2005).

[62] J. Tennyson, M. A. Kostin, P. Barletta, G. J. Harris, O. L. Polyansky, J. Ramanlal, and N. F. Zobov, Comput. Phys. Commun. **163**, 85 (2004).

[63] The full electronic lists of H_2D^+ and D_2H^+ transitions are not published, but can be obtained from Jonathan Tennyson.

[64] H. Kreckel, J. Tennyson, D. Schwalm, D. Zajfman, and A. Wolf, New J. Phys. **6**, 151 (2004).

[65] O. Asvany and S. Schlemmer (2007), in preparation.

[66] D. Oepts, A. F. G. van der Meer, and P. W. van Amersfoort, Infr. Phys. Tech. **36**, 297 (1995).

CHAPTER 5

Chemical modeling of L183 (=L134N) :an estimate of the ortho/para H$_2$ ratio

L. Pagani, C. Vastel, E. Hugo, V. Kokoouline, C.H. Greene, A. Bacmann, E. Bayet, C. Ceccarelli, R. Peng and S. Schlemmer

Context. The high degree of deuteration observed in some prestellar cores depends on the ortho-to-para H$_2$ ratio through the H$_3^+$ fractionation. **Aims.** We want to constrain the ortho/para H$_2$ ratio across the L183 prestellar core. This is mandatory to correctly describe the deuteration amplification phenomenon in depleted cores such as L183 and to relate the total (ortho+para) H$_2$D$^+$ abundance to the sole ortho–H$_2$D$^+$ column density measurement. **Methods.** To constrain this ortho/para H$_2$ ratio and derive its profile, we make use of the N$_2$D$^+$/N$_2$H$^+$ ratio and of the ortho–H$_2$D$^+$ observations performed across the prestellar core. We use two simple chemical models limited to an almost totally depleted core description. New dissociative recombination and trihydrogen cation–dihydrogen reaction rates (including all isotopologues) are presented in this paper and included in our models. **Results.** We estimate the H$_2$D$^+$ ortho/para ratio in the L183 cloud, and constrain the H$_2$ ortho/para ratio : we show that it is varying across the prestellar core by at least an order of magnitude being still very high (≈ 0.1) in most of the cloud. Our time-dependent model indicates that the prestellar core is presumably older than 1.5–2 $\times$ 10^5 years but that it may not be much older. We also show that it has reached its present density only recently and that its contraction from a uniform density cloud can be constrained. **Conclusions.** A proper understanding of deuteration chemistry cannot be attained without taking into account the whole ortho/para family of molecular hydrogen and trihydrogen cation isotopologues as their relations are of utmost importance in the global scheme. Tracing the ortho/para H$_2$ ratio should also give useful constrains on the dynamical evolution of prestellar cores.

133

5.1 INTRODUCTION

Studies of the earliest stages of star formation have been booming in the last ten years with the advent of new receivers acquiring better spatial and spectral resolution. Prestellar cores are dense and cold cores where gravitational collapse has not yet occured. In the densest regions of the core (where n_{H_2} is larger than a few 10^4 cm^{-3}) most heavy molecules containing Carbon, Nitrogen and Oxygen seem to deplete onto the dust grains and only light ions remain in the gas phase. There has been extensive observational evidence of CO and CS depletion in the center of prestellar cores [e.g. 1–5] which seems to be typical of the majority of dense cores. Nitrogen–bearing species like CN, NH_3 and N_2H^+ appear to subsist longer before freezing-out onto the dust grains [6–8].

In conditions under which heavy species are depleted, H^+ and H_3^+ (and its deuterated counterparts) are the most abundant ions subsisting in the gas phase. H_2D^+ has been widely detected and mapped in protostars and prestellar cores [9–11] through its ortho fundamental line, with abundances large enough to be explained by the CO depletion theory/observations. Although difficult to observe from Earth, the D_2H^+ molecule has been detected with its para line in the source IRAS 16293E [12] with an abundance similar to the ortho–H_2D^+ molecule as suggested by Phillips and Vastel [13].

Consequently many theoretical studies germinated which included all the deuterated forms of the H_3^+ ion [e.g. 14, 15]. However all nuclear spin states (ortho, meta, para, corresponding to the spin state of the protons or deuterons) must be taken into account in order to compare with the observational sets. Moreover the thermicity of the forward/backward reactions strongly depends on the symmetric state of the species. Though the influence of the ortho/para H_2 ratio on the chemistry of H_2D^+ [16] has been described several years before the first detection of the ion [17], it is only recently that this particular, spin-state dependent chemistry has been studied in detail [18, 19].

The motivation for our study is sparked by the many deuterated observations performed in the L183 prestellar core (PSC) and the main aim of this paper is to study the ortho/para H_2 ratio from some of these deuterated species observations. To this effect, we constrain two chemical models including all the symmetric states of H_2, D_2, H_3^+ and its deuterated counterparts with observations of ortho–H_2D^+, combined with previous N_2H^+ and N_2D^+ observations. These models have been set up using recent dissociative recombination rates computed for H_3^+ and its isotopologues as well as all non negligible reaction rates between H_2 and H_3^+ and their isotopologues (both presented for the first time in this paper).

5.2 OBSERVATIONS

5.2.1 Deuterated H_3^+

We first observed the ortho–H_2D^+ (and para–D_2H^+) with the Caltech Submillimeter Observatory (CSO) monopixel receiver and subsequently took advantage of the newly installed Heterodyne ARray Program, 16 channel 350 GHz band ("B-band") (HARP-B) camera on the James Clerk Maxwell Telescope (JCMT) to fully map its emission.

CSO observations

The H_2D^+ and D_2H^+ observations were carried out at the CSO, between August 2004 and April 2005, under good weather conditions (225 GHz zenith opacity always less than 0.06). Scans were taken, using the chopping secondary with a throw of $3'$, using the reference position: $\alpha_{2000} = 15^h 54^m 08^s.50$ and $\delta_{2000} = -02° 52' 48''$.

The 345 GHz (respectively 650 GHz) sidecab receiver with a 50 MHz acousto-optical spectrometer backend was used for all observations with an average velocity resolution of 0.04 km s^{-1} (respectively 0.02 km s^{-1}). At the observed frequencies of 372.421385(10) GHz for the H_2D^+ (1_{10}-1_{11}) and 691.660483(20) for the D_2H^+ (1_{10}-1_{01}) lines [21], the CSO 10.4 meters antenna has a HPBW of about $20''$ and $11''$ respectively. We performed a cut in declination across the main dust peak in L183 between ($30''$,-$70''$) and ($30''$,$100''$) for H_2D^+ and concentrated on the reference position for D_2H^+. The system temperature was typically 1000 to 2000 K for H_2D^+ and 2500 to 3500 K for D_2H^+.

The beam efficiency at 372 GHz (respectively 692 GHz) was measured on Saturn and Jupiter and found to be $\sim 60\%$ (respectively $\sim 40\%$) for point sources. Pointing was monitored every 1 hour and half and found to be better than $3''$. If the emission is extended compared to the beam size of CSO, as appears to be the case for H_2D^+ then the efficiency is about 70% at 372 GHz and 60 % at 692 GHz. The data reduction was performed using the CLASS program of the GAG software developed at IRAM and the Observatoire de Grenoble and the LTE data analysis with CASSIS developed at CESR (http://www.cassis.cesr.fr).

JCMT observations

The JCMT observations were obtained during semester 07A in service mode, using the HARP-B 16 pixel camera (one pixel, located in a corner, was unavailable). A third of the observations was obtained in Jiggle–chop[1] mode and two thirds in Position switch (PSw) mode. The Jiggle–chop mode appeared to be no faster, the displacement of the telescope in PSw mode seeming minor compared to other overheads, and because the Jiggle–chop mode works in the Nyquist regime each pixel receives much less integration time than in PSw mode. As adjacent pixels

---

[1]http://www.jach.hawaii.edu/software/jcmtot/het_obsmodes.html
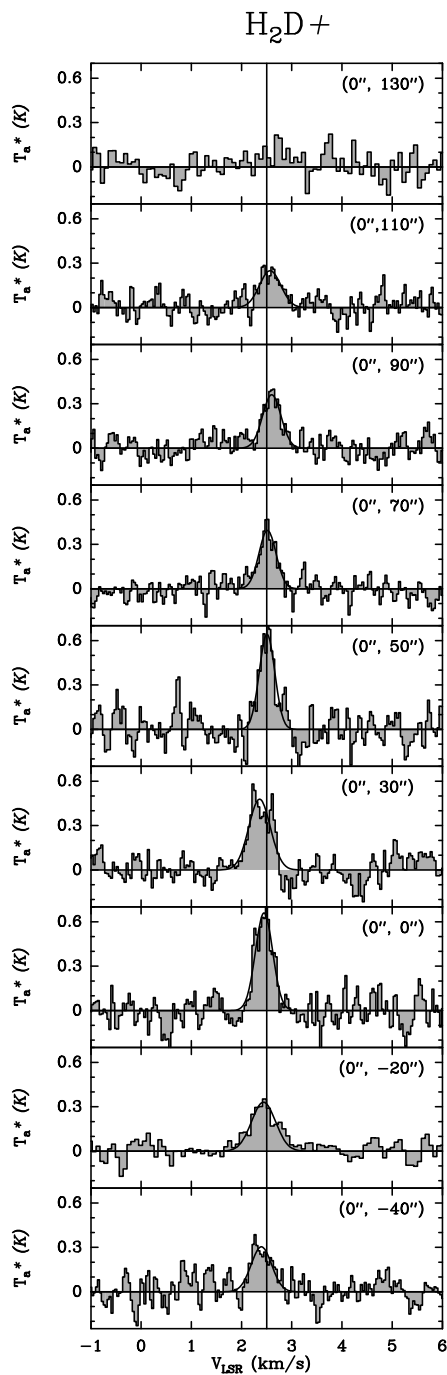
Figure 5.1: CSO map of the o–H_2D^+ (1_{10}-1_{11}) line. The position is indicated in arcseconds for each spectrum and the (0,0) position corresponds to $\alpha_{2000} = 15^h\ 54^m\ 08^s.50$, $\delta_{2000} = -02°\ 52'\ 48''$. The Y-axis represents the antenna temperature.

Table 5.1: Line parameters from the JCMT and CSO observations. The positions are offsets to the dust peak emission at $\alpha_{2000} = 15^h 54^m 08^s.50$, $\delta_{2000} = -02° 52' 48''$. For non–detected lines we give the 3σ upper limit. For JCMT and p–D_2H^+ at CSO, we give both the Monte-Carlo (MC) and the LTE column density estimates.

					JCMT		
Position ($''$)	rms (K)	δv km s^{-1}	Δv km s^{-1}	T_a^* K	$N(o–H_2D^+)_{MC}^{a,b}$ cm^{-2}	$N(o–H_2D^+)_{LTE}^{b}$ cm^{-2}	tau$_{LTE}^{b}$
(-45,0)	0.08	0.049	0.3	0.11	$3.6\ 10^{12}$	$2.9\ 10^{12}$	0.11
(-30,0)	0.08	0.049	0.26	0.28	$8.1\ 10^{12}$	$8.1\ 10^{12}$	0.31
(-15,0)	0.09	0.049	0.51	0.41	$2.0\ 10^{13}$	$1.3\ 10^{13}$	0.49
(0,0)	0.09	0.049	0.41	0.57	$2.3\ 10^{13}$	$2.0\ 10^{13}$	0.77
(15,0)	0.08	0.049	0.47	0.46	$2.0\ 10^{13}$	$1.5\ 10^{13}$	0.57
(30,0)	0.08	0.049	0.39	0.21	$8.1\ 10^{12}$	$5.7\ 10^{12}$	0.22
(45,0)	0.08	0.049	0.50	0.13	$3.6\ 10^{12}$	$3.4\ 10^{12}$	0.13
(60,0)	0.08	0.049		<0.06	$<1.8\ 10^{12}$	$<1.6\ 10^{12}$	< 0.06
					CSO		
Position ($''$)	rms (K)	δv km s^{-1}	Δv km s^{-1}	T_a^* K		$N(o–H_2D^+)_{LTE}^{b}$ cm^{-2}	tau$_{LTE}^{b}$
(0,130)	0.08	0.077		< 0.1		$< 3.0\ 10^{12}$	< 0.1
(0,110)	0.08	0.039	0.50	0.25		$8.0\ 10^{12}$	0.28
(0,90)	0.08	0.039	0.43	0.36		$1.0\ 10^{13}$	0.42
(0,70)	0.08	0.039	0.40	0.39		$1.1\ 10^{13}$	0.47
(0,50)	0.10	0.039	0.36	0.64		$2.0\ 10^{13}$	0.95
(0,30)	0.08	0.039	0.50	0.48		$1.8\ 10^{13}$	0.63
(0,0)	0.10	0.039	0.41	0.66		$2.4\ 10^{13}$	1.00
(0,-20)	0.06	0.039	0.56	0.33		$1.2\ 10^{13}$	0.38
(0,-40)	0.10	0.039	0.48	0.30		$9.5\ 10^{12}$	0.34
Position ($''$)	rms (K)	δv km s^{-1}	Δv km s^{-1}	T_a^* K	$N(p–D_2H^+)_{MC}^{c}$ cm^{-2}	$N(p–D_2H^+)_{LTE}^{c}$ cm^{-2}	tau$_{LTE}^{c}$
(0,0)	0.07	0.042		< 0.07	$<2.4\ 10^{13}$	$< 1.5\ 10^{13}$	< 0.48

[a] Column densities have been computed after averaging spectra at symmetrical distance from center.

[b] Column densities and opacities have been computed with a beam coupling correction of 70% for both JCMT and CSO.

[c] Upper limit column density and opacity have been computed with a beam coupling correction of 60% at CSO.
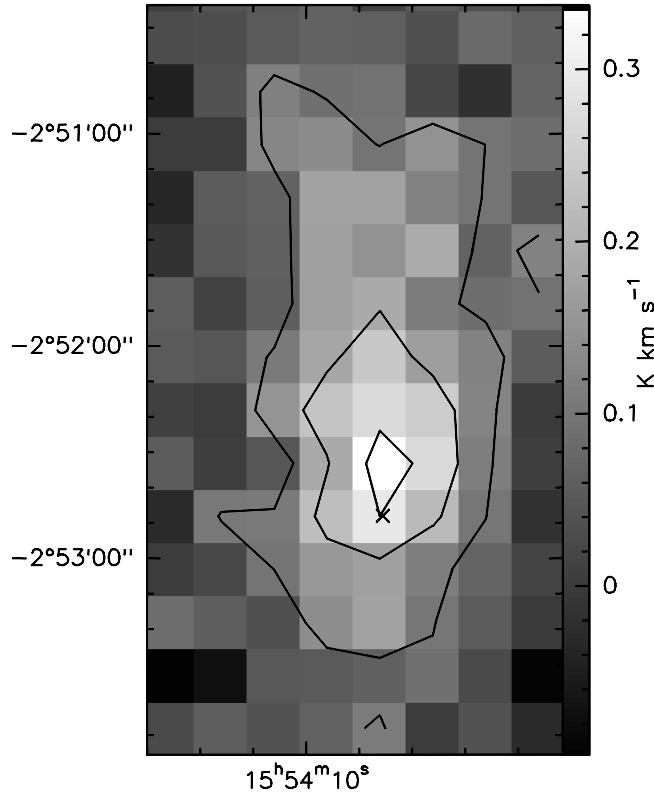
Figure 5.2: JCMT map of the o–H_2D^+ (1_{10}-1_{11}) line. The dust peak position [20] is indicated by a cross and corresponds to $\alpha_{2000} = 15^h\,54^m\,08^s.50$, $\delta_{2000} = -02°\,52'\,48''$. Contour levels are 0.1, 0.2 and 0.3 K km s^{-1}.

had the same off spectrum subtracted, spatial average did not give much improvement and we subsequently changed to Position switch mode because deep integration on weak signal appears more important than Nyquist sampling for this work. In PSw mode, we made 2×2 pointings to fill the gaps in the camera, achieving thus a full beam sampling. Two such sets were performed to cover the main dust peak and its northern extension (Fig 5.2) with one pixel row overlap between the two.

Most of the observations were run in band 1 weather ($\tau_{225GHz} < 0.05$) while a few were done in band 2 weather leading to rapid degradation of the system temperature. The source was observed only above 40 to 45°elevation and band 1 weather system temperature was in the range 500-1000 K depending on the pixels and on the elevation. To observe both H_2D^+ and N_2H^+ (J:4–3)(at 372.672509 GHz), we tuned the receiver half way between the two lines and used a frequency resolution of 61 kHz so that the backend could cover both lines at once.

Data pre-reduction was done with Starlink software (KAPPA, SMURF and STLCONVERT packages) and subsequently translated to CLASS format for final reduction.

5.2.2   CO depletion and dust content

All other observations used in this paper have been obtained and published previously. The dust content of L183, both in emission and in absorption has been described in Pagani et al. [20; 22]. The source size is half a degree and contains a long filament extending on $\sim$6$'$ from north to south. Two peaks are clearly visible, one just south of the middle of the filament (which we call the main peak) with an opacity of $\sim$150 A_V and a second one, 3$'$ north of the first one (the north peak) with an estimated opacity of $\sim$70 A_V. These peaks have the characteristics of prestellar cores. Most of the filament has an opacity above 40 A_V.

Two large scale $C^{18}O$ and $C^{17}O$ maps obtained with the Kitt Peak 12-m telescope fail to trace the dense filament [5]. It is now well-established that this is due to depletion of CO onto grains. Surprisingly, the opacity at which the depletion begins ($\sim$20 A_V) is twice higher than what is usually observed in other clouds [e.g. 2, 23, 24] though it still appears at a density ($\sim$3 $\times 10^4$ cm^{-3}) which is a typical depletion density threshold [5]. Possibly, the low density envelope, where depletion has not yet occurred, is very extended in this cloud (which is confirmed by its large influence on the $C^{18}O$ (J:2–1) line intensity [25]. Finally, the depletion factor in volume for CO has been estimated to be 43 on average [5] on the line of sight of the main dust peak and is probably much higher in the inner part of this core where density is above 1 $\times 10^5$ cm^{-3}.

5.2.3 N_2H^+ and N_2D^+

N_2H^+ and N_2D^+ have been mapped at both low [Kitt Peak 12-m, 5] and high (IRAM 30-m) resolutions. From the high resolution data, a strip crossing the main dust peak has been extracted and published [7]. In that paper, we performed a detailed analysis of the N_2H^+ and N_2D^+ emission with the help of a Monte-Carlo model treating exactly the hyperfine structure and line overlap of these species. We derived several physical properties, namely : a maximum density of 2 $\times 10^6$ cm^{-3}, with a radial dependence proportional to r^{-1} up to 4000 AU and proportional to r^{-2} beyond, a kinetic temperature of 7 ($\pm$ 1) K, a slight depletion of N_2H^+ in the inner 3000 AU of the core and a deuterium fractionation which is non-measurable at 10^4 AU ($<$ 0.03) and reaches $\sim$0.7 ($\pm$ 0.15) in the center. As far as we know this is the highest fractionation reported yet for a singly deuterated species. This may however not be exceptional when compared to the detection of triply deuterated species, like ND_3 [26, 27] and CD_3OH [28] or to the fact that most reported fractionations are line-of-sight averages and not derived from detailed profiles.

139

Table 5.2: Source parameters : distance from the core center, H_2 density, N_2H^+ abundance and N_2D^+/N_2H^+ ratio. The position is measured away from the PSC center along the R.A. axis [from 7].

Position		H_2 density	N_2H^+ abundance	N_2D^+/N_2H^+
(AU)	(arcsec)	(cm^{-3})		
0	0	$2.09\ 10^6$	2.40E-11	0.69 ± 0.15
1310	12	$9.23\ 10^5$	8.50E-11	0.42 ± 0.05
2620	24	$5.33\ 10^5$	1.10E-10	0.25 ± 0.02
3930	36	$3.22\ 10^5$	1.53E-10	0.16 ± 0.03
5240	48	$1.86\ 10^5$	1.27E-10	0.06 ± 0.02
6550	60	$7.08\ 10^4$	1.00E-10	≤ 0.03

5.3 ANALYSIS

We present 3 models in this paper : a Monte-Carlo model to compute H_2D^+ and D_2H^+ line intensities, a chemical steady-state model and a chemical time-dependent model.

Compared to previous works, we benefit here from two new sets of coefficients and a large set of observations in a PSC. The $H_3^+ + H_2$ (+isotopologues) set of rate coefficients are extracted from the PhD work of E. Hugo in advance of publication and the H_3^+ (and deuterated counterparts) recombination rates have been computed for this work by V. Kokoouline and C. Greene and are presented in Appendix 5.B. Rate coefficients, as computed by E. Hugo, describe all possible interactions between trihydrogen cation and dihydrogen isotopologues, including reactive and non-reactive, elastic and inelastic collisional rates, while recombination coefficients describe the dissociative recombination (DR) rates of trihydrogen cation isotopologues. Both works take into account all the ortho, para and (D_3^+) meta states.

5.3.1 Line emission

We have analysed the line emission of both ortho–H_2D^+ and para–D_2H^+ using a two-level Monte-Carlo code [adapted from 29] with our new collisional coefficients. Because the temperature of the PSC is around 7 K for both the gas [7] and the dust [20, 22], the possibility to populate the next rotational level, $J_{KK''} = 2_{12}$ at 114 K and 75 K above ground level for ortho–H_2D^+ and para–D_2H^+ respectively, is so low that it can be safely ignored. With the new coefficients, the critical densities are 1.1×10^5 and 4.9×10^5 cm^{-3} respectively and thus the lines are close to thermal equilibrium in the inner core. In the case of ortho–H_2D^+, the difference between LTE ($\sim 2.0 \pm 0.25 \times 10^{13}$ cm^{-2}) and Monte-Carlo ($\sim 2.3 \pm 0.25 \times 10^{13}$ cm^{-2})
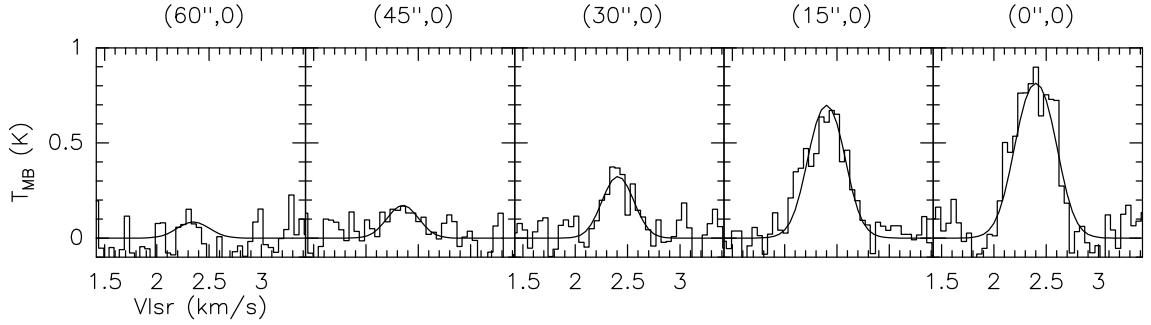
Figure 5.3: o–H_2D^+ (1_{10}-1_{11}) spectra across the main dust peak. East and west sides are folded together and fitted with a Monte-Carlo model. Density and temperature profiles are taken from Pagani et al. [7]. Spacing between spectra is $15''$.

column density estimates is typically 10–15% in the direction of the dust peak.

The para–D_2H^+ line has not been detected [see 11] and the 3 σ upper limit corresponds to a total column density of $\sim 2.4 \times 10^{13}$ cm^{-2} using the Monte-Carlo code. The LTE estimate yields $\sim 1.5 \times 10^{13}$ cm^{-2}.

5.3.2 Deuteration

H_3^+ ions are formed at a rate 0.96 ζ by cosmic ray ionization of H_2 [15, rapidly followed by a reaction with another H_2 to form H_3^+] and destroyed in reactions with neutral species and in dissociative recombination with free electrons, negatively charged grains and possibly negatively charged polycyclic aromatic hydrocarbons (PAHs$^-$). In prestellar cores, the primary reservoirs of hydrogen and deuterium are H_2 and HD, respectively, with HD/H_2 = 2(D/H)$_{cosmic}$ $\sim 3.2 \times 10^{-5}$ [30]. The proton exchanging reaction of H_3^+ with H_2 partly regulates the H_2 ortho–to–para ratio but has no effect on the H_3^+ abundance. Concurrently, the reaction with HD forms H_2D^+ and this primary fractionation is then followed by the subsequent fractionations and produces D_2H^+ and D_3^+ [13, 14]:

$$H_3^+ \ + HD \ \longleftrightarrow \ H_2D^+ + H_2 + 232K \qquad (5.1)$$

$$H_2D^+ + HD \ \longleftrightarrow \ D_2H^+ + H_2 + 187K \qquad (5.2)$$

$$D_2H^+ + HD \ \longleftrightarrow \ D_3^+ \ \ + H_2 + 234K \qquad (5.3)$$
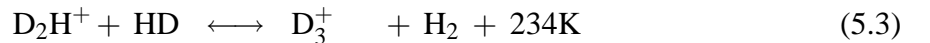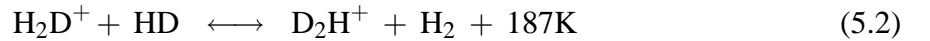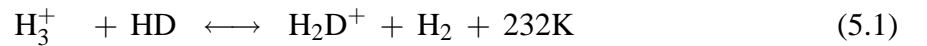
The backward reactions are endothermic with an energy barrier of about 200 K (when considering only the ground level for each species) and were thought to be negligible at the low temperatures found in prestellar cores ($\leq$ 20 K) in which case the abundance ratios $\frac{[H_n D_{3-n}^+]}{[H_{n+1} D_{2-n}^+]}_{n=0,1,2}$ would be greatly enhanced. However, such enhancement can be limited by various processes (see Fig. 5.4):
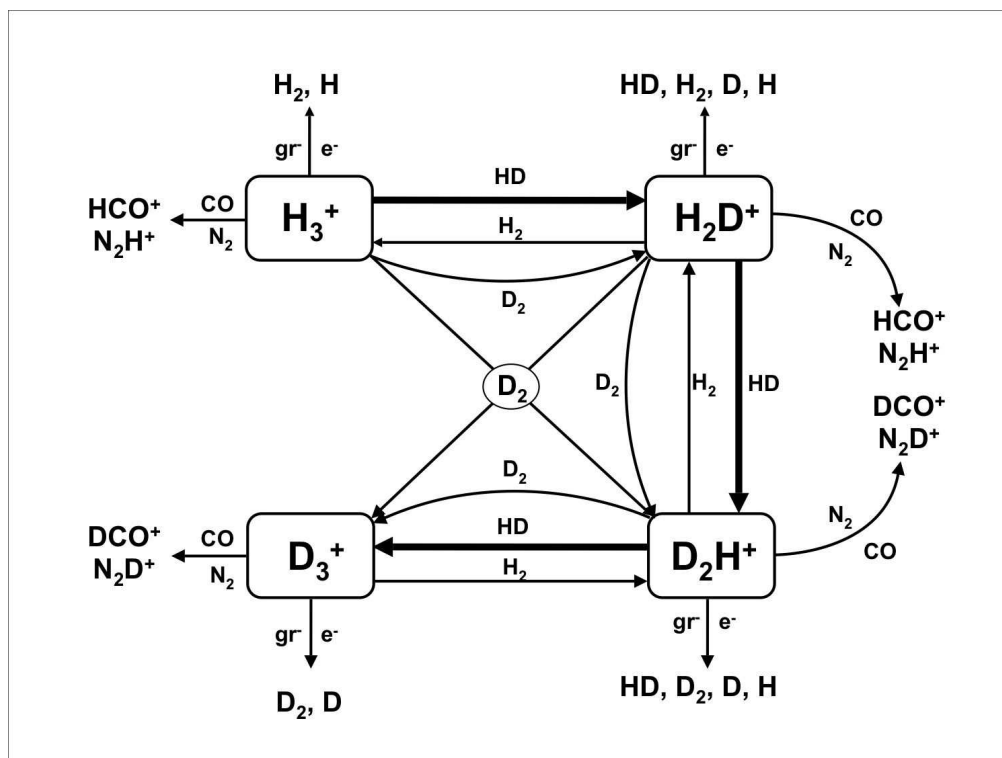
Figure 5.4: Main reactions involved in the H_3^+ chemical network. When CO and N_2 are depleted, the reactions with bold arrows are dominant.

- dissociative recombination of H_3^+ (and its deuterated counterparts) with free electrons or negatively charged grains (and $PAHs^-$?).

- reactions with "proton-friendly" molecules such as CO and N_2 which destroy the trihydrogen cations to produce HCO^+ and N_2H^+

- ortho–H_2 which can react with the deuterated trihydrogen cation and remove the Deuterium (see below)

In this modeling, we introduce the backward reactions to equations (1), (2), and (3) as we distinguish between ortho, meta and para states of the different species. When these reactions are completely neglected, the deuteration fractionation is considerably enhanced and observations towards pre-stellar cores cannot be reproduced [14]. Indeed, the importance of considering ortho and para states of various H/D carriers in the chemistry of trihydrogen cation and isotopologues was first discussed by Pagani et al. [16] and subsequently expanded in a series of papers by Flower and coworkers [15, 18, 19, 31, hereafter collectively referred to as FPdFW]. *Not only is this important to compare the chemical model predictions on the abundance of H_2D^+ to the sole observations of the ortho–H_2D^+ species but also because some important reactions*

are much faster with ortho–H_2 than with para–H_2 hence not anymore neglectable. Indeed, the 170K internal energy of the lowest ortho–H_2 level (J=1) is large with respect to the temperatures of concern and can significantly enhance the Boltzmann factor of endothermic reactions. In some cases, reactions which are endothermic with para–H_2 can turn out to be exothermic with ortho–H_2 i.e. fast and temperature independent. *In fact, the ortho–to–para ratio of H_2 is found to be a crucial parameter for the whole deuterium chemistry.*

The key reactions involving ortho–H_2 are essentially with meta–D_3^+, para–D_2H^+ and ortho–H_2D^+ as well as para–H_2D^+ (see rates in Appendix A) because the internal energy of the ortho–H_2 alone is not enough to overcome the endothermicity of reactions 1 to 3. Thus only those species which have also an internal energy high enough (so that the sum of the two internal energies is higher than the endothermicity of reactions 1 to 3) can react with ortho–H_2 at the Langevin rate in cold gas. Thus, the three reactions involving ortho–H_2 with meta–D_3^+, para–D_2H^+ and ortho–H_2D^+ present exothermic or thermoneutral channels to rehydrogenate the cations forming respectively ortho–D_2H^+, para–H_2D^+ and ortho/para–H_3^+ while the reaction between ortho–H2 and para–H_2D^+ can efficiently convert the latter to ortho–H_2D^+. The ortho–H_2 molecule thus opens a path to climb the 4 step energy ladder back from para–D_2H^+ to H_3^+ via para–H_2D^+ and ortho–H_2D^+ which can be very efficient in presence of large ortho–H_2 fractions. However, this efficient ladder scheme does not include D_3^+ because the conversion of ortho–D_2H^+ to para–D_2H^+ is strictly forbidden in collisions with H_2 and very inefficient in collisons with HD. Nevertheless, these reactions can be a strong limit to the isotopic fractionation of H_3^+ hence of other species. Any chemical model which includes Deuterium chemistry must distinguish between ortho and para states of dihydrogen and trihydrogen cation isotopologues and include reactions between the different spin states following Pagani et al. [16], Flower et al. [19; 31] and the present work.

5.3.3 CO and N_2 chemistry

The CO and N_2 abundances are critical parameters in the deuteration of the H_3^+ ion. CO is expected to freeze-out onto the grain mantles at large densities (a few 10^4 cm^{-3}) and low temperatures (≤ 20 K) [e.g. 1, 3, 5, 32, 33]. With an N_2 binding energy similar to the CO binding energy [34, 35], these two molecules are expected to behave similarly. However, observations towards prestellar cores prove that N_2H^+ (produced from N_2) remains in the gas phase at larger densities than CO. This can be explained by the fact that N_2H^+ is mainly destroyed by CO [5, 36, 37], so that the CO freeze-out implies a drop in the destruction rate of N_2H^+. This would partially balance the lower formation rate due to the N_2 freeze-out. Consequently, N_2H^+ is observed to survive in the gas phase at higher densities ($\sim 10^6$ cm^{-3}). In the case of L183, we have shown that N_2H^+ partially survives but suffers from depletion at densities starting at $\sim 5 \times 10^5$ cm^{-3} to reach a factor 6^{+13}_{-3} at the core centre ($\sim 2 \times 10^6$ cm^{-3}). Because of growing Deuterium fractionation, N_2D^+ abundance still increases towards the PSC center until the N_2 depletion becomes predominant over the Deuterium enhancement, and in turn, the N_2D^+

abundance slightly decreases in the inner most part of the core [7].

The N_2D^+ and N_2H^+ ions can be produced via the following routes:

$$H_3^+ + N_2 \rightarrow N_2H^+ + H_2 \tag{5.4}$$
$$H_2D^+ + N_2 \rightarrow N_2D^+ + H_2 \quad (1/3) \tag{5.5}$$
$$\rightarrow N_2H^+ + HD \quad (2/3) \tag{5.6}$$
$$D_2H^+ + N_2 \rightarrow N_2D^+ + HD \quad (2/3) \tag{5.7}$$
$$\rightarrow N_2H^+ + D_2 \quad (1/3) \tag{5.8}$$
$$D_3^+ + N_2 \rightarrow N_2D^+ + D_2 \tag{5.9}$$
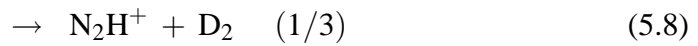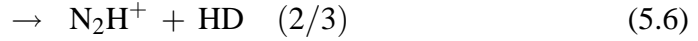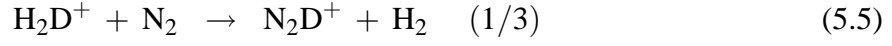
We assumed that all the H_3^+ isotopologues react at the Langevin rate k_{N_2} with N_2 (which is inversely proportional to the square root of the reduced mass of the colliding system, hence to the mass of the H3+ isotopologue) and that deuterium and hydrogen nuclei are equiprobably transferred. Consequently, H_3^+, H_2D^+, D_2H^+ and D_3^+ respectively produce a N_2D^+:N_2H^+ ratio of 0:3, 1:2, 2:1 and 3:0. The measured ratio of 0.7 ± 0.15 in the center of L183 thus implies significant fractions of D_2H^+ and D_3^+. It has been shown [15] that in the case of complete depletion of heavy species (C, N, O...), D_3^+ would be the dominant trihydrogen cation isotopologue which would imply that N_2D^+ be more abundant than N_2H^+. This is not the case here ; nevertheless the N_2H^+ deuterium fractionation is a good constraint to the abundance of the four trihydrogen cation isotopologues in our chemical model.

At steady state (d[N_2H^+]/dt=0 and d[N_2D^+]/dt=0), reaction 5.4 and its isotopic variants (5.5 to 5.9) being the main path to produce N_2D^+ and N_2H^+, we obtain :

$$\frac{[N_2D^+]}{[N_2H^+]} = \frac{[H_2D^+] + 2\,[D_2H^+] + 3\,[D_3^+]}{3\,[H_3^+] + 2\,[H_2D^+] + [D_2H^+]} \tag{5.10}$$

This ratio has been measured in the cut throughout the L183 main PSC. We describe in the following how our method can provide an estimate of the ortho/para H_2D^+ ratio using this variable and subsequently, of the ortho/para H_2 ratio itself as well as some indication of the cosmic ionization rate and mean grain size.

5.3.4 Grain distribution

Recombination of ions with electrons on negatively charged grain surfaces is an important process since it can be much faster than in the gas phase, especially in the case of H^+ [38]. The negatively charged grain surface area is therefore a crucial parameter [we can safely ignore positively and multiply negatively charged grains, advocated to be very rare in cold environments, 38]. The grain size distribution in prestellar cores is unknown since it mostly depends on grain condensation and also on ice condensation [e.g. 10]. We are thus treating the grain radius a_{gr} as a parameter of the model, assuming all the grains to have the same size and the dust to gas mass

ratio to be 0.01. Different values could be advocated [for example, in places where depletion is important, the ices increase the dust mass by up to 25%, 15] but the net result is to change slightly the average grain size which is not well-constrained in the PSCs in any case.

The focusing effect of the Coulomb attraction between charged particles and oppositely charged grains has been included using the Draine and Sutin [38] formalism:

$$\tilde{J}(Z=-1) = \left(1+\frac{1}{\tau}\right)\left(1+\sqrt{\frac{2}{2+\tau}}\right) \tag{5.11}$$

where τ is the reduced temperature ($\tau = a_{gr}kT/e^2$, e being the electron charge, k the Boltzman constant). Therefore the recombination rate of the H$^+$ ion on a negatively charged grain can be expressed as:

$$k_{gr} = \sqrt{\frac{8kT}{\pi m_H}}\pi a_{gr}^2 \big(S \times \tilde{J}(Z=-1)\big) \tag{5.12}$$

where a_{gr} is the grain radius, m_H is the hydrogen mass and S is the sticking coefficient ($S \leq 1$). The latter represents the probability that a colliding species will stick onto the grain surface. For ions, Draine and Sutin [38] concluded that the sticking coefficient should be unity. The same computation can be made to estimate the recombination rate of other ions, H$_3^+$, H$_2$D$^+$, D$_2$H$^+$, D$_3^+$,$\cdots$ by a simple correction on the atomic mass of the ions (respectively k$_{gr}/\sqrt{3}$, k$_{gr}/\sqrt{4}$, k$_{gr}/\sqrt{5}$, k$_{gr}/\sqrt{6}$, $\cdots$). In the case of collisions between charged particles and neutral grains, the attraction due to the polarization of the grain by the charged particle can be expressed through:

$$\tilde{J}(Z=0) = 1 + \sqrt{\frac{\pi}{2\tau}} \tag{5.13}$$

Therefore the sticking rate of electrons on neutral grains can be expressed as:

$$k_e = \sqrt{\frac{8kT}{\pi m_e}}\pi a_{gr}^2 \big(S \times \tilde{J}(Z=0)\big) \tag{5.14}$$

where m_e is the electron mass and S is the sticking coefficient. S is about unity [39] for a planar surface but curvature of the grain surface will tend to reduce this parameter. However we will use in the following a factor of about unity as this parameter did not seem to have a large influence on the results in our runs.

The grain abundance [gr] can be expressed using:

$$[gr] = \frac{m_{H_2}f_{d/g}}{\frac{4\pi}{3}a_{gr}^3\delta} \tag{5.15}$$

where δ is the mean grain density (assumed to be 3 g cm^{-3}, $f_{d/g}$ is the dust–to–gas mass ratio, and m_{H_2} is the mass of molecular hydrogen. Another important parameter in our model is the

abundance of the negatively charged grains ($[gr] = [gr^0] + [gr^-]$). At steady-state, assuming partial depletion of CO and N_2 and total depletion of all the other heavy species :

$$
\begin{aligned}
\frac{d[\mathrm{gr}^-]}{dt} \;=\; & [\mathrm{gr}^0][\mathrm{e}^-]k_e - [\mathrm{gr}^-][\mathrm{H}^+]k_{gr} \\
& - [\mathrm{gr}^-][\mathrm{H}_3^+]k_{gr3} - [\mathrm{gr}^-][\mathrm{H}_2\mathrm{D}^+]k_{gr4} \\
& - [\mathrm{gr}^-][\mathrm{D}_3^+]k_{gr6} - [\mathrm{gr}^-][\mathrm{D}_2\mathrm{H}^+]k_{gr5} \\
& - [\mathrm{gr}^-][\mathrm{N}_2\mathrm{H}^+]k_{N_2H^+} - [\mathrm{gr}^-][\mathrm{HCO}^+]k_{HCO^+} \\
& - [\mathrm{gr}^-][\mathrm{N}_2\mathrm{D}^+]k_{N_2D^+} - [\mathrm{gr}^-][\mathrm{DCO}^+]k_{DCO^+} \quad = 0
\end{aligned}
\tag{5.16}
$$

We have neglected here HD^+, D_2^+, He^+, *etc.*

5.3.5 Steady-state chemical model

The code we describe in the following is used to calculate the steady-state abundances of the chemical species found in the different layers of the L183 prestellar core as listed in Table 5.3.

In the steady-state approximation the abundance species are interlinked via their production rates and their destruction rates (production=destruction).
Since H_3^+ is produced at a rate 0.96ζ, the H^+ abundance can be expressed as (including only the main reactions) :

$$
[\mathrm{H}^+] = \frac{0.04\zeta}{n_{H_2}\left([\mathrm{e}^-]k_{rec} + [\mathrm{gr}^-]k_{gr}\right)}
\tag{5.17}
$$

The main production path of H_3^+ is via cosmic ray ionization of H_2 and proceeds in two steps :

$$
\zeta + \mathrm{o{-}H_2} \;\rightarrow\; \mathrm{o{-}H_2^+} + \mathrm{e}^-
\tag{5.18}
$$

$$
\zeta + \mathrm{p{-}H_2} \;\rightarrow\; \mathrm{p{-}H_2^+} + \mathrm{e}^-
\tag{5.19}
$$
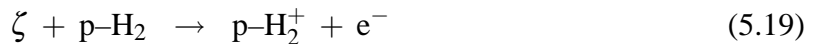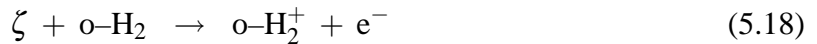
and H_2^+ rapidly reacts with another H_2 to form H_3^+ but the branching ratios between different combinations of spin states are non-trivial [40] :

$$\text{p--H}_2^+ + \text{p--H}_2 \quad \rightarrow \quad \text{p--H}_3^+ + \text{H} \tag{5.20}$$

$$\begin{aligned} \text{p--H}_2^+ + \text{o--H}_2 \quad &\rightarrow \quad \text{p--H}_3^+ + \text{H} \quad (2/3) \\ &\rightarrow \quad \text{o--H}_3^+ + \text{H} \quad (1/3) \end{aligned} \tag{5.21}$$

$$\begin{aligned} \text{o--H}_2^+ + \text{p--H}_2 \quad &\rightarrow \quad \text{p--H}_3^+ + \text{H} \quad (2/3) \\ &\rightarrow \quad \text{o--H}_3^+ + \text{H} \quad (1/3) \end{aligned} \tag{5.22}$$

$$\begin{aligned} \text{o--H}_2^+ + \text{o--H}_2 \quad &\rightarrow \quad \text{p--H}_3^+ + \text{H} \quad (1/3) \\ &\rightarrow \quad \text{o--H}_3^+ + \text{H} \quad (2/3) \end{aligned} \tag{5.23}$$
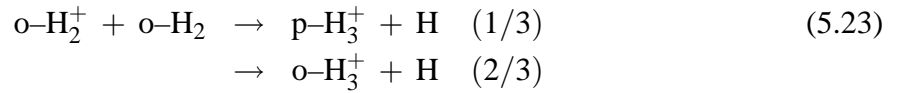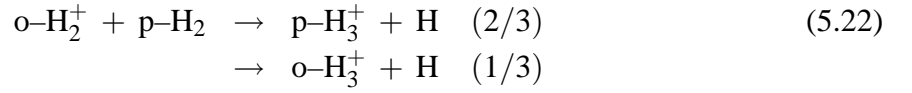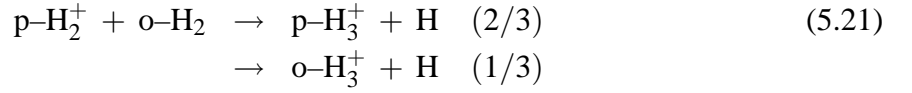
These are different from those advocated by FPdFW who took branching ratios of 1/2 for both species. The ortho–H_3^+ formation rate from cosmic ray ionization k_{cr-o} is therefore the sum of several terms:

$$k_{cr-o} = 0.96 \left(1/3 \, [\text{p--H}_2][\text{o--H}_2^+] + 1/3 \, [\text{o--H}_2][\text{p--H}_2^+] + 2/3 \, [\text{o--H}_2][\text{o--H}_2^+] \right) \tag{5.24}$$

The production rate for ortho–H_3^+ can be expressed as (including only the main reactions. The rates are listed in Table 5.3):

$$\zeta k_{cr-o} + n_{H_2} \left([\text{o--H}_2][\text{o--H}_2\text{D}^+] k\_1_{oood} + [\text{p--H}_3^+][\text{o--H}_2](k0_{poop} + k0_{pooo}) \right.$$
$$\left. + [\text{HD}][\text{p--H}_3^+] k1_{pdod} \right) \tag{5.25}$$

which represent respectively the formation from cosmic ray ionization, backward destruction of ortho–H_2D$^+$ with ortho–H_2, spin conversion of para–H_3^+ with ortho–H_2 and finally, spin conversion of para–H_3^+ with HD.

The destruction rate for ortho–H_3^+ can be expressed as (including only the main reactions):

$$n_{H_2} [\text{o--H}_3^+] \left([\text{e}^-] o\text{--}k_{rec1} + [\text{o--H}_2](k0_{oopp} + k0_{oopo}) \right.$$
$$+ [\text{HD}](k1_{odpd} + k1_{odpo} + k1_{odop} + k1_{odoo})$$
$$\left. + [\text{CO}]k_{co} + [\text{N}_2]k_{N2} + [\text{gr}^-]k_{gr1} \right) \tag{5.26}$$

which respectively represents its destruction by dissociative recombination with electrons, spin conversion with ortho-H_2, spin conversion and deuteration with HD, proton transfer reactions with CO and N_2 and finally, dissociative recombination on grains.

Similarly, the para–H_3^+ formation from cosmic ray ionization can be expressed as :

$$k_{cr-p} = 0.96 \Big(\quad [\text{p–H}_2][\text{p–H}_2^+] + 2/3 \, [\text{p–H}_2][\text{o–H}_2^+] +$$
$$2/3 \, [\text{o–H}_2][\text{p–H}_2^+] + 1/3 [\text{o–H}_2][\text{o–H}_2^+] \quad \Big) \tag{5.27}$$

The production rate for para–H_3^+ is :

$$\zeta k_{cr-p} + n_{H_2} \Big(\quad [\text{HD}][\text{o–H}_3^+] k1_{odpd} + [\text{o–H}_3^+][\text{o–H}_2](k0_{oopp} + k0_{oopo})$$
$$+ [\text{o–H}_2][\text{o–H}_2\text{D}^+] k\_1_{oopd} + [\text{o–H}_2][\text{p–H}_2\text{D}^+] k\_1_{popd} \quad \Big) \tag{5.28}$$

and the destruction rate is :

$$n_{H_2} \, [\text{p–H}_3^+] \Big(\quad [\text{e}^-] p\text{–}k_{rec1} + [\text{o–H}_2](k0_{poop} + k0_{pooo})$$
$$+ [\text{HD}](k1_{pdod} + k1_{pdpo} + k1_{pdop} + k1_{pdoo})$$
$$+ [\text{CO}]k_{co} + [\text{N}_2]k_{N2} + [\text{gr}^-]k_{gr1} \quad \Big) \tag{5.29}$$

The N_2 abundance has been solved numerically to obtain the observed N_2H^+ abundance. Electronic abundance is adjusted to reach equilibrium.

In our steady-state model, the H_2 ortho/para ratio, the average grain radius and the cosmic ionization rate ζ are the varying input parameters. Within each layer of the PSC model (Table 5.3), these parameters are adjusted to match the following :

- the H_2 density

- the N_2D^+/N_2H^+ ratio at 7K

- the observed ortho–H_2D^+ column density

- the upper limit on the p–D_2H^+ column density

Though the full range of grain sizes and ortho–to–para H_2 ratios have been explored for each H_2 density, we have not allowed solutions in which, for example, the grain size would oscillate from one layer to the next. We have searched solutions for these two parameters all through the layers which are either constant or we have allowed grain size to increase and ortho–to–para H_2 ratio to decrease with the H_2 density. In any case, ζ was kept constant throughout the layers. We neglected detailed reactions with D_2 as Flower et al. [18] have shown that its role is negligible in general and we have kept the HD abundance constant which is generally a good approximation.

5.3.6 Time-dependent chemistry

In a second step, we have constructed a pseudo time-dependent model based on NAHOON, a chemical model, a version of which has been made publicly available by V. Wakelam[2]. We have modified this model in two ways : 1) we have replaced electron (resp. ion) reactions with neutral (resp. charged) grains as provided in the Ohio State University (OSU) reaction file (delivered with NAHOON) by the set of equations described above (Sect. 5.3.4 and 5.3.5), which we have directly included in the program, to take into account Coulomb focusing ; 2) we have included the formation of HD and D_2 on grain surface and we have introduced the spin state of H_2 and D_2 taking the usual assumption that they are formed with the statistical ortho/para spin state ratio of 3 and 2 respectively. We have used the formation rate provided in Nahoon (5×10^{-17} $cm^3 s^{-1}$) for the formation of molecular hydrogen. Because grains are covered by ice in the environments here concerned, we consider that the only interaction between the atoms and the surface is physisorption. In this case, the formation rates of HD and D_2 (in $cm^3 s^{-1}$) is twice lower for HD and 10^5 times lower for D_2 with respect to H_2 formation [as dicussed in 41]. In environments where grains are not covered by icy mantles, on the other hand, one would have to consider chemisorption which strongly changes the efficiencies of the formation of HD and D_2 [42]. Finally, we have reduced the set of species and reactions to our needs, limiting ourselves to the most important reactions (see below) but differentiating all ortho and para (plus meta–D_3^+) species as independent species and including all the detailed rates between trihydrogen cation and dihydrogen isotopologues as computed by E. Hugo (see Sect. 5.3.7) including spin state conversions. We have however included more reactions than in the steady-state model, taking into account reactions with D_2, H_2^+, He^+, etc. and allowing the ortho/para H_2 ratio and the HD abundance to vary.

The main path to convert ortho–H_2 into para–H_2 is via the reaction

$$o–H_2 + H^+ \rightarrow p–H_2 + H^+ \qquad (5.30)$$

which proceeds seven orders of magnitude faster at 7 K than the reverse reaction.

5.3.7 Rate coefficients

Many groups have made available gas-phase rate coefficients. The University of Manchester Institute of Science and Technology (UMIST) Database for Astrochemistry contains information on 4500 reactions of which 35% have been measured experimentally, some at temperatures down to 20 K [43]. The OSU group provides approximately the same database but focuses more on low temperature chemistry. We accordingly use in our modeling some of the reactions in the latter (with the most recent version OSU2007), considering the low temperatures found in L183. Apart from the rates calculated by E. Hugo, V. Kokoouline and C. Greene that are

---

[2]http://www.obs.u-bordeaux1.fr/radio/VWakelam/Valentine%20Wakelam/Downloads.html

presented below, all reaction rates involving Deuterium have been taken from FPdFW (except recombination on grains for which we have used different sticking probabilities). We have given up the odd branching ratio of N_2H^+ dissociative recombination reported by Geppert et al. [44] to consider a single possibility, namely the liberation of the dinitrogen [45].

$H_3^+ + H_2$ isotopologues reaction rates

Phase space theory (PST) was used to derive thermal state-to-state rate coefficients for the whole $H_3^+ + H_2 \rightarrow H_3^+ + H_2$ system and isotopic variants in the temperature range 5–50K. This statistical method accounts for such quantities as mass, energy, rotational angular momentum, nuclear spin symmetry and their respective conservation laws. The ergodic hypothesis which is a requisite for PST as well as the full-scrambling hypothesis are assumed according to the topology of the PES [46, 47]. Reactants (products) trajectories are treated with the classical Langevin model. The resulting set of state-to-state rate coefficients deviates from the detailed balance principle by few percents at worst and is well consistent with thermodynamical equilibrium constants. Details will be given in a forthcoming publication (Hugo et al., in prep.)

In the present astrochemical model, nuclear spin states of the different molecules are treated as distinct species but their rotational states are not considered individually. We thus made the assumption that only the rotational ground states of each nuclear spin species were populated and used the ground state-to-species thermal rate coefficients obtained by summing ground state-to-state thermal rate coefficients over the product channels.

H_3^+ isotopologues dissociative recombination rates

The dissociative recombination (DR) rate of H_3^+ has a long story behind it due to the high difficulty to measure it experimentally. Since the early measurements e.g. by Adams et al. [48], numerous attempts have been carried out and summarized in two papers [49, 50]. In parallel, theoretical work has also been developed with the latest achievement published by Fonseca dos Santos et al. [50]. Extending upon that work, we present here, in Table 5.4, the H_3^+ updated DR rate [50] along with newly calculated H_2D^+, D_2H^+, and D_3^+ DR rates (see appendix B for more details). These calculations do not predict the branching ratio of the DR products. We have thus adopted the branching ratios published elsewhere [51–54] which we have applied to the calculated rates. The resulting DR rates at 7 K are listed in Table 5.3. Several remarkltyable effects at low temperature are visible (see Figs 5.10a, 5.10b, 5.10c, 5.10d) :

- the strong departure of ortho–H_3^+ DR rate from that of para–H_3^+. The difference is a factor of 10 at 10 K.

- D_2H^+ shows a large DR rate drop, by a factor of 10 at 10 K for both ortho and para species compared to the extrapolated value used by FPdFW.

- On the contrary, a large increase of the D_3^+ DR rate is predicted to occur but mostly at temperatures where deuteration is low and therefore the consequence on D_3^+ abundance is limited.

5.4 RESULTS AND DISCUSSION

5.4.1 H_2D^+ linewidth

In order to fit the observed ortho–H_2D^+ line profiles, we run the Monte-Carlo model using the "best model" velocity, density and temperature profiles derived from the N_2H^+ and N_2D^+ data analyzed in Pagani et al. [7]. However, the linewidth for the two stronger spectra (offsets (0,0) and (15″,0), Fig. 5.3) is too wide to be reproduced with the same micro–turbulent width which we have used for N_2H^+(Δv_{turb}(FWHM) ≈ 0.14 km s^{-1}). Indeed, the central spectrum linewidth measured by fitting a gaussian, yields 0.45 ($\pm$0.03) km s^{-1}. The thermal contribution being

$$\Delta v_{therm}(FWHM) = 2.336 \times \sqrt{\frac{kT}{m}} = 0.28 \text{ km s}^{-1} \tag{5.31}$$

at 7 K, k being the Boltzmann constant and m the mass of H_2D^+, the Δv_{turb}(FWHM) contribution is 0.35 km s^{-1}, 2.5 times larger than for N_2H^+. If we impose a turbulent velocity similar to the one modeled for N_2H^+, then the temperature needed to obtain such a wide line would be 16K which is completely ruled out by N_2H^+ observations [7]. Infall motion limited to the inner core could have explained the H_2D^+ width if only the central H_2D^+ spectrum had been wide combined with a large depletion of N_2H^+. In fact it is not possible because the H_2D^+ spectrum at (15″,0) has the largest width (0.49 $\pm$0.03 km s^{-1}) in a region where N_2H^+ is hardly depleted. This remains therefore a pending problem.

5.4.2 N_2H^+ deuteration

Requested conditions

We next discuss here the main parameters that control the N_2H^+ deuteration using the steady-state chemical model.

The models have been run for a temperature of 7 K which prevails in all the layers where N_2D^+ has been detected in the PSC cut presented in Pagani et al. [7]. We have also run the models for the corresponding density, N_2H^+ abundance and N_2D^+/N_2H^+ ratio of each layer (the parameters are listed in Table 5.3).

As discussed above, the abundance of ortho–H_2 is the main controlling factor of the trihydrogen cation isotopologue abundances and therefore of the N_2D^+/N_2H^+ ratio [and similarly of the DCO^+/HCO^+ ratio, see e.g. 55]. We have therefore explored the range of possible solutions for the ortho/para H_2 ratio in the two extreme layers of our core profile (n(H_2) = 7×10^4 cm^{-3}
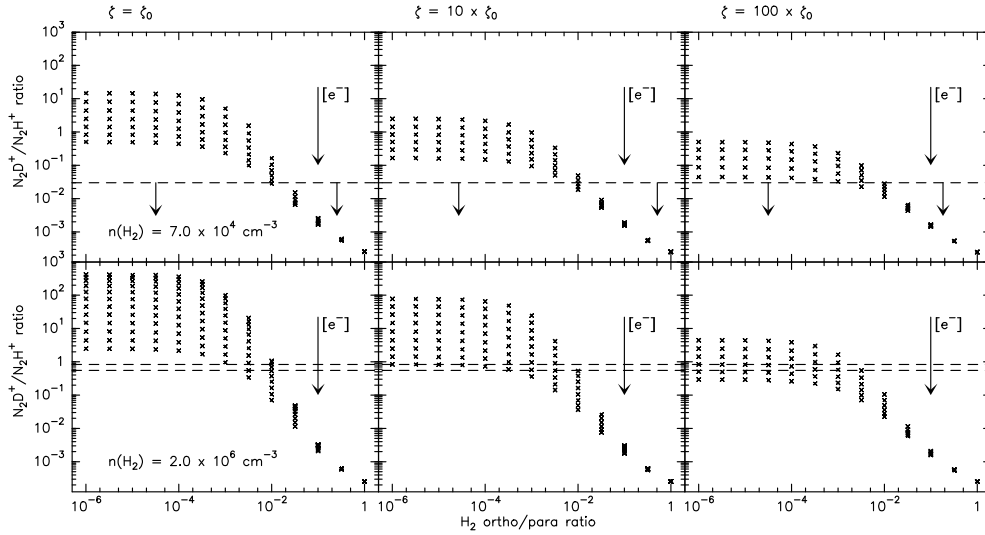
Figure 5.5: N_2D^+/N_2H^+ ratio as a function of ortho/para H_2 ratio for all possible electronic abundances and total CO depletion (steady-state chemical model). The lower row corresponds to the densest part of the PSC ($n(H_2) = 2 \times 10^6$ cm^{-3}) and the two horizontal dashed lines the measured range of N_2D^+/N_2H^+ ratio while the upper row corresponds to the external part of the PSC ($n(H_2) = 7 \times 10^4$ cm^{-3}) with the dashed line representing the N_2D^+/N_2H^+ ratio upper limit. The three columns represent different ζ values as indicated above ($\zeta_0 = 1 \times 10^{-17}$ s^{-1}) . The large arrow indicates the direction of increasing electronic abundance.
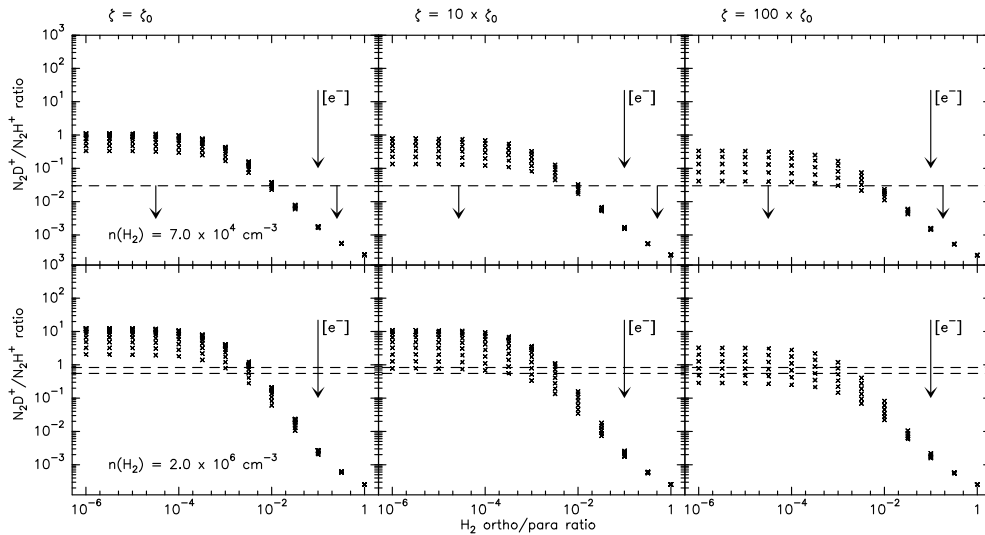
Figure 5.6: Same as Fig. 5.5 but with a CO/H_2 abundance of 10^{-5} in the outer layer ($n(H_2) = 7 \times 10^4$ cm^{-3}) and 10^{-6} in the inner layer ($n(H_2) = 2 \times 10^6$cm^{-3}).

and $2 \times 10^6 \mathrm{cm}^{-3}$) for which we have a $\mathrm{N_2D^+/N_2H^+}$ ratio of <0.03 and 0.7 ± 0.15 respectively (Fig. 5.5). We have done this for three cosmic ray ionization rates (10^{-17}, 10^{-16}, and 10^{-15} s^{-1}) covering the values generally discussed in the literature [e.g. 55] and for all possible electronic abundances (or average grain size as they are linked via the abundance of $\mathrm{H^+}$ which is mostly controlled by the grain surface area). In this first run, we have simulated total depletion by adjusting CO and $\mathrm{N_2}$ abundance[3] to 10^{-8}. We have also indicated the range of $\mathrm{N_2D^+/N_2H^+}$ ratio measured in both layers. The average grain radius has been varied from 0.01 μm to 5 μm and electronic abundance from 10^{-11} to 10^{-6} which are largely covering usually accepted values. We can see that $\mathrm{N_2D^+/N_2H^+}$ ratios above 100 are possible in dense gas though they require very low electronic abundances and therefore very small grains which are probably absent from these dense and cold regions due to grain coagulation [see e.g. 56].

In the lower density outer layer where no $\mathrm{N_2D^+}$ has been detected, ortho/para $\mathrm{H_2}$ ratio must be high enough, i.e. above ~ 0.01, to prevent any deuteration to occur whatever the cosmic ray ionization rate. On the contrary, the dense, strongly deuterated layer has solutions only below a maximum ortho/para $\mathrm{H_2}$ ratio of 0.01 (or lower for high ζ rates). Thus the ortho/para $\mathrm{H_2}$ ratio across the PSC clearly must vary from above 0.01 to below 0.01. In the case of low cosmic ray ionization rate (10^{-17} s^{-1}), though the ortho/para $\mathrm{H_2}$ ratio of 0.01 seems to be a common solution for both layers, it must be noticed that it requires a large electronic abundance (and large grains) in the outer layer and a low electronic abundance (and small grains) in the inner dense part. This is clearly improbable. Temperature being low enough in all the layers, warm layers (above 20 K) cannot be invoked instead of a high ortho/para $\mathrm{H_2}$ ratio to limit the deuteration in the outer parts of the PSC. CO total depletion is however questionable and we also used in the model a CO depletion factor of 10 (abundance of 10^{-5}) in the outer layer and a CO depletion factor of 100 (abundance of 10^{-6}) in the inner layer (Fig. 5.6). This only limits the maximum $\mathrm{N_2D^+/N_2H^+}$ ratio which decreases by one order of magnitude. Indeed, the destruction of $\mathrm{H_3^+}$ by CO dominates over recombination with electrons when their abundance is very low and conversely. However, the conditions to reach the observed $\mathrm{N_2D^+/N_2H^+}$ ratio remain unchanged and therefore *only a variable ortho/para $\mathrm{H_2}$ ratio can be invoked*. Such a variable ortho/para $\mathrm{H_2}$ ratio cannot be investigated with a steady-state model because in all layers, the ortho–$\mathrm{H_2}$ abundance would eventually decrease to values about 10^{-3}–10^{-4} as discussed by FPdFW.

The ortho/para $\mathrm{H_2}$ variation

We discuss here the possibilities to make the ortho/para $\mathrm{H_2}$ ratio vary across a single PSC.

It is commonly accepted that $\mathrm{H_2}$ is formed on grain surfaces with an ortho/para ratio of 3 because of spin statistics and the exothermicity of the reaction $\mathrm{H + H \rightarrow H_2}$. Subsequently, the ortho–$\mathrm{H_2}$ is converted into para–$\mathrm{H_2}$ following equation 5.30 and to a lesser extent with reactions involving $\mathrm{H_3^+}$ and its isotopologues. As already discussed by FPdFW, this conversion is slow and has probably not reached steady state in clouds with ages between 10^5 and 10^6 years.

---

[3]Here, we look for general solutions of the $\mathrm{N_2D^+/N_2H^+}$ ratio as a function of several parameters, we thus do not try to fit the $\mathrm{N_2}$ abundance to get the observed $\mathrm{N_2H^+}$ abundance

We have therefore run the modified Nahoon model to search for a coincidental solution for all layers which would get the necessary ortho/para H_2 gradient across the PSC to both explain the observed N_2D^+/N_2H^+ ratio and ortho–H_2D^+ abundance profiles. In this model, we have no direct measurement of the CO abundance but for the credibility of the model, we have set CO abundance to 10^{-5} in the outer layer and increased the depletion to reach a factor of 100 (i.e. a CO abundance of 10^{-6}) in the core. The results are presented in Figs. 5.7 & 5.8. We have searched for a solution where each modeled layer meets the two observational constraints (N_2D^+/N_2H^+ ratio and ortho–H_2D^+ abundance) at the same time, but it must be noticed that these solutions are not coincidental in between the different layers. We varied the average grain radius and the cosmic ray ionization rate, ζ. We could find solutions for grains of average radius 0.025 to 0.3 μm . No solution has been found for grains above 0.3 μm. Figs. 5.7 & 5.8 show the case for which the grain average radius is 0.1 μm and $\zeta = 2 \times 10^{-17}$ s^{-1}. In this case, the time range inside which all layers meet the requested conditions is 0.6 to 1.7×10^5 years. Figure 5.8 shows how the ortho/para H_2 ratio evolves for 3 selected layers. We have marked the appropriate time which is the solution for each of these layers as established from Fig. 5.7. In that figure, we can see that the o/p H_2 ratio is below 0.01 for the dense layers and still above 0.01 for the outer layer for which no H_2D^+ has been detected, as expected from the steady-state model. We can also see that the full o/p H_2 relaxation has not yet occurred even for the densest part of the cloud. Smaller grains have a larger interacting surface and therefore lower the abundance of H^+ ions which preferentially recombine on negatively charged grains (or PAHs$^-$), consequently slowing down the dominant ortho–H_2 relaxation reaction (eq. 5.30). Though smaller grains also imply a lower electronic density, therefore favouring a higher deuteration of N_2H^+ as shown in Fig. 5.5, the slower disappearance of ortho–H_2 is the dominant process here and finally, smaller grains slow down the deuteration process. For grains of average radius 0.025 μm, the range of ages matching the range of N_2H^+/N_2D^+ observed ratios is 2.7–3.8×10^5 years, while for grains of average radius 0.3 μm, the time range is only 3.8–7.2×10^4 years. Finally, Fig. 5.8 suggests that D_2 should become a sizeable fraction of available deuterium a short while after present state (typically 2–3×10^5 years) and that HD should drop a little, correspondingly.

5.4.3   Age of the core and collapse

Though it is normal that dense layers evolve faster than less dense ones, at least to account for a differential ortho/para H_2 ratio, they are evolving too fast in our model. The densest layers would have reached their present status 2 to 3 times faster than the outer, less dense layers. This could be possible only if the denser layers had reached their steady-state equilibrium. This is not the case here where the densest layer would reach its steady-state equilibrium after 2 $\times 10^5$ years only and this would imply a N_2D^+/N_2H^+ ratio of 6, almost an order of magnitude larger than observed. The most probable reason for this time discrepancy is that the core has undergone a contraction and therefore all layers were not so dense in the past. While the outer layers have little evolved in density (the most external one has probably started at 0.5–1×10^4
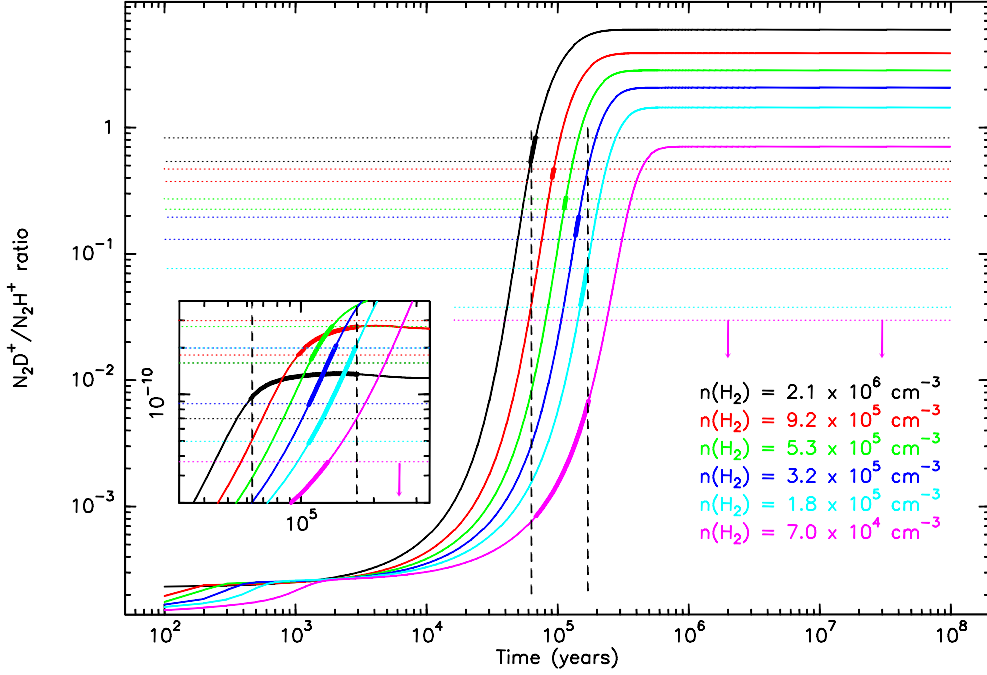
Figure 5.7: Time-dependent variation of the N_2D^+/N_2H^+ ratio for the 6 layers defined in Table 5.3. For each colour, the density of the layer is given. In the insert, the ortho–H_2D^+ abundance is represented with the same color code, zoomed on the epoch of interest. Horizontal dot lines represent the observed N_2D^+/N_2H^+ ratio range for each layer and the observed ortho– H_2D^+ abundance as derived from the Monte-Carlo model applied to the JCMT observations. The part of the chemical solution which fits in both these limits and the common time limits is set in bold. Vertical arrows indicate upper limits for the N_2D^+/N_2H^+ ratio. Vertical dashed lines are placed at 0.63 and 1.7×10^5 years to delimitate the period when all layers reach their observed N_2D^+ enrichment. This case has been computed for an average grain radius of 0.1 μm and $\zeta = 2 \times 10^{-17}$ s^{-1}.

cm^{-3} to reach 7×10^4 cm^{-3} today), the inner ones have undergone a much larger density increase. As constant density through the core would give no chemical differentiation while a time-frozen density profile as measured here gives too much differentiation, the solution is in between the two. Starting from a uniform gas, the chemical differential evolution of the core should therefore help us to constrain the duration of the contraction and the type of contraction. Of course the model should also include the evolution of depletion which also plays a role in the process acceleration.

As the core must have started to contract from a lower density region, typically 10^4 cm^{-3}, it is clear that all layers have accelerated their chemical evolution while their density has been increasing. Therefore, the layer with the longest time to reach the observed N_2D^+/N_2H^+ ratio is giving a lower limit to the age of the cloud. Depending on the exact average size of the
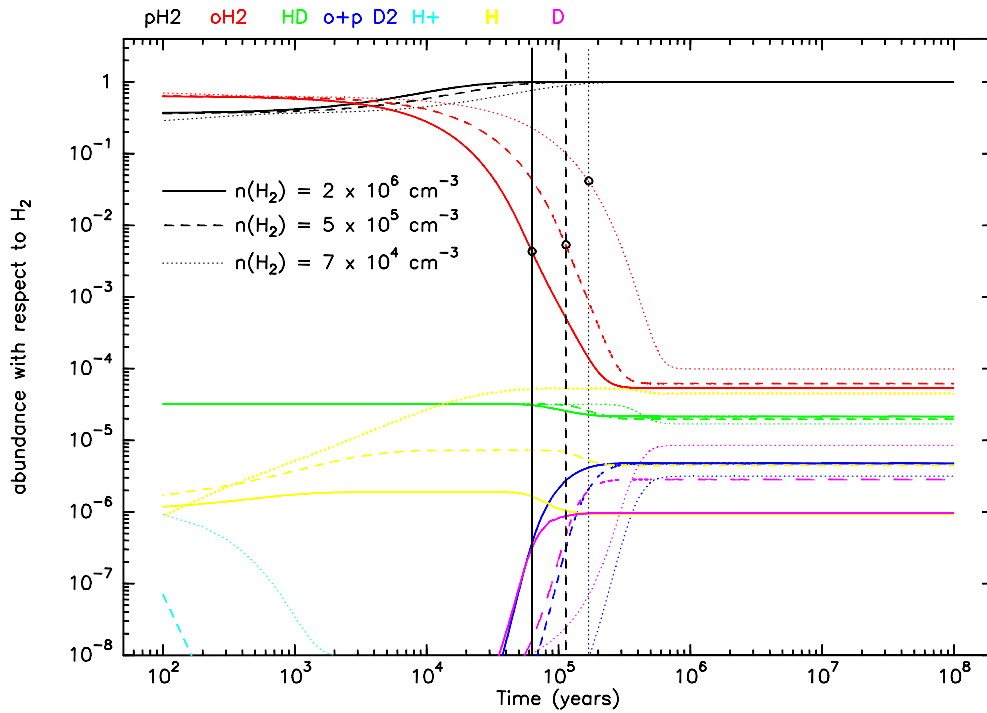
Figure 5.8: Time-dependent variation of the ortho– and para–H_2 and other related species for 3 of the 6 layers defined in Table 5.3 (layers 1, 3 and 6) . Vertical lines are placed at the times corresponding to the observed N_2D^+/N_2H^+ ratio in Fig. 5.7 for the same 3 densities. This case has been computed for an average grain radius of 0.1 μm and $\zeta = 2 \times 10^{-17}$ s^{-1}.

grains, this lower limit is 1.5–2 $\times$ 10^5 years here. In fact it is even larger because before the cloud underwent contraction, depletion had not yet occured and therefore, species like atomic sulfur, S, must have been present in quantities large enough to transfer notable quantities of electric charges from H^+ to S^+ ($H^+ + S \rightarrow H + S^+$) and PAHs must have also been abundant enough to help destroy H^+ ions [57]. All these phenomena contribute to the diminution of the H^+abundance, therefore slowing down the ortho–H_2 relaxation process. Indeed, Flower et al. [31] show that the relaxation process in some cases takes 3 $\times$ 10^7 years, typically 50 times slower than in the case presented here (and 15 times slower for similar conditions of grain size and cosmic ray ionization rate but without depletion in their case).

5.4.4 Para–D_2H^+

It must be noted that at 7 K, the strongest possible line intensity (LTE case) for the ground transition of para–D_2H^+ is below 0.3 K because of the Rayleigh-Jeans correction at 691 GHz which becomes very important. Moreover the thermalization of the line is difficult to obtain in this source beyond the radius of 3000 A.U. because the PSC density drops below the para–

D_2H^+ critical density ($n_{crit} = 4.9 \times 10^5$ cm^{-3}) beyond and a slight drop of the excitation temperature turns into exponential decrease of the brightness temperature. For $T_{ex} = 6$ K, $T_{bright} \leq$ 0.13 K. Therefore searches for para–D_2H^+ must reach very low noise level to have a chance of detection. From the models we present here, we predict an integrated line intensity of 11 mK km/s (34 mK peak) with the Monte-Carlo model, and an upper limit of 16 mK km/s (48 mK peak) in the case of LTE. This is a factor of 3 to 4 below the upper limit we have obtained from the observations.

5.4.5   The chemical profile

Finally, we obtain a detailed profile of the PSC which we present in Fig. 5.9. It represents the solution for the model which we presented in Figs. 5.7 & 5.8 taking for each layer the values at their respective best-fit time. The large variation of the ortho–H_2 species across the core (factor 15) makes D_3^+ change by an even larger amount (2 orders of magnitude) but it does not become the most abundant trihydrogen cation isotopologue in the core center at this stage because the ortho-H_2 abundance is not yet low enough. In the present case, for a density of 2 $\times$ 10^6 cm^{-3}, the inversion between H_3^+ and D_3^+ occurs when the abundance of ortho-H_2 drops below 3×10^{-3}.

The ortho/para H_2 ratio in the outer layer is 0.04 (as expected from Fig. 5.6 which indicates a lower limit of 0.01). As discussed above, the ortho/para H_2 ratio evolution speed is linked to density and grain size, both of which are lower outside the PSC, in its embedding parental cloud. We can thus expect this ratio to be at least 0.05 and probably above 0.1 in the envelope of the cloud.

N_2 is an input parameter in our model because we have not included all the Nitrogen chemistry. As reactions with H_3^+ isotopologues are the main path to destroy this molecule [31], we do not make a large error in determining its abundance directly from the N_2H^+ abundance itself and obtain a N_2 profile which is probably closer to the reality than if we had let the whole N-chemistry freely establish its abundance because of too many unknowns. The abundance profile thus starts at 1.5×10^{-7} with respect to H_2 in the low density layer to diminish to 3×10^{-8} in the densest layer. The undepleted N_2 abundance after attainment of the steady state is $\sim 3 \times 10^{-5}$ [31] but this is reached only after $\approx 5 \times 10^6$ years. As depletion of N_2 in the outer layer is possibly still small, we can conclude that N_2 has not yet reached its steady state abundance which puts an upper limit to the age of the cloud of about 1×10^5 years following the estimate of Flower et al. [31]. However, this depends very much upon several factors, like for example the C:O elemental abundance ratio. Consequently this information is only indicative.

Though our model does not deal with the nitrogen chemistry, it seems to indicate that low abundances of N_2 are sufficient to explain the observed N_2H^+ abundance. Therefore, the much debated contradiction between the presence of N_2H^+ in depleted cores while N_2 should deplete like CO does not seem to be a real problem. Low CO and electronic abundances, limiting the destruction rate of N_2H^+, seem to be sufficient to compensate for the N_2 depletion itself to
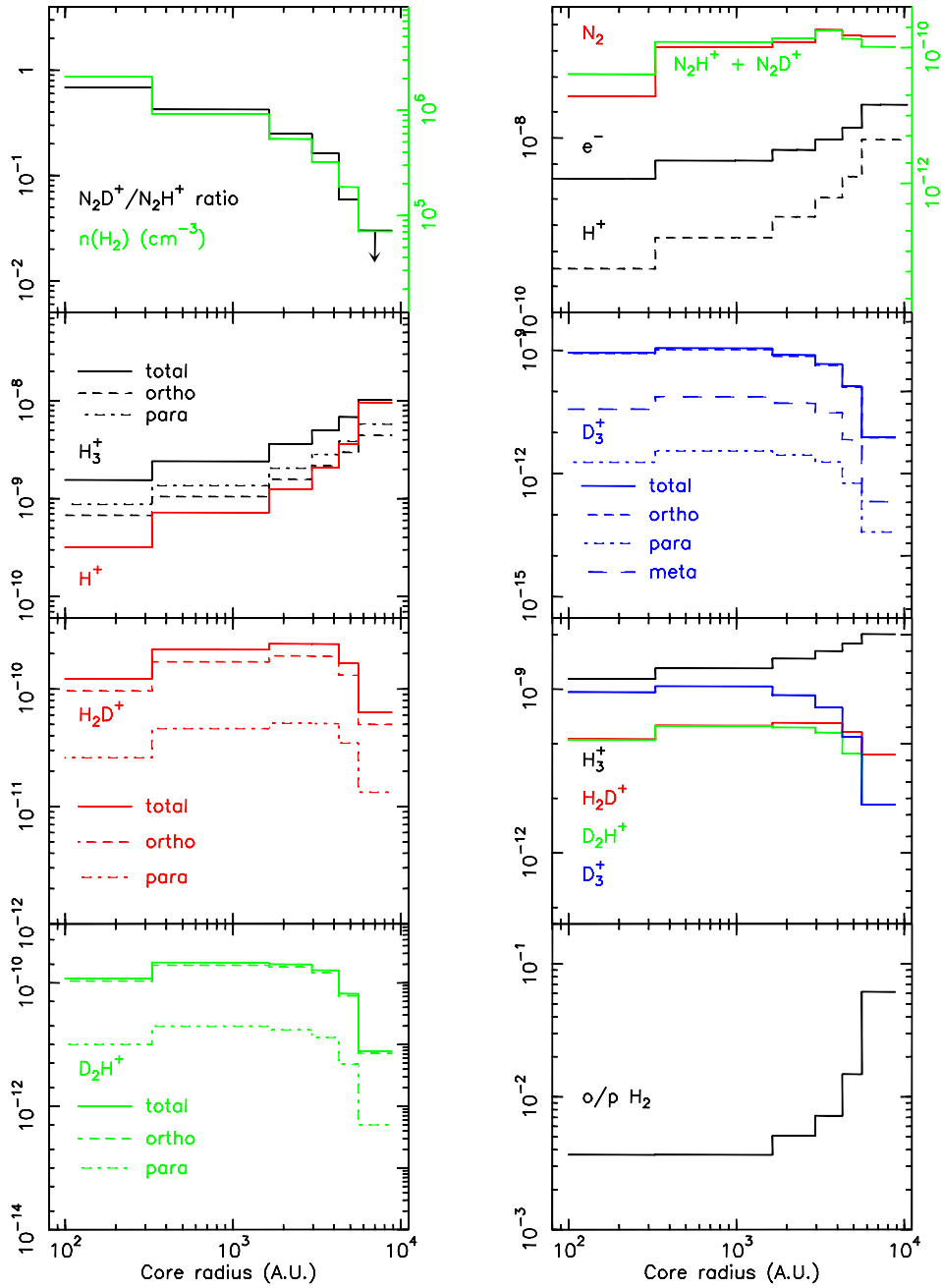
Figure 5.9: PSC profile for the different species. The n(H$_2$), N$_2$H$^+$ abundance, and N$_2$D$^+$/N$_2$H$^+$ ratio profiles are input data. The four trihydrogen cation isotopologue profiles are also grouped together to visualize their relative total abundances and H$^+$ is compared to both e$^-$ (upper right box) and to H$_3^+$ (2nd upper left box). The profile has been computed for the case presented in Fig. 5.7, i.e. $\zeta = 2 \times 10^{-17}$ s^{-1}, a$_{gr}$ = 0.1 μm. In the two upper boxes, the green curve refers to the green axis on the right. In the top left box, the arrow indicates the N$_2$D$^+$/N$_2$H$^+$ ratio upper limit for that layer.

a large extent. In the inner core, N_2 and N_2H^+ (+ N_2D^+) follow a similar decreasing trend, suggesting that N_2 depletion eventually forces N_2H^+ decrease.

Though ortho–H_2D^+ is 83 K above the para ground state, it is more abundant all over the core profile by almost an order of magnitude while the thermal equilibrium ratio would be ortho/para $H_2D^+ \approx 2 \times 10^{-5}$ at 7 K. This demonstrates the efficiency of the ortho–H_2 to convert para–H_2D^+ into ortho–$H_2D^+$and therefore limits the total abundance of H_2D^+, as the backward channel to H_3^+ remains open even at 7 K. This ortho/para population inversion does not occur for D_2H^+ as the needed species to perform this inversion is no more ortho–H_2 but the much rarer ortho–D_2. Therefore, the para–D_2H^+ remains the least abundant of the two spin state species which, combined with the fact that its ground transition is higher in frequency than the one of ortho–H_2D^+, makes its detection extremely difficult.

5.5 CONCLUSIONS

We have presented a pair of simple chemical models restricted to H-carriers, He plus CO and N_2 to account for the observed HCO^+, DCO^+ (not discussed in this paper), N_2H^+, and N_2D^+ ions. We have benefited from new computed reactions rates for both the H_3^+ + H_2 isotopologue combinations and for H_3^+ isotopologue dissociative recombination rates which take explicitly into account the nuclear states individually.

With the steady-state model we have shown that the ortho/para ratio of H_2 must vary from above 0.01 in the outer parts of the L183 PSC to less than 0.01 in the inner parts to explain the variation of deuteration across the core. Checking with a time-dependent model the reality of the ortho/para H_2 variation, we have also found that if the present PSC density profile is static, then the inner layer would have reached its present status 2 to 3 times faster than the outer layers. Because the present status is not in steady-state, the layers should evolve at a similar rate and therefore the density must have been lower in the past. The most probable explanation is that the core has probably evolved from a uniform density cloud to the present centrally condensed PSC. The time-dependent model also suggests that the ortho/para H_2 ratio is changing by one order of magnitude from $\sim$5% at a density of 7×10^4 cm^{-3} down to a few $\times$ 10^{-3} in the inner dense core. This has two important consequences :

- it is most probable that most of the cloud, outside the densest regions (i.e. the two PSC and the ridge in between) have an ortho/para H_2 ratio also above 5%, and possibly 10% contrarily to what is usually assumed in models.

- In principle, it should be possible to fit the PSC profile with this chemical model combined to a dynamical model including depletion, to set an age to this PSC and possibly discriminate between several types of collapse but it is beyond the scope of this paper.

We have already some indications that the age of the PSC is somewhat above 1.5–2 $\times$ 10^5 years though the N_2 abundance suggests a relatively short time (10^5 years, except if depletion

is compensating for its formation) when we compare our adjusted abundance to the formation rate of N_2 given by Flower et al. [31]. The low abundance of N_2 needed to explain the observed N_2H^+ abundance indicates that its depletion is not a real problem, though, obviously, N_2H^+ would be much more abundant if N_2 was not depleting but CO still was.

Finally, we stress the importance to consider ortho/meta/para chemistry when dealing with the deuteration of the interstellar medium. The importance of the ortho–H_2 on the amount of deuteration and the observations limited to the sole ortho–H_2D^+ make this inclusion compulsory. Moreover, a complete state-to-state chemical model should be developed to take into account rotational pumping, leading to a larger destruction rate of deuterated trihydrogen cation and possibly explaining the observed linewidth of ortho–H_2D^+.

Detecting para–D_2H^+ would be highly desirable to help constrain the models, but the high frequency and limited transparency of the atmosphere make it a difficult tool to use. Though observable from the ground, because of its weakness in cold dark clouds, which are the only places where it should be found, direct para–D_2H^+ observations should be made on a large number of Galactic lines of sight using the HIFI receiver on board the Heschel Space Observatory.

Acknowledgements

References

[1] P. Caselli, C. M. Walmsley, M. Tafalla, L. Dore, and P. C. Myers, Astrophys. J. Lett. **523**, L165 (1999).

[2] E. A. Bergin, J. Alves, T. Huard, and C. J. Lada, Astrophys. J. Lett. **570**, L101 (2002).

[3] A. Bacmann, B. Lefloch, C. Ceccarelli, A. Castets, J. Steinacker, and L. Loinard, Astron. Astrophys. **389**, L6 (2002).

[4] M. Tafalla, P. C. Myers, P. Caselli, and C. M. Walmsley, Astron. Astrophys. **416**, 191 (2004).

[5] L. Pagani, J.-R. Pardo, A. J. Apponi, A. Bacmann, and S. Cabrit, Astron. Astrophys. **429**, 181 (2005).

[6] M. Tafalla, J. Santiago-García, P. C. Myers, P. Caselli, C. M. Walmsley, and A. Crapsi, Astron. Astrophys. **455**, 577 (2006).

[7] L. Pagani, A. Bacmann, S. Cabrit, and C. Vastel, Astron. Astrophys. **467**, 179 (2007).

[8] P. Hily-Blant, M. Walmsley, G. Pineau Des Forêts, and D. Flower, Astron. Astrophys. **480**, L5 (2008).

[9] P. Caselli, F. F. S. van der Tak, C. Ceccarelli, and A. Bacmann, Astron. Astrophys. **403**, L37 (2003).

[10] C. Vastel, P. Caselli, C. Ceccarelli, T. Phillips, M. C. Wiedner, R. Peng, M. Houde, and C. Dominik, Astrophys. J. **645**, 1198 (2006).

[11] P. Caselli, C. Vastel, C. Ceccarelli, F. van der Tak, A. Crapsi, and A. Bacmann, ArXiv e-prints (2008), `0809.2803`.

[12] C. Vastel, T. Phillips, and H. Yoshida, Astrophys. J. **606**, L127 (2004).

[13] T. G. Phillips and C. Vastel, in *SFChem 2002: Chemistry as a Diagnostic of Star Formation*, edited by C. L. Curry and M. Fich (2003), p. 3.

[14] H. Roberts, E. Herbst, and T. J. Millar, Astrophys. J. **591**, L41 (2003).

[15] C. M. Walmsley, D. R. Flower, and G. Pineau des Forêts, Astron. Astrophys. **418**, 1035 (2004).

[16] L. Pagani, M. Salez, and P. G. Wannier, Astron. Astrophys. **258**, 479 (1992).

[17] R. Stark, F. van der Tak, and E. van Dishoeck, Astrophys. J. **521**, L67 (1999).

[18] D. R. Flower, G. Pineau des Forêts, and C. M. Walmsley, Astron. Astrophys. **427**, 887 (2004).

[19] D. R. Flower, G. Pineau Des Forêts, and C. M. Walmsley, Astron. Astrophys. **449**, 621 (2006).

[20] L. Pagani, G. Lagache, A. Bacmann, F. Motte, L. Cambrésy, M. Fich, D. Teyssier, M.-A. Miville-Deschênes, J.-R. Pardo, A. J. Apponi, et al., Astron. Astrophys. **406**, L59 (2003).

[21] T. Amano and T. Hirao, J. Mol. Spec. **233**, 7 (2005).

[22] L. Pagani, A. Bacmann, F. Motte, L. Cambrésy, M. Fich, G. Lagache, M.-A. Miville-Deschênes, J.-R. Pardo, and A. J. Apponi, Astron. Astrophys. **417**, 605 (2004).

[23] J. Alves, C. J. Lada, and E. A. Lada, Astrophys. J. **515**, 265 (1999).

[24] C. Kramer, J. Alves, C. J. Lada, E. A. Lada, A. Sievers, H. Ungerechts, and C. M. Walmsley, Astron. Astrophys. **342**, 257 (1999).

[25] L. Pagani, J.-R. Pardo, M. Fich, F. Motte, and B. Stepnik, in *EAS Publications Series*, edited by M. Giard, J. P. Bernard, A. Klotz, and I. Ristorcelli (2002), vol. 4 of *EAS Publications Series*, pp. 145–145.

[26] D. Lis, E. Roueff, M. Guerin, T. Phillips, L. Coudert, F. van der Tak, and P. Schilke, Astrophys. J. **571**, L55 (2002).

[27] F. F. S. van der Tak, P. Schilke, H. S. P. Müller, D. C. Lis, T. G. Phillips, M. Gerin, and E. Roueff, Astron. Astrophys. **388**, L53 (2002).

[28] B. Parise, A. Castets, E. Herbst, E. Caux, C. Ceccarelli, I. Mukhopadhyay, and A. G. G. M. Tielens, Astron. Astrophys. **416**, 159 (2004).

[29] C. Bernes, Astron. Astrophys. **73**, 67 (1979).

[30] J. L. Linsky, Space Science Reviews **130**, 367 (2007).

[31] D. R. Flower, G. Pineau Des Forêts, and C. M. Walmsley, Astron. Astrophys. **456**, 215 (2006).

[32] E. A. Bergin, D. R. Ciardi, C. J. Lada, J. Alves, and E. A. Lada, Astrophys. J. **557**, 209 (2001).

[33] M. Tafalla, P. C. Myers, P. Caselli, C. M. Walmsley, and C. Comito, Astrophys. J. **569**, 815 (2002).

[34] K. I. Öberg, F. van Broekhuizen, H. J. Fraser, S. E. Bisschop, E. F. van Dishoeck, and S. Schlemmer, Astrophys. J. Lett. **621**, L33 (2005).

[35] S. E. Bisschop, H. J. Fraser, K. I. Öberg, E. F. van Dishoeck, and S. Schlemmer, Astron. Astrophys. **449**, 1297 (2006).

[36] P. Caselli, Planet. Space Sci. **50**, 1133 (2002).

[37] Y. Aikawa, E. Herbst, H. Roberts, and P. Caselli, Astrophys. J. **620**, 330 (2005).

[38] B. T. Draine and B. Sutin, Astrophys. J. **320**, 803 (1987).

[39] T. Umebayashi and T. Nakano, Pub. Astron. Soc. Japan **32**, 405 (1980).

[40] T. Oka, J. Mol. Spec. **228**, 635 (2004).

[41] A. Lipshtat, O. Biham, and E. Herbst, Mon. Not. Roy. Astron. Soc. **348**, 1055 (2004).

[42] S. Cazaux, P. Caselli, V. Cobut, and J. Le Bourlot, Astron. Astrophys. **483**, 495 (2008).

[43] J. Woodall, M. Agúndez, A. J. Markwick-Kemper, and T. J. Millar, Astron. Astrophys. **466**, 1197 (2007).

[44] W. D. Geppert, R. Thomas, J. Semaniak, A. Ehlerding, T. J. Millar, F. Österdahl, M. af Ugglas, N. Djurić, A. Paál, and M. Larsson, Astrophys. J. **609**, 459 (2004).

[45] C. D. Molek, J. L. McLain, V. Poteyra, and N. G. Adams, J. Phys. Chem. A (2007).

[46] Y. Yamaguchi, J. F. Gaw, R. B. Remington, and H. F. Schaefer, III, J. Chem. Phys. **86**, 5072 (1987).

[47] Z. Xie, B. J. Braams, and J. M. Bowman, J. Chem. Phys. **122**, 224307 (2005).

[48] N. G. Adams, D. Smith, and E. Alge, J. Chem. Phys. **81**, 1778 (1984).

[49] D. R. Bates, M. F. Guest, and R. A. Kendall, Planet. Space Sci. **41**, 9 (1993).

[50] S. Fonseca dos Santos, V. Kokoouline, and C. H. Greene, J. Chem. Phys. **127**, 124309 (2007).

[51] S. Datz, M. Larsson, C. Stromholm, G. Sundström, V. Zengin, H. Danared, A. Källberg, and M. A. Ugglas, Phys. Rev. A **52**, 2901 (1995).

[52] S. Datz, G. Sundström, C. Biedermann, L. Broström, H. Danared, S. Mannervik, J. R. Mowat, and M. Larsson, Phys. Rev. Lett. **74**, 896 (1995).

[53] D. Strasser, L. Lammich, H. Kreckel, M. Lange, S. Krohn, D. Schwalm, A. Wolf, and D. Zajfman, Phys. Rev. A **69**, 064702 (2004).

[54] V. Zhaunerchyk, R. D. Thomas, W. D. Geppert, M. Hamberg, M. Kaminska, E. Vigren, and M. Larsson, Phys. Rev. A **77**, 034701 (2008).

[55] S. Maret and E. A. Bergin, Astrophys. J. **664**, 956 (2007).

[56] B. Stepnik, A. Abergel, J.-P. Bernard, F. Boulanger, L. Cambrésy, M. Giard, A. P. Jones, G. Lagache, J.-M. Lamarre, C. Meny, et al., Astron. Astrophys. **398**, 551 (2003).

[57] V. Wakelam and E. Herbst, Astrophys. J. **680**, 371 (2008).

[58] D. Gerlich, J. Chem. Phys. **92**, 2377 (1990).

[59] M. Larsson, H. Danared, Å. Larson, A. Le Padellec, J. R. Peterson, S. Rosén, J. Semaniak, and C. Strömholm, Phys. Rev. Lett. **79**, 395 (1997).

[60] V. Kokoouline and C. H. Greene, Phys. Rev. Lett. **90**, 133201 (2003).

[61] V. Kokoouline and C. H. Greene, Phys. Rev. A **68**, 012703 (2003).

[62] V. Kokoouline and C. H. Greene, Faraday Discuss. (2004).

[63] V. Kokoouline and C. H. Greene, Phys. Rev. A (2005).

[64] I. Mistrík, R. Reichle, H. Helm, and U. Müller, Phys. Rev. A **63**, 042711 (2001).

[65] L. Landau and E. Lifshitz, *Quantum Mechanics: Non-relativistic Theory* (Burlington MA: Butterworth Heinemann, 2003).

[66] V. Kokoouline, C. H. Greene, and B. D. Esry, Nature **412**, 891 (2001).

[67] P. Bunker and P. Jensen, *Molecular symmetry and spectroscopy* (NRC Research Press, Ottawa, 1998).

[68] E. S. Chang and U. Fano, Phys. Rev. A **6**, 173 (1972).

[69] H. Kreckel, M. Motsch, J. Mikosch, J. Glosík, R. Plašil, S. Altevogt, V. Andrianarijaona, H. Buhr, J. Hoffmann, L. Lammich, et al., Phys. Rev. Lett. **95**, 263201 (2005).

APPENDICES

5.A REACTION RATE TABLE

Table 5.3: Reaction rates used in the Nahoon modified chemical model. The rate coefficients are given for 7K. Reaction rates less than 10^{-15} cm^{-3}s^{-1} are not taken into account in our models. Reference (1) corresponds to Gerlich [58], references (2), (3), and (4) correspond to E. Hugo, OSU 07, and this paper respectively. For OSU 07, branching ratios involving spin states have been infered from quantum mechanical rules. For reactions involving grains, a grain radius of 0.1 μm and a sticking coefficient of 1 have been considered. (5) Datz et al. [52] (6) Datz et al. [51], (7) Zhaunerchyk et al. [54], (8) Larsson et al. [59], (9) Molek et al. [45].

Reaction						Rate		Ref.
						label	cm^3 s^{-1}	
H$^+$	+	o–H$_2$	$\rightarrow$	H$^+$	+	p–H$_2$		2.2 10^{-10}	(1)
p–H$_3^+$	+	o–H$_2$	$\rightarrow$	p–H$_3^+$	+	p–H$_2$		3.3 10^{-10}	(2)
			$\rightarrow$	o–H$_3^+$	+	p–H$_2$	k0$_{poop}$	3.9 10^{-10}	(2)
			$\rightarrow$	o–H$_3^+$	+	o–H$_2$	k0$_{pooo}$	7.8 10^{-12}	(2)
o–H$_3^+$	+	o–H$_2$	$\rightarrow$	p–H$_3^+$	+	p–H$_2$	k0$_{oopp}$	1.0 10^{-10}	(2)
			$\rightarrow$	p–H$_3^+$	+	o–H$_2$	k0$_{oopo}$	4.1 10^{-10}	(2)

Reaction							Rate		Ref.
							label	cm^3 s^{-1}	
			$\rightarrow$	o–H$_3^+$	+	p–H$_2$	k0$_{ooop}$	1.0 10^{-10}	(2)
p–H$_3^+$	+	HD	$\rightarrow$	o–H$_3^+$	+	HD	k1$_{pdod}$	8.2 10^{-13}	(2)
			$\rightarrow$	p–H$_2$D$^+$	+	p–H$_2$	k1$_{pdpp}$	3.2 10^{-10}	(2)
			$\rightarrow$	p–H$_2$D$^+$	+	o–H$_2$	k1$_{pdpo}$	4.3 10^{-10}	(2)
			$\rightarrow$	o–H$_2$D$^+$	+	p–H$_2$	k1$_{pdop}$	6.8 10^{-10}	(2)
			$\rightarrow$	o–H$_2$D$^+$	+	o–H$_2$	k1$_{pdoo}$	1.6 10^{-11}	(2)
o–H$_3^+$	+	HD	$\rightarrow$	p–H$_2$D$^+$	+	o–H$_2$	k1$_{odpo}$	1.7 10^{-10}	(2)
			$\rightarrow$	p–H$_3^+$	+	HD	k1$_{odpd}$	4.35 10^{-11}	(2)
			$\rightarrow$	o–H$_2$D$^+$	+	p–H$_2$	k1$_{odop}$	2.3 10^{-10}	(2)
			$\rightarrow$	o–H$_2$D$^+$	+	o–H$_2$	k1$_{odoo}$	1.0 10^{-9}	(2)
p–H$_2$D$^+$	+	o–H$_2$	$\rightarrow$	o–H$_2$D$^+$	+	p–H$_2$		1.3 10^{-9}	(2)
			$\rightarrow$	p–H$_3^+$	+	HD	k_1$_{popd}$	3.9 10^{-14}	(2)
			$\rightarrow$	o–H$_2$D$^+$	+	o–H$_2$		2.0 10^{-15}	(2)
o–H$_2$D$^+$	+	o–H$_2$	$\rightarrow$	p–H$_3^+$	+	HD	k_1$_{oopd}$	7.7 10^{-11}	(2)
			$\rightarrow$	o–H$_3^+$	+	HD	k_1$_{oood}$	8.3 10^{-11}	(2)
			$\rightarrow$	p–H$_2$D$^+$	+	p–H$_2$		9.2 10^{-11}	(2)
			$\rightarrow$	p–H$_2$D$^+$	+	o–H$_2$		1.8 10^{-10}	(2)
			$\rightarrow$	o–H$_2$D$^+$	+	p–H$_2$		2.35 10^{-10}	(2)
o–H$_2$D$^+$	+	p–H$_2$	$\rightarrow$	p–H$_2$D$^+$	+	o–H$_2$		4.2 10^{-15}	(2)
o–H$_2$D$^+$	+	HD	$\rightarrow$	p–H$_3^+$	+	o–D$_2$		1.2 10^{-15}	(2)
			$\rightarrow$	p–H$_2$D$^+$	+	HD		5.4 10^{-11}	(2)
			$\rightarrow$	p–D$_2$H$^+$	+	p–H$_2$		7.3 10^{-11}	(2)
			$\rightarrow$	p–D$_2$H$^+$	+	o–H$_2$		3.8 10^{-10}	(2)
			$\rightarrow$	o–D$_2$H$^+$	+	p–H$_2$		1.8 10^{-10}	(2)
			$\rightarrow$	o–D$_2$H$^+$	+	o–H$_2$		6.8 10^{-10}	(2)
p–H$_2$D$^+$	+	HD	$\rightarrow$	p–D$_2$H$^+$	+	p–H$_2$		4.8 10^{-10}	(2)
			$\rightarrow$	p–D$_2$H$^+$	+	o–H$_2$		2.1 10^{-12}	(2)
			$\rightarrow$	o–D$_2$H$^+$	+	p–H$_2$		7.5 10^{-10}	(2)
			$\rightarrow$	o–D$_2$H$^+$	+	o–H$_2$		2.3 10^{-10}	(2)
p–D$_2$H$^+$	+	o–H$_2$	$\rightarrow$	p–H$_2$D$^+$	+	HD		3.1 10^{-11}	(2)
			$\rightarrow$	p–D$_2$H$^+$	+	p–H$_2$		3.3 10^{-10}	(2)
			$\rightarrow$	o–H$_2$D$^+$	+	HD		1.2 10^{-13}	(2)
o–D$_2$H$^+$	+	o–H$_2$	$\rightarrow$	p–H$_2$D$^+$	+	HD		3.8 10^{-12}	(2)
			$\rightarrow$	o–D$_2$H$^+$	+	p–H$_2$		4.45 10^{-10}	(2)
p–D$_2$H$^+$	+	HD	$\rightarrow$	p–H$_2$D$^+$	+	o–D$_2$		2.8 10^{-15}	(2)
			$\rightarrow$	o–D$_2$H$^+$	+	HD		9.1 10^{-11}	(2)
			$\rightarrow$	p–D$_3^+$	+	p–H$_2$		3.3 10^{-11}	(2)
			$\rightarrow$	p–D$_3^+$	+	o–H$_2$		9.75 10^{-11}	(2)
			$\rightarrow$	m-D$_3^+$	+	p–H$_2$		2.6 10^{-10}	(2)

Reaction							Rate label	Rate cm^3 s^{-1}	Ref.
			$\rightarrow$	m-D$_3^+$	+	o–H$_2$		7.8 10^{-10}	(2)
o–D$_2$H$^+$	+	HD	$\rightarrow$	m-D$_3^+$	+	p–H$_2$		1.6 10^{-10}	(2)
			$\rightarrow$	m-D$_3^+$	+	o–H$_2$		4.5 10^{-10}	(2)
			$\rightarrow$	o–D$_3^+$	+	p–H$_2$		1.9 10^{-10}	(2)
			$\rightarrow$	o–D$_3^+$	+	o–H$_2$		4.7 10^{-10}	(2)
			$\rightarrow$	p–D$_2$H$^+$	+	HD		9.9 10^{-14}	(2)
m-D$_3^+$	+	o–H$_2$	$\rightarrow$	o–D$_2$H$^+$	+	HD		1.3 10^{-11}	(2)
			$\rightarrow$	p–D$_2$H$^+$	+	HD		1.9 10^{-14}	(2)
o–D$_3^+$	+	o–H$_2$	$\rightarrow$	o–D$_2$H$^+$	+	HD		4.4 10^{-14}	(2)
p–D$_3^+$	+	o–H$_2$	$\rightarrow$	p–D$_2$H$^+$	+	HD		2.6 10^{-13}	(2)
p–D$_3^+$	+	HD	$\rightarrow$	m-D$_3^+$	+	HD		7.75 10^{-10}	(2)
m-D$_3^+$	+	HD	$\rightarrow$	o–D$_3^+$	+	HD		2.5 10^{-10}	(2)
			$\rightarrow$	p–D$_3^+$	+	HD		9.5 10^{-12}	(2)
o–D$_3^+$	+	HD	$\rightarrow$	m-D$_3^+$	+	HD		8.45 10^{-13}	(2)
o–H$_3^+$	+	o–D$_2$	$\rightarrow$	o–H$_2$D$^+$	+	HD		2.1 10^{-10}	(2)
			$\rightarrow$	o–D$_2$H$^+$	+	o–H$_2$		1.3 10^{-9}	(2)
o–H$_3^+$	+	p–D$_2$	$\rightarrow$	o–H$_2$D$^+$	+	HD		5.0 10^{-10}	(2)
			$\rightarrow$	p–D$_2$H$^+$	+	o–H$_2$		9.7 10^{-10}	(2)
p–H$_3^+$	+	o–D$_2$	$\rightarrow$	p–H$_2$D$^+$	+	HD		1.6 10^{-10}	(2)
			$\rightarrow$	o–H$_2$D$^+$	+	HD		1.4 10^{-10}	(2)
			$\rightarrow$	o–D$_2$H$^+$	+	p–H$_2$		5.95 10^{-10}	(2)
			$\rightarrow$	o–D$_2$H$^+$	+	o–H$_2$		6.2 10^{-10}	(2)
p–H$_3^+$	+	p–D$_2$	$\rightarrow$	p–H$_2$D$^+$	+	HD		2.55 10^{-10}	(2)
			$\rightarrow$	o–H$_2$D$^+$	+	HD		3.45 10^{-10}	(2)
			$\rightarrow$	p–D$_2$H$^+$	+	p–H$_2$		4.0 10^{-10}	(2)
			$\rightarrow$	p–D$_2$H$^+$	+	o–H$_2$		4.9 10^{-10}	(2)
o–H$_2$D$^+$	+	o–D$_2$	$\rightarrow$	p–D$_2$H$^+$	+	HD		1.7 10^{-10}	(2)
			$\rightarrow$	o–D$_2$H$^+$	+	HD		3.9 10^{-10}	(2)
			$\rightarrow$	m-D$_3^+$	+	o–H$_2$		3.2 10^{-10}	(2)
			$\rightarrow$	o–D$_3^+$	+	o–H$_2$		5.3 10^{-10}	(2)
o–H$_2$D$^+$	+	p–D$_2$	$\rightarrow$	o–H$_2$D$^+$	+	o–D$_2$		4.8 10^{-11}	(2)
			$\rightarrow$	p–D$_2$H$^+$	+	HD		4.1 10^{-10}	(2)
			$\rightarrow$	o–D$_2$H$^+$	+	HD		3.6 10^{-10}	(2)
			$\rightarrow$	p–D$_3^+$	+	o–H$_2$		6.1 10^{-11}	(2)
			$\rightarrow$	m-D$_3^+$	+	o–H$_2$		5.05 10^{-10}	(2)
p–H$_2$D$^+$	+	o–D$_2$	$\rightarrow$	p–D$_2$H$^+$	+	HD		1.2 10^{-10}	(2)
			$\rightarrow$	o–D$_2$H$^+$	+	HD		2.7 10^{-10}	(2)
			$\rightarrow$	m-D$_3^+$	+	p–H$_2$		4.3 10^{-10}	(2)
			$\rightarrow$	o–D$_3^+$	+	p–H$_2$		5.8 10^{-10}	(2)

								Rate		Ref.
				Reaction				label	cm^3 s^{-1}	
p–H$_2$D$^+$	+	p–D$_2$	$\rightarrow$	p–H$_2$D$^+$	+	o–D$_2$			6.55 10^{-11}	(2)
			$\rightarrow$	p–D$_2$H$^+$	+	HD			4.1 10^{-10}	(2)
			$\rightarrow$	o–D$_2$H$^+$	+	HD			2.8 10^{-10}	(2)
			$\rightarrow$	p–D$_3^+$	+	p–H$_2$			6.9 10^{-11}	(2)
			$\rightarrow$	m-D$_3^+$	+	p–H$_2$			5.8 10^{-10}	(2)
o–D$_2$H$^+$	+	o–D$_2$	$\rightarrow$	p–D$_2$H$^+$	+	o–D$_2$			3.85 10^{-14}	(2)
			$\rightarrow$	m-D$_3^+$	+	HD			5.7 10^{-10}	(2)
			$\rightarrow$	o–D$_3^+$	+	HD			6.4 10^{-10}	(2)
o–D$_2$H$^+$	+	p–D$_2$	$\rightarrow$	p–D$_2$H$^+$	+	p–D$_2$			2.1 10^{-14}	(2)
			$\rightarrow$	p–D$_2$H$^+$	+	o–D$_2$			1.6 10^{-10}	(2)
			$\rightarrow$	o–D$_2$H$^+$	+	o–D$_2$			8.8 10^{-11}	(2)
			$\rightarrow$	p–D$_3^+$	+	HD			8.4 10^{-11}	(2)
			$\rightarrow$	m-D$_3^+$	+	HD			6.4 10^{-10}	(2)
			$\rightarrow$	o–D$_3^+$	+	HD			3.5 10^{-10}	(2)
p–D$_2$H$^+$	+	o–D$_2$	$\rightarrow$	o–D$_2$H$^+$	+	p–D$_2$			5.0 10^{-13}	(2)
			$\rightarrow$	o–D$_2$H$^+$	+	o–D$_2$			3.7 10^{-11}	(2)
			$\rightarrow$	p–D$_3^+$	+	HD			7.7 10^{-11}	(2)
			$\rightarrow$	m-D$_3^+$	+	HD			8.6 10^{-10}	(2)
			$\rightarrow$	o–D$_3^+$	+	HD			3.05 10^{-10}	(2)
p–D$_2$H$^+$	+	p–D$_2$	$\rightarrow$	p–D$_2$H$^+$	+	o–D$_2$			3.7 10^{-11}	(2)
			$\rightarrow$	o–D$_2$H$^+$	+	p–D$_2$			2.0 10^{-11}	(2)
			$\rightarrow$	o–D$_2$H$^+$	+	o–D$_2$			8.5 10^{-11}	(2)
			$\rightarrow$	p–D$_3^+$	+	HD			1.15 10^{-10}	(2)
			$\rightarrow$	m-D$_3^+$	+	HD			9.5 10^{-10}	(2)
m-D$_3^+$	+	o–D$_2$	$\rightarrow$	p–D$_3^+$	+	o–D$_2$			8.6 10^{-12}	(2)
			$\rightarrow$	m-D$_3^+$	+	p–D$_2$			1.7 10^{-15}	(2)
			$\rightarrow$	o–D$_3^+$	+	p–D$_2$			1.2 10^{-12}	(2)
			$\rightarrow$	o–D$_3^+$	+	o–D$_2$			3.0 10^{-10}	(2)
m-D$_3^+$	+	p–D$_2$	$\rightarrow$	p–D$_3^+$	+	p–D$_2$			5.9 10^{-12}	(2)
			$\rightarrow$	p–D$_3^+$	+	o–D$_2$			4.7 10^{-11}	(2)
			$\rightarrow$	m-D$_3^+$	+	o–D$_2$			6.1 10^{-10}	(2)
			$\rightarrow$	o–D$_3^+$	+	p–D$_2$			4.7 10^{-11}	(2)
			$\rightarrow$	o–D$_3^+$	+	o–D$_2$			5.1 10^{-11}	(2)
o–D$_3^+$	+	o–D$_2$	$\rightarrow$	m-D$_3^+$	+	o–D$_2$			1.0 10^{-12}	(2)
			$\rightarrow$	o–D$_3^+$	+	p–D$_2$			1.15 10^{-15}	(2)
o–D$_3^+$	+	p–D$_2$	$\rightarrow$	p–D$_3^+$	+	o–D$_2$			9.2 10^{-11}	(2)
			$\rightarrow$	m-D$_3^+$	+	p–D$_2$			1.6 10^{-13}	(2)
			$\rightarrow$	m-D$_3^+$	+	o–D$_2$			5.7 10^{-10}	(2)
			$\rightarrow$	o–D$_3^+$	+	o–D$_2$			1.6 10^{-10}	(2)

Reaction									Rate label	Rate cm^3 s^{-1}	Ref.
p–D$_3^+$	+	o–D$_2$	$\rightarrow$	m–D$_3^+$	+	p–D$_2$				$2.8\ 10^{-14}$	(2)
			$\rightarrow$	m–D$_3^+$	+	o–D$_2$				$7.0\ 10^{-10}$	(2)
			$\rightarrow$	o–D$_3^+$	+	p–D$_2$				$1.7\ 10^{-11}$	(2)
p–D$_3^+$	+	p–D$_2$	$\rightarrow$	m–D$_3^+$	+	p–D$_2$				$4.8\ 10^{-10}$	(2)
			$\rightarrow$	m–D$_3^+$	+	o–D$_2$				$4.4\ 10^{-10}$	(2)

The primes for k$_{CO}$ and k$_{N_2}$ indicate that the rates have been corrected
for the higher reduced mass of the system with respect to H$_3^+$

Reaction									Rate label	Rate cm^3 s^{-1}	Ref.
o–H$_3^+$	+	CO	$\rightarrow$	HCO$^+$	+	o–H$_2$			k_{CO}	$1.6\ 10^{-9}$	(3)
p–H$_3^+$	+	CO	$\rightarrow$	HCO$^+$	+	p–H$_2$			$1/2\ k_{CO}$	$8.1\ 10^{-10}$	(3)
			$\rightarrow$	HCO$^+$	+	o–H$_2$			$1/2\ k_{CO}$	$8.1\ 10^{-10}$	(3)
o–H$_2$D$^+$	+	CO	$\rightarrow$	HCO$^+$	+	HD			$2/3\ k'_{CO}$	$9.4\ 10^{-10}$	(3)
			$\rightarrow$	DCO$^+$	+	o–H$_2$			$1/3\ k'_{CO}$	$4.7\ 10^{-10}$	(3)
p–H$_2$D$^+$	+	CO	$\rightarrow$	HCO$^+$	+	HD			$2/3\ k'_{CO}$	$9.4\ 10^{-10}$	(3)
			$\rightarrow$	DCO$^+$	+	p–H$_2$			$1/3\ k'_{CO}$	$4.7\ 10^{-10}$	(3)
o–D$_2$H$^+$	+	CO	$\rightarrow$	HCO$^+$	+	o–D$_2$			$1/3\ k''_{CO}$	$4.3\ 10^{-10}$	(3)
			$\rightarrow$	DCO$^+$	+	HD			$2/3\ k''_{CO}$	$8.6\ 10^{-10}$	(3)
p–D$_2$H$^+$	+	CO	$\rightarrow$	HCO$^+$	+	p–D$_2$			$1/3k''_{CO}$	$4.3\ 10^{-10}$	(3)
			$\rightarrow$	DCO$^+$	+	HD			$2/3\ k''_{CO}$	$8.6\ 10^{-10}$	(3)
o–D$_3^+$	+	CO	$\rightarrow$	DCO$^+$	+	o–D$_2$			k'''_{CO}	$1.2\ 10^{-9}$	(3)
m-D$_3^+$	+	CO	$\rightarrow$	DCO$^+$	+	o–D$_2$			$1/2\ k'''_{CO}$	$6.0\ 10^{-10}$	(3)
			$\rightarrow$	DCO$^+$	+	p–D$_2$			$1/2\ k'''_{CO}$	$6.0\ 10^{-10}$	(3)
p–D$_3^+$	+	CO	$\rightarrow$	DCO$^+$	+	p–D$_2$			k'''_{CO}	$1.2\ 10^{-9}$	(3)
p–H$_3^+$	+	N$_2$	$\rightarrow$	N$_2$H$^+$	+	o-H$_2$			$1/2\ k_{N_2}$	$8.5\ 10^{-10}$	(3)
			$\rightarrow$	N$_2$H$^+$	+	p-H$_2$			$1/2\ k_{N_2}$	$8.5\ 10^{-10}$	(3)
o–H$_3^+$	+	N$_2$	$\rightarrow$	N$_2$H$^+$	+	o-H$_2$			k_{N_2}	$1.7\ 10^{-9}$	(3)
o–H$_2$D$^+$	+	N$_2$	$\rightarrow$	N$_2$H$^+$	+	HD			$2/3\ k'_{N_2}$	$1.0\ 10^{-9}$	(3)
			$\rightarrow$	N$_2$D$^+$	+	o-H$_2$			$1/3\ k'_{N_2}$	$5.0\ 10^{-10}$	(3)
p–H$_2$D$^+$	+	N$_2$	$\rightarrow$	N$_2$H$^+$	+	HD			$2/3\ k'_{N_2}$	$1.0\ 10^{-9}$	(3)
			$\rightarrow$	N$_2$D$^+$	+	p-H$_2$			$1/3\ k'_{N_2}$	$5.0\ 10^{-10}$	(3)
o–D$_2$H$^+$	+	N$_2$	$\rightarrow$	N$_2$H$^+$	+	p–D$_2$			$1/3\ k''_{N_2}$	$4.5\ 10^{-10}$	(3)
			$\rightarrow$	N$_2$D$^+$	+	HD			$2/3\ k''_{N_2}$	$9.1\ 10^{-10}$	(3)
p–D$_2$H$^+$	+	N$_2$	$\rightarrow$	N$_2$H$^+$	+	p–D$_2$			$1/3\ k''_{N_2}$	$4.5\ 10^{-10}$	(3)
			$\rightarrow$	N$_2$D$^+$	+	HD			$2/3\ k''_{N_2}$	$9.1\ 10^{-10}$	(3)
o–D$_3^+$	+	N$_2$	$\rightarrow$	N$_2$D$^+$	+	o–D$_2$			k'''_{N_2}	$1.3\ 10^{-9}$	(3)
m-D$_3^+$	+	N$_2$	$\rightarrow$	N$_2$D$^+$	+	o–D$_2$			$1/2\ k'''_{N_2}$	$6.3\ 10^{-10}$	(3)
			$\rightarrow$	N$_2$D$^+$	+	p–D$_2$			$1/2\ k'''_{N_2}$	$6.3\ 10^{-10}$	(3)
p–D$_3^+$	+	N$_2$	$\rightarrow$	N$_2$D$^+$	+	p–D$_2$			k'''_{N_2}	$1.3\ 10^{-9}$	(3)
H$^+$	+	e$^-$	$\rightarrow$	H					k_{rec}	$4.9\ 10^{-11}$	(3)
o–H$_3^+$	+	e$^-$	$\rightarrow$	H	+	H	+	H	$3/4$ o–k_{rec1}	$3.6\ 10^{-8}$	(4,5)

Reaction									Rate		Ref.
									label	cm^3 s^{-1}	
			$\rightarrow$	o–H$_2$	+	H			1/4 o–k$_{rec1}$	1.2 10^{-8}	(4,5)
p–H$_3{}^+$	+	e$^-$	$\rightarrow$	H	+	H	+	H	3/4 p–k$_{rec1}$	5.6 10^{-7}	(4,5)
			$\rightarrow$	p–H$_2$	+	H			1/8 p–k$_{rec1}$	9.4 10^{-8}	(4,5)
			$\rightarrow$	o–H$_2$	+	H			1/8 p–k$_{rec1}$	9.4 10^{-8}	(4,5)
o–H$_2$D$^+$	+	e$^-$	$\rightarrow$	H	+	H	+	D	3/4 o–k$_{rec2}$	2.6 10^{-7}	(4,6)
			$\rightarrow$	o–H$_2$	+	D			$\sim$0.07 o–k$_{rec2}$	2.5 10^{-8}	(4,6)
			$\rightarrow$	HD	+	D			$\sim$0.18 o–k$_{rec2}$	6.25 10^{-8}	(4,6)
p–H$_2$D$^+$	+	e$^-$	$\rightarrow$	H	+	H	+	D	3/4 p–k$_{rec2}$	1.8 10^{-7}	(4,6)
			$\rightarrow$	p–H$_2$	+	D			$\sim$0.07 p–k$_{rec2}$	1.7 10^{-8}	(4,6)
			$\rightarrow$	HD	+	D			$\sim$0.18 p–k$_{rec2}$	4.3 10^{-8}	(4,6)
o–D$_2$H$^+$	+	e$^-$	$\rightarrow$	H	+	D	+	D	$\sim$0.77 o–k$_{rec3}$	4.3 10^{-8}	(4,7)
			$\rightarrow$	HD	+	D			$\sim$0.13 o–k$_{rec3}$	7.3 10^{-9}	(4,7)
			$\rightarrow$	o–D$_2$	+	H			$\sim$0.10 o–k$_{rec3}$	5.6 10^{-9}	(4,7)
p–D$_2$H$^+$	+	e$^-$	$\rightarrow$	H	+	D	+	D	$\sim$0.77 p–k$_{rec3}$	4.6 10^{-8}	(4,7)
			$\rightarrow$	HD	+	D			$\sim$0.13 p–k$_{rec3}$	7.8 10^{-9}	(4,7)
			$\rightarrow$	p–D$_2$	+	H			$\sim$0.10 p–k$_{rec3}$	6.0 10^{-9}	(4,7)
o–D$_3{}^+$	+	e$^-$	$\rightarrow$	D	+	D	+	D	3/4 o–k$_{rec4}$	1.8 10^{-7}	(4,8)
			$\rightarrow$	o–D$_2$	+	D			1/4 o–k$_{rec4}$	6.1 10^{-8}	(4,8)
p–D$_3{}^+$	+	e$^-$	$\rightarrow$	D	+	D	+	D	3/4 p–k$_{rec4}$	1.5 10^{-7}	(4,8)
			$\rightarrow$	p–D$_2$	+	D			1/4 p–k$_{rec4}$	5.0 10^{-8}	(4,8)
m–D$_3{}^+$	+	e$^-$	$\rightarrow$	D	+	D	+	D	3/4 m–k$_{rec4}$	3.6 10^{-7}	(4,8)
			$\rightarrow$	o–D$_2$	+	D			1/8 m–k$_{rec4}$	6.0 10^{-8}	(4,8)
			$\rightarrow$	p–D$_2$	+	D			1/8 m–k$_{rec4}$	6.0 10^{-8}	(4,8)
N$_2$H$^+$	+	e$^-$	$\rightarrow$	H	+	N$_2$			k$_{N_2H^+}$	6.8 10^{-7}	(9)
N$_2$D$^+$	+	e$^-$	$\rightarrow$	D	+	N$_2$			k$_{N_2D^+}$	6.8 10^{-7}	(9)
HCO$^+$	+	e$^-$	$\rightarrow$	H	+	CO			k$_{HCO^+}$	3.2 10^{-6}	(2)
DCO$^+$	+	e$^-$	$\rightarrow$	D	+	CO			k$_{DCO^+}$	3.2 10^{-6}	(2)
gr^0	+	e$^-$	$\rightarrow$	gr$^-$					k$_e$	3.7 10^{-3}	(4)
H$^+$	+	gr$^-$	$\rightarrow$	H	+	gr^0			k$_{gr}$	6.0 10^{-4}	(4)
HD$^+$	+	gr$^-$	$\rightarrow$	H	+	D	+	gr^0	2/3 k$_{gr1}$	2.3 10^{-4}	(4)
			$\rightarrow$	HD	+	gr^0			1/3 k$_{gr1}$	1.2 10^{-4}	(4)
o–D$_2^+$	+	gr$^-$	$\rightarrow$	D	+	D	+	gr^0	2/3 k$_{gr2}$	2.0 10^{-4}	(4)
			$\rightarrow$	o–D$_2$	+	gr^0			1/3 k$_{gr2}$	1.0 10^{-4}	(4)
p–D$_2^+$	+	gr$^-$	$\rightarrow$	D	+	D	+	gr^0	2/3 k$_{gr2}$	2.0 10^{-4}	(4)
			$\rightarrow$	p–D$_2$	+	gr^0			1/3 k$_{gr2}$	1.0 10^{-4}	(4)
He$^+$	+	gr$^-$	$\rightarrow$	He	+	gr^0				3.0 10^{-4}	(4)
p–H$_3^+$	+	gr$^-$	$\rightarrow$	p-H$_2$	+	H	+	gr^0	1/6 k$_{gr3}$	5.8 10^{-5}	(4)
			$\rightarrow$	o-H$_2$	+	H	+	gr^0	1/6 k$_{gr3}$	5.810^{-5}	(4)
			$\rightarrow$	3H	+	gr^0	+		2/3 k$_{gr3}$	2.3 10^{-4}	(4)

Reaction									Rate label	Rate cm^3 s^{-1}	Ref.
o–H$_3^+$	+	gr$^-$	→	o-H$_2$	+	H	+	gr^0	1/3 k$_{gr3}$	1.2 10^{-4}	(4)
			→	3H	+	gr^0	+		2/3 k$_{gr3}$	2.3 10^{-4}	(4)
p–H$_2$D$^+$	+	gr$^-$	→	p-H$_2$	+	D	+	gr^0	1/6 k$_{gr4}$	5.0 10^{-5}	(4)
			→	HD	+	H	+	gr^0	1/3 k$_{gr4}$	1.0 10^{-4}	(4)
			→	2H	+	D	+	gr^0	1/2 k$_{gr4}$	1.5 10^{-4}	(4)
o–H$_2$D$^+$	+	gr$^-$	→	2H	+	D	+	gr^0	1/2 k$_{gr4}$	1.5 10^{-4}	(4)
			→	o-H$_2$	+	D	+	gr^0	1/6 k$_{gr4}$	5.0 10^{-5}	(4)
			→	HD	+	H	+	gr^0	1/3 k$_{gr4}$	1.0 10^{-4}	(4)
o–D$_2$H$^+$	+	gr$^-$	→	2D	+	H	+	gr^0	1/2 k$_{gr5}$	1.3 10^{-4}	(4)
			→	o–D$_2$	+	H	+	gr^0	1/6 k$_{gr5}$	4.4 10^{-5}	(4)
			→	HD	+	D	+	gr^0	1/3 k$_{gr5}$	8.9 10^{-5}	(4)
p–D$_2$H$^+$	+	gr$^-$	→	p–D$_2$	+	H	+	gr^0	1/6 k$_{gr5}$	4.4 10^{-5}	(4)
			→	HD	+	D	+	gr^0	1/3 k$_{gr5}$	8.9 10^{-5}	(4)
			→	2D	+	H	+	gr^0	1/2 k$_{gr5}$	1.3 10^{-4}	(4)
o–D$_3^+$	+	gr$^-$	→	3D	+	gr^0			2/3 k$_{gr6}$	1.6 10^{-4}	(4)
			→	o–D$_2$	+	D	+	gr^0	1/3 k$_{gr6}$	8.1 10^{-5}	(4)
m–D$_3^+$	+	gr$^-$	→	3D	+	gr^0			2/3 k$_{gr6}$	1.2 10^{-4}	(4)
			→	o–D$_2$	+	D	+	gr^0	1/6 k$_{gr6}$	4.1 10^{-5}	(4)
			→	p–D$_2$	+	D	+	gr^0	1/6 k$_{gr6}$	4.1 10^{-5}	(4)
p–D$_3^+$	+	gr$^-$	→	3D	+	gr^0			2/3 k$_{gr6}$	1.6 10^{-4}	(4)
			→	p–D$_2$	+	D	+	gr^0	1/3 k$_{gr6}$	8.1 10^{-5}	(4)
HCO$^+$	+	gr$^-$	→	H	+	CO	+	gr^0	k$_{HCO^+}$	1.1 10^{-4}	(4)
DCO$^+$	+	gr$^-$	→	D	+	CO	+	gr^0	k$_{DCO^+}$	1.1 10^{-4}	(4)
N$_2$H$^+$	+	gr$^-$	→	H	+	N$_2$	+	gr^0	k$_{N_2H^+}$	1.1 10^{-4}	(4)
N$_2$D$^+$	+	gr$^-$	→	D	+	N$_2$	+	gr^0	k$_{N_2D^+}$	1.1 10^{-4}	(4)

5.B DR RATE COEFFICIENTS OF THE H$_3^+$ ISOTOPOLOGUES

The dissociative recombination (DR) rate coefficients for ortho– and para–H$_3^+$ have been recently published by Fonseca dos Santos et al. [50]. Here, we present the results obtained for the all four H$_3^+$ isotopologues. The DR rate coefficients for different species of the nuclear spin are calculated using the approach described in a series of papers devoted to DR theory for triatomic molecular ions. See Fonseca dos Santos et al. [50], Kokoouline and Greene [60; 61] for H$_3^+$ and D$_3^+$ calculations and Kokoouline and Greene [62; 63] for H$_2$D$^+$ and D$_2$H$^+$. The scope of this paper does not allow to review the theoretical approach in detail. We only list its main ingredients.

The theoretical approach is fully quantum mechanical and incorporates no adjustable parameters. It relies on *ab initio* calculations of potential surfaces for the ground electronic state of the H$_3^+$ ion and several excited states of the neutral molecule H$_3$, performed by Mistrík et al. [64].

The total wave function of the system is constructed by an appropriate symmetrization of products of vibrational, rotational, electronic, and nuclear spin factors. Therefore, rovibronic and nuclear spin degrees of freedom are explicitly taken into account.

The electronic Born-Oppenheimer potentials for the four H_3^+ (and H_3) isotopologues have the C_{3v} symmetry group. The C_{3v} symmetry group has a two–dimensional irreducible representation E. The ion has a closed electronic shell. The lowest electronic state of the outer electron in H_3 has the p-wave character. The p-wave state of the electron also belongs to the E representation. Due to the Jahn-Teller theorem [65], this leads to a strong non-adiabatic coupling between the E-degenerate vibrational modes of the ion and the p-wave states of the incident electron. The coupling is responsible for the fast DR rate [66] in H_3^+. In the present model, only the p-wave electronic states are included because other partial waves have a much smaller effect on the DR probability : the s-wave states don't have the E-type character and, therefore, are only weakly coupled to the dissociative electronic states of H_3; d-wave electronic states are coupled to the E-vibrational modes, but the coupling is rather small because the d-wave of the incident electron does not penetrate sufficiently close to the ionic core owing to the d-wave centrifugal potential barrier.

All three internal vibrational coordinates are taken into account. Vibrational dynamics of the ionic core are described using the hyper-spherical coordinates, which represent the three vibrational degrees of freedom by a hyperradius and two hyperangles. The hyperradius is treated as a dissociation coordinate that represents uniformly the two possible DR channels, three-body (such as H+H+H) and two-body (such as H_2+H). Although the initial vibrational state of the ion is the ground state, after recombination with the electron, other vibrational states of the ionic target molecule can be populated. Therefore, in general, many vibrational states have to be included in the treatment. In particular, the states of the vibrational continuum have to be included, because only such states can lead to the dissociation of the neutral molecule. The vibrational states of the continuum are obtained using a complex absorbing potential placed at a large hyperradius to absorb the flux of the outgoing dissociative wave.

Since the rovibrational symmetry is D_{3h} for H_3^+ and D_3^+ and C_{2v} for H_2D^+ and D_2H^+, the rovibrational functions are classified according to the irreducible representations of the corresponding symmetry groups, i.e. A_1', A_1'', A_2', A_2'', E', and E'' for D_{3h} and A_1, A_2, B_1, and B_2 for C_{2v}. We use the rigid rotor approximation, i.e. the vibrational and rotational parts of the total wave function are calculated independently by diagonalizing the corresponding Hamiltonians. In our approach, the rotational wave functions must be obtained separately for the ions and for the neutral molecules. They are constructed in a different way for the D_{3h} and C_{2v} cases. The rotational eigenstates and eigenenergies of the D_{3h} molecules are symmetric top wave functions [see, for example 67]. They can be obtained analytically if the rotational constants are known. The rotational constants are obtained numerically from vibrational wave functions, i.e. they are calculated separately for each vibrational level of the target molecule. The rotational functions for the C_{2v} ions are obtained numerically by diagonalizing the asymmetric top Hamiltonian [63, 67].

Once the rovibrational wave functions are calculated, we construct the electron-ion scatter-

ing matrix (S-matrix). The S-matrix is calculated in the framework of quantum defect theory (QDT) [see, for example, 61, 63, 68] using the quantum defect parameters obtained from the *ab initio* calculation [64]. The constructed scattering matrix accounts for the Jahn-Teller effect and diagonal with respect to the different irreducible representations Γ and the total angular momentum N of the neutral molecule. Thus, the actual calculations are made separately for each Γ and N. Elements of the matrix describe the scattering amplitudes for the change of the rovibrational state of the ion after a collision with the electron. However, the S-matrix is not unitary due to the presence of the dissociative vibrational channels (i.e. continuum vibrational states of the ion, discussed above), which are not explicitly listed in the computed S-matrix. The "defect" from unitarity of each column of this S-matrix is associated with the dissociation probability of the neutral molecule formed during the scattering process. The dissociation probability per collision is then used to calculate the DR cross-sections and rate coefficients.

The nuclear spin states are characterized by one of the A_1, A_2, or E irreducible representations of the symmetry group S_3 for D_{3h} molecules and by the A or B irreducible representations of the symmetry group S_2 for C_{2v} molecules. The irreducible representation Γ_{ns} of a particular nuclear spin state determines its statistical weight and is related to the total nuclear spin $\vec{I}$ of the state. Here, $\vec{I}$ is the vector sum of spins $\vec{i}$ of identical nuclei.

For H_3^+, the $\Gamma_{ns} = A_1$ states (A_2' and A_2'' rovibrational states) correspond to $I = 3/2$ (ortho); the $\Gamma_{ns} = E$ states (E' and E'' rovibrational states) correspond to $I = 1/2$ (para). The statistical ortho:para weights are $2 : 1$. **For H_2D^+**, the $\Gamma_{ns} = A$ states (B_1 and B_2 rovibrational states) correspond to $I = 1$ (ortho); the $\Gamma_{ns} = B$ states (A_1 and A_2 rovibrational states) correspond to $I = 0$ (para). The statistical ortho:para weights are $3 : 1$. **For D_2H^+**, the $\Gamma_{ns} = A$ states (A_1 and A_2 rovibrational states) correspond to $I = 0, 2$ (ortho); the $\Gamma_{ns} = B$ states (B_1 and B_2 rovibrational states) correspond to $I = 1$ (para). The statistical ortho:para weights are $2 : 1$. Finally, **for D_3^+**, the $\Gamma_{ns} = A_1$ states (A_1' and A_1'' rovibrational states) correspond to $I = 1, 3$ (ortho); the $\Gamma_{ns} = A_2$ states (A_2' and A_2'' rovibrational states) correspond to $I = 0$ (para); the $\Gamma_{ns} = E$ states (E' and E'' rovibrational states) correspond to $I = 1, 2$ (meta). The statistical ortho:para:meta weights are $10 : 1 : 8$.

Figures (5.10a), (5.10b), (5.10c), and (5.10d) summarize the obtained DR thermal rate coefficients calculated separately for each nuclear spin species of the four H_3^+ isotopologues and the numerical values are listed in Table 5.4. For comparison, the figures show also the analytical dependences used in previous models of prestellar core chemistry (FPdFW). As one can see, the rates for different nuclear spin species are similar to each other (for a given isotopologue) at high temperatures. However, for lower temperatures, the rates for different ortho/para/meta-nuclear spin species significantly differ from each other. The difference in behavior at small temperatures is explained by different energies of Rydberg resonances present in DR cross-sections at low electron energies. The actual energies of such resonances are important for the thermal average at temperatures below or similar to the energy difference between ground rotational levels of different nuclear spin species. At higher temperatures, the exact energy of the resonances is not important. The averaged rate is determined by the density and the widths of the resonances, which are similar for all nuclear spin species over a large range of collision energies.
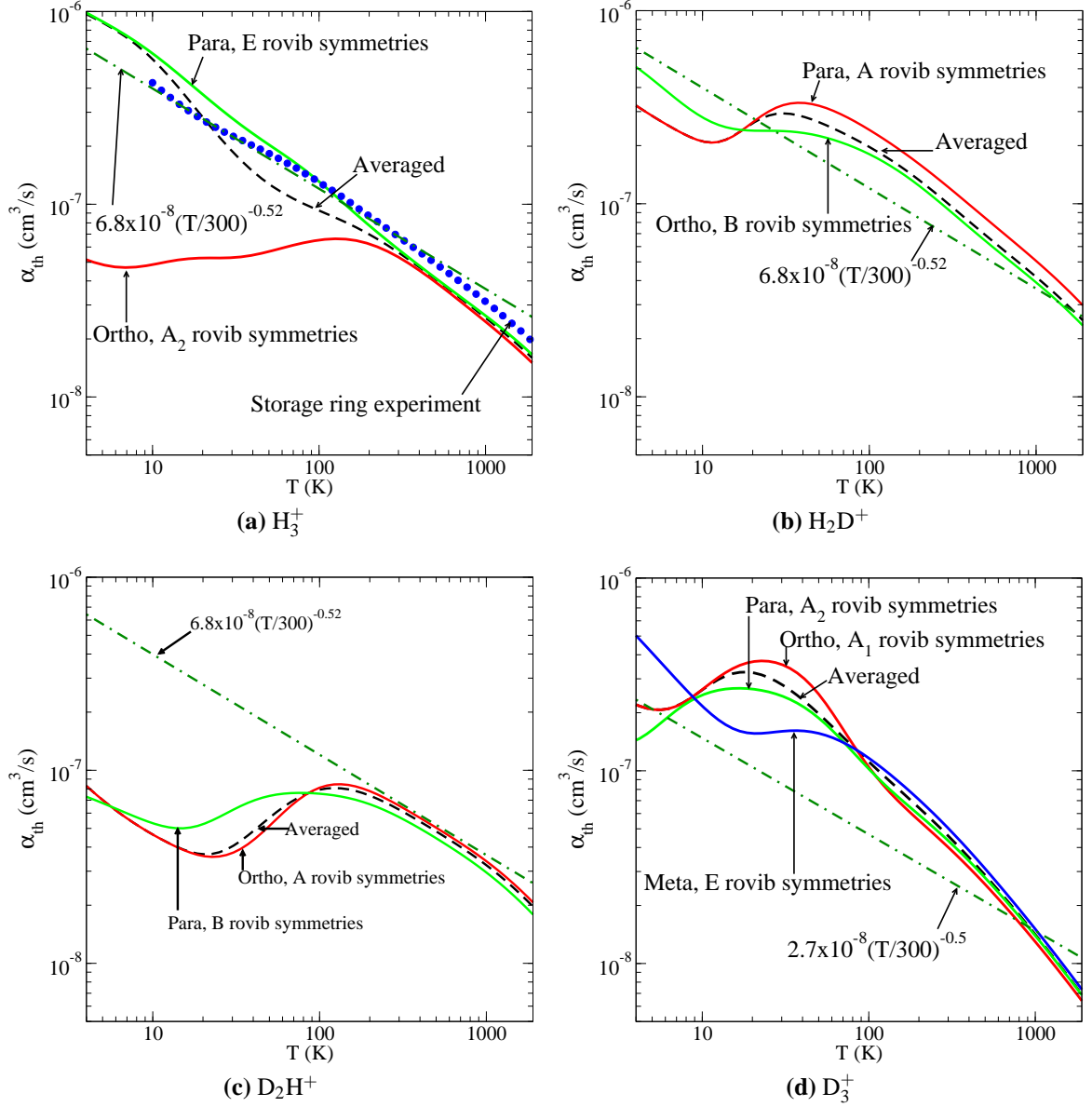
172

Figure 5.10: Theoretical DR rate coefficients as a function of temperature for the ortho, para (and meta) nuclear spin species of (a) H_3^+ (b) H_2D^+ (c) D_2H^+ (d) D_3^+. The figures also show the species-averaged rate coefficient. For comparison, we show the analytical dependence for the coefficient used in earlier models of prestellar cores by FPdFW. The rate coefficients obtained for H_3^+ in the TSR storage ring by Kreckel et al. [69] are also shown in figure (a).

Table 5.4: Dissociative recombination rates of H_3^+, H_2D^+, D_2H^+, and D_3^+ for each individual nuclear spin state species.

Temperature K	para–H_3^+ cm^3 s^{-1}	ortho–H_3^+ cm^3 s^{-1}	para–H_2D^+ cm^3 s^{-1}	ortho–H_2D^+ cm^3 s^{-1}	ortho–D_2H^+ cm^3 s^{-1}	para–D_2H^+ cm^3 s^{-1}	ortho–D_3^+ cm^3 s^{-1}	meta–D_3^+ cm^3 s^{-1}	para–D_3^+ cm^3 s^{-1}
1.28	1.81e-06	8.21e-08	6.63e-07	8.74e-07	2.18e-07	9.59e-08	6.33e-07	2.38e-06	2.61e-07
1.41	1.71e-06	7.86e-08	6.23e-07	8.46e-07	2.02e-07	9.36e-08	5.90e-07	2.22e-06	2.47e-07
1.56	1.61e-06	7.52e-08	5.85e-07	8.17e-07	1.87e-07	9.16e-08	5.49e-07	2.06e-06	2.34e-07
1.72	1.52e-06	7.20e-08	5.48e-07	7.87e-07	1.72e-07	8.98e-08	5.10e-07	1.90e-06	2.22e-07
1.90	1.44e-06	6.90e-08	5.14e-07	7.56e-07	1.58e-07	8.82e-08	4.73e-07	1.75e-06	2.10e-07
2.10	1.36e-06	6.61e-08	4.81e-07	7.25e-07	1.45e-07	8.65e-08	4.39e-07	1.61e-06	1.98e-07
2.32	1.29e-06	6.34e-08	4.51e-07	6.93e-07	1.32e-07	8.47e-08	4.08e-07	1.48e-06	1.88e-07
2.56	1.22e-06	6.08e-08	4.23e-07	6.60e-07	1.21e-07	8.28e-08	3.79e-07	1.35e-06	1.79e-07
2.83	1.16e-06	5.84e-08	3.97e-07	6.27e-07	1.11e-07	8.08e-08	3.52e-07	1.23e-06	1.72e-07
3.12	1.11e-06	5.62e-08	3.73e-07	5.94e-07	1.02e-07	7.87e-08	3.29e-07	1.12e-06	1.66e-07
3.45	1.06e-06	5.42e-08	3.51e-07	5.60e-07	9.35e-08	7.64e-08	3.08e-07	1.01e-06	1.62e-07
3.81	1.01e-06	5.23e-08	3.31e-07	5.28e-07	8.62e-08	7.41e-08	2.90e-07	9.18e-07	1.61e-07
4.20	9.63e-07	5.08e-08	3.13e-07	4.95e-07	7.98e-08	7.17e-08	2.74e-07	8.30e-07	1.63e-07
4.64	9.19e-07	4.94e-08	2.96e-07	4.63e-07	7.41e-08	6.94e-08	2.62e-07	7.49e-07	1.66e-07
5.13	8.77e-07	4.83e-08	2.81e-07	4.33e-07	6.90e-08	6.70e-08	2.52e-07	6.75e-07	1.73e-07
5.66	8.36e-07	4.76e-08	2.67e-07	4.04e-07	6.45e-08	6.47e-08	2.46e-07	6.07e-07	1.80e-07
6.25	7.95e-07	4.71e-08	2.54e-07	3.76e-07	6.04e-08	6.24e-08	2.43e-07	5.46e-07	1.90e-07
6.90	7.55e-07	4.69e-08	2.42e-07	3.51e-07	5.69e-08	6.02e-08	2.45e-07	4.92e-07	1.99e-07
7.62	7.14e-07	4.71e-08	2.31e-07	3.28e-07	5.37e-08	5.81e-08	2.50e-07	4.42e-07	2.09e-07
8.41	6.74e-07	4.75e-08	2.22e-07	3.08e-07	5.08e-08	5.61e-08	2.59e-07	3.98e-07	2.18e-07
9.29	6.35e-07	4.81e-08	2.14e-07	2.91e-07	4.82e-08	5.43e-08	2.72e-07	3.59e-07	2.27e-07
10.25	5.96e-07	4.88e-08	2.09e-07	2.77e-07	4.59e-08	5.28e-08	2.87e-07	3.25e-07	2.34e-07
11.32	5.58e-07	4.96e-08	2.07e-07	2.65e-07	4.38e-08	5.15e-08	3.04e-07	2.95e-07	2.39e-07
12.50	5.21e-07	5.05e-08	2.09e-07	2.56e-07	4.19e-08	5.06e-08	3.22e-07	2.69e-07	2.44e-07
13.80	4.86e-07	5.12e-08	2.14e-07	2.49e-07	4.02e-08	5.01e-08	3.39e-07	2.48e-07	2.46e-07
15.24	4.53e-07	5.18e-08	2.24e-07	2.44e-07	3.87e-08	5.01e-08	3.55e-07	2.30e-07	2.48e-07
16.82	4.21e-07	5.22e-08	2.36e-07	2.41e-07	3.74e-08	5.05e-08	3.68e-07	2.16e-07	2.49e-07
18.57	3.92e-07	5.25e-08	2.52e-07	2.40e-07	3.65e-08	5.15e-08	3.79e-07	2.06e-07	2.48e-07
20.51	3.65e-07	5.26e-08	2.68e-07	2.39e-07	3.58e-08	5.30e-08	3.85e-07	1.98e-07	2.46e-07
22.64	3.40e-07	5.26e-08	2.85e-07	2.39e-07	3.56e-08	5.49e-08	3.87e-07	1.92e-07	2.43e-07
25.00	3.17e-07	5.26e-08	3.01e-07	2.39e-07	3.58e-08	5.73e-08	3.85e-07	1.89e-07	2.40e-07

Temperature K	para–H_3^+ cm^3 s^{-1}	ortho–H_3^+ cm^3 s^{-1}	para–H_2D^+ cm^3 s^{-1}	ortho–H_2D^+ cm^3 s^{-1}	ortho–D_2H^+ cm^3 s^{-1}	para–D_2H^+ cm^3 s^{-1}	ortho–D_3^+ cm^3 s^{-1}	meta–D_3^+ cm^3 s^{-1}	para–D_3^+ cm^3 s^{-1}
27.60	2.96e-07	5.27e-08	3.14e-07	2.38e-07	3.64e-08	5.98e-08	3.79e-07	1.86e-07	2.35e-07
30.48	2.77e-07	5.29e-08	3.24e-07	2.38e-07	3.75e-08	6.26e-08	3.68e-07	1.83e-07	2.28e-07
33.65	2.59e-07	5.32e-08	3.31e-07	2.37e-07	3.92e-08	6.53e-08	3.53e-07	1.81e-07	2.21e-07
37.15	2.44e-07	5.38e-08	3.33e-07	2.35e-07	4.14e-08	6.78e-08	3.34e-07	1.78e-07	2.12e-07
41.02	2.29e-07	5.46e-08	3.32e-07	2.32e-07	4.42e-08	7.01e-08	3.11e-07	1.75e-07	2.02e-07
45.29	2.16e-07	5.57e-08	3.28e-07	2.29e-07	4.76e-08	7.21e-08	2.85e-07	1.71e-07	1.91e-07
50.01	2.04e-07	5.68e-08	3.22e-07	2.24e-07	5.15e-08	7.36e-08	2.57e-07	1.66e-07	1.79e-07
55.21	1.92e-07	5.81e-08	3.13e-07	2.20e-07	5.59e-08	7.48e-08	2.29e-07	1.60e-07	1.67e-07
60.96	1.81e-07	5.95e-08	3.03e-07	2.14e-07	6.06e-08	7.56e-08	2.01e-07	1.54e-07	1.54e-07
67.31	1.71e-07	6.08e-08	2.91e-07	2.08e-07	6.54e-08	7.61e-08	1.76e-07	1.47e-07	1.42e-07
74.31	1.61e-07	6.21e-08	2.79e-07	2.02e-07	7.01e-08	7.63e-08	1.54e-07	1.40e-07	1.30e-07
82.05	1.51e-07	6.33e-08	2.67e-07	1.95e-07	7.44e-08	7.63e-08	1.34e-07	1.33e-07	1.19e-07
90.59	1.41e-07	6.43e-08	2.54e-07	1.88e-07	7.82e-08	7.61e-08	1.18e-07	1.25e-07	1.09e-07
100.02	1.31e-07	6.52e-08	2.41e-07	1.81e-07	8.12e-08	7.56e-08	1.05e-07	1.18e-07	1.00e-07
110.43	1.22e-07	6.58e-08	2.29e-07	1.73e-07	8.33e-08	7.50e-08	9.35e-08	1.10e-07	9.21e-08
121.93	1.13e-07	6.61e-08	2.17e-07	1.65e-07	8.45e-08	7.42e-08	8.42e-08	1.03e-07	8.50e-08
134.62	1.05e-07	6.61e-08	2.05e-07	1.57e-07	8.46e-08	7.31e-08	7.65e-08	9.58e-08	7.87e-08
148.64	9.70e-08	6.58e-08	1.93e-07	1.48e-07	8.40e-08	7.19e-08	7.00e-08	8.91e-08	7.31e-08
164.11	8.99e-08	6.50e-08	1.82e-07	1.40e-07	8.25e-08	7.04e-08	6.44e-08	8.27e-08	6.80e-08
181.20	8.35e-08	6.38e-08	1.71e-07	1.32e-07	8.05e-08	6.86e-08	5.94e-08	7.67e-08	6.34e-08
200.06	7.76e-08	6.23e-08	1.60e-07	1.23e-07	7.80e-08	6.67e-08	5.50e-08	7.09e-08	5.90e-08
220.89	7.23e-08	6.04e-08	1.50e-07	1.15e-07	7.51e-08	6.46e-08	5.11e-08	6.54e-08	5.49e-08
243.88	6.73e-08	5.83e-08	1.40e-07	1.08e-07	7.21e-08	6.23e-08	4.73e-08	6.02e-08	5.10e-08
269.27	6.28e-08	5.59e-08	1.31e-07	1.00e-07	6.90e-08	5.99e-08	4.38e-08	5.53e-08	4.73e-08
297.31	5.87e-08	5.34e-08	1.22e-07	9.34e-08	6.58e-08	5.74e-08	4.04e-08	5.07e-08	4.37e-08
328.26	5.48e-08	5.08e-08	1.14e-07	8.68e-08	6.27e-08	5.49e-08	3.73e-08	4.64e-08	4.03e-08
362.43	5.13e-08	4.81e-08	1.06e-07	8.07e-08	5.97e-08	5.24e-08	3.43e-08	4.23e-08	3.71e-08
400.16	4.80e-08	4.54e-08	9.85e-08	7.51e-08	5.67e-08	4.99e-08	3.15e-08	3.86e-08	3.41e-08
441.82	4.49e-08	4.27e-08	9.17e-08	6.99e-08	5.38e-08	4.74e-08	2.88e-08	3.51e-08	3.12e-08
487.81	4.21e-08	4.01e-08	8.53e-08	6.50e-08	5.11e-08	4.51e-08	2.63e-08	3.18e-08	2.85e-08
538.60	3.95e-08	3.76e-08	7.94e-08	6.06e-08	4.85e-08	4.27e-08	2.40e-08	2.88e-08	2.60e-08
594.67	3.70e-08	3.52e-08	7.40e-08	5.65e-08	4.59e-08	4.05e-08	2.19e-08	2.61e-08	2.36e-08
656.58	3.47e-08	3.29e-08	6.88e-08	5.27e-08	4.35e-08	3.83e-08	1.99e-08	2.35e-08	2.14e-08

Temperature K	para–H_3^+ cm^3 s^{-1}	ortho–H_3^+ cm^3 s^{-1}	para–H_2D^+ cm^3 s^{-1}	ortho–H_2D^+ cm^3 s^{-1}	ortho–D_2H^+ cm^3 s^{-1}	para–D_2H^+ cm^3 s^{-1}	ortho–D_3^+ cm^3 s^{-1}	meta–D_3^+ cm^3 s^{-1}	para–D_3^+ cm^3 s^{-1}
724.93	3.26e-08	3.08e-08	6.41e-08	4.91e-08	4.11e-08	3.62e-08	1.80e-08	2.12e-08	1.94e-08
800.40	3.05e-08	2.87e-08	5.96e-08	4.58e-08	3.88e-08	3.41e-08	1.63e-08	1.91e-08	1.76e-08
883.72	2.86e-08	2.68e-08	5.55e-08	4.27e-08	3.66e-08	3.20e-08	1.47e-08	1.72e-08	1.59e-08
975.72	2.68e-08	2.50e-08	5.15e-08	3.98e-08	3.43e-08	3.01e-08	1.33e-08	1.55e-08	1.43e-08
1077.30	2.51e-08	2.33e-08	4.78e-08	3.70e-08	3.22e-08	2.81e-08	1.20e-08	1.39e-08	1.29e-08
1189.45	2.35e-08	2.17e-08	4.43e-08	3.44e-08	3.00e-08	2.62e-08	1.08e-08	1.25e-08	1.16e-08
1313.28	2.20e-08	2.02e-08	4.09e-08	3.19e-08	2.80e-08	2.43e-08	9.70e-09	1.12e-08	1.04e-08
1450.00	2.05e-08	1.87e-08	3.77e-08	2.95e-08	2.59e-08	2.25e-08	8.70e-09	1.00e-08	9.33e-09
1600.95	1.90e-08	1.73e-08	3.47e-08	2.72e-08	2.40e-08	2.08e-08	7.80e-09	8.95e-09	8.36e-09
1767.62	1.76e-08	1.60e-08	3.18e-08	2.50e-08	2.21e-08	1.91e-08	6.97e-09	7.99e-09	7.47e-09
1951.64	1.63e-08	1.47e-08	2.91e-08	2.29e-08	2.02e-08	1.75e-08	6.23e-09	7.12e-09	6.67e-09
2154.81	1.50e-08	1.35e-08	2.66e-08	2.09e-08	1.85e-08	1.60e-08	5.55e-09	6.34e-09	5.94e-09
2379.14	1.38e-08	1.24e-08	2.42e-08	1.91e-08	1.69e-08	1.45e-08	4.94e-09	5.64e-09	5.29e-09
2626.82	1.26e-08	1.13e-08	2.19e-08	1.73e-08	1.53e-08	1.32e-08	4.39e-09	5.00e-09	4.70e-09
2900.28	1.15e-08	1.03e-08	1.98e-08	1.57e-08	1.38e-08	1.19e-08	3.90e-09	4.44e-09	4.17e-09
3202.22	1.04e-08	9.36e-09	1.79e-08	1.42e-08	1.25e-08	1.07e-08	3.46e-09	3.93e-09	3.70e-09
3535.58	9.48e-09	8.47e-09	1.61e-08	1.28e-08	1.12e-08	9.65e-09	3.06e-09	3.48e-09	3.27e-09
3903.65	8.57e-09	7.66e-09	1.45e-08	1.15e-08	1.01e-08	8.66e-09	2.71e-09	3.08e-09	2.90e-09
4310.04	7.75e-09	6.91e-09	1.30e-08	1.03e-08	9.04e-09	7.76e-09	2.40e-09	2.72e-09	2.57e-09
4758.74	6.99e-09	6.23e-09	1.16e-08	9.26e-09	8.10e-09	6.95e-09	2.13e-09	2.41e-09	2.27e-09
5254.15	6.31e-09	5.61e-09	1.04e-08	8.31e-09	7.26e-09	6.23e-09	1.89e-09	2.14e-09	2.02e-09
5801.13	5.70e-09	5.06e-09	9.39e-09	7.47e-09	6.51e-09	5.58e-09	1.68e-09	1.90e-09	1.79e-09
6405.05	5.15e-09	4.58e-09	8.45e-09	6.73e-09	5.85e-09	5.02e-09	1.50e-09	1.69e-09	1.60e-09
7071.85	4.67e-09	4.14e-09	7.63e-09	6.08e-09	5.27e-09	4.52e-09	1.34e-09	1.51e-09	1.43e-09
7808.06	4.24e-09	3.77e-09	6.91e-09	5.50e-09	4.77e-09	4.08e-09	1.20e-09	1.36e-09	1.29e-09
8620.92	3.87e-09	3.43e-09	6.28e-09	5.01e-09	4.33e-09	3.71e-09	1.09e-09	1.23e-09	1.16e-09
9518.40	3.55e-09	3.14e-09	5.73e-09	4.57e-09	3.95e-09	3.38e-09	9.86e-10	1.11e-09	1.05e-09
10509.31	3.26e-09	2.89e-09	5.26e-09	4.20e-09	3.61e-09	3.09e-09	8.99e-10	1.01e-09	9.60e-10
11603.38	3.01e-09	2.67e-09	4.85e-09	3.87e-09	3.33e-09	2.85e-09	8.25e-10	9.29e-10	8.80e-10
12811.35	2.80e-09	2.48e-09	4.50e-09	3.58e-09	3.08e-09	2.63e-09	7.61e-10	8.56e-10	8.12e-10
14145.07	2.61e-09	2.31e-09	4.19e-09	3.34e-09	2.86e-09	2.45e-09	7.05e-10	7.94e-10	7.53e-10
15617.64	2.45e-09	2.16e-09	3.92e-09	3.12e-09	2.67e-09	2.29e-09	6.58e-10	7.40e-10	7.01e-10

Declaration on honour

Ich versichere, dass ich die von mir vorgelegte Dissertation selbstständig angefertigt, die benutzten Quellen und Hilfsmittel vollständig angegeben und die Stellen der Arbeit - einschließlich Tabellen, Karten und Abbildungen-, die anderen Werken im Wortlaut oder dem Sinn nach entnommen sind, in jedem Einzelfall als Entlehnung kenntlich gemacht habe; dass diese Dissertation noch keiner anderen Fakultät oder Universität zur Prüfung vorgelegen hat; dass sie - abgesehen von unten angegebenen Teilpublikationen - noch nicht veröffentlicht worden ist sowie, dass ich eine solche Veröffentlichung vor Abschluss des Promotionsverfahrens nicht vornehmen werde. Die Bestimmungen der Promotionsordnung sind mir bekannt. Die von mir vorgelegte Dissertation ist von Herrn Professor Dr. S. Schlemmer betreut worden.

List of publications

Chapter 2

"Nuclear spins in reactive collisions: angular monetum and symmetry viewpoints", E. Hugo, S. Schlemmer and P. Jensen, in preparation

Chapter 3

"The H_3^+ + H_2 isotopic system at low temperatures: Microcanonical model and experimental study", E. Hugo, O. Asvany and S. Schlemmer, submitted to *Journal of Chemical Physics* (2008)

Chapter 4

"Overtone spectroscopy of H_2D^+ and D_2H^+ using laser induced reactions", O. Asvany, E. Hugo, F. Müller, F. Kühnemann, S. Schiller, J. Tennyson and S. Schlemmer, *Journal of Chemical Physics*, **127**, 154317 (2007)

Chapter 5

"Chemical modeling of L183 (=L134N): an estimate of the ortho/para H_2 ratio", L. Pagani, C. Vastel, E. Hugo, V. Kokoouline, C.H. Greene, A. Bacmann, E. Bayet, C. Ceccarelli, R. Peng and S. Schlemmer, accepted by *Astronomy & Astrophysics* (2008)

Not in this thesis

"Deuterium Fractionation and Ion-Molecule Reactions at Low Temperatures", S. Schlemmer, O. Asvany, E. Hugo, and D. Gerlich, in *Astrochemistry: Recent Successes and Current Challenges*, edited by D.C. Lis, G.A. Blake and E. Herbst (2005), vol. 231 of *IAU Symposium*, pp. 125–134

"Toward understanding of H_3^+ isotopic and nuclear spin fractionations in cold space", E. Hugo, O. Asvany, J. Harju and S. Schlemmer, in *Molecules in Space and Laboratory*, edited by J.L. Lemaire and F. Combes (2007), pp. 119

Curriculum Vitae

Edouard Jean–Marie H\ **UGO**

Date of birth:	17th of October 1979
Place of birth:	Alençon, France
Nationality:	French

Education

1985–1988	Primary school in Oisly, Choussy, Coudes (France, 41)
1988–1991	French–Irish primary and secondary school in Dublin (Ireland)
1991–1994	Secondary school (Collège) in Cesson–Sévigné (France, 35)
1994–1997	Secondary school (Lycée) in Cesson–Sévigné (France, 35)
1997	Baccalauréat série S

Studies

1997–2003	National Institut for Applied Science (INSA) in Rennes (France, 35)
2002–2003	Master of Advanced Studies (DEA) at the University of Rennes I (France, 35)
2003	Engineer Master's degree in Physics, "Materials science and Nanotechnology"
	University Master's degree in Physics, "Matter and Radiation"

Work experience

02/2003–06/2003	Master training in the *Laboratory Astrochemistry* workgroup
	at the Institut de Physique UMR – 6251, University of Rennes I (France)
09/2004–09/2005	1st year Ph.D. in the *Laboratory astrophysics and astrochemistry* workgroup
	at the Leiden Observatory (Netherlands)
Since 10/2005	Last years Ph.D. in the *Laboratory astrophysics* workgroup
	at the I. Physikalisches Institut, University of Köln (Germany)

Acknowledgements

I also want to acknowledge the many people who played important roles in my work. That includes the two master students, Serjoscha Wahed and Sabrina Gaertner, who helped me for the characterisation of the p–H_2 generator and conducing exciting LIR experiments, Laurent Pagani and Charlotte Vastel for the fruitful astronomical collaboration which gave this completeness flavour to my thesis, the helpful secretaries and workshop who are the essential gears of the institute and Robert Georges, my master thesis' supervisor who gave me the taste for research. I must also acknowledge the people and entities which contribute to the universality of knowledge against the marketisation logic. I support in particular Wikipedia as well as Linux and GNU projects which helped me a lot during this doctorate.

These four years abroad were also an enriching experience out of the work frame. Although I cannot give a full list, I would like to cite some people who took part in this unforgettable human adventure: Sophie, Maud, Laure, Alberto & Bea, Cedric, Toto, Niruj, Estelle, Anne, Marie & Patricia, Chiara, Nina, Julia, Katia & Markus, Vincent and last but not least, Kora. I address a special mention to my two flatmates with whom I shared a lot of intense moments forever anchored in my memory and are thus very dear to my heart: Cyril and Franzi !

The only negative aspect of this doctorate has been the distance which limited the encounters with my family and my friends from Cesson and the INSA. Nevertheless, they have always been of great support and for that, I am thankful. Mais celle qui m'a surtout fait souffrir, c'est cette distance avec toi, Cathel, que j'aime tant.

Finally, I would like to apologize to the less "developed" countries, plants, animals and their future generations for the finite ressources dissipated, the negative perturbations of our common environment and any indirect arm caused by this whole Ph.D. project. Our society and its Science machinery are non–sustainable and will have to change fundamentally some day. *What we do* and *how we do it* are important questions but the essence remains *why we do it*.

Köln, the 12th of February 2009

184